

Mechanical Fatigue Testing of High-Burnup Fuel for Transportation Applications

AVAILABILITY OF REFERENCE MATERIALS IN NRC PUBLICATIONS

NRC Reference Material

As of November 1999, you may electronically access NUREG-series publications and other NRC records at the NRC's Public Electronic Reading Room at <http://www.nrc.gov/reading-rm.html>. Publicly released records include, to name a few, NUREG-series publications; *Federal Register* notices; applicant, licensee, and vendor documents and correspondence; NRC correspondence and internal memoranda; bulletins and information notices; inspection and investigative reports; licensee event reports; and Commission papers and their attachments.

NRC publications in the NUREG series, NRC regulations, and Title 10, "Energy," in the *Code of Federal Regulations* may also be purchased from one of these two sources.

1. The Superintendent of Documents

U.S. Government Publishing Office
Mail Stop SSOP
Washington, DC 20402-0001
Internet: <http://bookstore.gpo.gov>
Telephone: 1-866-512-1800
Fax: (202) 512-2104

2. The National Technical Information Service

5301 Shawnee Road
Alexandria, VA 22161-0002
<http://www.ntis.gov>
1-800-553-6847 or, locally, (703) 605-6000

A single copy of each NRC draft report for comment is available free, to the extent of supply, upon written request as follows:

U.S. Nuclear Regulatory Commission

Office of Administration
Publications Branch
Washington, DC 20555-0001
E-mail: distribution.resource@nrc.gov
Facsimile: (301) 415-2289

Some publications in the NUREG series that are posted at the NRC's Web site address <http://www.nrc.gov/reading-rm/doc-collections/nuregs> are updated periodically and may differ from the last printed version. Although references to material found on a Web site bear the date the material was accessed, the material available on the date cited may subsequently be removed from the site.

Non-NRC Reference Material

Documents available from public and special technical libraries include all open literature items, such as books, journal articles, transactions, *Federal Register* notices, Federal and State legislation, and congressional reports. Such documents as theses, dissertations, foreign reports and translations, and non-NRC conference proceedings may be purchased from their sponsoring organization.

Copies of industry codes and standards used in a substantive manner in the NRC regulatory process are maintained at—

The NRC Technical Library

Two White Flint North
11545 Rockville Pike
Rockville, MD 20852-2738

These standards are available in the library for reference use by the public. Codes and standards are usually copyrighted and may be purchased from the originating organization or, if they are American National Standards, from—

American National Standards Institute

11 West 42nd Street
New York, NY 10036-8002
<http://www.ansi.org>
(212) 642-4900

Legally binding regulatory requirements are stated only in laws; NRC regulations; licenses, including technical specifications; or orders, not in NUREG-series publications. The views expressed in contractor-prepared publications in this series are not necessarily those of the NRC.

The NUREG series comprises (1) technical and administrative reports and books prepared by the staff (NUREG-XXXX) or agency contractors (NUREG/CR-XXXX), (2) proceedings of conferences (NUREG/CP-XXXX), (3) reports resulting from international agreements (NUREG/IA-XXXX), (4) brochures (NUREG/BR-XXXX), and (5) compilations of legal decisions and orders of the Commission and Atomic and Safety Licensing Boards and of Directors' decisions under Section 2.206 of NRC's regulations (NUREG-0750).

DISCLAIMER: This report was prepared as an account of work sponsored by an agency of the U.S. Government. Neither the U.S. Government nor any agency thereof, nor any employee, makes any warranty, expressed or implied, or assumes any legal liability or responsibility for any third party's use, or the results of such use, of any information, apparatus, product, or process disclosed in this publication, or represents that its use by such third party would not infringe privately owned rights.



United States Nuclear Regulatory Commission

Protecting People and the Environment

NUREG/CR-7198, Rev. 1
ORNL/TM-2016/689

Mechanical Fatigue Testing of High-Burnup Fuel for Transportation Applications

Manuscript Completed: December 2016
Date Published: October 2017

Prepared by: Jy-An Wang and Hong Wang

Oak Ridge National Laboratory
Managed by UT-Battelle, LLC
Oak Ridge, TN 37831-6069

Bruce Bevard, ORNL Program Manager

Michelle Flanagan-Bales, NRC Project Manager

NRC Job Code N6686/N6789

Office of Nuclear Regulatory Research

ABSTRACT

Testing was conducted at Oak Ridge National Laboratory (ORNL) to determine the ability of high burnup (HBU) (>45 GWd/MTU) spent nuclear fuel (SNF) to maintain its integrity under conditions relevant to storage and transport. The cyclic integrated reversible-bending fatigue tester (CIRFT) is an innovative system used in these tests. The CIRFT can impose pure bending loads on SNF test specimens and can measure the in situ curvature of the fuel rod during bending. *Pure bending* is a condition of stress in which a bending moment is applied to a beam without the simultaneous presence of axial, shear, or torsional forces. The CIRFT is composed of a U-frame equipped with load cells. A setup with three linear variable differential transformers (LVDTs) was used.

Since the initial publication of this NUREG in May 2015, several new factors were identified that influence the recorded curvature measurement data. Because these factors were not accounted for in the first publication, the initial quantitative results are not considered valid. This revision provides updated results of the 2015 CIRFT tests.

After the 2015 publication, a new phase of testing was implemented that used samples treated to induce radial hydrides. This revision includes the results of CIRFT tests on segments subjected to hydride reorientation treatment (HRT), thus broadening the applicability of the research results. This first revision entirely replaces the initial May 2015 publication.

The HBU SNF rods with Zircaloy-4 (Zry-4) cladding were studied under static and dynamic (cyclic) bending. They survived static unidirectional bending to a maximum curvature of 2.2–2.5 m⁻¹, or a maximum moment of 85–87 N·m. The maximum longitudinal cladding strain before failure or before reaching CIRFT displacement capacity was 1.2–1.3%. The segment composite structure of an HBU rod introduces numerous stress riser sites into the rod system, often resulting in specimen fracture at the pellet-to-pellet interface regions under both static and dynamic CIRFT testing. Nevertheless, the static CIRFT test results on HBU rods indicate that fueled rods have a significantly greater flexural rigidity than the calculated flexural rigidity for HBU cladding alone.

During dynamic testing, the fatigue life of HBU rods mainly depended on the level of loading. Under loading with moments of ±5.08 to ±35.56 N·m, which resulted in an equivalent strain (ϵ) of ±0.025 to ±0.31% strain at 5 Hz, the fatigue life (N) ranged from 5.5×10^3 to 2.3×10^6 cycles. Considering the complexity and nonuniformity of the HBU fuel cladding system, it was significant to find that the ϵ -N data for the HBU were characterized by a curve that would be expected for standard uniform materials. The ϵ -N curve of the HBU rods can be described by a power function of $y = 3.839 \cdot x^{-0.298}$, where x is the number of cycles to failure, and y is the strain amplitude (%). It was also significant to find that, if an endurance limit is defined by survival of $>10^7$ cycles (as is typical for material fatigue endurance limits), then the HBU rods tested exhibited an endurance limit. The endurance limit for the HBU rods tested is likely between strains 0.03–0.05%.

The maxima of the imposed curvature κ during dynamic testing ranged from ±0.07 to ±0.62 m⁻¹ at 5 Hz. The κ -N curve of the HBU rods can be described by a power function of $y = 6.864 \cdot x^{-0.283}$, where x is the number of cycles to failure and y is the maxima of clad tensile curvature $|\kappa|_{\max}$ (m⁻¹). An endurance limit is likely between 0.07–0.12 m⁻¹ when it is defined at 10^7 cycles.

From very limited CIRFT test results of rods that underwent HRT, the following phenomena were observed.

- HRT rods in static testing showed that the maximum moment decreased in comparison to that of as-irradiated fuel rods at similar curvature levels.
- Both the HRT static and dynamic flexural rigidity are less than that of as-irradiated baseline data.
- The load amplitude vs. failure frequency trend indicated that HRT rods had slightly less fatigue life than those indicated in the as-irradiated baseline CIRFT data.

FOREWORD

To obtain certification for a spent nuclear fuel (SNF) storage cask and transportation package, the US Nuclear Regulatory Commission (NRC) requires evaluation of nuclear fuel performance under normal and accident conditions as specified in 10 Code of Federal Regulations (CFR) Parts 71 and 72. The safety and security of SNF storage and transportation systems must be demonstrated to obtain certification. As part of the requirement to demonstrate safety, the applicant must assess the condition and performance of SNF in the storage and transportation system during operations and design-basis accidents.

In the United States, SNF is expected to be transported off site to at least one storage facility before permanent disposal. While the SNF is in transport or in dry storage, it will experience various localized stresses. As nuclear fuel is now regularly irradiated to high-burnup (HBU) values (>45 GWd/MTU), any phenomena associated with HBU SNF that could impact fatigue resistance (e.g., hydride reorientation) should be evaluated under storage and transportation conditions.

For these reasons, the NRC tasked the Oak Ridge National Laboratory (ORNL) to investigate the flexural rigidity and fatigue life of HBU SNF. Testing was designed to evaluate the fuel rod as a composite system, including the presence of fuel inside the cladding and any pellet/cladding bonding effects. The project proceeded in two phases. Phase I involved testing HBU SNF in the as-irradiated state, in which hydrides are expected to be predominantly in the circumferential-axial orientation. Phase II involved testing HBU SNF segments following a treatment designed to reorient the hydrides in the cladding to be predominantly in the radial-axial orientation. The properties measured in this testing program should be observed to evaluate SNF integrity under storage and transportation conditions, including the details of SNF package or cask design and expected loads.

This first revision entirely replaces the initial May 2015 publication. It includes revised results of previous CIRFT tests, as well as new results of testing on the samples treated to induce radial hydrides.

TABLE OF CONTENTS

ABSTRACT	iii
FOREWORD	v
TABLE OF CONTENTS	vii
LIST OF FIGURES	ix
LIST OF TABLES	xi
EXECUTIVE SUMMARY	xiii
ACKNOWLEDGMENTS	xv
LIST OF ACRONYMS, ABBREVIATIONS, AND UNITS	xvii
1 INTRODUCTION	1
2 APPROACH	3
3 EXPERIMENTAL METHOD	7
3.1 The U-Frame Setup	7
3.2 Grip Design	9
3.3 LVDT Measurements and Corrections	13
3.3.1 Correction for Disk-Type LVDT Head Bias.....	13
3.3.2 Curvature Adjustment for LVDT Stem Dynamic Stability.....	16
3.4 Test Segment Selection and Preparation	17
3.4.1 Hydride-Reorientation Treatment (HRT) Procedure	19
3.5 Test Protocol.....	20
3.5.1 Static Testing.....	20
3.5.2 Dynamic Testing.....	21
3.6 Data Processing.....	22
3.6.1 Flexural Rigidity Calculation.....	23
4 RESULTS	26
4.1 Static Tests	26
4.1.1 Characteristics of Moment-Curvature Curve	32
4.1.2 Comparison of Static Results with PNNL Cladding Data.....	34
4.2 Dynamic Testing	36
4.2.1 κ -N Curve	50
4.3 Post-Irradiation Examination	55
4.3.1 As-Irradiated Samples PIE.....	55
4.3.2 HRT Samples PIE	58
4.4 Cladding Oxide Effect Study.....	59
4.5 HRT CIRFT Test Data Evaluation	60
5 CONCLUSIONS	63

6	REFERENCES	65
APPENDIX A	ROD SEGMENTS AND CUTTING PLAN	A-1
APPENDIX B	METROLOGY OF ROD SEGMENTS	B-1
APPENDIX C	BENCHMARKING OF TEST SYSTEM.....	C-1
APPENDIX D	STATIC TEST RESULTS	D-1
APPENDIX E	DYNAMIC TEST RESULTS.....	E-1
APPENDIX F	POST-IRRADIATION EXAMINATION (PIE)	F-1
APPENDIX G	VERIFICATION OF CURVATURE MEASUREMENT	G-1
APPENDIX H	HYDRIDE REORIENTATION SAMPLE PREPARATION.....	H-1

LIST OF FIGURES

Figure 1	The cyclic integrated reversible-bending fatigue tester developed by ORNL.....	3
Figure 2	Determination of the rod's bending curvature by use of deflections measured at three points.....	4
Figure 3	Key fuel and cladding features and fuel rod phenomena of (a) an unloaded fuel rod, and (b) a fuel rod under a bending load.	5
Figure 4	(a) Horizontal layout of ORNL U-frame setup; (b) rod specimen and three LVDTs for curvature measurement; and (c) front view of CIRFT installed in ORNL hot cell.	8
Figure 5	Schematic drawings of U-frame setup for reversal bending when rigid arms are (a) closing, (b) neutral, and (c) opening. Δ is the rigid rod end displacement at loading joint.	9
Figure 6	Assembled grip blocks (left) and two views (right) of detached grip body.....	10
Figure 7	Image showing the grip design of CIRFT with one end-block removed.	10
Figure 8	(a) Vise mold for assembling octagonal rigid sleeves into a rod, (b) rod (Demo1, 606B2) to be inserted, (c) one pin turned away, rigid sleeve loaded with epoxy inserted into the lower chamber.	12
Figure 9	LVDT disk-type probe bias: effect of LVDT probe with disk shape on curvature measurement where contact points are shifted outwards (on the compression side of the rod) and inwards (on the tension side of the rod).	14
Figure 10	Diagram of circle showing quantities in calculating half gauge length of bent rod.	15
Figure 11	Curvature measurements of polycarbonate rod based on M-based estimate, and disk type probe, 2.50 mm sensor spacing correction.....	16
Figure 12	Variations of (a) peak strain and (b) valley strain as a function of driving frequency. At 5 Hz, corrected strain level is about 18% higher than strain gauge estimate for both peak and valley strain plots.	17
Figure 13	Segment 608C4B for DL2 taken from rod G10, with the storage tube.....	18
Figure 14	Sample temperature as a function of time for HR1.....	20
Figure 15	Flowchart for cyclic testing of SNF rod.....	21
Figure 16	Moment, curvature time series, and moment-curvature hysteresis loop for rod D1. Two measurements are displayed with relative displacement 0.8 and 1.2 mm at the loading points of U-frame.	23
Figure 17	Empty-run conducted without specimen installed, for which the load and displacement were plotted; associated with static test on D1.....	25
Figure 18	Curve of moment versus curvature.....	26
Figure 19	Mating fracture surfaces (a) and (b); lateral sides near the neutral axis of the bending rod for S1 (606C3C) (c) and (d).....	27
Figure 20	(a) Moment-curvature curves measurements and (b) stress and strain curves in static tests.....	29
Figure 21	Characteristic points of moment-curvature curve.	32
Figure 22	Comparison of CIRFT global data with theoretical PNNL moment-curvature derived from PNNL cladding only stress-strain data.....	34
Figure 23	Moment and curvature as a function of time and moment-curvature loops based on measurements when (a) $N=1$ and (b) $N = 111,000$ cycles for D1 (607C4B); measurements were made with 0.8 and 1.2 mm relative displacements; $N_f = 1.1 \times 10^5$ cycles under ± 15.24 N-m, 5 Hz. Fuel particles collected < 1.0 g.	37

Figure 24	(a) Moment-curvature relation and (b) moment-flexural rigidity relation at various numbers of cycles for D1 (607C4B); $N_f = 1.1 \times 10^5$ cycles under ± 15.24 N·m, 5 Hz. Fuel particles collected <1.0 g.....	38
Figure 25	Variations of (a) curvature range, (b) moment range, (c) flexural rigidity as a function of number of cycles for D1 (607C4B); $N_f = 1.1 \times 10^5$ cycles under ± 15.24 N·m, 5 Hz; fuel particles collected <1.0 g.	38
Figure 26	Variations of (a) curvature range, (b) applied moment range, (c) flexural rigidity, (d) maximum and minimum values of curvature, (e) maximum and minimum values of moment, and (f) flexural hysteresis as a function of number of cycles for D1 (607C4B); $N_f = 1.1 \times 10^5$ cycles under ± 15.24 N·m, 5 Hz; fuel particles collected <1.0 g.	39
Figure 27	Moment and curvature as a function of time at (a) 26 and (b) 1.10×10^5 cycles; results based on online monitoring;the initial unsymmetrical curvature deformation mode of the tested rod was stabilized and replaced with a symmetrical curvature deformation mode at higher cycles.....	41
Figure 28	(a) and (b) mating fracture surfaces, (c) frontal, and (d) back sides for D1 (607C4B), $N_f = 1.1 \times 10^5$ cycles under ± 15.24 N·m, 5 Hz. Fuel particles collected <1.0 g.	42
Figure 29	Equivalent strain amplitudes ($\Delta\varepsilon/2$) as a function of the number of cycles to failure. Markers with arrows indicate that the tests stopped without failure.	49
Figure 30	Equivalent strain amplitudes ($\Delta\varepsilon/2$) as a function of number of cycles to failure with curve fitting extended to include data points without failure;markers with arrows indicate that the tests stopped without failure.	50
Figure 31	(a) Maxima of absolute curvature extremes and curvature amplitudes as a function of number of cycles to failure, and (b) maxima of absolute strain extremes and strain amplitudes as a function of number of cycles to failure; markers with arrows indicate that the tests were stopped without failure.....	52
Figure 32	(a) Curvature amplitudes, (b) maxima of absolute curvature extremes, and (c) maxima of absolute strain extremes as a function of number of cycles to failure; Curve-fitting was extended to include the no-failure data points; markers with arrows indicate that the tests were stopped without failure.	54
Figure 33	Images of untested segment 605D1D for (a) overall axial cross section and (b) enlarged area A.	56
Figure 34	(a) Axial cross section of S2/ 605D1E, (b) fracture surface near back side of rod and an enlarged area, and (c) fracture surface near front side of rod and an enlarged area (A = delamination of circumferential hydride layers, B = spalling and cracking of oxide layer).	57
Figure 35	(a) High magnification micrograph showing radial hydrides of Sample HR-1 ($H \approx 360\text{--}400$ ppm); the HBU HBR specimen was pressurized to 140 MPa at 400 °C with five thermal cycles; (b) high magnification micrograph showing radial hydrides of a sample of unirradiated, hydrogen charged zircaloy-4 ($H \approx 286 \pm 20$ ppm); the specimen was sectioned at the mid-plane of a sample that was 6 inches long.	58
Figure 36	(a) Moment amplitude vs. number of failure cycles, (b) strain amplitude vs. number of failure cycles, as function of clad oxide thickness; HR4 only has thermal annealing treatment without pressurization applied.....	60
Figure 37	Metallographic examination of fuel and cladding: results of HR1, which show debonding phenomenon and gap formation at pellet-clad interface and high density of radial hydride formation in HRT treated rod.	61

LIST OF TABLES

Table 1	Correction Factors for LVDT Measurement Data	13
Table 2	Specifications of specimens used in hot-cell testing.....	19
Table 3	Summary of static tests.....	30
Table 4	Characteristic points and quantities based on curvature-moment curves.....	33
Table 5	Comparison of flexural rigidity results between CIRFT testing and PNNL data	35
Table 6	Summary of dynamic test results	43
Table 7	Failure modes of rods from dynamic tests.....	44
Table 8	Curve-fitting parameters of curvature and strain as a function of cycles*	54
Table 9	HBR SNF CIRFT data with the associated tested rod's oxide thickness	59

EXECUTIVE SUMMARY

This report describes testing designed to determine the ability of high burnup (HBU) (>45 GWd/MTU) spent nuclear fuel (SNF) to maintain its integrity under conditions relevant to storage and transportation. The project included two phases. Phase I involved testing HBU fuel in the as-irradiated state, in which hydrides are expected to be predominantly in the circumferential-axial orientation. Phase II involved testing HBU fuel segments following a treatment designed to reorient the hydrides in the cladding to be predominantly in the radial-axial orientation.

In 2011, Oak Ridge National Laboratory (ORNL) proposed a bending fatigue system for testing HBU SNF rods. This system is composed of a U-frame equipped with load cells and is used to impose pure bending loads on SNF rod specimens and measure the in-situ curvature of the SNF rod specimen during bending. This is accomplished using a set-up of three linear variable differential transformers (LVDTs). *Pure bending* is a condition of stress in which a bending moment is applied to a beam without the simultaneous presence of axial, shear, or torsional forces.

On August 19, 2013, the testing system was installed in ORNL's Irradiated Fuels Examination Laboratory (IFEL) hot cell and was formally named the *cyclic integrated reversible-bending fatigue tester* (CIRFT). After tuning the CIRFT and performing benchmark testing in September 2013, Phase I testing began on HBU SNF rod segments with Zircaloy-4 (Zry-4) cladding irradiated in the H. B. Robinson (HBR) nuclear plant. ORNL completed four static tests under displacement control at the rate of 0.1mm/s to a maximum displacement of 12.0 mm. In early November 2013, the benchmark and static test results were critically reviewed at a meeting between representatives from the US Nuclear Regulatory Commission (NRC) and ORNL. Dynamic testing was then initiated, and 16 cyclic tests were completed in the IFEL. Load ranges varied from ± 5.08 to ± 35.56 N·m; there were 12 tests with rod fracture and 4 tests without rod fracture. One of the cyclic tests reached 1.3×10^7 cycles with no rod fracture and was terminated for practical reasons.

Phase II testing began in 2016 using HBU HBR SNF rods with Zry-4 cladding which had been subjected to a hydride reorientation treatment (HRT). ORNL completed CIRFT testing on four specimens following HRT: one in static loading, and three in dynamic loading. The samples subjected to HRT showed reduced lifetimes and reduced flexural rigidity when compared to as-irradiated samples.

The following observations can be made regarding static testing:

- The static CIRFT results indicate a significant increase in the flexural rigidity of a fueled SNF rod compared to the flexural rigidity in a calculated response for cladding only. This applies to both as-irradiated and HRT SNF rods.
- The sample that was subjected to HRT and tested under a static bending load showed reduced flexural rigidity compared to as-irradiated samples. Nevertheless, materials tested in the as-irradiated and HRT states both had higher flexural rigidity than materials considered in the calculated response for cladding only.
- The HBU HBR rods in the as-irradiated state survived static unidirectional bending to a maximum curvature of $2.2\text{--}2.5\text{ m}^{-1}$, or a maximum moment of $85\text{--}87\text{ N}\cdot\text{m}$. The

maximum static unidirectional bending values were bounded by the CIRFT device's displacement capacity. The maximum equivalent strain was 1.2–1.3%.

- The HBU HBR rods in the as-irradiated state exhibited a multiple-stage constitutive response, with the two linear stages followed by a nonlinear stage. The flexural rigidity at the initial stage was 63–78 N·m², corresponding to an elastic modulus of 101–125 GPa. The flexural rigidity at the second stage was 55–61 N·m², and the corresponding elastic modulus was 88–97 GPa.
- Most HBU HBR rods in the as-irradiated state under static unidirectional loading fractured at a location coincident with the pellet-to-pellet interface, as validated by the post-test examinations showing pellet end faces in most of the fracture surfaces. Fragmentation of the pellets also occurred to a limited degree, along with cladding failure.

The following observations can be made regarding dynamic testing:

- The fatigue life of HBU HBR rods in the as-irradiated state in the cyclic tests depended on the level of loading. Under loading with moments of ± 8.89 to ± 35.56 N·m—namely ± 0.03 to $\pm 0.38\%$ strain at 5 Hz—the fatigue life ranged from 5.5×10^3 to 2.3×10^6 cycles.
- The ε -N curve of the HBU HBR rods in the as-irradiated state can be described by a power function of $y = 3.839 \cdot x^{-0.298}$, where x is the number of cycles to failure, and y is the strain amplitude (%).
- Maxima of the curvature during dynamic tests in the as-irradiated state ranged from ± 0.08 to ± 0.78 m⁻¹ at 5 Hz. The κ -N curve of the HBU HBR rods can be described by a power function of $y = 6.864 \cdot x^{-0.283}$, where x is the number of cycles to failure, and y is the maxima of cladding tensile curvature $|\kappa|_{\max}$ (m⁻¹). A fatigue limit is likely located between 0.08 and 0.15 m⁻¹ if it is defined at 10⁷ cycles (as is typical for material fatigue endurance limits).
- The failure of HBU HBR rods under cyclic loading often occurred near pellet-to-pellet interfaces.
- The samples subjected to HRT showed a slightly reduced lifetime compared to as-irradiated samples in dynamic testing.

ACKNOWLEDGMENTS

This research was sponsored by the US Nuclear Regulatory Commission (NRC). The authors would like to thank Michelle Flanagan-Bales, NRC Program Manager, for providing guidance and support, and Gordon Bjorkman, Bob Einziger, and Patrick Raynaud, NRC staff members, for providing invaluable input and comments during program development and execution.

The authors gratefully acknowledge Oak Ridge National Laboratory program managers Bruce Bevard and Rob Howard for their guidance, Ting Tan and Hao Jiang for providing finite element method simulation support, Yong Yan for providing hydride reorientation (HR) specimens, Chuck Baldwin for providing post-irradiation examination support, Josh Schmidlin for performing fuel rod cutting and dimension measurement, Brian Woody and Scot Thurman for providing hot-cell operation support, Thomas Cox, Brian Sparks, and Randy Parten for providing drawing and machining support, and Rose Raney for providing editorial review of this report.

LIST OF ACRONYMS, ABBREVIATIONS, AND UNITS

ANL	Argonne National Laboratory
BE	bonding efficiency
CFR	Code of Federal Regulations
CIRFT	cyclic integrated reversible-bending fatigue tester
EPRI	Electric Power Research Institute
FEA	finite element analysis
FEM	finite element method
GWd	gigawatt-day
HBR	H. B. Robinson
HBU	high burnup
HR	hydride reorientation
HRT	hydride reorientation treatment
ID	inner diameter
IFEL	Irradiated Fuels Examination Laboratory
LVDT	linear variable differential transformer
MET	metallographic examination
MOX	mixed oxide
MTU	metric ton of uranium
NCT	normal conditions of transport
N·m	newton-meter
NRC	US Nuclear Regulatory Commission
OD	outer diameter
ORNL	Oak Ridge National Laboratory
PIE	post-irradiation examination
PNNL	Pacific Northwest National Laboratory
PWR	pressurized water reactor
SEM	scanning electron microscope
SNF	spent nuclear fuel
SS	stainless steel
Zry-4	Zircaloy-4
d1, d2, d3	deflection of rod at LVDT1, LVDT2, LVDT3, mm
E1, E2, E3	elastic modulus, GPa
EI, EI1, EI2, EI3	flexural rigidity, N·m ²
F	load, N

h, h_1, h_2	sensor spacing, m
I	moment of inertia, m^4
I_c	moment of inertia for clad, m^4
I_p	moment of inertia for pellet, m^4
L	loading arm, m
$\kappa, \kappa_A, \kappa_B, \kappa_C$	curvature, m^{-1}
$ k _{\max}$	maximum cladding curvature,
M, M_A, M_B, M_C	moment, $N \cdot m$
ΔM	moment range, $N \cdot m$
$\Delta \kappa$	curvature range, m^{-1}
$\sigma, \sigma_A, \sigma_B, \sigma_C$	engineering stress, MPa
$\varepsilon, \varepsilon_A, \varepsilon_B, \varepsilon_C$	engineering strain, %
y_{\max}	maximum y of cross section of rod, m

1 INTRODUCTION

Current practice is for nuclear fuel to be regularly irradiated to high burnup (HBU) values (>45 GWd/MTU). Several phenomena associated with HBU fuel have been identified, such as hydride reorientation (HR) that could influence cladding integrity. Increased burnup, the use of advanced materials, and variability in material properties may also influence fuel performance during transportation.^{1,2}

As part of the planned fuel cycle, spent nuclear fuel (SNF) will be transported at least once before permanent disposal. Under normal conditions of transport (NCT), packages will experience cyclical force due to vibration. This cyclical force will be transmitted to the contents of the packages and SNF assemblies, resulting in localized stresses in the fuel rods. The response of SNF to NCT oscillation has been investigated: the US Nuclear Regulatory Commission (NRC) tasked Oak Ridge National Laboratory (ORNL) to investigate the bending stiffness and fatigue life of HBU fuel during transportation. *Bending stiffness* (or *flexural rigidity*) is the critical rod property that dictates the rod's vibration response. The testing was designed to evaluate the fuel rod as a composite system, including fuel pellets and any pellet/cladding bonding effects. Although the original objective was to determine the response of HBU SNF to vibration under NCT, the stresses applied to the HBU SNF rods throughout the program can be applied to all transportation and storage conditions. In addition to determining the results of fatigue testing, another objective was to determine the effect of the fuel pellets' presence on the overall behavior of the fuel rod.

Testing was conducted on HBU SNF with Zircaloy-4 (Zry-4) cladding from a pressurized water reactor (PWR). Five static tests were conducted using fuel rod segments from five rods with very similar power histories and burnups. This was followed by nineteen cyclic fatigue tests in a range of load amplitudes. The average burnup of the tested rod segments ranged between 63.8–66.8 GWd/MTU. The estimated oxide layer thickness on the waterside surface was approximately 40–110 μm , and corresponding hydrogen contents of hydrides within the cladding wall were estimated to be between 360–800 wppm. In the first phase of testing, all fuel rod segments were tested in an as-irradiated state in which there is no oxide layer removal, with most hydrides in the circumferential orientation. Because both circumferential and radial hydrides are oriented in the planes parallel to the principal normal tensile stress during bending loading, SNF rod fatigue strength was not expected to be sensitive to the hydride orientation.³ However, the potential effect of radial hydrides on the bending fatigue response of the HBU fuel rods was investigated in Phase II of the program.

Since the first publication of this NUREG-7198 in May 2015, several factors that influence the recorded curvature measurement data were identified. In this first revision, updated results from previous CIRFT tests are reported. In addition, after the first publication, a new phase of testing began using samples treated to induce radial hydrides. This revision includes results of CIRFT tests on segments subjected to hydride reorientation treatment (HRT), broadening the applicability of the research results. This first revision of NUREG-7198 is entirely replaces the initial May 2015 publication.

2 APPROACH

The cyclic integrated reversible-bending fatigue tester (CIRFT) shown in Figure 1 is the test hardware developed by ORNL.^{4,5,6,7,8,9,10,11,12} Test protocols were designed to oscillate short segments of HBU SNF until fatigue failure occurred. The results of these tests were evaluated to gain a better understanding of the expected fatigue lifetime of SNF during NCT and the potential effects of phenomena such as HR.

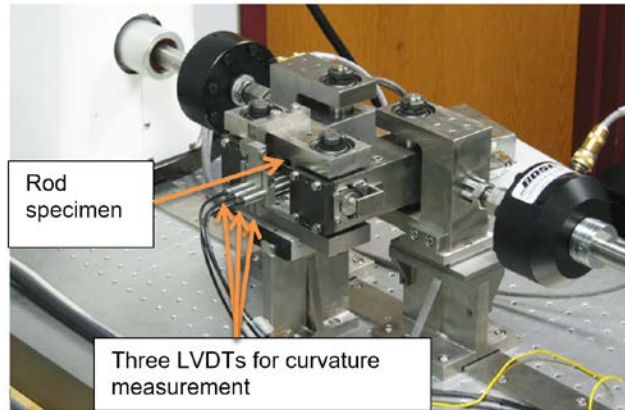


Figure 1 The cyclic integrated reversible-bending fatigue tester developed by ORNL

Static tests were used to define the fuel rod system's elastic and plastic responses. Dynamic testing defined the fatigue life of the fuel rod system under constant amplitude loading. The effects of cyclic loading were tested over a wide range of loading amplitudes to develop an understanding of HBU fuel fatigue life. Relations of fuel rod strain vs. the number of cycles to failure (ϵ -N), or curvature vs. the number of cycles to failure (κ -N), were developed to estimate the influence of imposed bending on the fatigue strength, where

ϵ is the gauge strain, or strain amplitude, experienced by the SNF composite segment during the test, and equal to $\kappa \times y_{max}$,

y_{max} is the maximum distance to the neutral axis of the test rod section and is set equal to the outer radius of the cladding,

N is defined as the number of recorded cycles to failure, and

κ is defined as the average curvature of the oscillating rod, assumed circular, measured during the test using three sensors (d_1 , d_2 , and d_3), and evaluated as follows:

$$\kappa = [(x_0 - d_2)^2 + y_0^2]^{-1/2}, \quad (1)$$

$$x_0 = \frac{-2m_a m_b h - m_a (d_2 + d_3) + m_b (d_1 + d_2)}{2(m_b - m_a)},$$

$$y_0 = -\frac{1}{m_a} \left(x_0 - \frac{d_1 + d_2}{2} \right) - \frac{h}{2},$$

where

$$m_a = \frac{h}{d_2 - d_1},$$

$$m_b = \frac{h}{d_3 - d_2}, \text{ and}$$

h is the sensor distance, 12 mm.

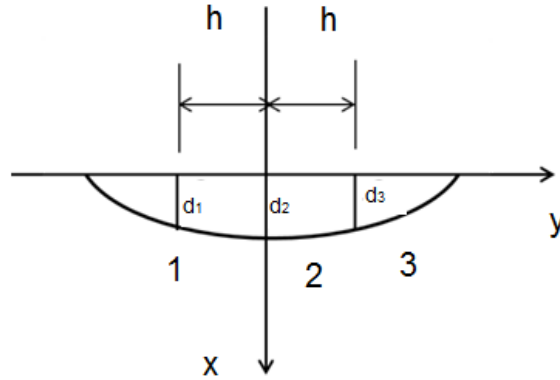


Figure 2 Determination of the rod's bending curvature by use of deflections measured at three points

Under the CIRFT load-controlled mode, the curvature response of a rod (Figure 2) is not necessarily symmetric in one cycle of loading due to potential nonsymmetry in the SNF rod, as well as the associated SNF system flaws and defects. Thus the curvature is described by a mean value of the maximum curvature, κ_{max} , and minimum curvature, κ_{min} , from the tension and compression cycle of CIRFT testing, κ_m :

$$\kappa_m = 0.5 \times (\kappa_{max} + \kappa_{min}), \quad (2)$$

and the maximum of absolute curvature extremes, $|\kappa|_{max}$, is

$$|\kappa|_{max} = \max(|\kappa_{max}|, |\kappa_{min}|). \quad (3)$$

For a given specimen, the $|\kappa|_{max}$ given by Eq. (3) corresponds to the curvature that creates the maximum tensile stress in the cladding. Time series plots of applied bending moment and curvature were also generated. The uniform moment applied to the rod is derived simply from the following equation:

$$M = F \times L, \quad (4)$$

where F is the averaged value of applied bending loads registered from two load cells, and L is the fixed loading arm length, 101.60 mm.

Figure 3 illustrates some of the terms used in the discussion and indicates the surfaces and locations involved in bonding, pellet-cladding interaction, and pellet-to-pellet pinning. The effects

of stress risers caused by pellet-to-pellet pinning were studied using finite element methods (FEMs).¹³

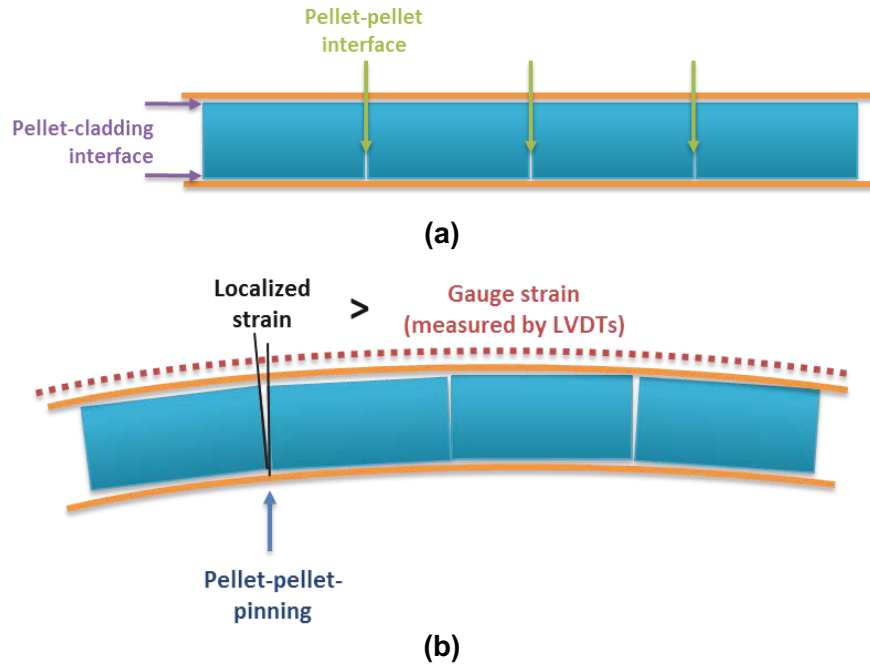


Figure 3 Key fuel and cladding features and fuel rod phenomena of (a) an unloaded fuel rod, and (b) a fuel rod under a bending load

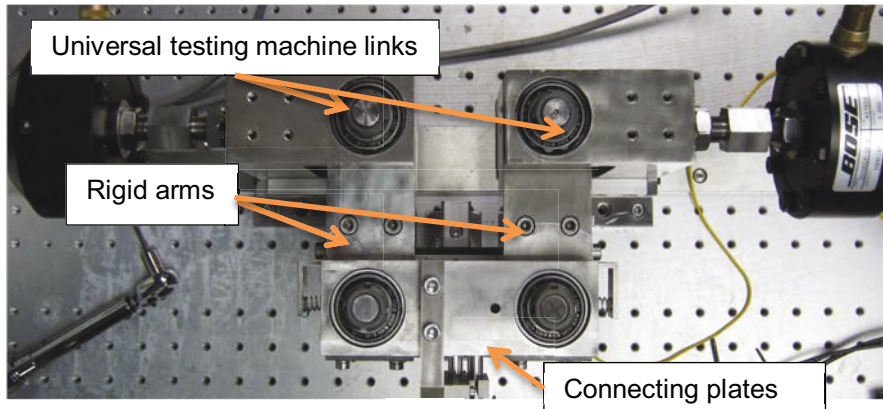
The instrumentation used on the CIRFT device measured the global rod deformation within the gauge section, which is the gauge strain that covers several pellet lengths with several pellet-to-pellet interfaces. The localized strain at the pellet-to-pellet interfaces cannot be precisely known for these experiments, but it is clear that the local strain will be greater than the gauge strain measured in the tests, as indicated in Figure 3.

3 EXPERIMENTAL METHOD

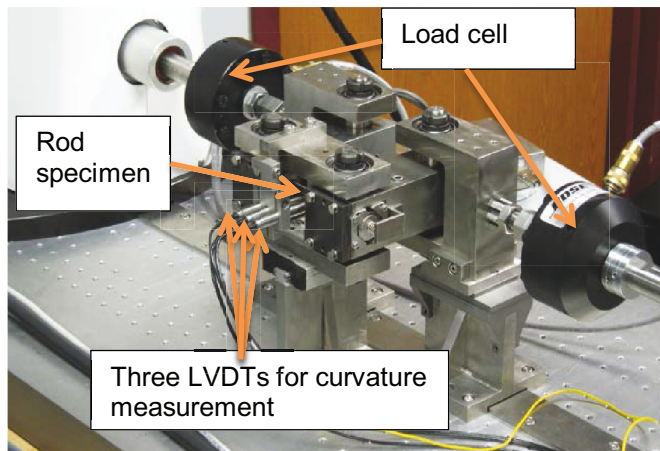
The objective of this testing program was to evaluate the bending deformation and the associated fatigue mechanical properties for HBU fuel rods relevant to transportation and storage conditions. Currently, most mechanical testing devices require a particular design of the specimen such as a pre-notch or reduced gauge section to prevent failure at the grip location and to ensure meaningful data. For this testing program, the testing equipment was designed to obviate the need for the test segment to be altered by machining a gauge section. Such alteration could have introduced or removed localized features relevant to the bending deformation. Therefore, an innovative U-frame and grip design were developed, key features of which are discussed in this section. Cost considerations also had a significant influence on the development of the testing program. Hot-cell space and time are extremely limited and expensive, as is testing material. For this testing program, the intent was to use a small test segment, design a compact test device, and develop a test protocol for efficiency. Important features of the test segments and test protocol are discussed later in this report. Finally, the curvature response of the test segment was to be measured with as little interpretation as possible. It was not practical to weld strain gauges onto the segments or use lasers to measure deflection on HBU material in a hot cell. Therefore, three adjacent linear variable differential transformers (LVDTs) were used to measure lateral deflections of the test specimen so the curvature of the specimen could be calculated without interpretation or assumptions about the deformation of various components of the testing system. The important aspects of the three LVDTs and the calculation of specimen curvature are discussed in this section.

3.1 The U-Frame Setup

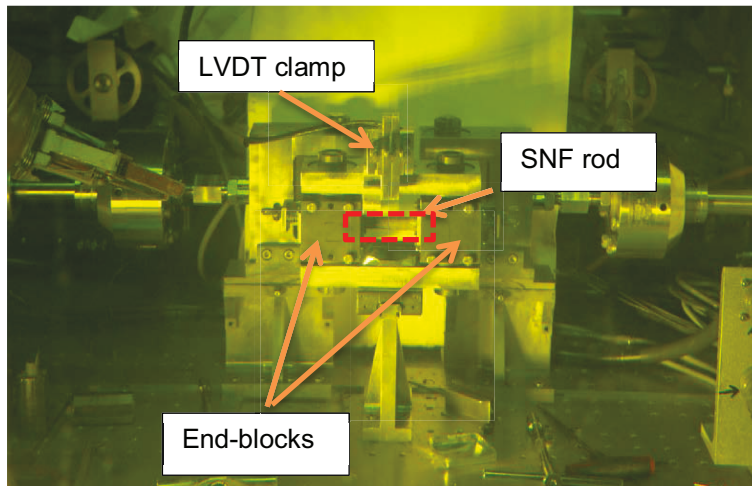
The integrated CIRFT U-frame is shown in Figure 4. The U-frame includes two rigid arms, connecting plates, and universal testing machine links. The rod specimen is coupled to the rigid arms through two specially designed grips. The U-frame setup is oriented in a horizontal plane and is driven by Bose dual linear electromagnetic motors. With help from the coupling, linear motions applied at the loading points of the rigid arms are converted into bending moments exerted on the rod. The dual linear motor (model LM2) test bench has a maximum load capacity of $\pm 3,000$ N for each motor and a total maximum stroke of ± 25.6 mm.



(a)



(b)



(c)

Figure 4 (a) Horizontal layout of ORNL U-frame setup, (b) rod specimen and three LVDTs for curvature measurement, and (c) front view of CIRFT installed in ORNL hot cell

Bending is imposed through a U-frame with dual driving points and a 101.60 mm loading arm. Under a pair of forces or displacements that face outward, the rigid arms are opened, and bending moments force the rod to deflect outward, away from the operator, as shown in Figure 5.

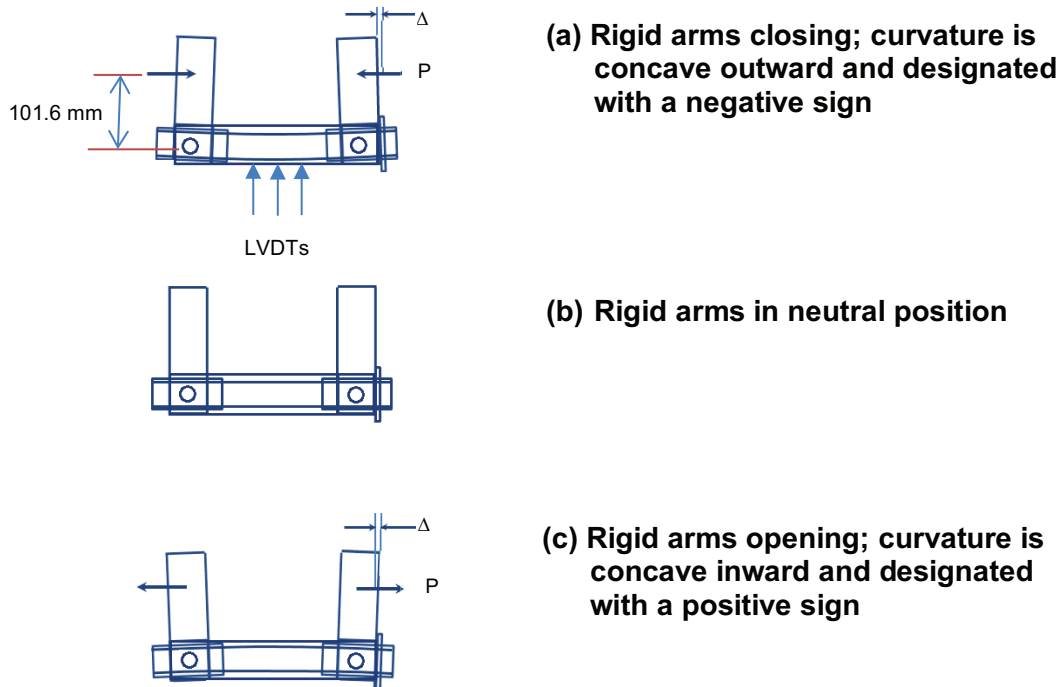


Figure 5 Schematic drawings of U-frame setup for reversal bending when rigid arms are (a) closing, (b) neutral, and (c) opening. Δ is the rigid rod end displacement at the loading joint

Under a pair of forces facing each other, the rigid arms are closed, forcing the rod to deflect inward. With the special grips described in Section 3.2, a pure, reversible bending condition can be obtained. The CIRFT can deliver dynamic loading to a rod specimen in the load-control mode at 5–10 Hz. The current configuration enables the system to test a rod 9.70 to 11.74 mm in diameter, 152.40 mm (6 in.) in length, and 50.80 mm (2 in.) in gauge section. Three LVDTs measure rod deflections at three adjacent points within the gauge section to determine rod curvature, which is then correlated to the applied moment to characterize the mechanical properties of the bending rod. Online monitoring can capture mechanical property changes to reveal fatigue behavior during testing.

3.2 Grip Design

Each grip consists of a V-shaped block integrated into the rigid arm of the U-frame and a V-shaped end block (Figure 6). The surfaces of the blocks serve as contacts to the specimen assembly and are equipped with embedded linear roller bearing sets to ensure free axial movement of the specimen when the force is being transferred. The rod specimen is secured by opening and closing the end blocks in two grips.^{5,6,7,8}



Figure 6 Assembled grip blocks (left) and two views (right) of detached grip body

Figure 7 shows an exposed view of one end of the specimen with the end block removed. The specimen has a pair of rigid sleeves over both holding areas to protect the specimen from any contact damage through a compliant layer between the specimen and sleeves. The rigid sleeves also enable the specimen to move freely in the axial direction while being set against the embedded linear roller bearing sets. The free axial movement of the specimen is a critical requirement in pure bending⁴ for cases in which the stress condition of a tested rod under the applied bending moment does not have the simultaneous presence of axial, shear, or torsional forces.

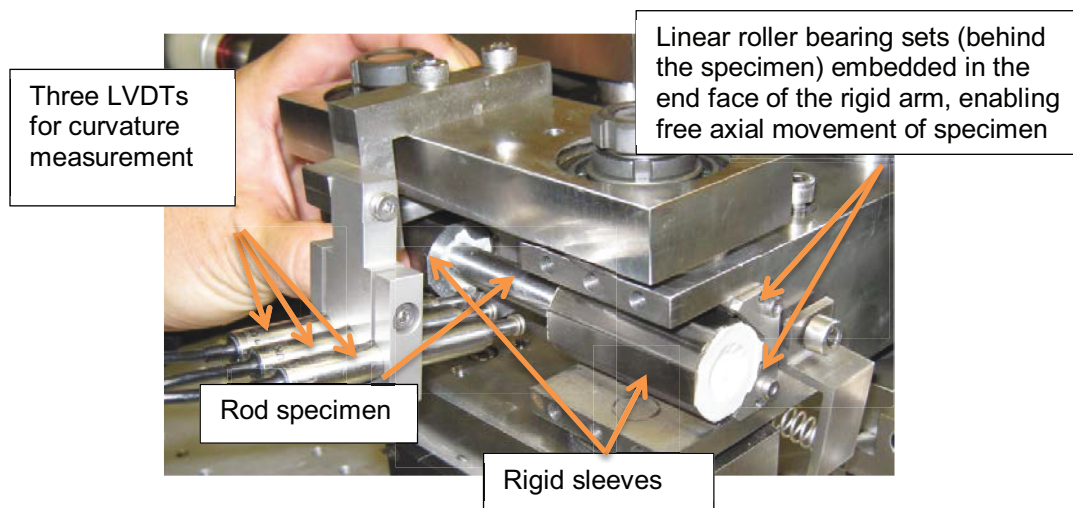


Figure 7 Image showing the grip design of CIRFT with one end-block removed

The mounting of rigid sleeves onto the rod is achieved using casting epoxy, which serves as the compliant layer the size of which depends on the dimensions of the rigid sleeve and rod. The current rigid sleeves have an inner diameter (ID) of 15 mm, an outer diameter (OD) of 25 mm, and a length of 50 mm. For HBR fuel rods with an OD of 10.70 mm, the cast epoxy layer be 2.15 mm thick and would be the same length as the rigid sleeves. Related physical and mechanical properties of the cast epoxy, along with those of the stainless steel in the U-frame setup, are defined in the literature.^{5,8} The use of cast epoxy as a compliant layer has been demonstrated to be effective in meeting requirements for both specimen protection and pure bending boundary conditions.^{5,8} Since the CIRFT tests are conducted under constant load

control and the curvature resulting from the applied load is measured directly on the sample, the properties of the compliant layer do not need to be accounted for when determining the load-curvature response.

Epoxy casting and durability has been demonstrated over time in the hot cell environment with a series of tests of samples exposed to high radiation in the hot-cell. A vise mold was designed and built to cast the epoxy, and procedures were developed to cast the epoxy and mount the rigid sleeves into the rod specimen.^{5,6} Several modifications were made to adapt the vise mold to hot cell testing.¹⁰ Images in Figure 8(a) show different views of the vise mold, and those in Figure 8 (b) and (c) illustrate the process of epoxy casting in the hot cell.

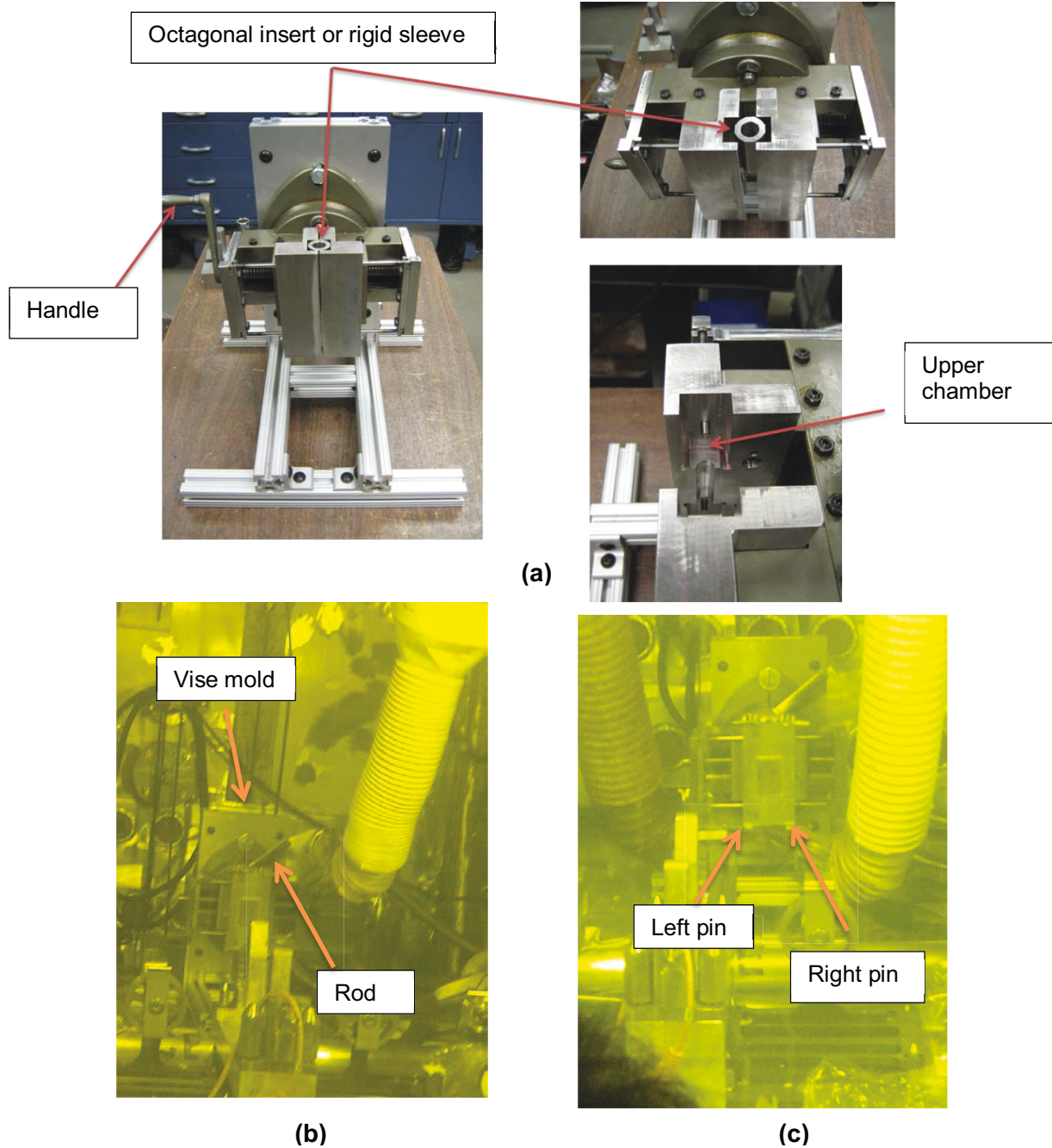


Figure 8 (a) Vise mold for assembling octagonal rigid sleeves into a rod, (b) rod (Demo1, 606B2) to be inserted, (c) one pin turned away, rigid sleeve loaded with epoxy inserted into the lower chamber

The robust mold design enables two important functions for casting the CIRFT specimen in a hot cell environment: (1) the rod ends up in the center every time, and (2) the compliant layer is applied the same way each time to avoid introducing a variable. The amount of fresh epoxy for each rigid sleeve is determined in the hot cell as needed based on results from an out-of-cell study. For the HBR rods, 5 g of epoxy will adequately fill the gap. Typically the rod released from the vise mold is visually examined, and if a substantial cavity is seen between the rod and the rigid sleeves, the gap is refilled.

3.3 LVDT Measurements and Corrections

Theoretically, the bending radius and maximum strain of a rod can be estimated based on the traveling displacement at the loading points of the rigid arm. However, the displacement measured includes the contribution of the compliant layers and depends on the materials used in them and the level of loading. To take these factors into consideration, direct measurement of the specimen displacement using LVDTs at three adjacent points along the rod method was proposed¹⁴ and implemented to evaluate the curvature of a bending rod in this study,^{5,8} as established in Section 2.

A number of factors influence the translation of LVDT measurements into curvature measurement data. Since the first publication of NUREG-7198 in May 2015, some new factors were identified. The primary factors accounted for in the CIRFT data processing procedure are (1) load cell and LVDT measurement data smoothing, (2) LVDT probe contact point/sensor spacing corrections, and (3) LVDT system dynamic vibration correction factor. Table 1 summarizes the primary correction factors and their relative impact on the curvature measurement data. Additional discussion is provided below on correcting for the probe width and dynamic vibration effects.

Table 1 Correction Factors for LVDT Measurement Data

Origin of Correction	Δh	Impact on results	Correction made to data in Rev 0	Correction made to data in Rev 1
Probe width effect as evaluated by tests with strain gauges and half-gauge length methodology	2.5	50% (+) 37% (-)	No	Yes
Data smoothing	No	No	No	Yes
LVDT probe dynamic vibration adjustment procedure	No	18%	No	Yes

3.3.1 Correction for Disk-Type LVDT Head Bias

The arrangement of the three LVDTs and their installation in the CIRFT can be seen in Figures 2 and 7. The LVDTs measure the gauge strain as defined in Figure 3. A series of static tests was performed to confirm the measurement method by using multiple surrogate rods composed of various materials. The curvature obtained by the LVDT measurements has been shown to correlate well with the calculated flexural rigidity of the specimen based on the estimated moment of inertia and Young's modulus for various materials. However, the offset in the contact position of the disk-shaped LVDT probes with the rod (Figure 9) introduced a bias in the curvature measurements.

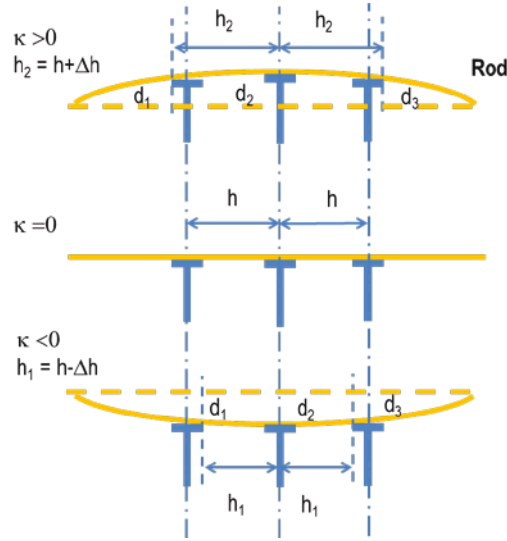


Figure 9 LVDT disk-type probe bias: effect of LVDT probe with disk shape on curvature measurement where contact points are shifted outward (on the compression side of the rod) and inward (on the tension side of the rod)

In the neutral position ($\kappa=0$), the bias is zero, but as the specimen is flexed from the neutral position, a bias is introduced into the d_1 and d_3 measurements due to the offset induced by the LVDT disk. The LVDT contact points with the test sample are offset by the LVDT probe disk, and the reported rod curvature coordinates ($-h, d_1$ and h, d_3) used in the curvature calculation are offset. The d_2 measurement is considered accurate, with no offset due to the LVDT probe geometry. The direction of flexure also influences the bias. Flexure toward the LVDTs shifts the probe contact coordinates inward, and the positive curvature with flexure away from the LVDTs shifts the probe contact coordinates outward, as illustrated in Figure 9. The bias introduced by the curvature calculation is significant and must be addressed. For example, an out-of-cell study comparing disk-type LVDT probes with chisel-type probes indicates that biases of 40–50% can be introduced.¹⁵ Because the radius of the sensor head disk is known and the offset from the true contact coordinates is known, the bias offset can be calculated and applied retroactively to the measured data. It can also be applied during testing. The coordinate adjustment for the bias is applied within the data reduction as a modification to the gauge length of the rod, L_g (in the Figure 9 illustration, h_1 and h_2 are the half-gauge length) and is based on the measured center LVDT deflection, d_2 , and the reported curvature, κ (before the bias adjustment is made). The bent rod is considered as an elastic curve that can be represented by a part of circle with radius R (see Figure 10 below). The half-gauge length can be expressed by arc AB , which has a central angle of θ ,

$$L_g / 2 = \theta \cdot R . \quad (5)$$

The deflection BD of the bent rod at the middle LVDT is measured as d_2 and can be expressed in terms of chord AB :

$$d_2 = \overline{AB} \sin \angle BAD , \text{ where } \angle BAD = \angle ABC = \theta / 2 .$$

$\angle ABC$ is so small that

$$\sin \angle ABC \cong \angle ABC = \theta / 2, \quad \overline{AB} \cong L_g / 2.$$

So,

$$d_2 = L_g / 2 \cdot \theta / 2. \quad (6)$$

Dividing left and right sides of Eq. (5) and by those of Eq. (6), respectively, the result is

$$L_g / 2 = \sqrt{2d_2 \cdot R}. \quad (7)$$

It is known that the R is the inverse of curvature κ . Therefore, we have the following:

$$L_g / 2 = \sqrt{2d_2 / \kappa}. \quad (8)$$

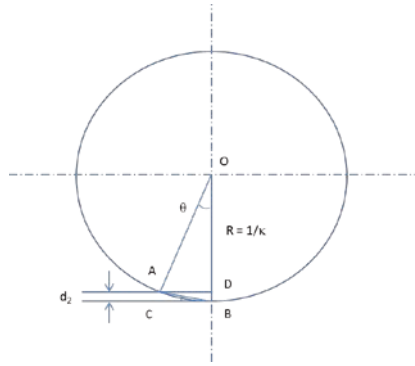


Figure 10 Diagram of circle showing quantities in calculating half gauge length of bent rod

While the magnitude of the half gauge length bias adjustment is considered to be the same whether the rod is bent in a positive or negative direction, it must be applied appropriately depending on the flexure direction. Resolving Eq. (8) to accommodate flexure direction results in the following relation:

$$d_{2p}^+ / \kappa_p^+ |_{h_2=h+\Delta h} = d_{2p}^- / \kappa_p^- |_{h_1=h-\Delta h}. \quad (9)$$

The spacing correction Δh can thus be obtained by solving Eq. (9).¹⁶

Application of the bias correction was tested using a polycarbonate rod (11.11 mm diameter and 152.40 mm length) with a displacement control of ± 6 mm at each loading point. With this input, the rod was expected to behave elastically. Note that the flexural rigidity of the rod, EI , is 1.80 Nm^2 . Therefore, the curvature of the rod can be effectively calculated when the moment M is provided, namely,

$$\kappa = M / EI, \quad (10)$$

so the associated gauge strain is:

$$\varepsilon = \kappa \times y_{\max} \quad (11)$$

where y_{\max} is the radius of the clad's outer surface. The three LVDT-based curvature curves obtained with a disk probe are presented in Figure 11 with and without the correction applied.

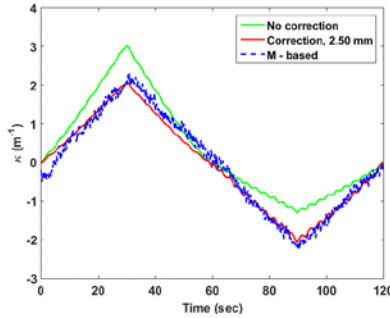


Figure 11 Curvature measurements of polycarbonate rod based on M-based estimate and disk type probe, 2.50 mm sensor spacing correction

Implementation of the correction procedure in the polycarbonate rod example suggested that a Δh of 2.50 mm is needed. The corrected curvature showed a good correspondence with the M-based curvature according to Eq. (10). In the monotonic test, $\Delta h = 2.50$ mm obtained from the calibration can be used for spacing correction in data analysis. In the reversed cyclic bending, the Δh is applied directly using Eq. (9) because the peak and valley pair is available in the data block. This is preferred since, as discussed further in Section 4.2, with the same loading in both directions, the flexure/ curvature of an irradiated fuel rod can be asymmetric due to local bonding and pellet-cladding interface effects. The experimental details and results obtained in the out-of-cell study using surrogate rods can be found in Appendix G. All data reported here have been adjusted for LVDT head bias.

3.3.2 Curvature Adjustment for LVDT Stem Dynamic Stability

To verify the curvatures calculated from the three LVDT readings under dynamic loading, an out-of-cell benchmark exercise was conducted using a strain gauge fixed on the sample. A strain gauge (EA-06-250BF-350, Appendix G) was mounted on calibration rod SS30402 and tested under load control at varying frequencies. Correction was applied to the probe sensor spacing as shown in Figure 12.

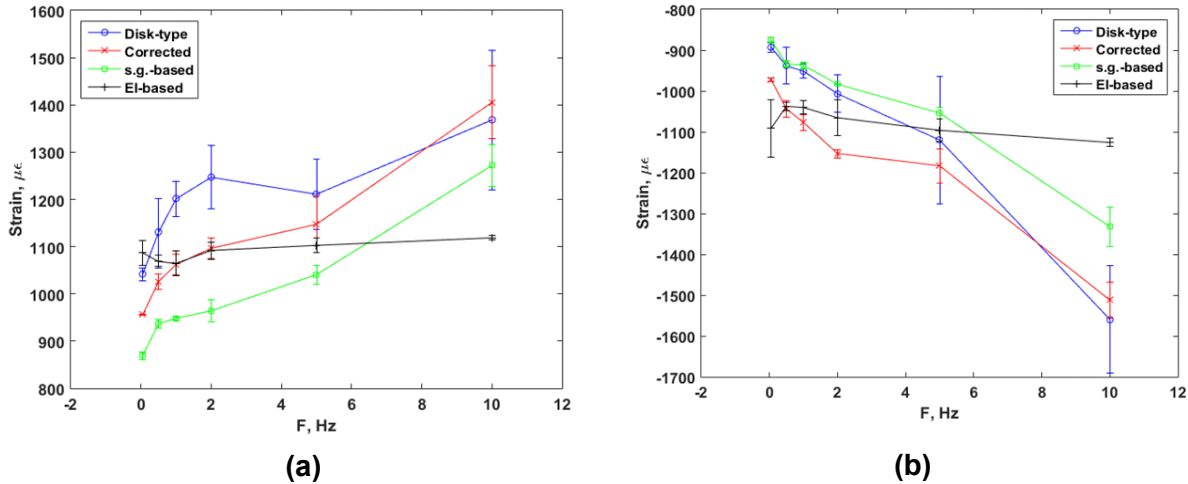


Figure 12 Variations of (a) peak strain and (b) valley strain as a function of driving frequency. At 5 Hz, corrected strain level is about 18% higher than strain gauge estimate for both peak and valley strain plots

Peak and valley strains based on the corrected exhibit have demonstrated a trend similar to the response of strain gauge as a function of driving frequency as shown in Figure 12. The level of the three-LVDT-based strains is usually higher than those of the strain gauge in both peak and valley directions, which may be induced by the dynamic response of LVDT. The overestimate is ~18% at 5Hz. Therefore, all curvatures and gauge strains reported here are reduced by 18% in addition to the LVDT bias correction to take into account the variance induced by LVDTs stem dynamic instability.

3.4 Test Segment Selection and Preparation

The Zry-4 15 × 15 cladding (1.41 wt. % Sn, 0.22 Fe, 0.12 Cr, and 0.14 O) tested in this study was irradiated for seven cycles in the HBR Unit 2 PWR. The rod-average fuel burnup was 67 GWd/MTU. The test segments for Phases I and II were taken from rods at E04, E14, F07, G10 and R05 locations in assembly S-15H. The irradiation history of these rods and their associated details can be found in the literature.¹ The specimen cutting plan and the specimen locations in the father rods can be found in Appendix A. According to the cutting plan presented in Appendix A, 6-inch segments were cut. Figure 13 shows one segment (608C4B) taken from the father rod G10, along with the tube used for specimen storage. The rod diameter of the fuel segments was measured using a dedicated setup in the hot cell.¹⁷ The measurement details are provided in Appendix B. Readings were taken at each half inch from one end of the rod and at three angles (0, 120, and 240°) on cross sections at each reading distance. The mean value and standard deviation of the diameter readings were found to be 10.763 mm (0.4237 in.) and

0.003 mm (0.0012 in.), respectively. It can be seen that the calculated mean value is close to the nominal diameter of the fuel cladding at HBR.¹



Figure 13 Segment 608C4B for DL2 taken from rod G10, with the storage tube

Twenty CIRFT tests were completed in Phase I on the HBR specimens in the as-irradiated state, including four static tests (S1–S4) and sixteen dynamic tests (D0–D15). Four CIRFT tests were completed in Phase II on the HBR specimens following HRT. These consisted of one static test (HR2) and three dynamic tests (HR1, HR3, and HR4). A summary of specimen information for hot cell testing is provided in Table 2.

Table 2 Specifications of specimens used in hot-cell testing

Specimen label	ORNL inventory label ("Seg. ID")	Span	Burnup ¹ (GWd/MTU)	Estimated oxide ¹ (μm)	Estimated hydrogen of span* (wppm)	Outer diameter (mm)
Static Tests						
S1	606C3C	4	66.8	70–100	550–750	10.748
S2	605D1E	2–3	66.5	40–70	360–550	10.746
S3	609C5	4	66.5	70–100	550–750	10.736
S4	609C6	4	66.5	70–100	550–750	10.740
HR2	607D4A	2	63.8	40–44	360–400	10.720
Dynamic Tests						
D0	605D1F	2–3	66.5	40–70	360–550	10.746
D1	607C4B	4	63.8	70–100	550–750	10.834
D2	608C4B	4	63.8	70–100	550–750	10.781
D3	605C10A	4	66.5	70–100	550–750	10.774
D4	605D1C	2–3	66.5	40–70	360–550	10.750
D5	605D1B	2–3	66.5	40–70	360–550	10.771
D6	609C4	4	66.5	70–100	550–750	10.748
D7	609C3	4	66.5	70–100	550–750	10.777
D8	606C3E	4	66.8	70–100	550–750	10.739
D9	609C7	4	66.5	70–100	550–750	10.738
D10	606C3A	4	66.8	70–100	550–750	10.759
D11	607C4A	4	63.8	70–100	550–750	10.832
D12	608C4A	4	63.8	70–100	550–750	10.821
D13	606B3E	5	66.5	100–110	750–800	10.765
D14	606B3D	5	66.5	100–110	750–800	10.765
D15	606B3C	5	66.5	100–110	750–800	10.768
HR1	607D4C	2	63.8	40–44	360–400	10.760
HR3	608D4A	2	63.8	40–44	360–400	10.720
HR4	608D4C	2	63.8	40–44	360–400	Not measured

*From References 18,19

3.4.1 Hydride Reorientation Treatment (HRT) Procedure

Phase II involved testing HBU SNF segments following a treatment designed to reorient the hydrides in the cladding to be predominantly in the radial-axial orientation. The HBU SNF samples for the HRT tests were prepared in the Irradiated Fuel Examination Laboratory (IFEL). After samples were sectioned into pieces 6 inches long, the outer surface oxide layer, fuel, and inner surface oxide were removed from both ends to a depth of approximately 0.5 inch. End caps were welded at both ends, and the HBR fuel specimens were then pressurized with argon gas. Thermal cycling was performed to maximize the radial hydrides (see Appendix H for additional information on the extent of radial hydrides induced in a range of HRT conditions). The specimens were placed in a holder in the furnace for heating. The specimen was pressurized to induce a maximum hoop stress of 140 MPa at a target temperature of 400 °C. The test specimens were held at 400 °C and 140 MPa for 3 hours, cooled at 1 °C/min to 170 °C, and then heated at 1 °C/min to the hold temperature of 400 °C (see Figure 14). This thermal

cycling was repeated for five cycles. The samples were furnace cooled from 170 °C to room temperature after the last cycle and pressure was released. Specimens HR1, HR2, and HR3 were prepared according to the procedures described above, while HR4 only underwent the thermal treatment (the specimen could not be pressurized due to a weld failure).

The rod internal pressure, cladding temperature, and number of cycles used in the HRT procedure are each recognized to be above best-estimate predictions for rod internal pressure and cladding temperature during drying-transfer operations. The reorientation recipe was selected because it resulted in the highest degree of hydride reorientation in an out-of-cell benchmark study (documented in Appendix H) and therefore provides mechanical properties in the most limiting condition to bound all other conditions. For reference, the reorientation procedure typically used at Argonne National Laboratory (ANL)²⁰ was 1 cycle, 140 or 110 MPa pressure, 1-hour hold at 400 C and a cooling rate of 0.1C/min.

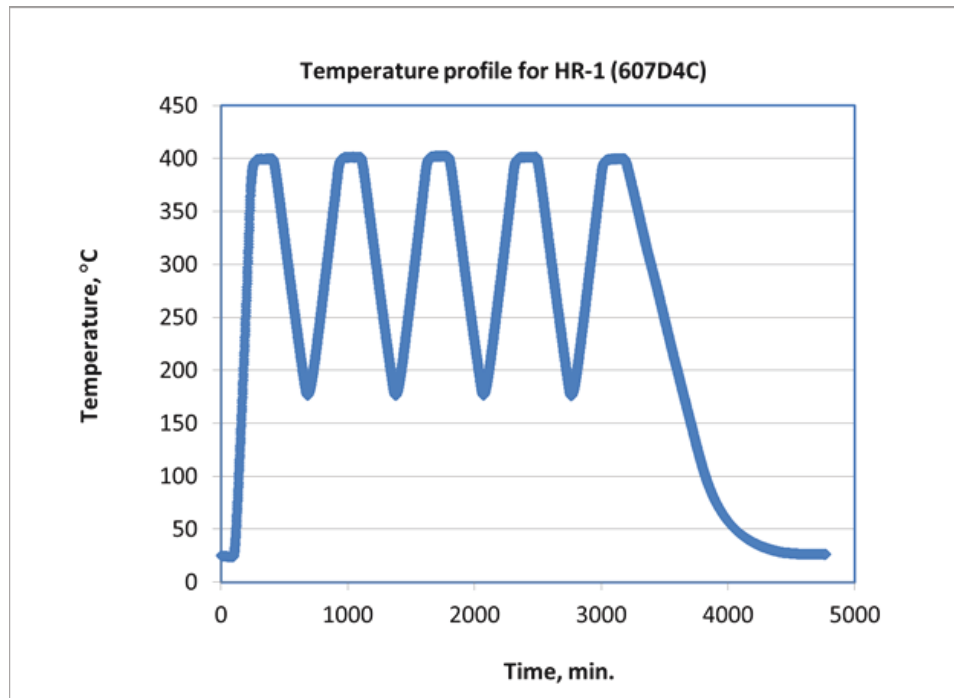


Figure 14 Sample temperature as a function of time for HR1

3.5 Test Protocol

The test system was calibrated under static and dynamic testing conditions using three surrogate rods consisting of stainless steel cladding and alumina pellets. The system was tuned and benchmarked by testing several specimens. The results can be found in Appendix C. All testing of irradiated HBU SNF was conducted on unpressurized specimens.

3.5.1 Static Testing

The purpose of static testing is to measure the flexural rigidity or bending strength of SNF. The static test measures the bending strength of *fueled* SNF rods so that the contribution of the fuel to the SNF rod's bending strength can be evaluated. Analysis of the static test results also

provides a reference to establish the bending moments of interest for the dynamic tests. Static testing is carried out using displacement control. The procedure below was followed.

1. Perform the standard CIRFT static bending test by ramping both loading arms of the U-frame at 0.1 mm/s beyond SNF rod yielding to failure or up to the device stroke capacity of 12 mm.
2. If the machine capacity is reached before specimen failure or before the specimen's yield strength is reached, repeat unidirectional static testing using the same conditions for a few more loading/unloading cycles, or to specimen failure, whichever comes first.
3. If the SNF rod does not fail after 3–4 static loading/unloading cycles, apply the cyclic dynamic test to fracture the test specimen to support postmortem examination. This type of cyclic test is called a *post-static dynamic test* to differentiate the test results from other dynamic tests since it is likely that the static test has deflected the sample beyond yield. Also, it may have affected the pellet/cladding bonding, in addition to inducing significant residual stress generated in clad materials,
4. Collect and weigh any fuel fragments that may have dislodged during the test.

Steps 2 and 3 were instituted because the device did not have sufficient stroke capacity to test some of the specimens to failure.

3.5.2 Dynamic Testing

Dynamic testing consists of two major activities—dynamic real-time online monitoring and periodic quasi-static deformation measurements (see Figure 15).

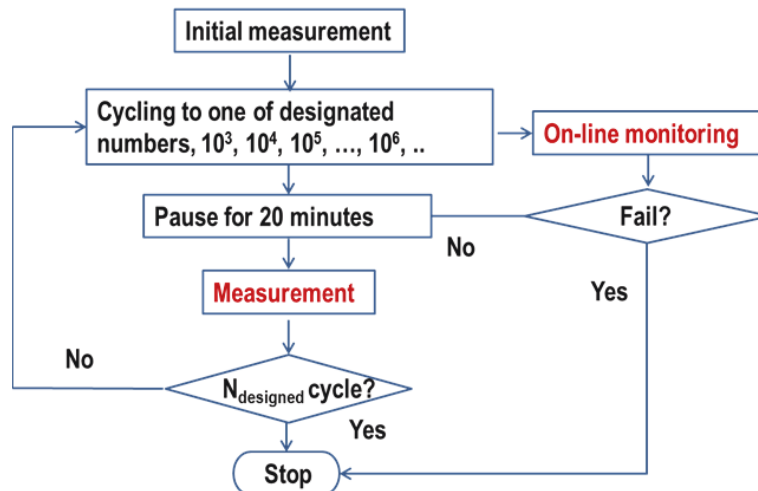


Figure 15 Flowchart for cyclic testing of SNF rod

The procedure is as follows:

1. Set the cycle frequency at 5 Hz and select the loading amplitudes for individual cycle tests considering the target cycles to be achieved with each test. The cycle frequency of 5 Hz was chosen to optimize the CIRFT machine performance. Loading

amplitudes were chosen based on the static testing results and the desire to provide a wider range of fatigue life data.

2. Perform the dynamic cyclic test under constant load control using a sine wave input in reverse bending mode.
3. Monitor the SNF fatigue evolution at defined intervals: perform static measurements of the rod deformation at the end of each target cycle with a frequency of 0.05 Hz and reduced loading amplitude relative to the dynamic loading amplitude under displacement control. Using the reduced loading amplitude for the periodic measurements ensures there is no fatigue damage accumulated during the measurement procedure.
4. Stop the dynamic test when fracture is detected or when the preselected number of cycles is reached.
5. Weigh any fuel fragments that fall out of the fracture.

3.6 Data Processing

Online monitoring data are converted into the applied moment and curvature based on the load channel (load1 and load2) information, the loading arm length (101.60 mm), and LVDT data (LVDT1, 2, and 3). This information is used to generate the time series plots of moment and curvature and the moment-curvature hysteresis loops. These loops are those illustrated in Figure 16 for specimen D1. The data are processed using the approach defined in Section 2 for the applied deflection, moment, and strain.

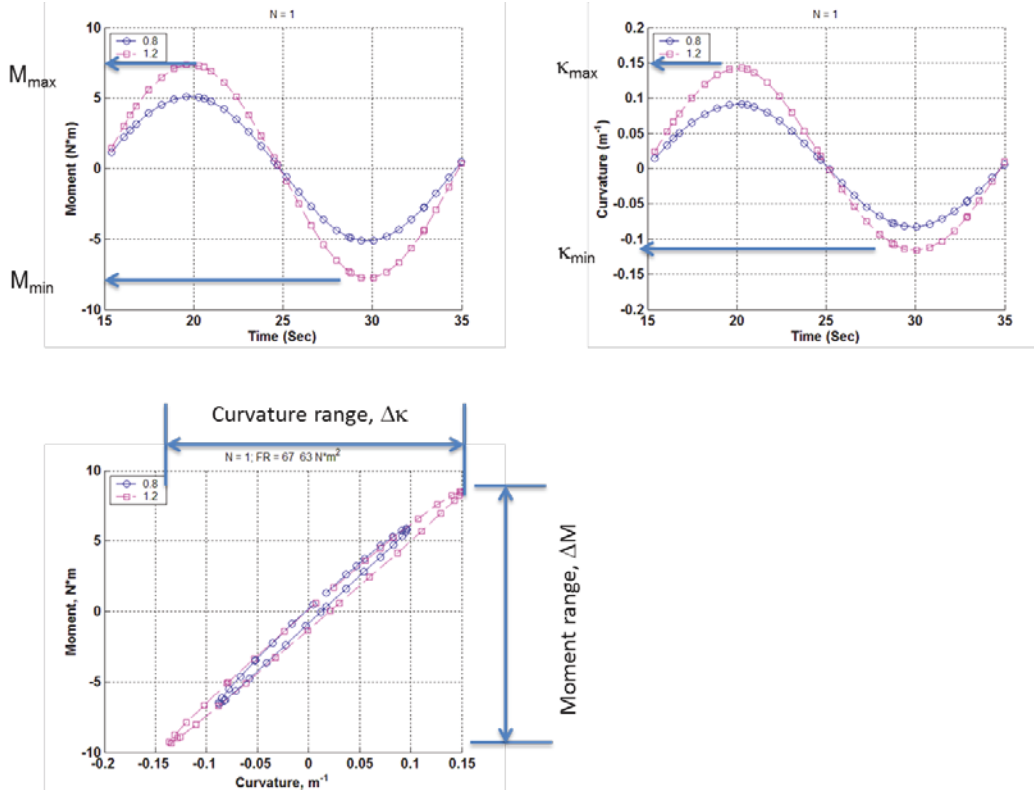


Figure 16 Moment, curvature time series, and moment-curvature hysteresis loop for rod D1. Two measurements are displayed with relative displacement 0.8 and 1.2 mm at the loading points of U-frame

3.6.1 Flexural Rigidity Calculation

The SNF system includes the cladding, pellets, and oxide layers. Thus, an SNF rod is not a homogeneous material. However, regardless of whether the cladding-pellet interfaces and pellet-to-pellet interfaces are perfectly bonded or not, a nonsegmented rod flexural rigidity EI can be expressed as

$$EI = E_c I_c + E_p I_p, \quad (12)$$

where I_c and I_p are moments of inertia of the cladding and pellet, respectively, and the value of I_p is based on dimensions provided in the reference.¹ E_c and E_p are the Young's modulus of the cladding and pellet. The associated strain evaluations of Eq. (11) can still be used. Unfortunately, because the rod is segmented and cladding-pellet and pellet-to-pellet interfaces are not perfectly bonded (either mechanically or chemically), the effective flexural rigidity is reduced by a bonding efficiency correction factor, F , which accounts for the deviation from perfect bonding with no pellet segmentation:

$$EI = E_c I_c + E_p I_p - F. \quad (13)$$

The CIRFT data are not resolved to a low enough level to specifically differentiate the interface bonding efficiency.²¹ However, based on the static measurements of CIRFT testing, the EI data trend indicates that pellet-to-pellet bonding is fairly weak and likely becomes debonded after only a few CIRFT cycles. The resulting reduction of flexural rigidity is evidenced by a significant variation in LVDTs measured curvatures between the cladding tensile stress and cladding

compressive stress regions shown in Figure 16. At the compressive cladding stress region, the fuel reinforcement remains intact in the form of the fuel pellet pinning effect. This results in a shift of neutral axis in an SNF system under reversal bending.

This phenomenon was also observed from the CIRFT test online monitoring data, in which the tensile cladding stress stage shows a higher curvature reading than the compressive stress stage, as shown in Figure 26(d). The EI values also change accordingly in each moment reversal cycle, as shown in the moment-curvature plot of Figure 16 above, where the EI (the slope of moment-curvature) in the clad compression cycle is higher than that of the clad tension cycle. Furthermore, a detailed three-dimensional finite element analysis with a 6.25 N·m uniform moment also predicted that the localized strain in the cladding at the pellet-to pellet cladding interface region is about three to four times (depending on the interface cohesive bond parameters)²¹ that of the global strain for the tensile cladding stress region. The associated localized stress is about 2.6 times the average global tensile cladding stress. Another complication is that the neutral axis of the SNF rod will no longer reside in the geometric center of the SNF system, and the EI value will shift alternatively around the geometry center under cyclic loading reversals.^{21,22} Therefore, the conventional approach, as stated in Eqs. (9) and (10) from a global M - κ consideration, is no longer valid for describing the cladding failure mechanism associated with localized flexural rigidity degradation at the rod's pellet-to-pellet interface. Conducting detailed localized stress-strain evaluation at the pellet-to-pellet interface using global measurements is beyond the current scope of the project. Therefore, only the mechanical response derived from direct measurements (the LVDTs) will be used in this study and discussion.

Generally, the moment range (ΔM), curvature range ($\Delta \kappa$), and flexural rigidity EI are used to characterize the mechanical properties of the fuel rod. These are defined as:

$$\begin{aligned}\Delta M &= M_{max} - M_{min}, \\ \Delta \kappa &= \kappa_{max} - \kappa_{min}, \text{ and} \\ EI &= \Delta M / \Delta \kappa,\end{aligned}\tag{14}$$

where the subscripts *max* and *min* represent the maximum and minimum waveforms in each loading cycle (Figure 16).

Under a load controlling mode, the curvature response of a rod is not necessarily symmetric in one cycle of loading (Section 4.1). The offset of the M - κ loop on the κ axis with respect to the origin can be described by a mean value of curvatures, κ_m :

$$\kappa_m = 0.5 \times (\kappa_{max} + \kappa_{min}),\tag{15}$$

and the maximum of absolute curvature extremes, $|\kappa|_{max}$, is

$$|\kappa|_{max} = \max(|\kappa_{max}|, |\kappa_{min}|).\tag{16}$$

For a given specimen, the $|\kappa|_{max}$ given by Eq. (16) corresponds to the curvature that creates the maximum tensile stress in the cladding. The resistance force of the CIRFT system may be significant, depending on the amplitude of the rigid arm movement. The CIRFT system static resistance force was measured at different displacement levels without a specimen loaded. The net applied load at each displacement level was estimated by subtracting the measured resistance from the applied static test load shown in Figure 17.

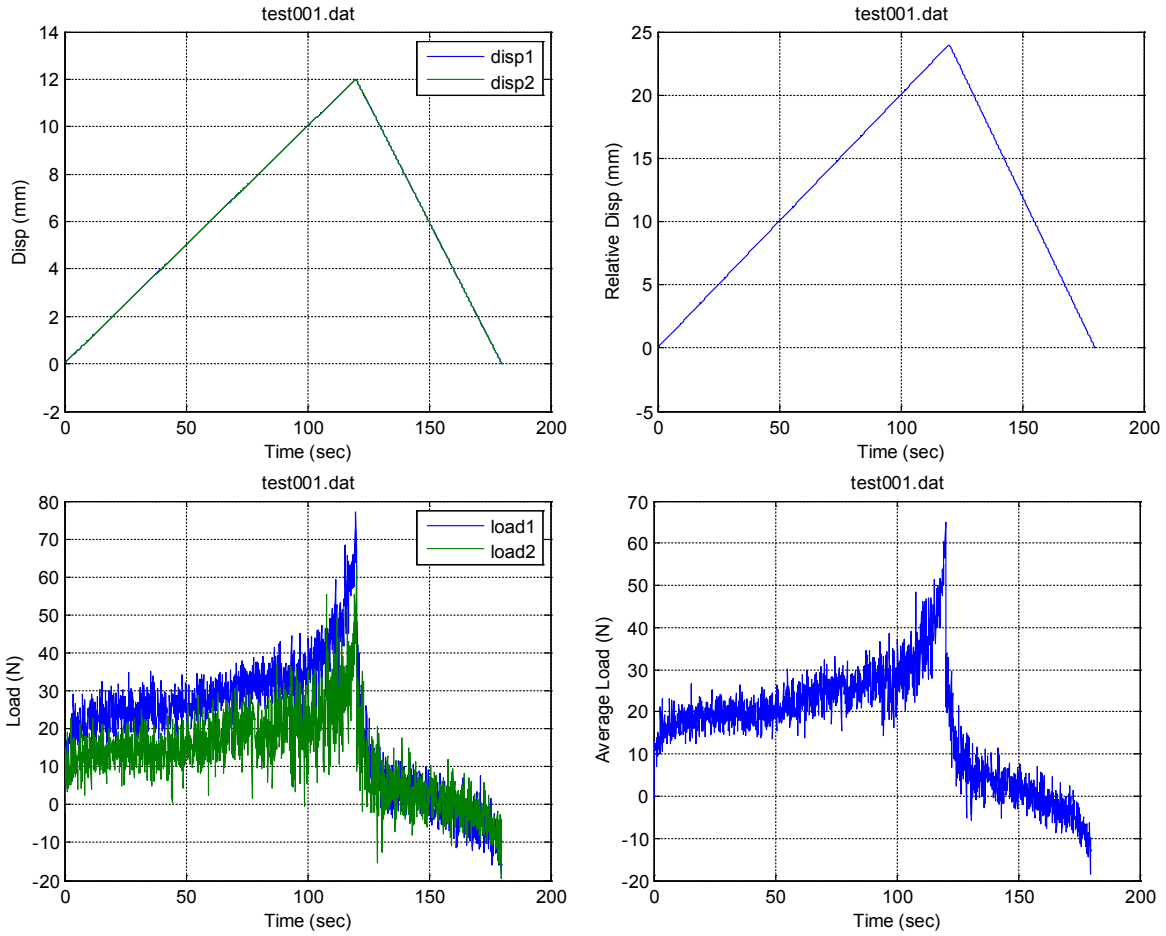


Figure 17 Empty-run conducted without specimen installed, for which the load and displacement were plotted; associated with static test on D1

The CIRFT system resistance was tested and evaluated by using empty runs in which the specimen was not loaded on the testing machine. These empty runs were conducted in the specified period, or whenever the calibration is needed.

4 RESULTS

4.1 Static Tests

Three specimens were tested under static loading in the hot cell for test system benchmarking. Five static tests were subsequently conducted: four on HBU segments as irradiated, and one on an HBU segment following HRT. This chapter focuses on these five static tests, while Appendix C covers the static benchmarking tests.

S1 (606C3C, 66.8 GWd/MTU burnup, 70–100 μm oxide layer) survived four static loading/unloading cycles of unidirectional bending without failure. The moment-curvature curve for the initial cycle is presented in Figure 18(a). (The curves of subsequent cycles overlay one another to a great extent and for clarity are not plotted.) The maximum moment achieved in this test was 85.5 N·m, corresponding to a maximum curvature of 2.2 m^{-1} . The slope changes of the linear portion of moment-curvature curves could be seen near moment levels 12 and 59 N·m. Due to pellet end dish-in design, the pellet-to-pellet interface's bonding strength would be fairly weak, and the pellet-to-pellet debonding would likely occur in the early phase of the bend loading. The slope-changed points indicate that the flexural rigidity changed in the SNF rod system within the linear elastic range.

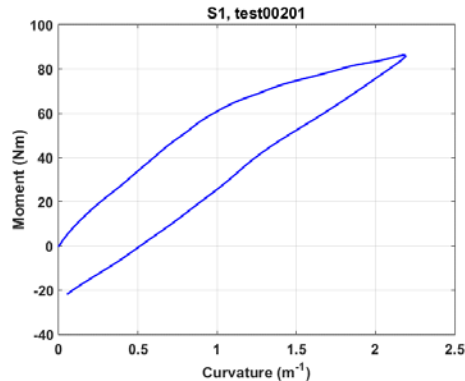


Figure 18 Curve of moment versus curvature

Based on a static loading cycle in which the maximum relative displacement was 24 mm; rates at the loading points of the U-frame were set at 0.1 and 0.2 mm/s for loading and unloading, respectively.

Since the machine's capacity was reached and no failure occurred to the specimen after four unidirectional loadings, a post-static dynamic test was conducted with reversible bending under ± 25.40 to 30.48 N·m at 5 Hz. As mentioned above, the purpose of this procedure was to test the specimen to failure for further postmortem examination. The rod failed after approximately 1.4×10^4 cycles. The failure occurred near motor 1 (right side) with a fuel release of 0.9 g. Optical images of the fracture surfaces are shown in Figure 19. The pellet end-face can be identified from the haze zone characterized by a brown-blue color indicated by the triangular marker in Figure 19(a). This indicates that the rod failure may have initiated at the pellet-to-pellet interface. At the same time, a serrated shear fracture surface of the cladding was

observed. The serrated fracture surface was believed to be the end stage of the crack propagation, when the fatigued CIRFT sample fractured.

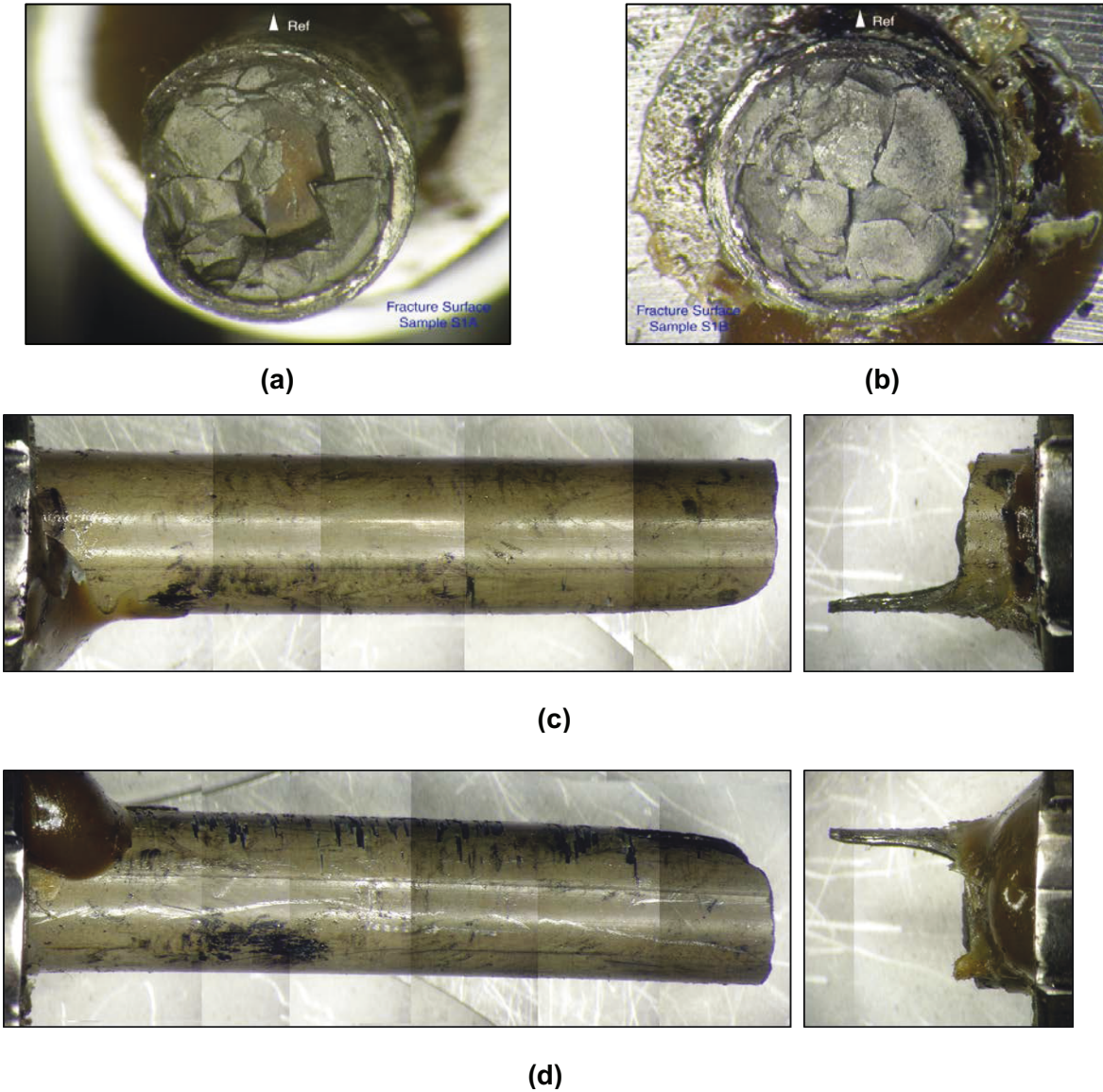


Figure 19 Mating fracture surfaces (a) and (b); lateral sides near the neutral axis of the bending rod for S1 (606C3C) (c) and (d)

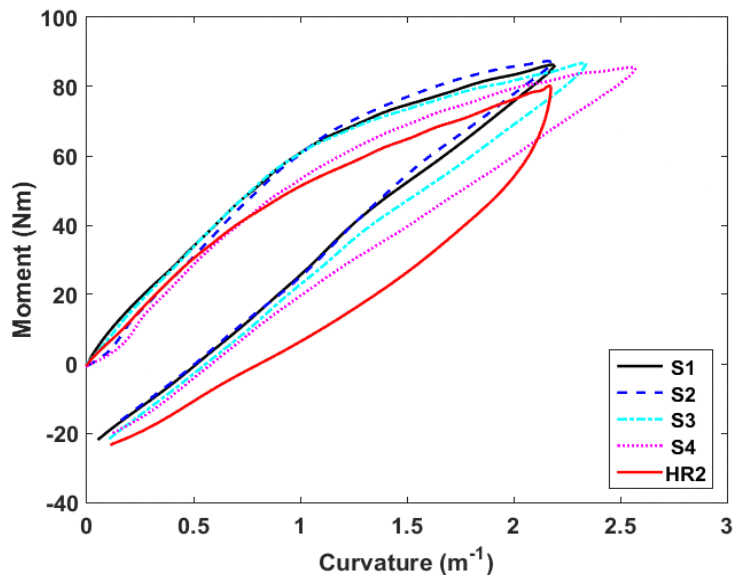
Specimens S2 and S3 were both tested under static loading for three loading/unloading cycles without any sign of failure. They failed in post-static dynamic tests under ± 30.48 N·m at 5Hz. The amplitude of applied moment in the post-static dynamic test was 35–36% of the maximum applied moments used in the respective unidirectional bending process, located in the early second stage of moment-curvature curves. These applied moment amplitudes were selected to generate the failure of the tested specimens within a reasonable number of cycles. S4 was tested under static conditions for three cycles and failed during the fourth cycle. Failure measurements and images are shown in Table 3.

One HBU segment following HRT, HR2, was initially tested under unidirectional bending six times, and then it was tested under the reverse 4 more times, and no failure was observed before the machine stroke capacity was reached. HR2 was further tested under 16.26Nm and failed at 9.47×10^3 cycles. The details of the HRT procedure are provided in Appendix H.

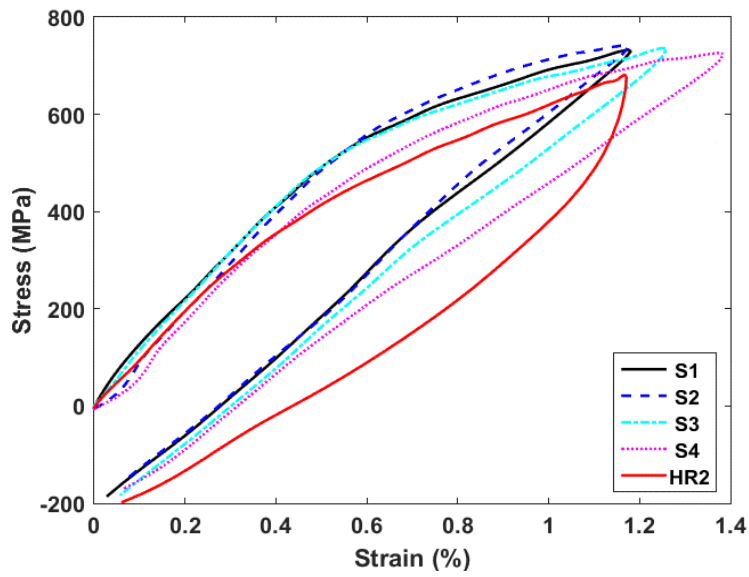
In the static tests described above, loading/unloading cycles did not result in apparent or catastrophic failure of specimens because of the limited stroke of the CIRFT machine. (Measurement details of all static tests can be found in Appendix D.) However, failure did occur in the initial loading cycle of two benchmarking tests on HBU SNF fueled specimens, Scal1 and Scal2. The peak moment of Scal1 was 78.2 N·m, and the peak moment of Scal2 was 80.7 N·m. Details of these benchmarking tests can be found in Appendix C. Therefore, it is reasonable to assume that the maximum bending moment for static tests S1–S4 were not significantly greater than 80 N·m.

A summary of the moment-curvature curves is shown in Figure 20 for the five static tests. A summary of static test results is provided in Table 3. Several important observations can be made with respect to the responses of the test specimens during the first loading cycle.

- The results from the four Phase I static test results (as-irradiated segments) all show relatively similar elastic behavior.
- The initial moment-curvature response of Phase I static tests is characterized by a flexural rigidity of 63–79 N·m².
- There is a change in the flexural rigidity in the Phase I static tests at the moment of 12–21 N·m. This change is quantified in Section 4.1.1.
- After this change, the moment-curvature response of the Phase I static tests is characterized by a decreased flexural rigidity of 55–61 N·m².
- Both Phase I and Phase II static test segments experienced 1.2–1.4% strain without failure.
- The unloading flexural rigidity of the Phase I static tests is close to the loading flexural rigidity in the second stage after the moment reaches 42 to 53 N·m.
- The single Phase II static test, HR2, showed a similar loading behavior, but with lower flexural rigidity compared to that of as-irradiated specimens under similar curvature. Furthermore, the unloading of the HR2 sample appeared to be a curve with a varying slope. A significant load drop was observed shortly after unloading.
- Overall, all tested rods failed within the gauge sections. The majority of the rod fractures involved the pellet-to-pellet interfaces. S3 was exceptional in that the failure location seemed away from the pellet-to-pellet interface, as no end face of the pellet can be identified from the fracture surface of the fuel.



(a)



(b)

Figure 20 (a) Moment-curvature curves measurements and (b) stress and strain curves in static tests

Table 3 Summary of static tests

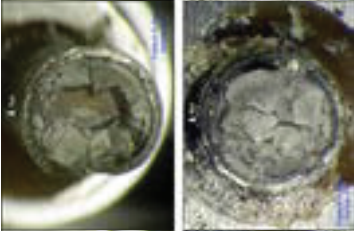

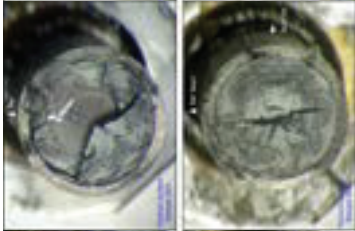
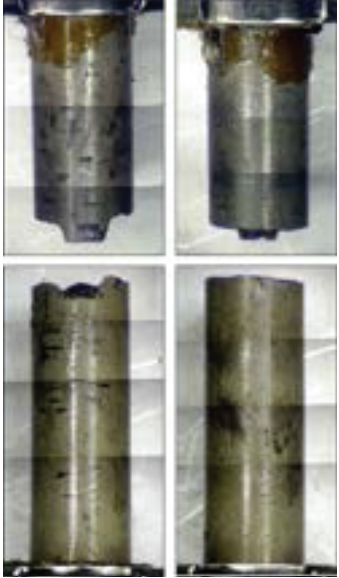
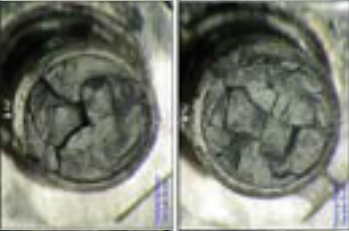

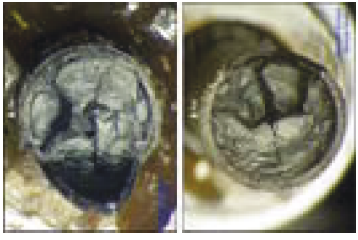
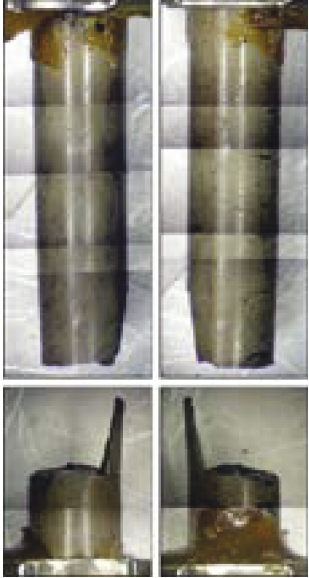
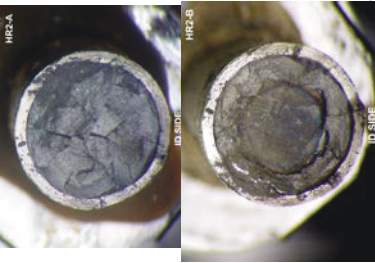
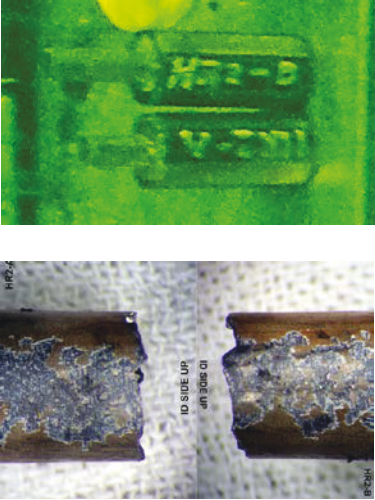
Specimen ID	Specimen burnup	Testing condition and result	Fracture surfaces	Side view of fractured specimens
S1, 606C3C	66.8 GWd/MTU	Four static cycles to 24 mm maximum relative displacement, 85.5 N·m maximum moment without failure, followed by post-static dynamic test to induce failure. 0.9 g fuel fragments were collected when the sample failed.		
S2, 605D1E	66.5 GWd/MTU	Three static cycles to 24 mm maximum relative displacement, 87.2 N·m maximum moment without failure, followed by post-static dynamic test to induce failure. 0.6 g fuel particles were collected when the sample failed.		
S3, 609C5	66.5 GWd/MTU	Three static cycles to 24 mm maximum relative displacement, 85.8 N·m maximum moment without failure, followed by post-static dynamic test to induce failure. 0.2 g fuel particles were collected when the sample failed.		

Table 3 Summary of static tests (continued)

Specimen label/ ID	Specimen condition	Testing condition and result	Fracture surfaces	Lateral surfaces of fractured specimens
S4, 609C6	66.5 GWd/MTU	Three repeat static loadings to 24 mm maximum relative displacement and failed at 85.5 N·m in the 4 th cycle, 1.3 g fuel particles were collected when the sample failed.		
HR2, 607D4A	63.8 GWd/MTU	Six repeated bending to 24 mm, 4 repeated to ±24 mm relative displacement without failure; failed during post-static dynamic. No attempt was made to collect fuel during failure for this test.		

4.1.1 Characteristics of Moment-Curvature Curve

The moment-curvature responses of the four HBU SNF as-irradiated specimens were similar. They are characterized by two distinct linear responses, EI1 and EI2, followed by a nonlinear response during the loading and a linear response upon unloading, EI3. It was observed that when reloaded, the moment-curvature response of the rod followed the same slope of the linear unloading curve and proceeded with nonlinear response after passing the previous maximum load. Such loading/unloading/reloading responses can be found in many mechanical systems where irreversible changes occur during loading.⁸ An effort was made to characterize the moment-curvature response based on characteristic points to facilitate understanding of the test results. The values for EI1, EI2, and EI3 were obtained, corresponding to the slopes of the first and second linear regions and of the unloading region, by using curve fitting with the first order polynomial (Figure 21).

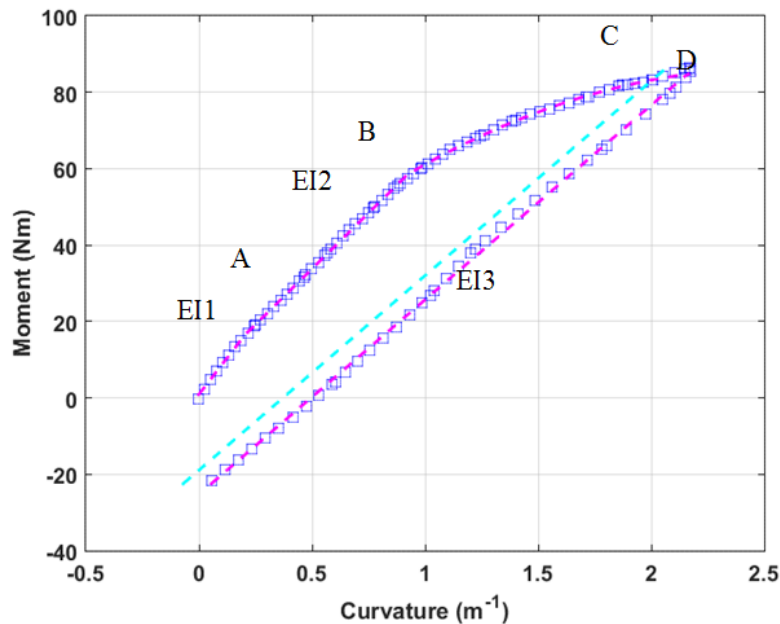


Figure 21 Characteristic points of moment-curvature curve.

The characteristic curvatures and moments at the slopes' changed points A and B were then identified. In addition, the moment at point C corresponding to a 0.37 m^{-1} irreversible curvature, or 0.2% equivalent plastic strain, was found by using a line with the same slope as that of unloading, EI3, and horizontal axis intercept 0.37 m^{-1} . The quantities corresponding to points A, B, and C are designated by κ_A , κ_B , κ_C , and M_A , M_B , and M_C . The results are summarized in Table 4. For as-irradiated rods, the points are generally $EI1 > EI2 > EI3$, with a marginal difference between the latter two. However, for HR2, the linear stages are not defined as well as those in as-irradiated specimens and $EI1 > EI3 > EI2$.

Table 4 Characteristic points and quantities based on curvature-moment curves

Spec label	Segment ID	EI1	EI2	EI3	κ_A	κ_B	κ_C	κ_D	M_A	M_B	M_C	M_D
		N·m ²	N·m ²	N·m ²	m ⁻¹	m ⁻¹	m ⁻¹	m ⁻¹	N·m	N·m	N·m	N·m
S1	606C3C	78.655	57.33	51.027	0.202	0.968	2.009	2.166	16.695	60.599	83.595	85.413
S2	605D1E	73.016	60.848	52.699	0.32	1.009	2.001	2.154	20.18	62.133	86.914	87.294
S3	609C5	71.517	59.369	47.101	0.311	0.933	2.149	2.308	22.338	59.288	83.728	85.235
S4	609C6	63.117	54.849	41.704	0.503	0.862	2.329	2.507	28.54	48.244	81.656	85.02
As-irradiated Avg.		71.576	58.099	48.133	0.334	0.943	2.122	2.284	21.938	57.566	83.723	85.741
As-irradiated Std. Dev.		6.422	2.603	4.886	0.125	0.062	0.154	0.164	4.977	6.322	1.741	1.048
HR2	607D4A	62.769	41.517	43.333	0.487	1.007	1.585	2.158	30.301	51.884	66.809	79.606

The HR2 sample had a lower flexural rigidity than the as-irradiated test segments. While HR2 might be expected to survive larger deformation before failure than the as-irradiated segments, limitations of the CIRFT test device indicate that this could not be confirmed. Nevertheless, the flexural rigidity is consistently reduced under the similar curvature, and the maximum moment level of HR2 was 80 Nm instead of 86 Nm for the as-irradiated condition.

4.1.2 Comparison of Static Results with PNNL Cladding Data

To investigate the contribution of fuel pellets in the fuel rod structure, analysis was performed to compare the measured static results to predicted values considering cladding alone. The cladding properties used for this analysis were obtained from a database maintained by Pacific Northwest National Laboratory (PNNL).²³ The database allows the user to specify the cladding type, temperature, fluence and cold work of the cladding of interest. For this study, the following values were specified:

- Cladding – Zry-4
- Temperature – 75 °F
- Fluence – 12×10^{25} n/m²
- Cold work – 0.5
- Cladding ID - 0.364 inches
- Cladding OD – 0.423 inches
- Cladding Thickness – 0.0295 inches
- Calculated cladding moment of inertia (I_c) – 0.0114 in.⁴

To estimate the contribution of the fuel pellets to the composite bending response, the comparison based on CIRFT M- κ data was completed as described below.

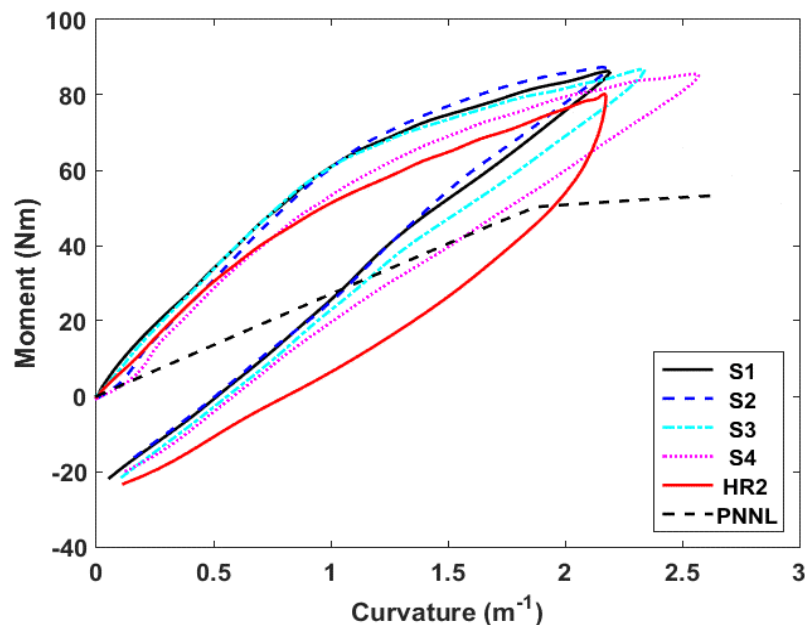


Figure 22 Comparison of CIRFT global data with theoretical PNNL moment-curvature derived from PNNL cladding only stress-strain data

For comparison, the PNNL data (σ - ε curve) were converted to a moment-curvature curve (shown in Figure 22 as “PNNL”) using the following equations, with the consideration of stress distribution appropriate for a thin-walled tube under uniform bending,

$$M = \sigma \cdot I/y_{\max}, \quad (17)$$

and

$$\kappa = \varepsilon/y_{\max}, \quad (18)$$

where $I = I_c$, and other quantities have the same meanings as in Eqs. (1)–(12). The hypothetical *cladding only* moment-curvature response was plotted, together with the moment-curvature response of the high burnup fuel rod system, as shown in Figure 22, where data for the SNF rod show much higher flexural rigidity compared to that of PNNL data with cladding alone. A comparison of CIRFT testing results with cladding-only rigidity based on PNNL data is given in Table 5.

Table 5 Comparison of flexural rigidity results between CIRFT testing and PNNL data

	E11 (N·M ²)	E12 (N·M ²)	E13 (N·M ²)
As-irradiated	71.576	58.099	48.133
HR2	62.769	41.517	43.333
PNNL data	26.933		

The data comparison shows a distinct difference from that of the HBU fuel rod systems. This difference was observed in the slope of the PNNL data. The slopes of both the as-irradiated and HR-treated HBU fuel rod systems are greater than those shown in the PNNL data. By focusing on the initial slope between 0–15 N·m, it was seen that the slope (flexural rigidity) of HBU fuel rods was approximately twice that of the PNNL data for cladding alone.

The increase of SNF rod system stiffness is attributed to the fuel pellet’s mechanical properties and moment of inertia. However, the measured flexural rigidity of a fuel rod system is much less than that estimated from a direct summation of $E_c I_c + E_p I_p$, assuming a perfect mechanical bond between the fuel and the cladding, as well as perfect bonding between the pellet-to-pellet interfaces and a single pellet. However, bonding at fuel-cladding and fuel pellet-to-pellet interfaces is not perfect, and it evolves during the test. The initial fuel-clad gap size also influences the system’s response. Furthermore, due to segmental pellet structure, numerous stress riser sites within cladding at pellet-to-pellet interfaces in an SNF rod are created. In general, the stress riser sites will reduce the lifetime of the structure as compared to the very same system without stress riser sites or discontinuous materials interfaces. The stress riser effect due to an HBU rod segment structure was further validated from the dynamic testing, where the CIRFT test specimens are all failed at pellet-to-pellet interfaces. Moreover, the intensity of the stress riser or the pellet-clad interaction is strongly dependent on the loading intensity. Thus, at a low loading level, pellet-to-pellet interface stress risers are expected to be small, so the cladding alone likely dictates the SNF rod’s composite flexural response.

All these factors affect the degree to which the presence of fuel results in an increase in the rod’s flexural rigidity relative to cladding alone. This research effort did not attempt to account for and quantify each of these factors, so the preliminary conclusion based on CIRFT SNF static bending testing is that flexural rigidity was approximately twice what would be obtained if cladding properties alone were used to predict behavior.

4.2 Dynamic Testing

Nineteen dynamic tests were conducted on the HBU HBR fuel in the hot cell, including tests on 16 as-irradiated (one for benchmark testing and fifteen according to dynamic testing plan) and 3 HRT fuel rod specimens. Input amplitudes varied from ± 5.08 to ± 35.56 N·m; 12 tests were completed with specimen failure and 4 without failure. The fatigue life ranged from 5.5×10^3 to 2.3×10^6 cycles. The tests without failure were conducted under ± 5.08 to ± 8.89 N·m, with the accumulated cycles beyond 6.4×10^6 . Details of the dynamic tests can be found in Appendix E; only typical results are described in this section.

The test on D1 (607C4B, 63.8 GWd/MTU burnup, 70–100 μm oxide layer) was conducted under ± 15.24 N·m, 5 Hz. A fatigue life of 1.1×10^5 cycles was obtained, and less than 1 g of fuel fragments was collected at the failure site.

For each cyclic fatigue test, periodic quasi-static measurements of rod deformation were conducted at a reduced load at the target intervals described in Section 3.5.2. Time series of moment and curvature and moment-curvature loops obtained at the first cycle and after approximately 11,000 cycles are shown in Figure 23.

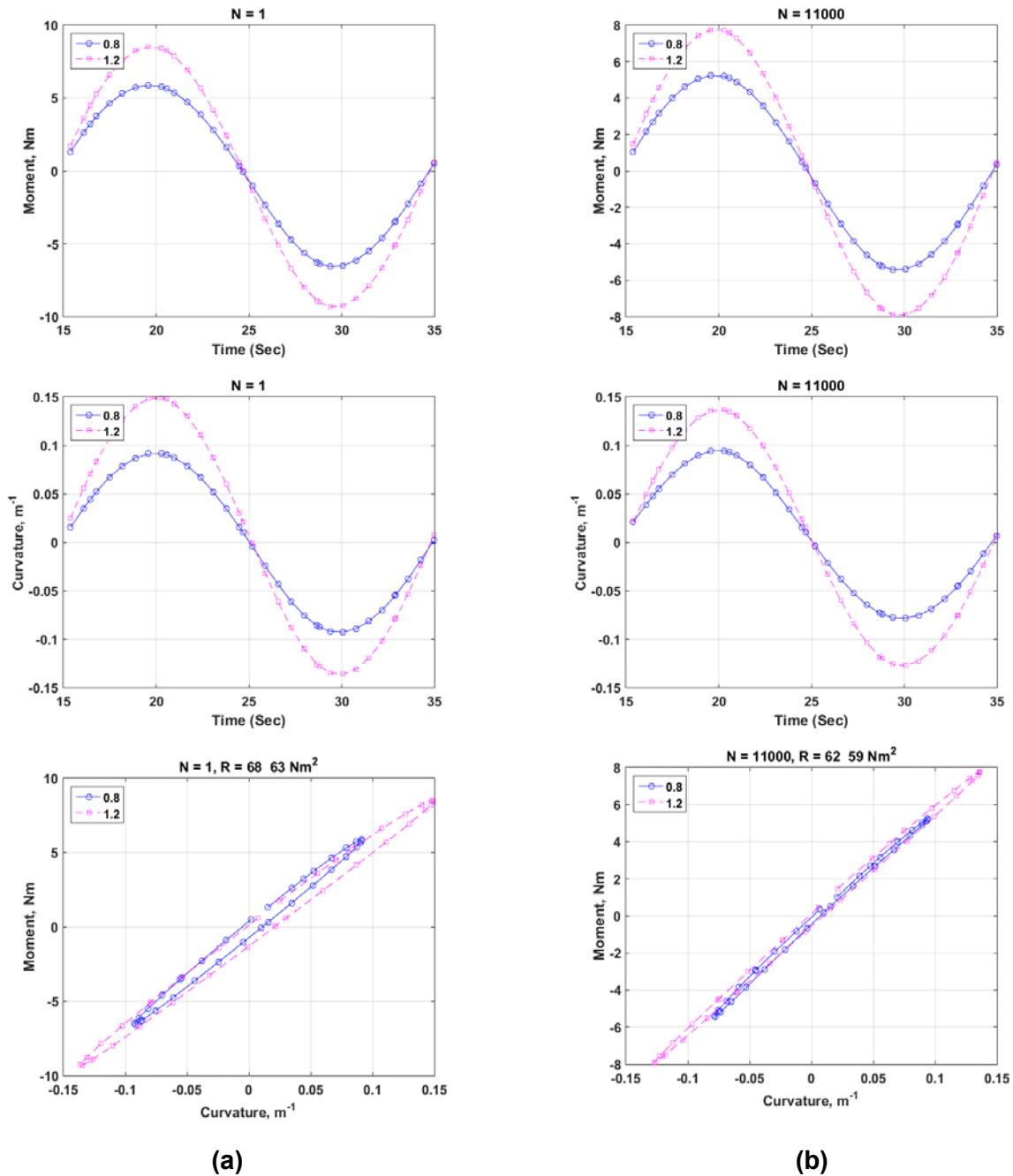
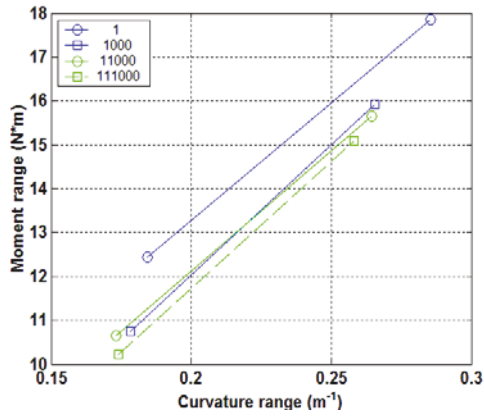
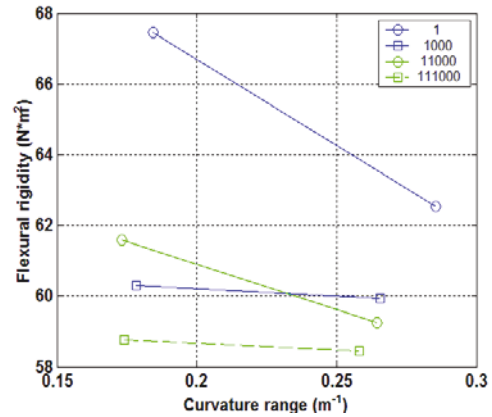


Figure 23 Moment and curvature as a function of time and moment-curvature loops based on measurements when (a) $N=1$ and (b) $N = 111,000$ cycles for D1 (607C4B); measurements were made with 0.8 and 1.2 mm relative displacements; $N_f = 1.1 \times 10^5$ cycles under ± 15.24 N-m, 5 Hz. Fuel particles collected < 1.0 g

Comparing the moment-curvature plots in Figures 23(a) and (b), the loops became slender with accumulated cycles. The relations of moment-range versus curvature-range and flexural rigidity are illustrated in Figure 24.



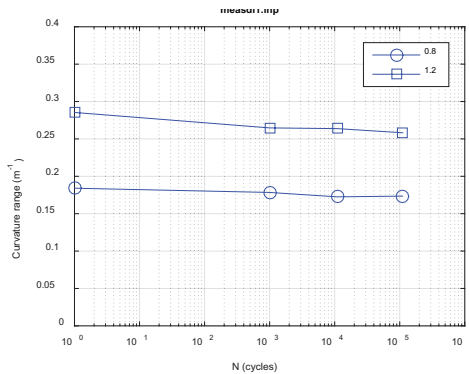
(a)



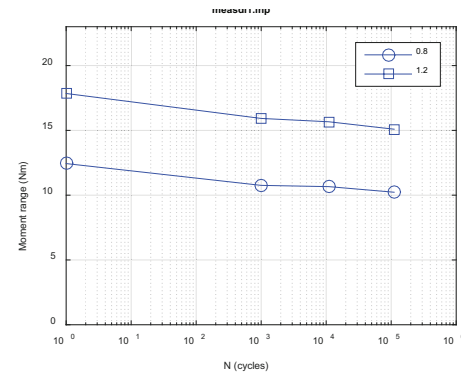
(b)

Figure 24 (a) Moment-curvature relation and (b) moment-flexural rigidity relation at various numbers of cycles for D1 (607C4B); $N_f = 1.1 \times 10^5$ cycles under ± 15.24 N·m, 5 Hz Fuel particles collected < 1.0 g

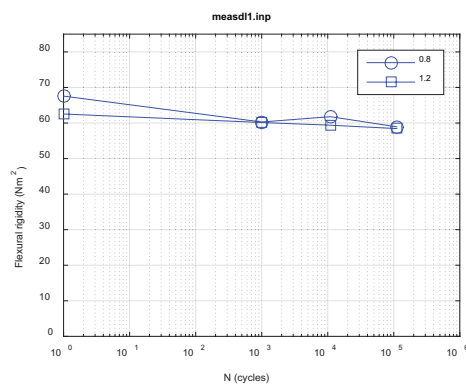
Most of the rigidity degradation occurred in the first 1,000 cycles. Variations of these quantities as a function of number of cycles are provided in Figure 25. The flexural rigidity of the measurements at two displacements converged before the failure and exhibited a slightly declining trend.



(a)



(b)



(c)

Figure 25 Variations of (a) curvature range, (b) moment range, (c) flexural rigidity as a function of number of cycles for D1 (607C4B); $N_f = 1.1 \times 10^5$ cycles under ± 15.24 N·m, 5 Hz; fuel particles collected < 1.0 g

The curvature, moment, and rigidity based on online monitoring data are presented in Figure 26.

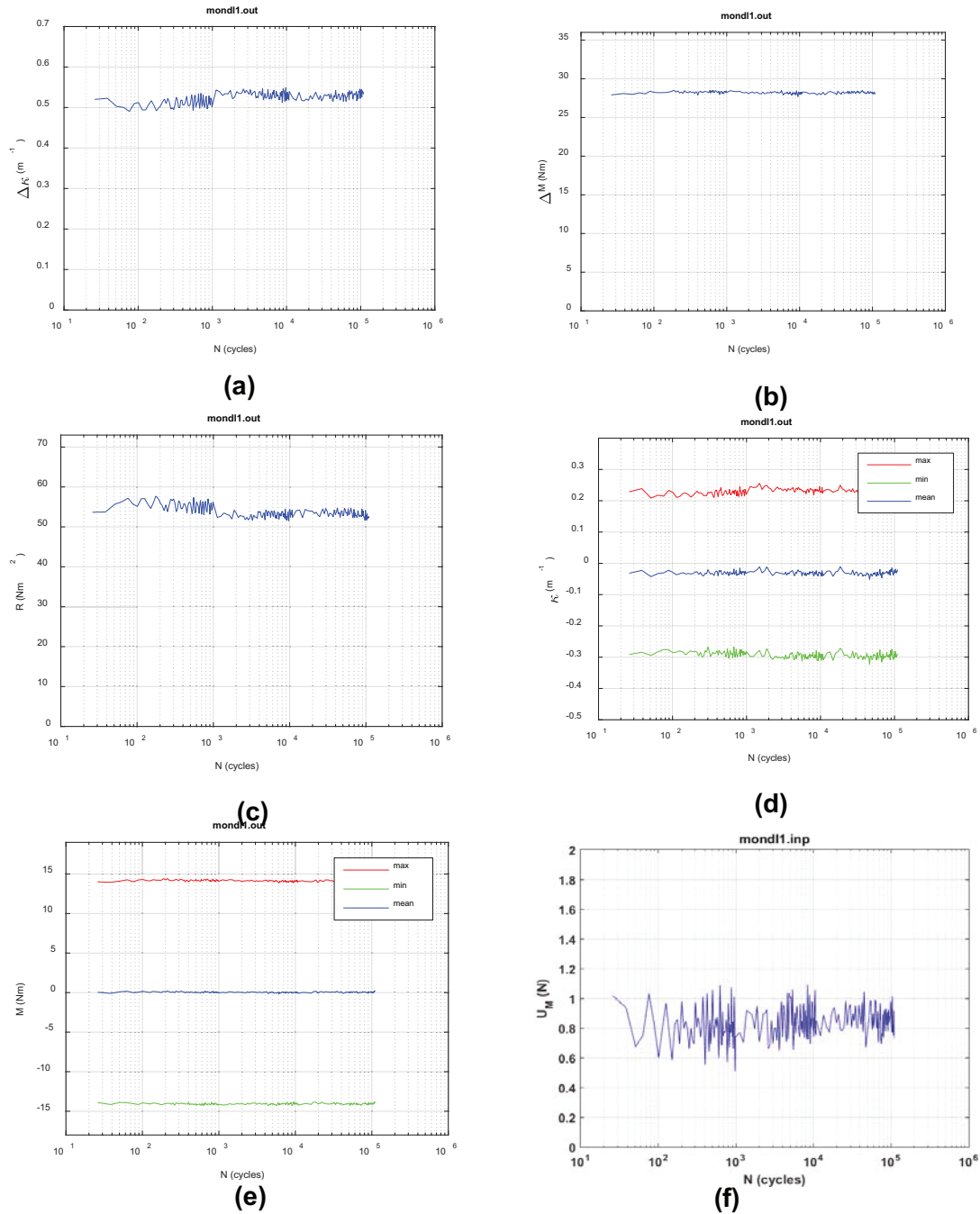


Figure 26 Variations of (a) curvature range, (b) applied moment range, (c) flexural rigidity, (d) maximum and minimum values of curvature, (e) maximum and minimum values of moment, and (f) flexural hysteresis as a function of number of cycles for D1 (607C4B); $N_f = 1.1 \times 10^5$ cycles under ± 15.24 N·m, 5 Hz; fuel particles collected < 1.0 g

The online monitoring showed an initial flexural rigidity of about 55 N·m², a little lower than that observed in quasi-static measurements. This occurred because different loading conditions were used in quasi-static measurement and online measurements. A curvature range of less than 0.3 m⁻¹ was used in the quasi-static measurement, which is lower than that used in the

online measurement of the cyclic test. This will ensure that the measurement process did not affect the dynamic cycle data.

In general, the flexural rigidity tends to increase with decreasing curvature. This is likely due to a better interface bond at a relatively low load resulting in less stiffness reduction. Overall, a stable rod response was exhibited before the final failure. The curvature history shown in Figure 26(d) clearly indicated a non-symmetric deformation under reversal loading where the cladding tension site has much higher deformation (about 1.6 times) compared to that at the cladding compression site. This phenomenon could be the consequence of debonding at the pellet-to-pellet interface and the stress riser occurring at the pellet-to-pellet interface region at the tension side of the cladding, in addition to sensor probe sensitivity.

In general, the flexural hysteresis history shown in Figure 26(f) remains quite uniform throughout the reversal bending test, except with slightly reduction at higher cycles. Similar flexural hysteresis reduction at higher cycle was also observed from the periodic measurement data shown in Figure 23; at 1.1×10^5 cycle the moment-curvature loading and unloading curves had smaller loop compared to that of 26th cycle. Under relatively low loading amplitude of dynamic testing, the clad or fuel pellet would be mainly under linear elastic behavior. The root cause of hysteresis energy dissipation under cyclic loading could be the system's nonlinear response associated with segment pellets induced by the stress riser at interface regions, as well as uncertainly resulting from sensor probe sensitivity.

Moment and curvature time history based on online monitoring data collected during dynamic tests at 26 and 1.1×10^5 cycles are shown in Figure 27. The asymmetrical curvature deformation mode of the tested rod at 26th cycle and 1.1×10^5 cycle was also observed.

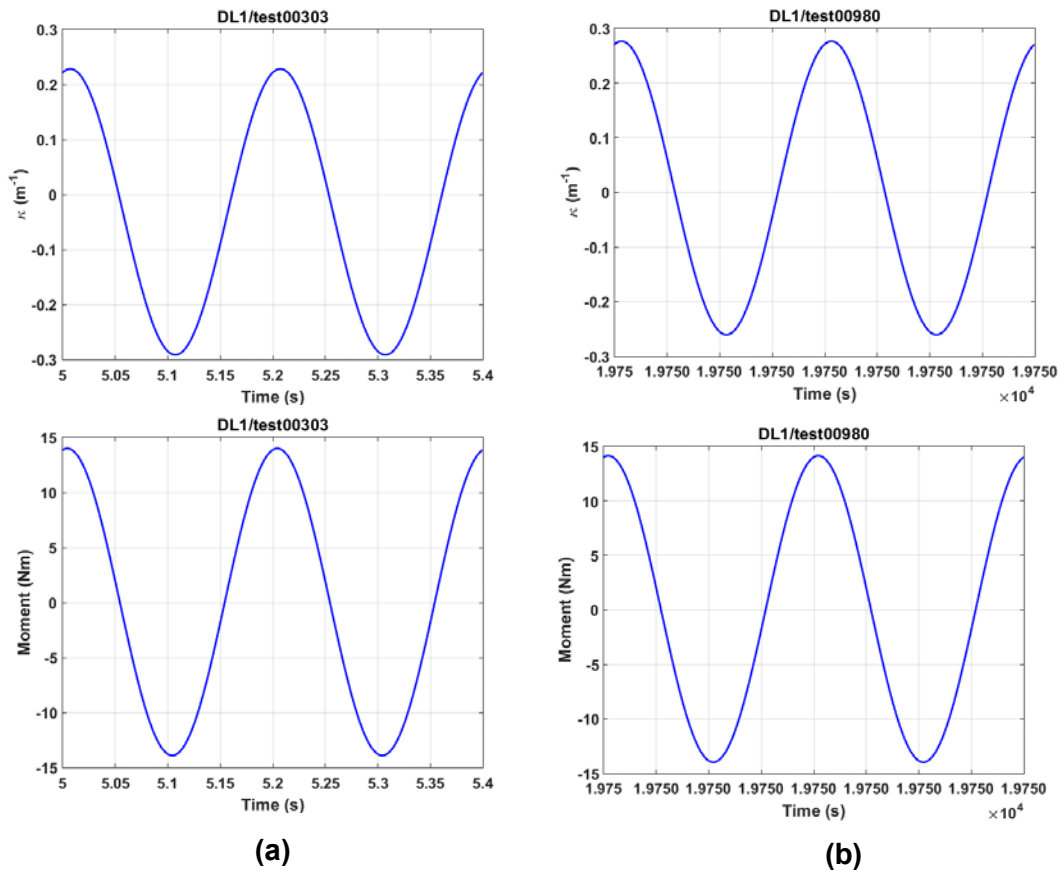


Figure 27 Moment and curvature as a function of time at (a) 26 and (b) 1.10×10^5 cycles; results based on online monitoring; the initial unsymmetrical curvature deformation mode of the tested rod was stabilized and replaced with a symmetrical curvature deformation mode at higher cycles

The end faces of the two neighboring pellets were essentially clean. Both stressed cylinder surfaces of the rod were found covered with equally spaced circumferential cracks throughout the gauge section. Spalling only occurred on the local area near the fracture. The degree of damage shown on both stressed cylinder surfaces of specimen D1 is different from the damage in test specimens undergoing only unidirectional bending. The large deformation arising from the unidirectional bending can produce a greater extent of damage or spalling on one side of the test specimen, with much less spalling on the other side of the specimen (e.g., S3 [609C5] in Table 3).

The failure in test D1 was observed in the gauge section near motor 2 (left side of the U-frame setup). The failure occurred at the pellet-to-pellet interface, as illustrated in Figure 28.

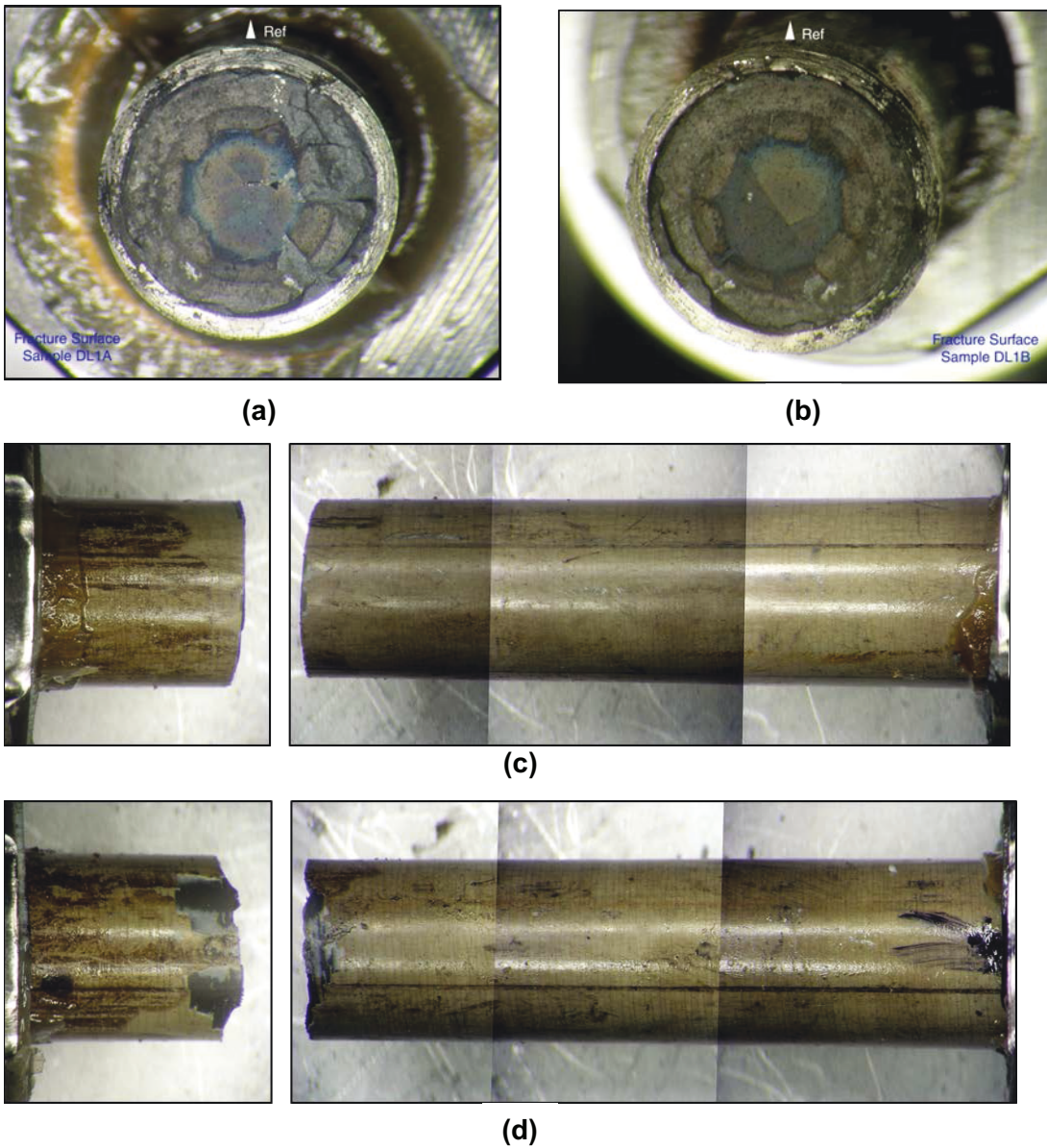


Figure 28 (a) and (b) mating fracture surfaces, (c) front and (d) back sides for D1 (607C4B), $N_f = 1.1 \times 10^5$ cycles under ± 15.24 N·m, 5 Hz; fuel particles collected < 1.0 g

The details of the other dynamic tests can be seen in Appendix E. The dynamic testing results for as-irradiated and HRT HBR rods are summarized in Table 6.

Table 6 Summary of dynamic test results

Spec label	Segment ID	Load amp.	Moment amp.	Number of cycles	Failure*	κ_a	$ \kappa _{\max}$	σ_a	ϵ_a	$ \epsilon _{\max}$
		N	N-m			m^{-1}	m^{-1}	MPa	%	%
D0	605D1F	250	24.068	2.50E+04	Yes	0.439	0.444	206.109	0.236	0.239
D1	607C4B	150	14.107	1.10E+05	Yes	0.215	0.24	117.26	0.117	0.13
D2	608C4B	50	4.207	6.40E+06	No	0.046	0.067	35.496	0.025	0.036
D3	605C10A	100	9.17	1.00E+06	Yes	0.125	0.171	77.938	0.067	0.092
D4	605D1C	75	6.726	1.10E+07	No	0.089	0.12	57.596	0.048	0.065
D5	605D1B	90	8.201	2.30E+06	Yes	0.114	0.123	69.706	0.061	0.066
D6	609C4	125	11.624	2.50E+05	Yes	0.205	0.218	99.546	0.11	0.117
D7	609C3	200	18.923	6.50E+04	Yes	0.351	0.37	160.835	0.189	0.199
D8	606C3E	87.5	7.743	1.28E+07	No	0.107	0.118	66.309	0.057	0.063
D9	609C7	350	33.667	7.10E+03	Yes	0.576	0.624	288.308	0.31	0.335
D10	606C3A	125	11.552	1.80E+05	Yes	0.174	0.213	98.185	0.094	0.115
D11	607C4A	300	29.021	5.50E+03	Yes	0.469	0.564	241.223	0.254	0.306
D12	608C4A	110	9.986	3.86E+05	Yes	0.144	0.171	83.617	0.078	0.092
D13	606B3E	135	12.551	1.29E+05	Yes	0.151	0.199	106.677	0.081	0.107
D14	606B3D	87.5	7.842	2.74E+05	Yes	0.112	0.135	66.652	0.06	0.073
D15	606B3C	75	6.639	2.24E+07	No	0.087	0.125	56.426	0.047	0.067
HR1	607D4C	150	15.152	4.19E+04	Yes	0.424	0.433	128.788	0.228	0.233
HR3	608D4A	100	8.982	2.44E+05	Yes	0.219	0.233	76.342	0.118	0.125
HR4	608D4C	160	14.759	5.47E+04	Yes	0.323	0.344	125.449	0.174	0.185

Optical microscopy was conducted on the fracture surfaces of selected test specimens. Among the seven specimens examined, at least five failures were determined to be dominated by the pellet-to-pellet interfaces (PPIs). Table 7 shows the failure modes of rods from the dynamic tests. Most of the SNF rod failures initiated and propagated through the pellet-to-pellet clad interface region in a typical tensile failure mode except for the HR1 tested sample. The HR1 fractured sample showed that the crack initiated at a pellet-to-pellet interface, but the crack propagation was in a mixed-mode (tensile + shear) failure mechanism. The postmortem examination of HR1 fractured sample also indicated that a large area of the pellet-cladding bond was disrupted during testing or never formed during operation (see the lateral view provided in Table 7 of item HR1 607D4C).

Table 7 Failure modes of rods from dynamic tests

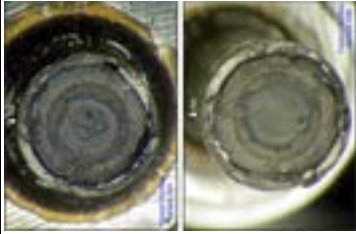

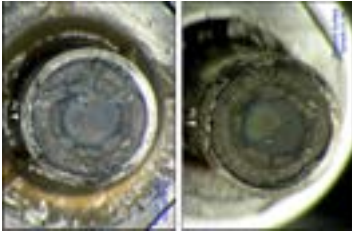

Spec label	Applied moment amplitude		Average curvature (κ_a)	Number of cycles to failure	Cross section	Lateral view
	N·m	m^{-1}				
D0, 605D1F	24.068	0.439	2.50×10^4			
D1, 607C4B	14.107	0.215	1.10×10^5			

Table 7 Failure modes of rods from dynamic tests (continued)

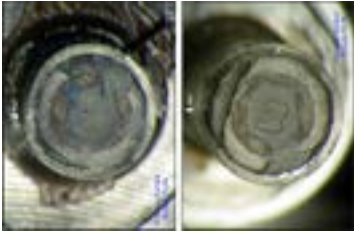
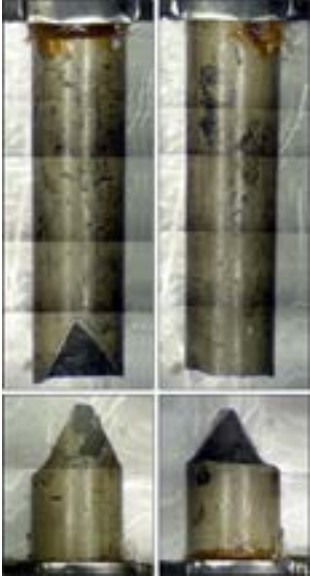


Spec label	Applied moment amplitude		Average curvature (κ_a)	Number of cycles to failure	Cross section	Lateral view
	N·m	m^{-1}				
D2, 608C4B	4.207	0.046	6.40 × 10 ⁶ without failure; follow-up 35.56 N·m, 5 Hz with 1.8 × 10 ³ cycles to failure			
D3, 605C10A	9.170	0.125	1.00 × 10 ⁶			

Table 7 Failure modes of rods from dynamic tests (continued)






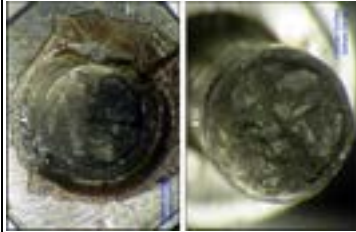




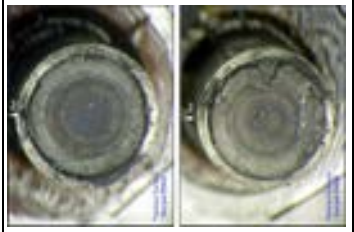




Spec label	Moment amplitude N·m	$\Delta\kappa$ m^{-1}	Number of cycles to failure	Cross section	Lateral view			
					D5, 605D1B		D6, 609C4	
D5, 605D1B	8.201	0.114	2.30×10^6					
D6, 609C4	11.624	0.205	2.50×10^5					
D7, 609C3	18.923	0.351	6.50×10^4					

Table 7 Failure modes of rods from dynamic tests (continued)

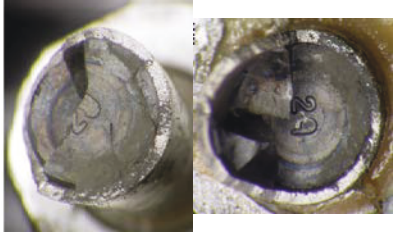
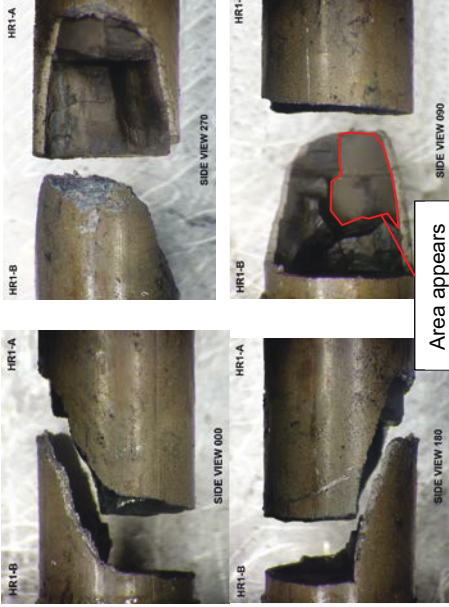
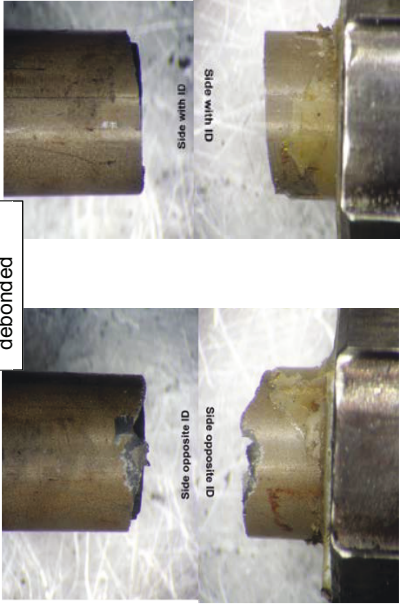
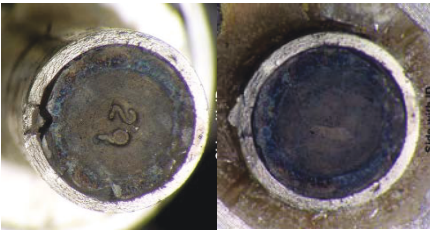
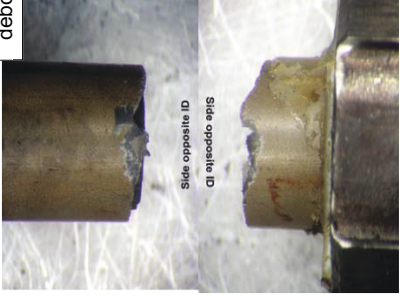
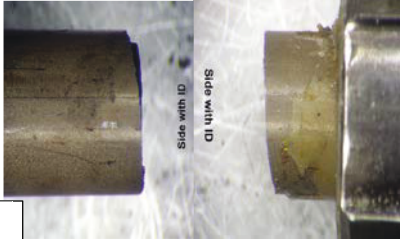
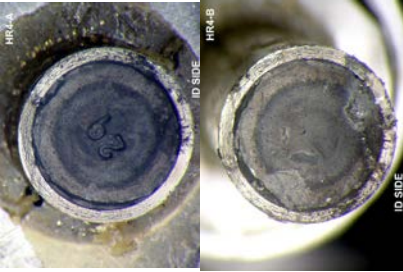
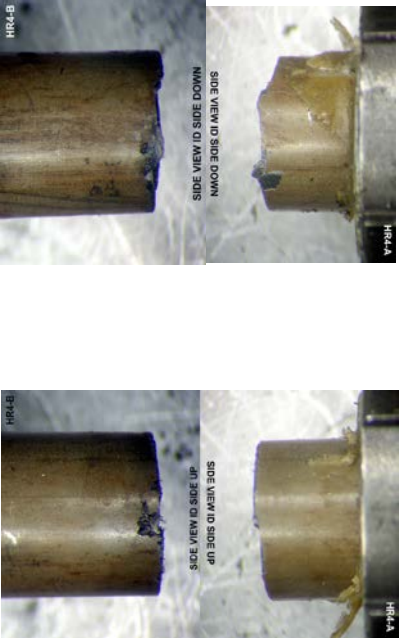
Spec label	Moment amplitude N·m	$\Delta\kappa$ m ⁻¹	Number of cycles to failure	Cross section	Lateral view	
HR1, 607D4C	15.152	0.424	4.19 × 10 ⁴			
HR3, 608D4A	8.982	0.219	2.44 × 10 ⁵			

Table 7 Failure modes of rods from dynamic tests (continued)

Spec label	Moment amplitude N·m	$\Delta\kappa$ m ⁻¹	Number of cycles to failure	Cross section	Lateral view	
HR4, 608D4C	14.759	0.323	5.47 × 10 ⁴			

- The gauge strain amplitudes (ϵ_a , half of strain range $\Delta\epsilon / 2$) of as-irradiated fuel rods are shown in Figure 29 as a function of the number of failure cycles, along with those which were subject to HRT. For as-irradiated specimens that failed during the tests, the fatigue life decreases with increasing strain amplitude according to a well-defined ϵ -N curve. The data points can be fit by using the power function $y = 3.839 \cdot x^{-0.298}$ with an R^2 value as high as 0.849, where x is the number of cycles to failure, and y is the strain amplitude (%).

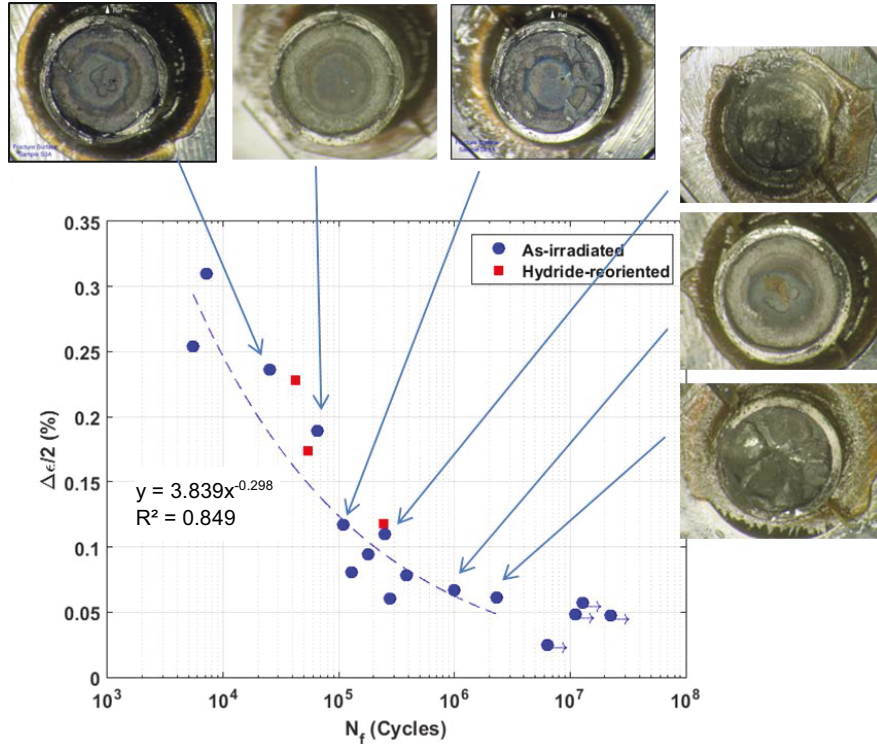


Figure 29 Equivalent strain amplitudes ($\Delta\epsilon/2$) as a function of the number of cycles to failure. Markers with arrows indicate that the tests stopped without failure.

A curve fit was derived by distinguishing failed and non-failed results separately and using two power functions, as shown in Figure 30. For $N \leq 10^6$, the power function was based on failure data points $y = 5.130 \cdot x^{-0.325}$ and for $N > 10^6$, $y = 0.069 \cdot x^{-0.026}$. The R^2 was lower for the second power function, which is expected because the amplitude is close to the endurance limit, and the number of failure cycles is likely to be independent of the applied load.

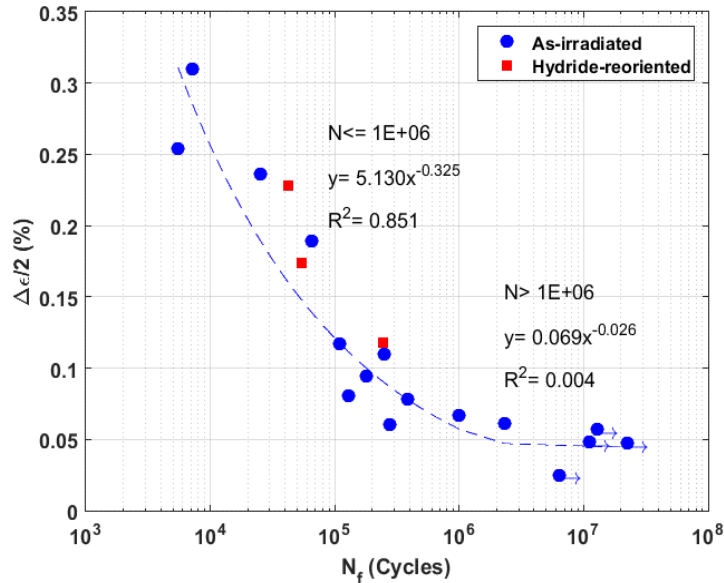


Figure 30 Equivalent strain amplitudes ($\Delta\epsilon/2$) as a function of number of cycles to failure with curve fitting extended to include data points without failure; markers with arrows indicate that tests stopped without failure

Several important observations can be made with respect to the dynamic test results.

- In both as-irradiated and HRT specimens that failed during testing, the fatigue life decreases with increasing strain amplitude, as expected.
- An endurance limit for as-irradiated HBU rods is likely between 0.03–0.05% strain, if it is defined at 10^7 cycles. Below this limit, there does not appear to be a number of cycles that will cause failure.
- There was a large variation of hydrogen content in the cladding for both as-irradiated and HRT test specimens used in the dynamic tests. However, the contribution of hydrogen content to the number of cycles to failure appears to be secondary to the effect of imposed loading amplitudes.
- When reviewing the fatigue life as a function of the calculated gauge strain amplitude, HRT rods showed extended life relative to the as-irradiated rods, but when reviewing the fatigue life as a function of the applied moment amplitude, the HRT rods showed reduced life relative to as-irradiated rods. Further discussion on this subject is provided in Section 4.5, “HRT CIRFT Test Data Evaluation.”

4.2.1 κ -N Curve

The gauge strain amplitude was used to describe the loading condition imposed on the rods. The use of equivalent strain provides an expedient means to estimate the global response of the tested rod. However, the more elaborated localized deformation mechanism involved with pellet-to-pellet interfaces cannot be readily represented by this simplified approach. To provide a more accurate representation of a fatigue lifetime estimate (in addition to the curvature range), a new parameter of maximum curvature was defined. Due to dishing on the pellet end and the existence of an oxide contact interface, HBU fuel is expected to have a weak interface bond at

the pellet-to-pellet interface. This theory is supported by CIRFT test results, in which the flexural rigidity dropped off quickly in the initial cycles of testing, and a nonsymmetric curvature response was revealed in the reverse loading cycle.

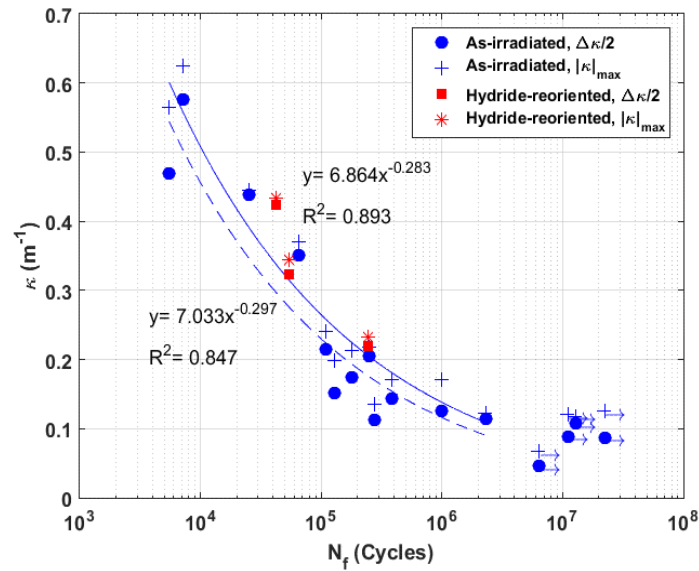
Asymmetrical deformation response is an important signature of the HBU SNF due to pellet-to-pellet cladding interaction. The curvature at the cladding tensile stress site has the highest deformation during fatigue cycles, so it was used to develop the maximum curvature plots shown in Figure 31 to serve as another important index for the HBU SNF fatigue life.

Observations based on curvature amplitude (κ_a , half of curvature range $\Delta\kappa/2$) are similar to those of strain amplitude since conversion simply involved a multiplication factor as shown in Eq. (11).

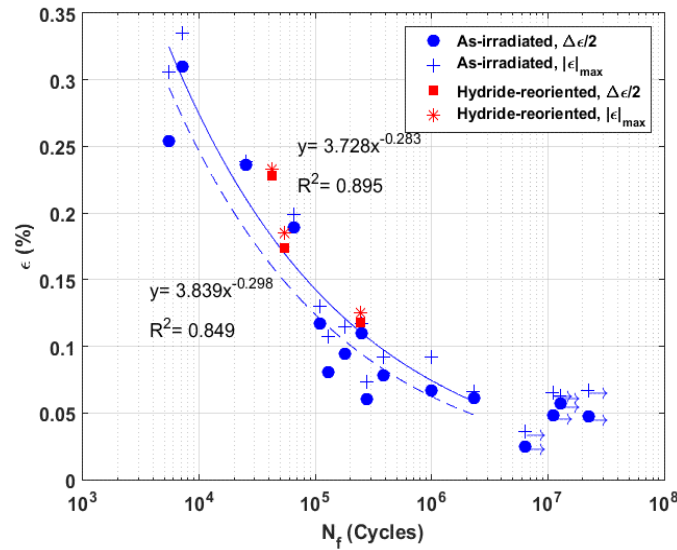
- The fatigue life decreases with increasing curvature amplitude with a defined κ -N curve. The curve fitting generated a power function $y = 7.033 \cdot x^{-0.297}$ with $R^2 = 0.847$, where x is the number of cycles to failure, and y is the curvature amplitude (m^{-1}).
- An endurance limit may be located near $0.05\text{--}0.10 m^{-1}$ if it is defined at 10^7 cycles.

Dynamic tests were conducted under load control, and the curvature response of the rods was not necessarily symmetric, as shown above in Figure 26(d).

An investigation of the maxima of absolute values of curvature extremes ($|\kappa|_{max}$, defined in Section 2) was pursued as an alternative quantity for describing the loading imposed on fuel. This is relevant because the maxima actually reflect the maximum tensile loading levels to which the specimen is subjected during the dynamic testing. The results are shown in Figure 31.



(a)



(b)

Figure 31 (a) Maxima of absolute curvature extremes and curvature amplitudes as a function of number of cycles to failure, and (b) maxima of absolute strain extremes and strain amplitudes as a function of number of cycles to failure; markers with arrows indicate that the tests were stopped without failure

The κ -N curve in terms of maxima of cladding curvature $|\kappa|_{\max}$ has been demonstrated to be similar to that of the curvature amplitude κ_a ; the exponents of the curve-fit power function are similar. The scatter plots based on the two approaches are similar, with some changes in the relative positions of points between 1.1 and 3.9×10^5 cycles. Overall, the maxima of absolute curvature are larger than the curvature amplitude, depending on the magnitude of κ_m .

The following observations can be made with regard to absolute curvature maxima:

- For as-irradiated specimens that failed during the tests, the fatigue life decreases with increasing curvature maxima according to a well-defined κ -N curve. The data points can be fit by using the power function $y = 6.864 \cdot x^{-0.283}$ with a R^2 value as high as 0.893, where x is the number of cycles to failure, and y is the curvature maxima (m^{-1}).
- A fatigue limit may be located near 0.07 to 0.12 m^{-1} if it is defined at 10^7 cycles.
- Due to the unsymmetrical deformation nature of HBU SNF under dynamic cycling, the bending neutral axis of the deformed rod is expected to shift away from the cladding tensile stress site. A first order approximation of simplified strain conversion from the curvature was used to derive the strain maxima.

The associated strain maxima and strain amplitude vs. the number of cycles to failure are given in Figure 31(b). Overall, the maxima of absolute strain are larger than the strain amplitude.

Additional curve fitting to the fatigue lifetime as a function of curvature amplitudes, curvature maxima, and strain maxima was completed using piece-wise power fits; the graphical results are presented in Figure 32, and the curve-fitting parameters are given in Table 8. Note that R^2 values associated with the high-cycle power fit are generally quite low. This is likely because many of the tests at low amplitudes were discontinued without reaching sample fracture.

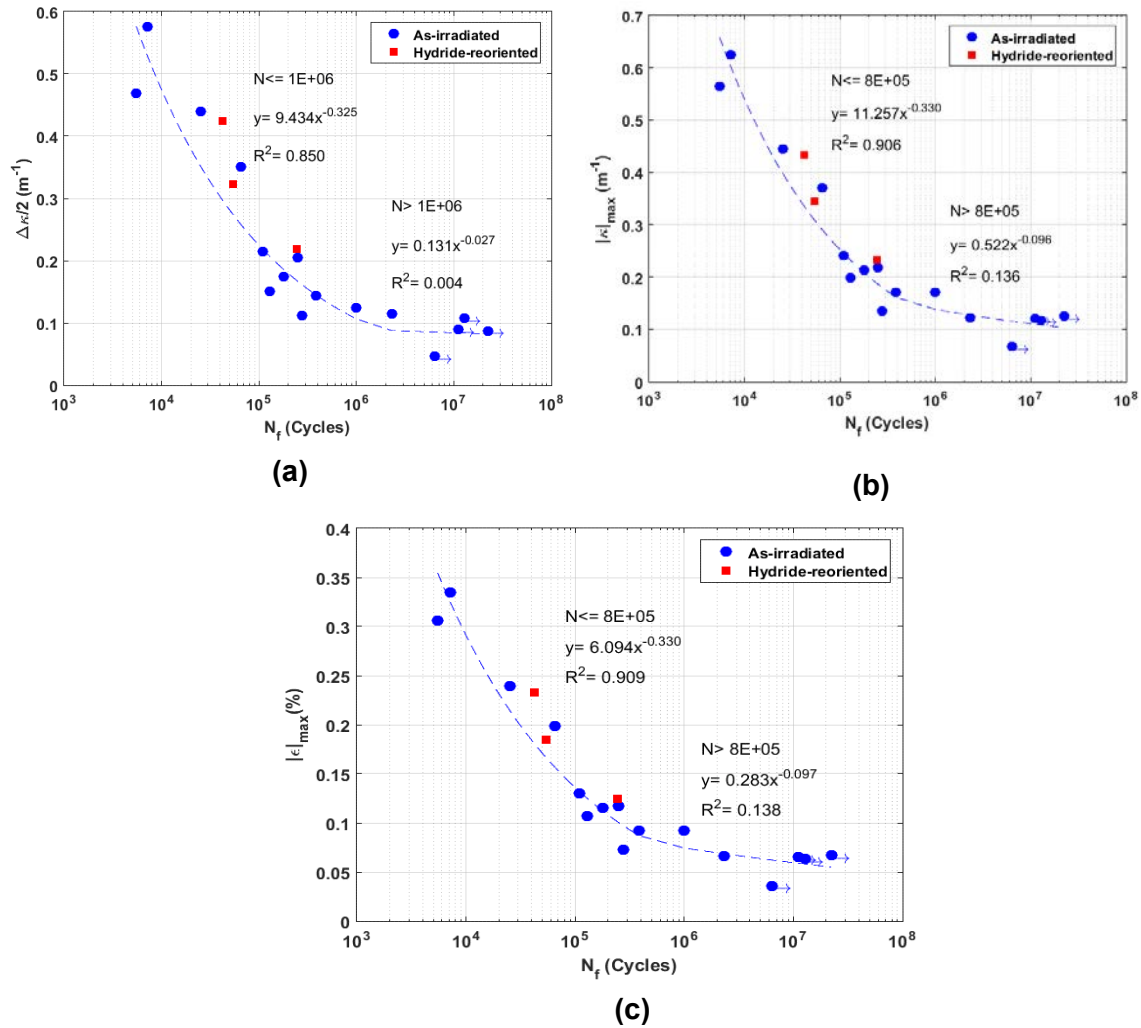


Figure 32 (a) Curvature amplitudes, (b) maxima of absolute curvature extremes, and (c) maxima of absolute strain extremes as a function of number of cycles to failure; Curve-fitting was extended to include the no-failure data points; markers with arrows indicate that the tests were stopped without failure.

Table 8 Curve-fitting parameters of curvature and strain as a function of cycles*

	A	a	R ²	A	a	R ²
	N ≤ 1E+06			N > 1E+06		
Curvature amplitude	9.434	-0.325	0.850	0.131	-0.027	0.004
Strain amplitude	5.130	-0.325	0.851	0.069	-0.026	0.004
	N ≤ 8E+05			N > 8E+05		
Curvature maxima	11.257	-0.330	0.906	0.522	-0.096	0.136
Strain maxima	6.094	-0.330	0.909	0.283	-0.097	0.138

*Based on $y = A \cdot x^a$, where x represents cycles and y represents amplitude or maxima.

4.3 Post-Irradiation Examination

The objective of the post-irradiation examination (PIE) was to gather meaningful information to identify underlying failure mechanisms. The primary focuses were:

- to generate information on cladding features such as hydrides and incipient cracks near pellet-to-pellet interfaces and near the mid-pellet,
- to reveal information about the fuel/cladding bond, and
- in order to preserve SNF system damage profile, the PIE was performed with fuel pellet intact.

4.3.1 As-Irradiated Samples PIE

PIE was conducted on five as-irradiated fuel segments taken from the same father rod (E02-605) but with different mechanical loading histories:

- Untested – 605D1D
- Tested and failed under static loading condition at a pellet-to-pellet interface: S2/ 605D1E
- Tested but non-failed under dynamic loading condition: D4/ 605D1C
- Tested and failed under dynamic loading at a pellet-to-pellet interface: D3/ 605C10A
- Tested and failed under dynamic loading but not at pellet-to-pellet interface: D5/ 605D1B

PIEs were generally conducted on axial sections, but one PIE was carried out on a transverse section. For the tested and failed specimen, the preparation of axial sections involved the following steps:

- (1) Cut a one-inch segment on the fracture end.
- (2) Mount the segment with the bending plane in the horizontal direction, and cut the top half away.
- (3) Back-pot the remaining half to keep all the fuel in place.
- (4) Grind and polish the section to the required finish for metallography.

Examinations were then performed on an optical microscope.²¹ The procedure for preparing sections for all the segments/specimens was similar to the procedure outlined above.

PIE on the transverse section was conducted only on D3. The section was prepared using a piece of fuel rod approximately a 0.25-inch long cut away from the fracture surface of the specimen. The segment was defueled using hot nitric acid. The defueled cladding was removed from the hot cell and cleaned with water and alcohol in an ultrasonic cleaner. The inside and outside surfaces of the cladding were then coated with a thin layer of epoxy. Then the section was ground and polished to the required finish for examination using scanning electron microscopy (SEM). Observations on the transverse section can be found in Appendix F, and those for the axial sections will be briefly discussed below.

An optical image of an untested axial section of segment 605D1D is shown in is shown in Figure 33. The one partial and three complete fuel pellets shown in the image can be easily differentiated because the as-fabricated pellet dishing at both ends of each pellet is clearly visible.

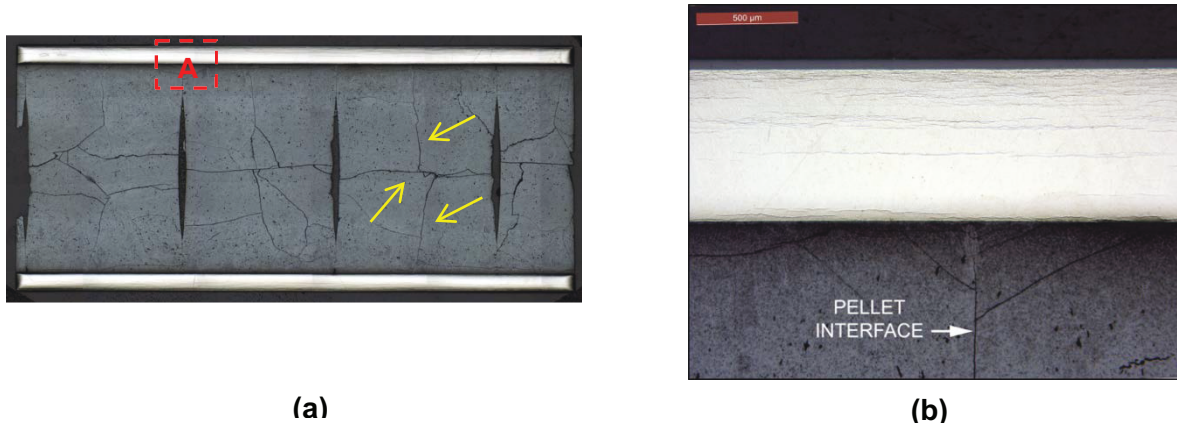
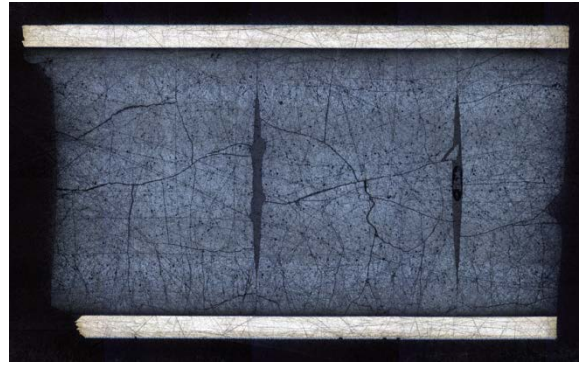


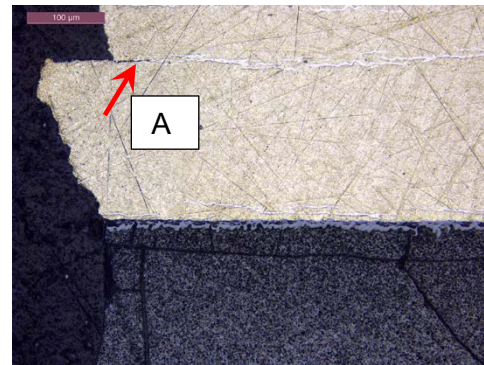
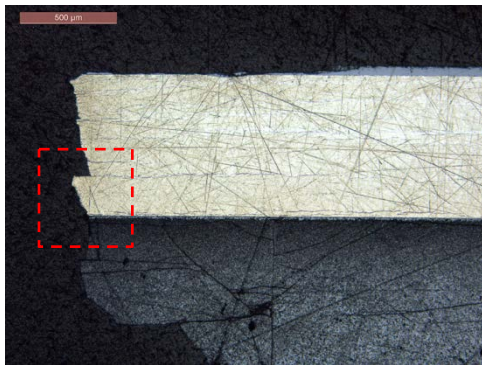
Figure 33 Images of untested segment 605D1D for (a) overall axial cross section and (b) enlarged area A

In Figure 33(a), two primary fractures with sizes of pellet length and pellet radius were developed along and normal to the axial direction, respectively. Detailed study showed that the pellet-to-pellet interface near the edge of the dish and the pellet-to-cladding interface were fairly close, with no visible gaps. Secondary fractures developed within the pellets close to the pellet-to-cladding interfaces. A cavity is also observed around some triple boundaries of pellets and cladding. The circumferential hydride layers can be seen clearly over the cladding thickness, as shown in Figure 33(b). The circumferential hydrides are widely spaced in the large middle part of the wall. The density of the hydrides increases significantly toward the outside of the cladding and in the cladding-pellet interface area. The circumferential hydride layers are very sizable, and in the middle of the cladding wall, the layers can run axially more than 1,000 μm in length. The outside surface of cladding is covered with a continuous thinner oxide layer that measured about 75 μm.

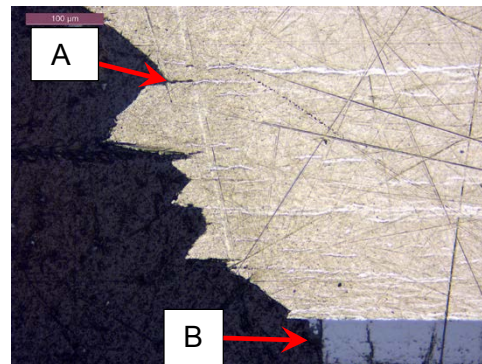
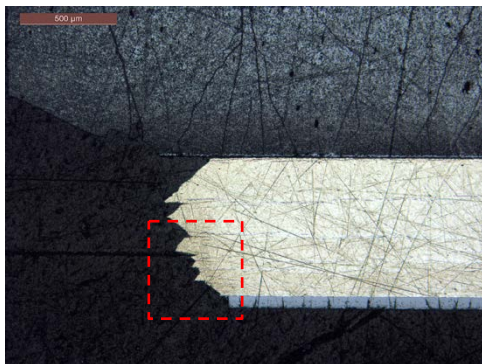
Images based on the axial section of S2 specimen are shown in Figure 34. The fuel failure occurred at the pellet-to-pellet interface PPI, as seen from images b) and c). Unlike the pellet fractures that occurred as a result of operation observed in the fuel segment prior to CIRFT testing, the axial fractures did not align. Instead, they tilted toward the axial direction. The pellet-to-cladding interface appeared to be in good contact. The fracture surface in the cladding exhibited a zigzag pattern on the back and front sides of the specimen. The unique fracture pattern of the cladding is presumed to result from the combination of the brittle fracture of hydrides and the ductile failure of the metal matrix under tension. Delamination can be seen between the circumferential hydride layers near the fracture surface. In addition, spalling and cracking of the surface oxide layer can be seen in Figure 34(c).



(a)



(b)



(c)

Figure 34 (a) Axial cross section of S2/ 605D1E, (b) fracture surface near back side of rod and an enlarged area, and (c) fracture surface near front side of rod and an enlarged area (A = delamination of circumferential hydride layers, B = spalling and cracking of oxide layer)

Information on the PIEs of the other fuel segments can be found in Appendix F, including data on five axial sections and one transverse section.

The following observations were made based on the PIE.

- Pellet-to-pellet interface and pellet-cladding interfaces (PCIs) near the edges or peripheral areas of pellets appeared to be in good contact. No significant gap or filling was observed in the interfaces.
- The pellets exhibited fracturing that was normal for as-irradiated fuel. These fractures were observed in both untested and tested fuel segments.
- Tested specimen failures occurred primarily at pellet-to-pellet interface.
- The density of the hydride layers increases significantly toward the outside of cladding wall. The cladding outer wall was covered with an oxide layer that was 75 μm thick.

4.3.2 HRT Samples PIE

The segments subjected to HRT were subjected to CIRFT testing at room temperature to evaluate the materials' performance after HRT. After the tests were completed in the CIRFT, the specimens were examined to verify that radial hydrides had been generated. Figure 35 shows the hydride morphology of HR1 sample following HRT.

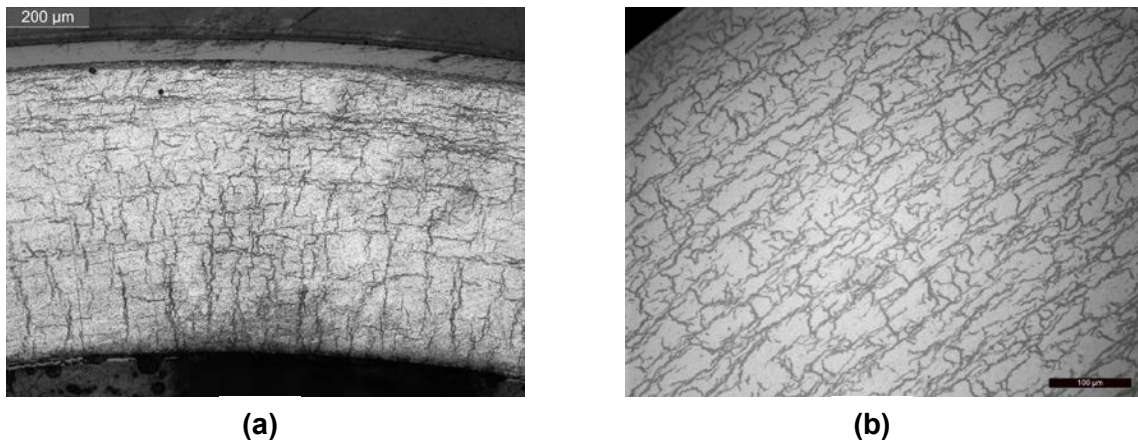


Figure 35 (a) High magnification micrograph showing radial hydrides of Sample HR-1 ($H \approx 360\text{--}400$ ppm); the HBU HBR specimen was pressurized to 140 MPa at 400 °C with five thermal cycles; (b) high magnification micrograph showing radial hydrides of a sample of unirradiated, hydrogen charged zircaloy-4 ($H \approx 286 \pm 20$ ppm); the specimen was sectioned at the mid-plane of a sample that was 6 inches long

The hydrogen concentration of this sample was about 360–400 wppm. The specimen used for metallography was sectioned at the midplane of a sample 6 inches long. Although the in-cell HRT test conditions were the same as the out-of-cell test HR-HBR#2 (detailed in Appendix H), and the hydrogen concentration of these two samples were compatible, the morphology of HBU sample HR1 was different from hydrided sample HR-HBR#2. For the unirradiated sample, the circumferential hydrides were uniformly distributed across the wall, and the maximum length of its radial hydrides was about 50–60 μm . For HBU samples, the radial hydrides were mainly distributed near the inner surface, and the circumferential hydrides were mostly seen near the outer surface. The length of the radial hydride of the HBU sample shown in Figure 35(a) was also much longer than the unirradiated sample shown in Figure 35(b).

4.4 Cladding Oxide Effect Study

CIRFT test data and the associated oxide thickness are shown in Table 9.

Table 9 HBR SNF CIRFT data with the associated tested rod's oxide thickness

Spec label ID	Moment amplitude	Number of cycles	Flexural rigidity	κ_a	S_a	ϵ_a	Oxide thickness ¹
Unit	N-m	#	N-m ²	m ⁻¹	MPa	%	μm
As-irradiated CIRFT data							
D8	7.74	>1.28E+07	72.3	0.107	66.31	0.057	70–100
D14	7.84	2.74E+05	70.0	0.112	66.65	0.06	100–110
D5	8.20	2.30E+06	71.9	0.114	69.71	0.061	40–70
D3	9.17	1.00E+06	73.4	0.125	77.94	0.067	70–100
D12	9.99	3.86E+05	69.4	0.144	83.62	0.078	70–100
D10	11.55	1.80E+05	66.4	0.174	98.19	0.094	70–100
D6	11.62	2.50E+05	56.7	0.205	99.55	0.11	70–100
D13	12.55	1.29E+05	83.1	0.151	106.68	0.081	100–110
D1	14.11	1.10E+05	65.6	0.215	117.26	0.117	70–100
D7	18.92	6.50E+04	53.9	0.351	160.84	0.189	70–100
D0	24.07	2.50E+04	54.8	0.439	206.11	0.236	40–70
D11	29.02	5.50E+03	61.9	0.469	241.22	0.254	70–100
D9	33.67	7.10E+03	58.5	0.576	288.31	0.31	70–100
HRT CIRFT data							
HR1	15.15	4.19E+04	35.7	0.424	128.79	0.228	40-44
HR3	8.98	2.44E+05	41.0	0.219	76.34	0.118	40-44
HR4	14.76	5.47E+04	45.7	0.323	125.45	0.174	40-44

Under similar loading amplitudes, the CIRFT data of as-irradiated specimens suggest reduced fatigue life for higher oxide thicknesses. For instance, the D8 sample with 70–100 μm oxide thickness and the D14 sample with 100–110 μm oxide thickness had similar loading amplitudes; the D8 sample had much longer fatigue life (>12M cycles) compared to the D14 sample (2.74E5 cycles). The CIRFT data are shown with distinct labels for four oxide thickness ranges in Figure 36.

The plots of as-irradiated baseline data for moment amplitude and strain amplitude input from HBR baseline data show a self-consistent trend: as-irradiated CIRFT data with higher oxide thickness showed less fatigue life, while for HRT data, a different trend was observed from moment amplitude and strain amplitude input plots. In the moment amplitude plot, HRT data showed reduced fatigue life below the mean trend curve of 70–100 μm oxide thickness, while as in strain amplitude, plot HRT data showed increased fatigue life above the mean trend curve. The HRT samples had the lowest oxide thickness, as shown in Figure 36. Thus, HRT data would have been expected to trend above the mean fatigue strength trend curve of 70–100 μm oxide thickness per the as-irradiated results, which suggests that reorientation may dominate any oxide effects.

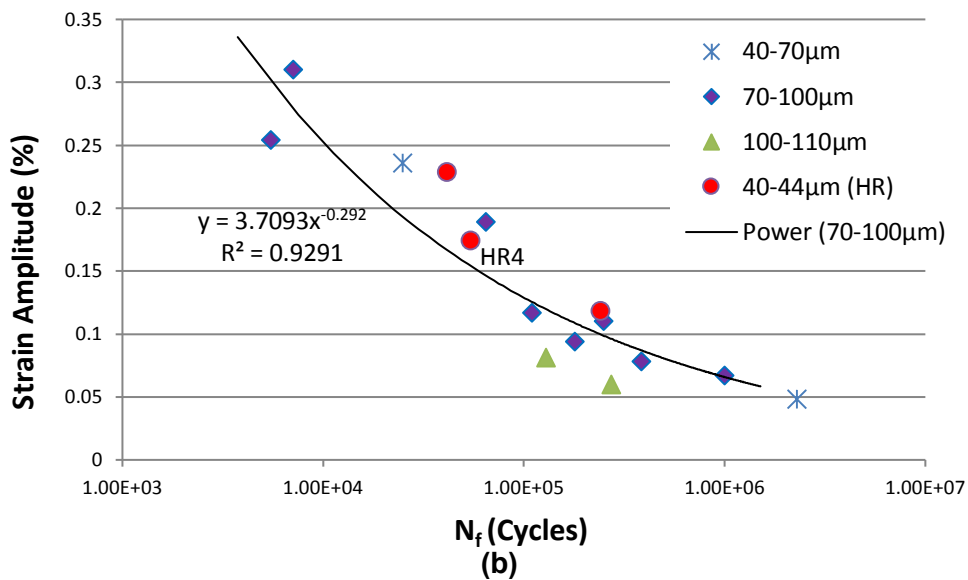
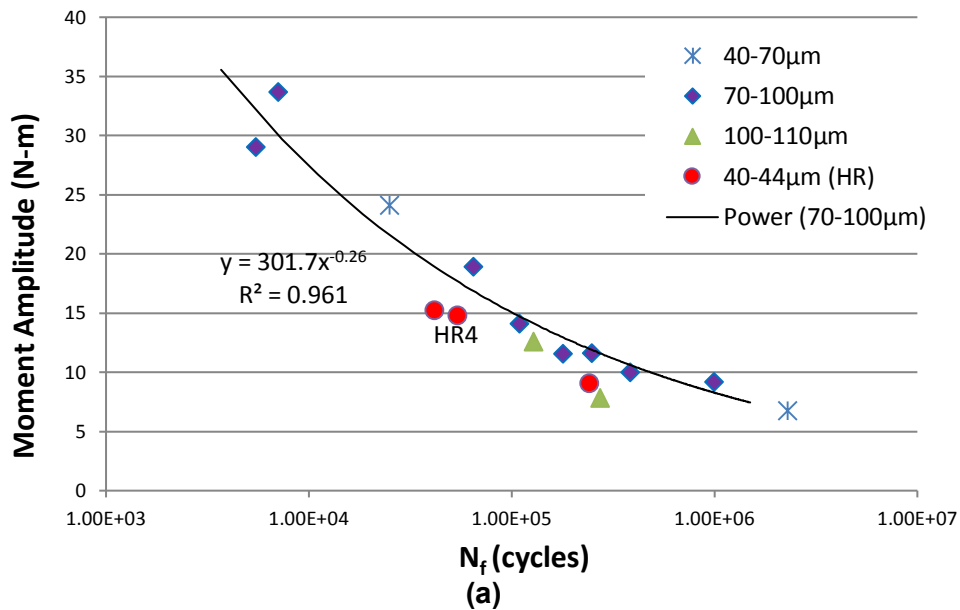


Figure 36 (a) Moment amplitude vs. number of failure cycles, (b) strain amplitude vs. number of failure cycles, as function of clad oxide thickness; HR4 only has thermal annealing treatment without pressurization applied

4.5 HRT CIRFT Test Data Evaluation

The detailed HRT procedure used for developing HRT CIRFT test samples is provided in Appendix H. Reoriented hydrides can change the SNF rod system response. In addition, the procedure used to reorient the hydrides may result in other physical changes to the specimen, including changing pellet-cladding bonding efficiency or developing gaps at pellet-clad interface regions due to the thermal treatment (400 °C) and clad tubing pressurization (140 MPa hoop

stress). Evidence of pellet-clad interface bonding disruption and gap formation in the HRT rod system was verified through PIE on HR1 sample, as shown in Figure 37; such gap formation was not observed in as-irradiated PIE shown earlier in Figures 33 or 34. The consequences of pellet-cladding interface bonding disruption¹³ or increase in gap density at the interface would be reduced flexural rigidity and increased contact load intensity of pellet-cladding mechanical interaction in HRT samples. Table 9 also shows that HRT samples had lower flexural rigidity compared to as-irradiated samples. The reduced flexural rigidity of HRT samples resulted in an increase in strain amplitude to failure under similar loading amplitudes when compared to as-irradiated samples. Furthermore, the reduction in flexural rigidity may indicate that the HRT sample has a different composite system when compared to as-irradiated sample; thus, using the HRT gauge strain amplitude vs. the failure frequency trend for comparison to as-irradiated samples may be misleading.

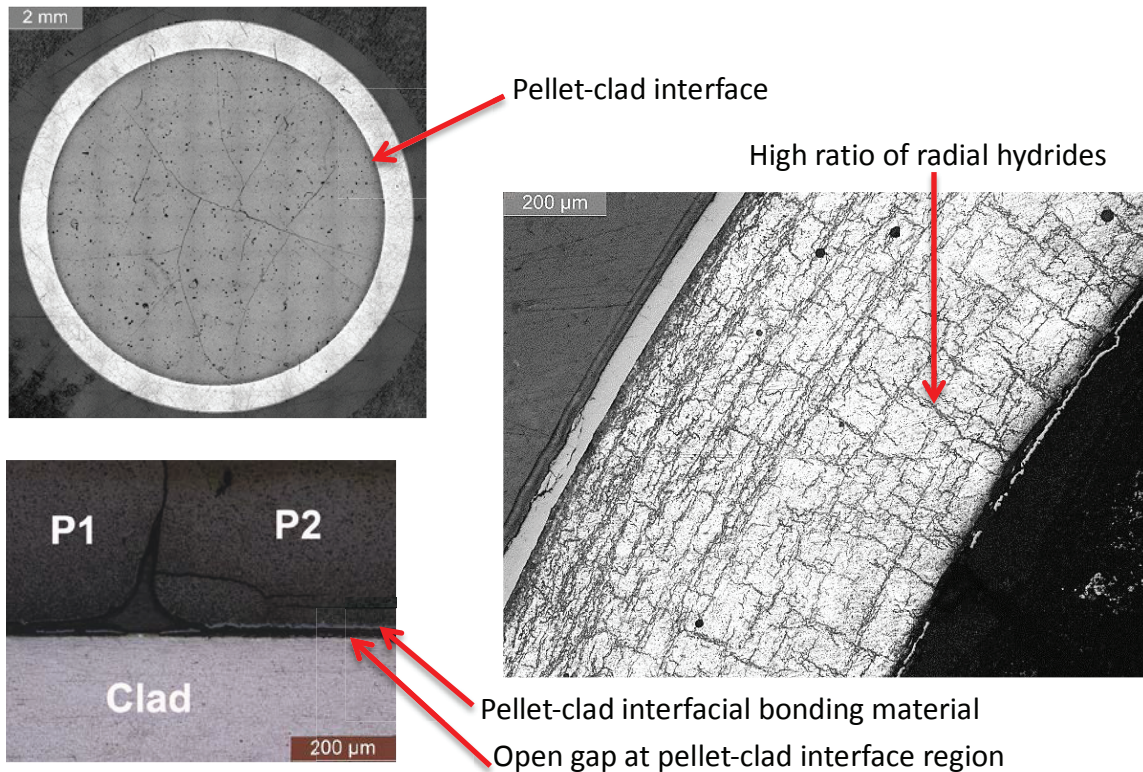


Figure 37 Metallographic examination of fuel and cladding: results of HR1, which show debonding phenomenon and gap formation at pellet-clad interface and high density of radial hydride formation in HRT treated rod

Furthermore, the HR1 sample showed significant radial hydride populations. However, HR1 data only had a marginal reduction in fatigue life compared to HR4 data with thermal treatment only (see Figure 36). HR1 and HR4 have similar oxide thicknesses, as shown in Table 9.

5 CONCLUSIONS

High burnup HBR fuel rods were tested and evaluated under both static and dynamic loading conditions using the CIRFT equipment developed at ORNL. The CIRFT system is composed of a U-frame equipped with load cells for imposing pure bending loads on the spent fuel rod test specimen and measuring the *in-situ* curvature of the fuel rod during bending using a 3-LVDT set-up. In general, the static CIRFT test results indicate a significant increase in flexural rigidity compared to that of the defueled HBU rod specimen, even considering the numerous stress riser sites into an HBU rod system.

The static tests were conducted under displacement control at a rate of 0.1 mm/s to a maximum displacement of 12.0 mm at each loading point. Dynamic tests were conducted under load control of ± 5.08 to ± 35.56 N·m, 5 Hz. PIEs were performed on selected specimens. Both as-irradiated fuel rods and HR-treated fuel rods were tested.

- The HBU as-irradiated HBR rods survived static unidirectional bending to a maximum curvature of 2.2–2.5 m^{-1} , or a maximum moment of 85–87 N·m (Table 3). The maximum equivalent strain was 1.2–1.3%.
- The HBU as-irradiated HBR rods exhibited a multiple-stage constitutive response with two linear stages followed by a nonlinear stage. The flexural rigidity at the initial stage was 63–79 N·m², corresponding to an elastic modulus of 101–125 GPa (Table 4).
- The deformation of the HBU HBR subjected to HRT showed a similar loading behavior, but with lower flexural rigidity compared to that of as-irradiated specimens under similar curvature.
- A large majority of the specimen failures of the HBU HBR rods for both as-irradiated or HRT samples under static unidirectional loading occurred or initiated near the pellet-to-pellet interface, as validated by the post-test or PIEs.
- Comparing the HBU HBR static bending response to a theoretical calculated response of cladding alone, the flexural rigidity was approximately twice what would be obtained if cladding properties alone were used to predict behavior.
- The fatigue life of HBU as-irradiated HBR rods in the cyclic test depended on the level of loading. Under loading with moments of ± 8.89 to ± 35.56 N·m and strain of ± 0.03 to $\pm 0.38\%$ at 5 Hz (Table 6), the fatigue life ranged from 5.5×10^3 to 2.3×10^6 cycles.
- The ϵ -N curve of the HBU as-irradiated HBR rods can be described by a power function of $y = 3.839 \cdot x^{-0.298}$, where x is the number of cycles to failure, and y is the strain amplitude (%).
- Based on strain amplitude, a fatigue limit is likely located between 0.03–0.05% if it is defined at 10^7 cycles.

- Maxima of the curvature in dynamic tests ranged from ± 0.07 to $\pm 0.62 \text{ m}^{-1}$ at 5 Hz (Table 6). The κ -N curve of the HBU as-irradiated HBR rods can be described by a power function of $y = 6.864 \cdot x^{-0.283}$, where x is the number of cycles to failure, and y is the maxima of cladding tensile curvature $|\kappa|_{\max} (\text{m}^{-1})$. A fatigue limit based on maxima of curvature is likely located between 0.07 – 0.12 m^{-1} if it is defined at 10^7 cycles.
- The failure of HBU HBR rods under cyclic reverse loading was primarily due to pellet-cladding interaction and generally resided at the pellet-to-pellet interface, as validated by the PIE.
- Review of the fatigue life as a function of the calculated gauge strain amplitude indicates that the HRT rods showed extended life relative to the as-irradiated rods. On the other hand, review of the fatigue life as a function of the applied moment amplitude indicates that the HRT rods showed reduced life relative to the as-irradiated rods. However, reduction is largely within the scatter of the as-irradiated rods.

6 REFERENCES

- 1 E. J. Ruzauskas and K. N. Fardell, "Design, Operation, and Performance Data for High Burnup PWR Fuel from H. B. Robinson Plant for Use in the NRC Experimental Program at Argonne National Laboratory," Electric Power Research Institute, EPRI Report 1001558, 2001.
- 2 B. Hanson, H. Alsaed, C. Stockman, D. Enos, R. Meyer, and K. Sorenson, "Gap Analysis to Support Extended Storage of Used Nuclear Fuel," Rev. 0, US Department of Energy Used Fuel Disposition Campaign, January 31, 2012.
- 3 D. Tang, A. Rigato, R. Einziger, "Flaw Effects and Flaw Reorientation on Spent Fuel Rod Performance, a Simulation with Finite Element Analysis," Proceedings of the ASME 2015 Pressure Vessels and Piping Conference, July 19–23, 2015, Boston, MA, USA.
- 4 J.-A. J. Wang, H. Wang, Y. Yan, R. Howard, and B. Bevard. "High Burn-up Spent Fuel Vibration Integrity Study Progress Letter Report Out-of-Cell Fatigue Testing Development—Task 2.1)," ORNL/TM-2010/288, Oak Ridge National Laboratory, Oak Ridge, TN, January 2011.
- 5 J.-A. J. Wang, H. Wang, T. Tan, H. Jiang, T. Cox, and Y. Yan. "Progress Letter Report on U Frame Test Setup and Bending Fatigue Test for Vibration Integrity Study (Out-of-Cell Fatigue Testing Development—Task 2.2)," ORNL/TM-2011/531, Oak Ridge National Laboratory, Oak Ridge, TN, January 2012.
- 6 J.-A. J. Wang, H. Wang, T. Cox, and Y. Yan. "Progress Letter Report on U-Frame Test Setup and Bending Fatigue Test for Vibration Integrity Study (Out-of-Cell Fatigue Testing Development—Task 2.3)," ORNL/TM-2012/417, Oak Ridge National Laboratory, Oak Ridge, TN, August 2012.
- 7 J.-A. J. Wang, H. Wang, and Ting Tan, "An Innovative Dynamic Reversal Bending Fatigue Testing System for Evaluating Spent Nuclear Fuel Rod Vibration Integrity or Other Materials Fatigue Aging Performance," ORNL Invention Disclosure 201102593, DOE S 124, 149, April 8, 2011. Patent in review, 13/396,413, February 14, 2012.
- 8 H. Wang, J.-A. J. Wang, T. Tan, H. Jiang, T. S. Cox, R. L. Howard, B. B. Bevard, and M. E. Flanagan, "Development of U-Frame Bending System for Studying the Vibration Integrity of Spent Nuclear Fuel," *Journal of Nuclear Materials* 440, 201–213, 2013.
- 9 J.-A. J. Wang, B. B. Bevard, R. L. Howard, and M. E. Flanagan, "SNF Test System for Bending Stiffness and Vibration Integrity," *International High-Level Radioactive Waste Management Conference*, Albuquerque, NM, April 28–May 2, 2013.
- 10 J.-A. J. Wang, H. Wang, T. Cox, and C. Baldwin, "Progress Letter Report on Bending Fatigue Test System Development for Spent Nuclear Fuel Vibration Integrity Study (Out-of-Cell Fatigue Testing Development, Task 2.4)," ORNL/TM-2013/225, Oak Ridge National Laboratory, Oak Ridge, TN, July 2013.

-
- 11 J.-A. J. Wang, H. Wang, B. B. Bevard, R. L. Howard, and M. E. Flanagan, "Reversible Bending Fatigue Test System for Investigating Vibration Integrity of Spent Nuclear Fuel During Transportation," *Proceedings of the 17th International Symposium on the Packaging and Transportation of Radioactive Materials*, PATRAM 2013, San Francisco, CA, August 18, 2013.
 - 12 J.-A. J. Wang and H. Wang, "Progress Letter Report on Reversible Bending Fatigue Testing of Zry-4 Surrogate Rod (Out-of-Cell Fatigue Testing Development—Task 2.4)," ORNL/TM-2013/297. Oak Ridge National Laboratory, Oak Ridge, TN, August 2013.
 - 13 Jiang Hao, Jy-An Wang, and Hong Wang, "The Impact of Interface Bonding Efficiency on High-Burnup Spent Nuclear Fuel Vibration Integrity," *Journal of Nuclear Engineering and Design*, 309, 40–52, 2016.
 - 14 G. Bjorkman, "High Burnup Spent Fuel Testing Program Objectives," NRC Program Review Meeting, Oak Ridge National Laboratory, August 8, 2011.
 - 15 J.-A. J. Wang and H. Wang, 2014 Semi-Annual Progress Letter Report on Used Nuclear Fuel Integrity Study in Transportation Environments, ORNL/TM-2014/63, April 2014.
 - 16 H. Wang and J.-A. J. Wang, "Bending testing and characterization of surrogate nuclear fuel rods made of Zircaloy-4 cladding and aluminum oxide pellets," *Journal of Nuclear Materials*, 479, 470–482, 2016.
 - 17 C. Baldwin, Oak Ridge National Laboratory, Mar. 6, 2013.
 - 18 M. C. Billone, T. Burtseva, and Y. Y. Liu, "Baseline Properties and DBTT of High-Burnup PWR Cladding Alloys," *Proceedings of the 17th International Symposium on the Packing and Transportation of Radioactive Materials*, PATRAM 2013, San Francisco, CA, August 18–23, 2013.
 - 19 US Nuclear Regulatory Commission, "Cladding Embrittlement during Postulated Loss-of-Coolant Accidents," NUREG/CR-6967/ANL-07/04, Office of Nuclear Regulatory Research, Nuclear Regulatory Commission, July 2008.
 - 20 M.C. Billonea, T.A. Burtsevaa, R.E. Einziger, "Ductile-to-brittle transition temperature for high-burnup cladding alloys exposed to simulated drying-storage conditions," *Journal of Nuclear Materials*, Volume 433, Issues 1–3, 431–448, February 2013.
 - 21 J-A Wang and H. Jiang, "Quantification of CIRFT System Biases and Uncertainties When Testing High-Burnup Spent Nuclear Fuel," ORNL/TM-2014/288, DOE FCRFD-2014-000604, September 2014.
 - 22 J.-A. Wang, H. Jiang, and H. Wang, "Using Finite Model Analysis and Out of Hot Cell Surrogate Rod Testing to Analyze High Burnup Used Nuclear Fuel Mechanical Properties," ORNL/TM-2014/257, DOE FCRD-UFD-2014-000603, August 2014.
 - 23 Geelhood, K. J. et al., PNNL Stress/Strain Correlation for Zircaloy, PNNL-17700, Pacific Northwest National Laboratory, Richland, Washington, July 2008.

APPENDIX A ROD SEGMENTS AND CUTTING PLAN

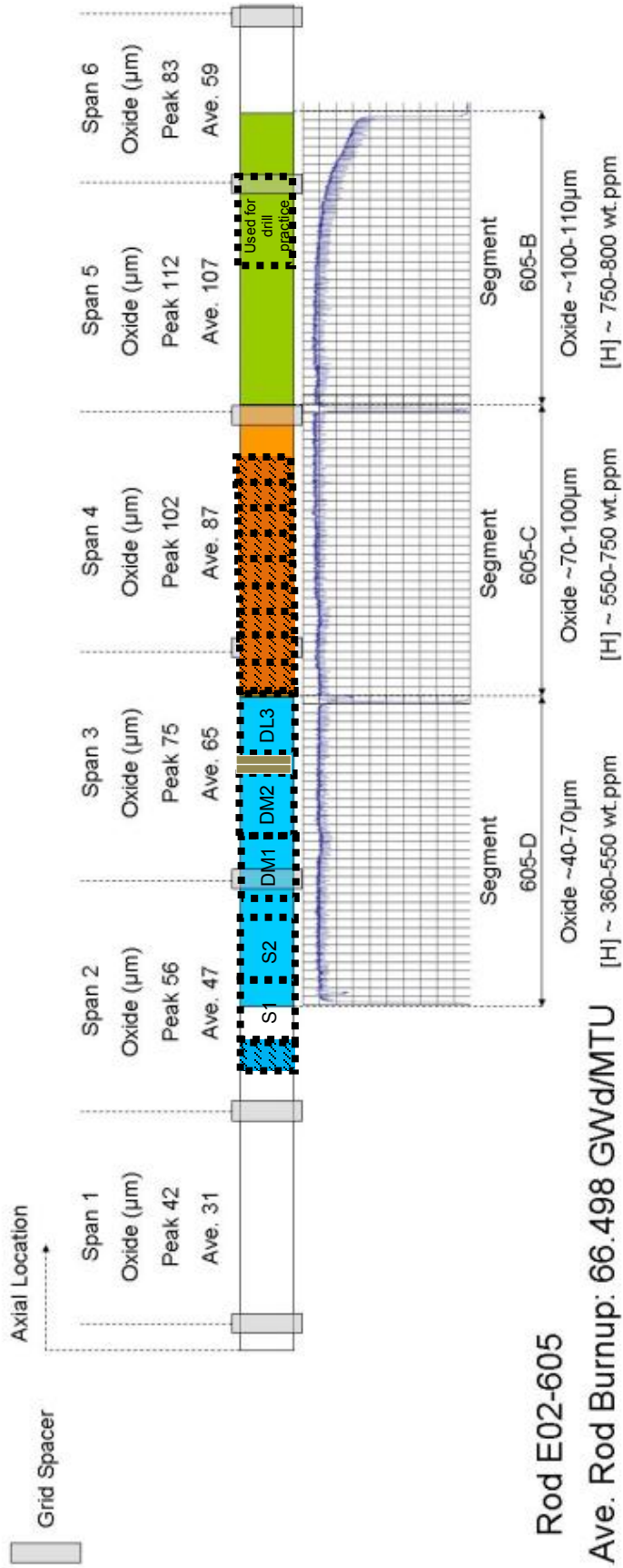
APPENDIX A ROD SEGMENTS AND CUTTING PLAN

Table A.1 Specification of rod segments to be used in hot cell testing

Spec Label	ORNL Label	NRC Original Label	ORNL Inventory Label ("Seg. ID")	Span	Burnup* (rod average, GWD/MTU)	Estimated Oxide* (µm)	Estimated Hydrogen of Span** (wppm)	Estimated Local Hydrogen (wppm)
S1	S1	S3	606C3C	4	66.8	70-100	550-750	650
S2	S2	S2	605D1E	2-3	66.5	40-70	360-550	400
S3	DCAL	DCAL	609C5	4	66.5	70-100	550-750	550
S4	SCAL	SCAL	609C6	4	66.5	70-100	550-750	550
D1	DL1	DL1	607C4B	4	63.8	70-100	550-750	700
D2	DL2	DL2	608C4B	4	63.8	70-100	550-750	700
D3	DL3	DL3	605C10A	4	66.5	70-100	550-750	550
D4	DM1	DM1	605D1C	2-3	66.5	40-70	360-550	500
D5	DM2	DM2	605D1B	2-3	66.5	40-70	360-550	550
D6	DH1	DH1	609C4	4	66.5	70-100	550-750	700
D7	DH2	DH2	609C3	4	66.5	70-100	550-750	750
D8	DM3	DM3	606C3E	4	66.8	70-100	550-750	550
D9	DH3	DH3	609C7	4	66.5	70-100	550-750	550
D10	S5	S5	606C3A	4	66.8	70-100	550-750	750
D11	R1	R1	607C4A	4	63.8	70-100	550-750	700
D12	R2	R2	608C4A	4	63.8	70-100	550-750	700
D13	R3	R3	606B3E	5	66.5	100-110	750-800	750
D14	R4	R4	606B3D	5	66.5	100-110	750-800	750
D15	R5	R5	606B3C	5	66.5	100-110	750-800	750
D16/ Dcal	S3	S1	605D1F	2-3	66.5	40-70	360-550	360
Demo1	DEMO1	DEMO1	606B2	5	66.5	100-110	750-800	750
Scal1	DEMO2	DEMO2	606B3B	5	66.5	100-110	750-800	750
Scal2	S4	S4	606C3B	4	66.8	70-100	550-750	700
HR1	HR1	HR1	607D4C	2	63.8	40-44	360-400	400
HR2	HR2	HR2	607D4A	2	63.8	40-44	360-400	400
HR3	HR3	HR3	608D4A	2	63.8	40-44	360-400	400
HR4	HR4	HR4	608D4C	2	63.8	40-44	360-400	400

* E. J. Ruzauskas, and K. N. Fardell, "Design, Operation, and Performance Data for High Burnup PWR Fuel from H. B. Robinson Plant for Use in the NRC Experimental Program at Argonne National Laboratory," Electric Power Research Institute, EPRI Report 1001558, 2001.

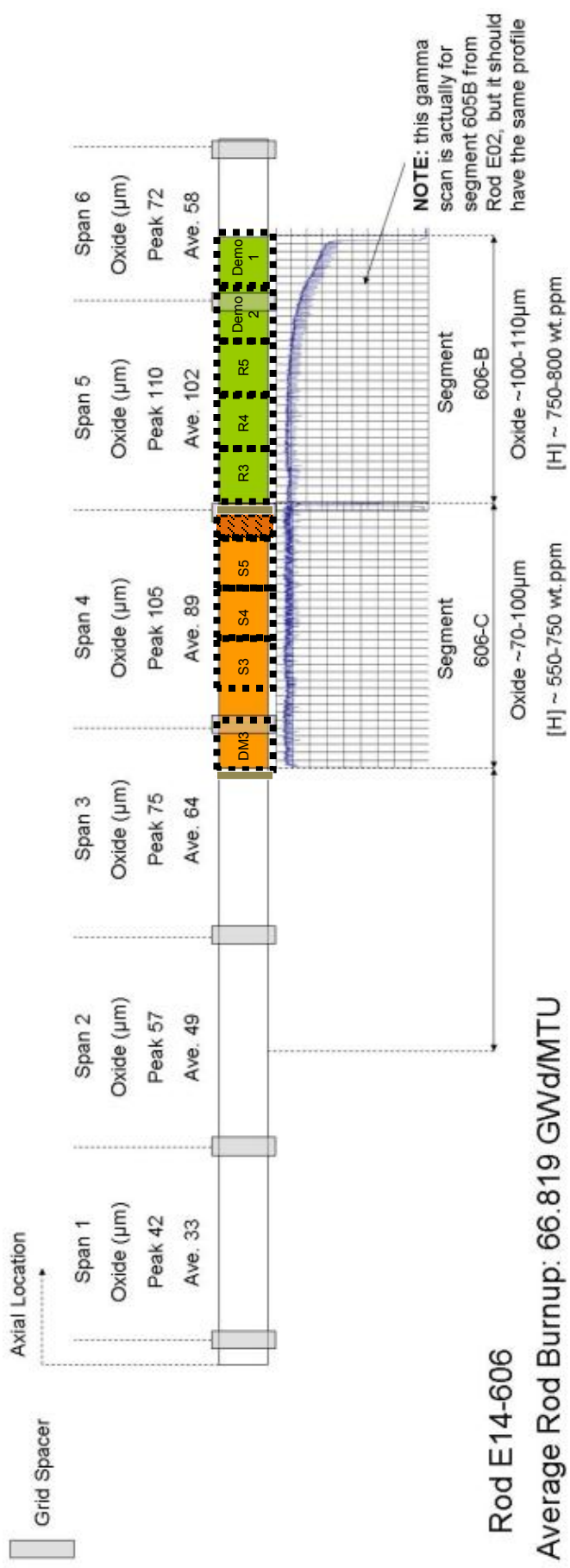
** M.C. Billone, T. Burtseva, and Y.Y. Liu, "Baseline Properties and DBTT of High-Burnup PWR Cladding Alloys," Proceedings of the 17th International Symposium on the Packaging and Transportation of Radioactive Materials, PATRAM 2013, San Francisco, CA, August 18-23, 2013; C. Baldwin, Oak Ridge National Laboratory, Mar. 6, 2013.



Rod E02-605

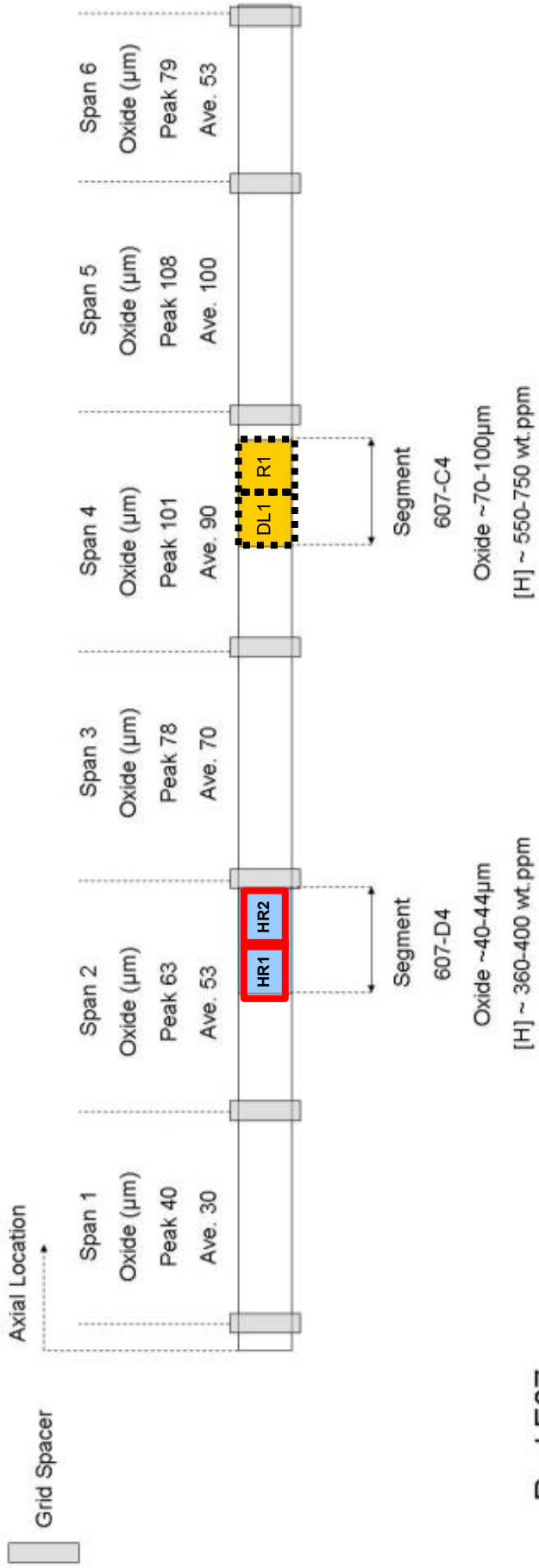
Ave. Rod Burnup: 66.498 GWd/MTU

(a)



Rod E14-606
Average Rod Burnup: 66.819 GWd/MTU

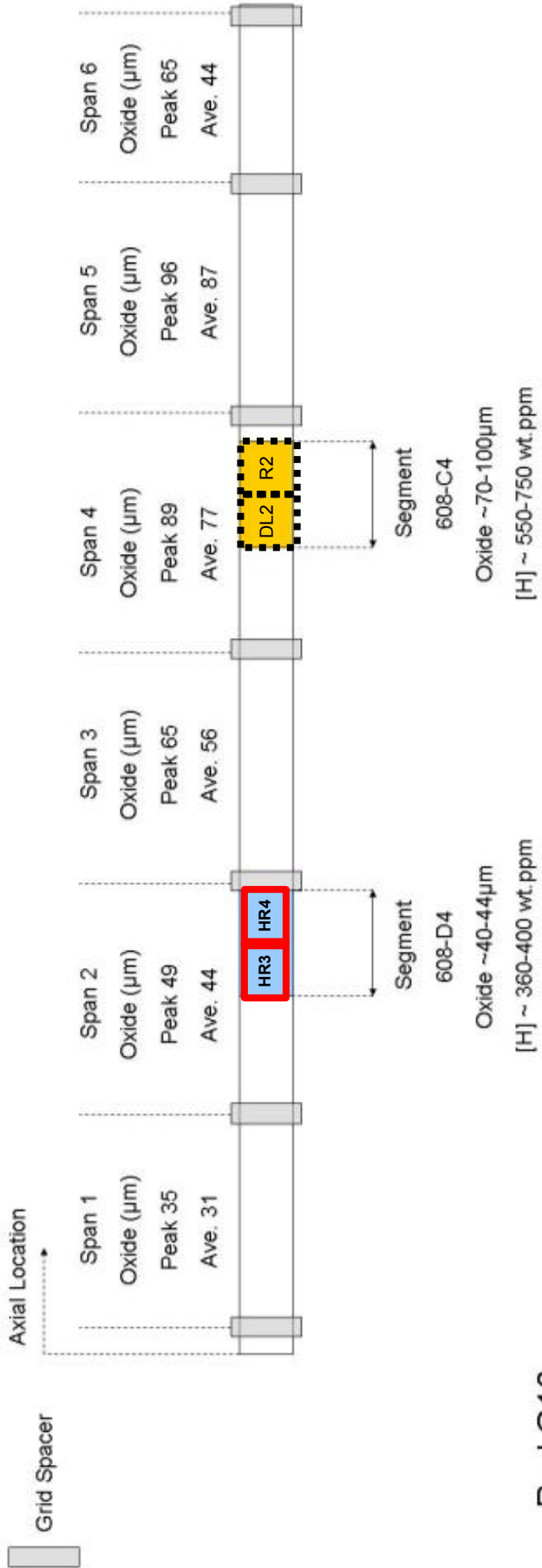
(b)



Rod F07

Average Rod Burnup: 63.755 GWd/MTU

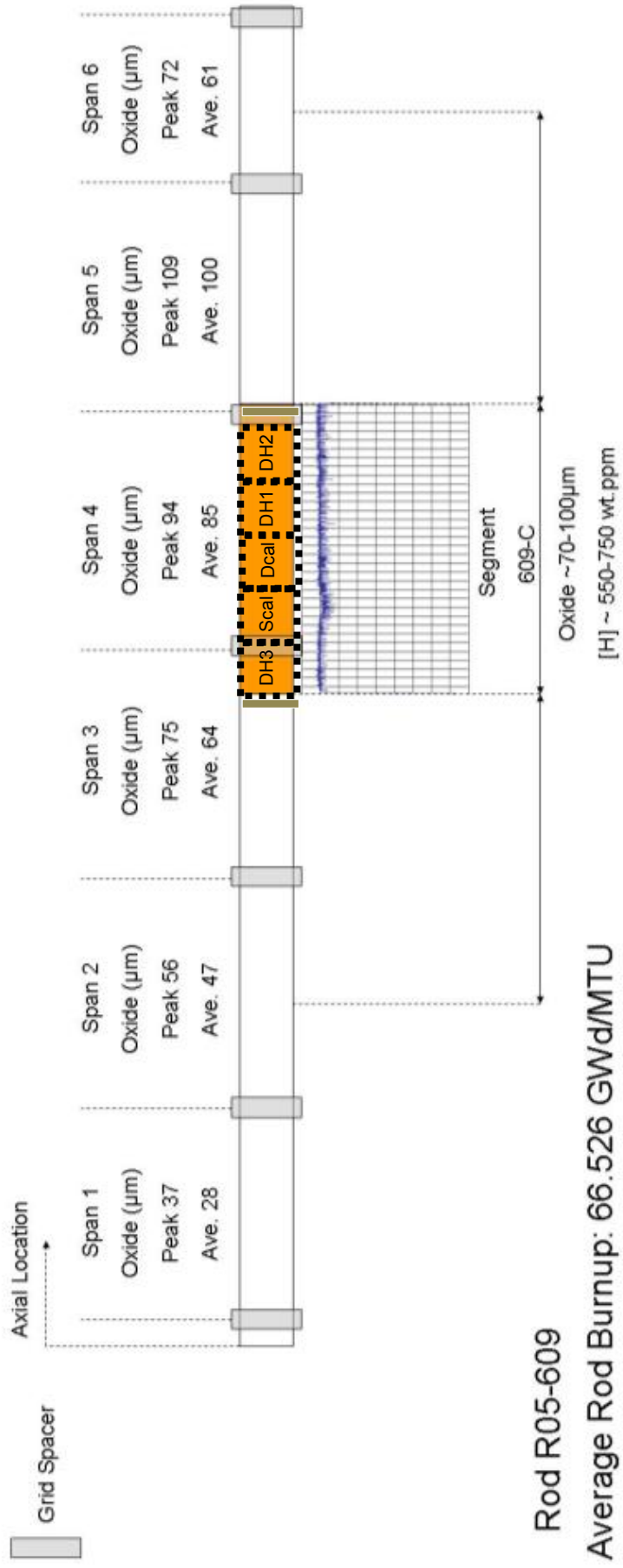
(c)



Rod G10

Average Rod Burnup: 63.838 GWd/MTU

(d)



(e)

Figure A.1 Cutting plan for (a) E02-605, (b) E14-606, (c) F07-607, (d) G10-608, and (e) R05-609

APPENDIX B METROLOGY OF ROD SEGMENTS

APPENDIX B METROLOGY OF ROD SEGMENTS

Table B.1 Diameter measurements on fuel rod segment R5 (606B3C) (unit: inch)*

Distance from End (Inches)	0.5	1.0	1.5	2.0	2.5	3.0	3.5	4.0	4.5	5.0	5.5
A - (000)	0.42450	0.42436	0.42450	0.42440	0.42402	0.42390	0.42388	0.42400	0.42430	0.42392	0.42368
B - (120)	0.42428	0.42416	0.42400	0.42416	0.42392	0.42396	0.42370	0.42404	0.42402	0.42374	0.42382
C - (240)	0.42432	0.42430	0.42386	0.42412	0.42374	0.42390	0.42446	0.42506	0.42474	0.42384	0.42382
Maximum	0.42450	0.42436	0.42450	0.42440	0.42402	0.42396	0.42446	0.42506	0.42474	0.42392	0.42382
Minimum	0.42428	0.42416	0.42386	0.42412	0.42374	0.42390	0.42370	0.42400	0.42402	0.42374	0.42368
Mean	0.42437	0.42427	0.42412	0.42423	0.42389	0.42392	0.42401	0.42437	0.42435	0.42383	0.42377
Std. Dev.	0.00012	0.00010	0.00034	0.00015	0.00014	0.00003	0.00040	0.00060	0.00036	0.00009	0.00008
Overall											
Maximum	0.42506										
Minimum	0.42368										
Mean	0.42410										
Std. Dev.	0.00032										

*Based on C. Baldwin, ORNL, Mar. 6, 2013.

Table B.2 Diameter measurements on HBR fuel rod segments (unit: inch)*

Spec Label	ORNL Label	NRC Original Label	Segment ID	0 Degree			90 Degree			Average	Std. Dev.
				-0.5	0.0	+0.5	-0.5	0.0	+0.5		
S1	S1	S3	606C3C	0.42324	0.42304	0.42306	0.42320	0.42306	0.42332	0.42315	0.00012
S2	S2	S2	605D1E	0.42322	0.42298	0.42298	0.42310	0.42310	0.42310	0.42308	0.00009
S3	DCAL	DCAL	609C5	0.42222	0.42248	0.42272	0.42298	0.42288	0.42288	0.42269	0.00029
S4	SCAL	SCAL	609C6	0.42320	0.42308	0.42288	0.42228	0.42252	0.42298	0.42282	0.00035
D1	DL1	DL1	607C4B	0.42634	0.42650	0.42664	0.42690	0.42640	0.42640	0.42653	0.00021
D2	DL2	DL2	608C4B	0.42442	0.42422	0.42410	0.42482	0.42462	0.42454	0.42445	0.00026
D3	DL3	DL3	605C10A	0.42398	0.42402	0.42422	0.42444	0.42418	0.42420	0.42417	0.00016
D4	DM1	DM1	605D1C	0.42314	0.42336	0.42352	0.42302	0.42310	0.42316	0.42322	0.00019
D5	DM2	DM2	605D1B	0.42376	0.42412	0.42396	0.42426	0.42424	0.42410	0.42407	0.00019
D6	DH1	DH1	609C4	0.42338	0.42336	0.42286	0.42288	0.42310	0.42322	0.42313	0.00023
D7	DH2	DH2	609C3	0.42464	0.42404	0.42394	0.42430	0.42446	0.42426	0.42427	0.00026
D8	DM3	DM3	606C3E	0.42250	0.42280	0.42268	0.42284	0.42292	0.42292	0.42278	0.00016
D9	DH3	DH3	609C7	0.42324	0.42296	0.42304	0.42236	0.42256	0.42230	0.42274	0.00039
D10	S5	S5	606C3A	0.42368	0.42378	0.42374	0.42344	0.42326	0.42348	0.42356	0.00020
D11	R1	R1	607C4A	0.42642	0.42690	0.42676	0.42614	0.42616	0.42644	0.42647	0.00031
D12	R2	R2	608C4A	0.42630	0.42588	0.42618	0.42622	0.42574	0.42592	0.42604	0.00022
D13	R3	R3	606B3E	0.42402	0.42396	0.42408	0.42334	0.42356	0.42400	0.42383	0.00030
D14	R4	R4	606B3D	0.42416	0.42404	0.42378	0.42368	0.42368	0.42358	0.42382	0.00023
D15	R5	R5	606B3C	0.42430	0.42390	0.42388	0.42392	0.42396	0.42370	0.42394	0.00020
D16/ Dcal	S3	S1	605D1F	0.42326	0.42306	0.42298	0.42324	0.42294	0.42306	0.42309	0.00013
Demo1	DEMO 1	DEMO 1	606B2	0.42342	0.42356	0.42364	0.42346	0.42364	0.42372	0.42357	0.00012
Scal1	DEMO 2	DEMO 2	606B3B	0.42406	0.42388	0.42424	0.42402	0.42394	0.42406	0.42403	0.00012
Scal2	S4	S4	606C3B	0.42376	0.42354	0.42340	0.42390	0.42376	0.42374	0.42368	0.00018
HR1	HR1	HR1	607D4C							0.42360	
HR2	HR2	HR2	607D4A							0.42200	
HR3	HR3	HR3	608D4A							0.42200	
HR4	HR4	HR4	608D4C								
									Average	0.4237	
									Std. Dev.	0.0012	

*Based on C. Baldwin, ORNL, Mar. 6, 201.

APPENDIX C BENCHMARKING OF TEST SYSTEM

APPENDIX C BENCHMARKING OF TEST SYSTEM

C.1 TUNING AND STATIC TEST ON DEMO1/ 606B2 (+ DYNAMIC)

Tuning was completed September 23, 2013 on test specimen Demo1 (606B2) by using TuneIQ on both motors (Table C.1).

Table C.1 Tuning parameters obtained for test specimen Demo1

Axial 1		Axial 2	
TuneIQ1	1.5860	TuneIQ1	1.8869
TuneIQ2	0.0192	TuneIQ2	0.0193
TuneIQ3	-9.6663	TuneIQ3	-11.0162

Demo1 (606B2, 66.5 GWd/MTU burnup, 100–110 μm oxide layer, 750 ppm H content) was initially tested to the relative displacement of 2 mm at a rate of 0.1 mm/s at each loading point on the U-frame. Such a displacement level was low to serve as a pilot test to detect the response of the rod. The rod was then tested for 11 cycles with an increased relative displacement of 20 mm, corresponding to a moment of 77.7 Nm (load correction applied regarding the resistive force from testing system; the same applies in the following unless specified otherwise), and the rod appeared to be stable. Four additional cycles were carried out with further increased displacement of 24 mm (moment 85 N·m), and the rod was found to still work fine. The responses of the rod during the loading processes specified above are presented in Figure C.1.

A follow-up cycle test was conducted by using ± 300 N or 30.48 N·m 5 Hz. The rod eventually fractured in the gauge section near motor 1 around 3.96×10^3 cycles. The monitored curvature, moment, and deduced flexural rigidity as a function of number of cycles are provided in Figure C.2. The fracture surfaces (Figure C.3) of the rod indicate that the failure likely involved the fracture of a fuel pellet near the interface as can be seen from the attached fragments.

It has been observed that at a low displacement level, the rod exhibited a linear response. A flexural rigidity of 40 N·m² was obtained from the slope of the curvature-moment curve. A nonlinear response was exhibited under increased displacement. Three deformation stages can be delineated with two turning points near 20 and 55 N·m, at which point the slope of the curve changed. Below the first turning point, the response appeared repeatable under loading. Beyond the second turning point, the response of the rod became nonlinear. Unloading and loading curves were mostly overlaid if the loading level was less than the previous maximum level; otherwise, the loading curve followed the response of the rod in a monotonic loading process.

The following be seen based on testing of the first fuel rod:

- The testing system worked stably for both static and dynamic loadings when the tuning parameters generated above were used.
- A three-stage deformation process was evident when the deformation was substantially large.
- No failure was seen from the use of Demo1 under static loading, even though the displacement imposed almost reached the system capacity (25 mm). Therefore, a cyclic loading process is required to observe the failure mode of the rod.

- The testing setup worked as designed, confining the final failure within the gauge section of the rod.

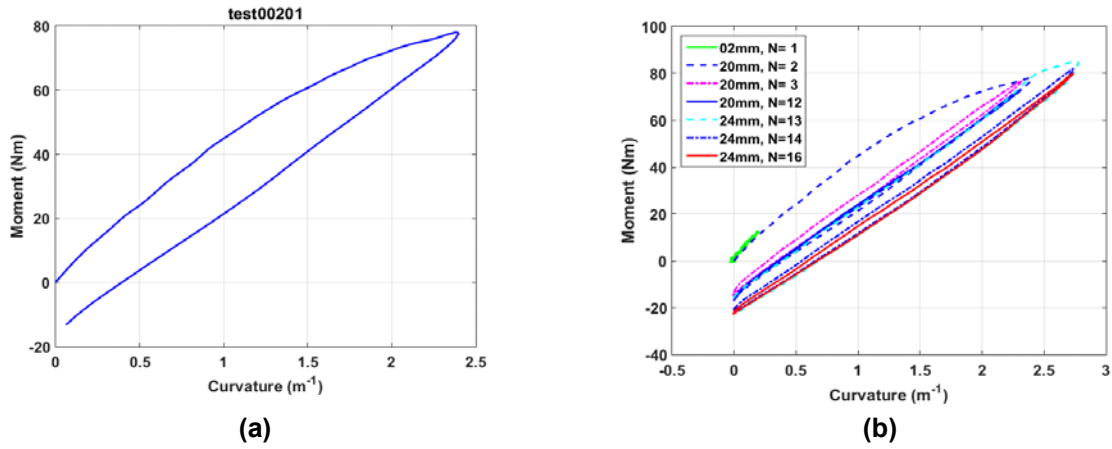


Figure C.1 (a) Curve of moment versus curvature with maximum relative displacement of 20 mm, and (b) moment versus curvature in the subsequent repeats of static tests with relative displacement of 20 or 24 mm for Demo1 (606B2).

The rate at the U-frame loading point was set at 0.1 and 0.2 mm/s for loading and unloading, respectively.

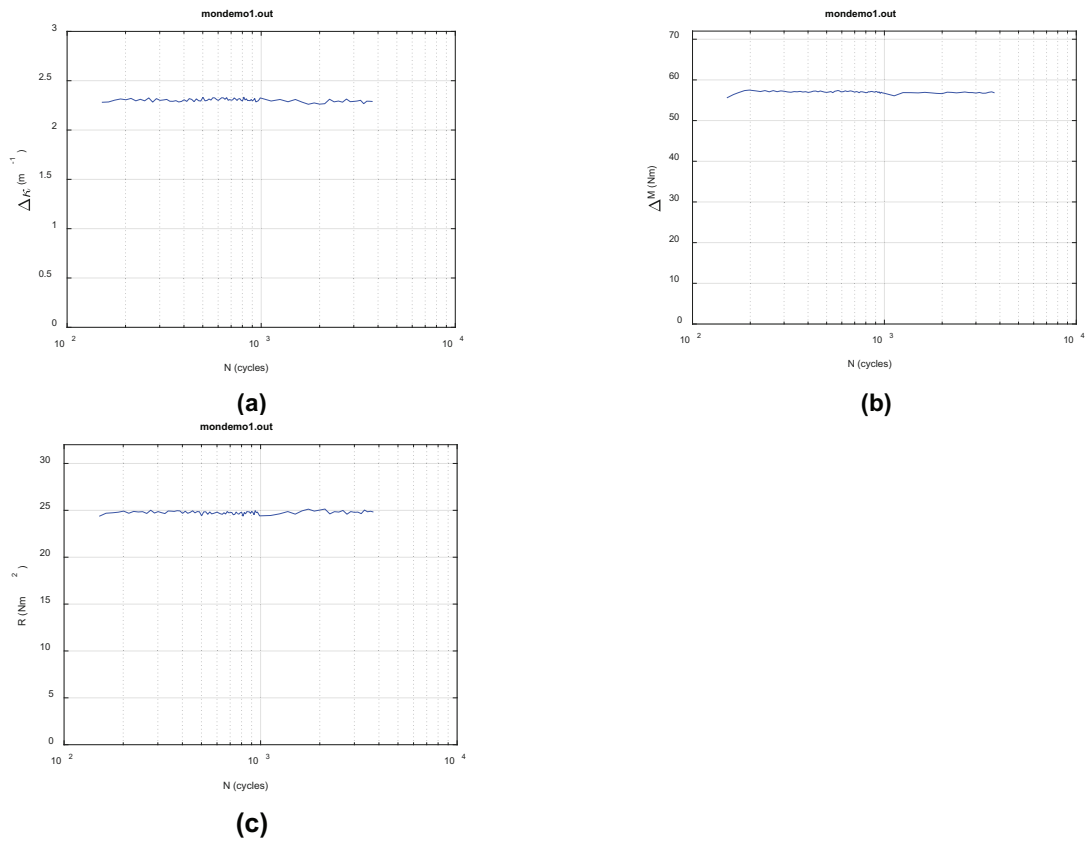


Figure C.2 Variations in (a) curvature range, (b) applied moment range, and (c) flexural rigidity as a function of number of cycles for Demo1 (606B2); $N_f = 3.96 \times 10^3$ cycles under ± 30.48 N·m 5 Hz.

The specimen was subjected to repeated static loading before the cycle test.

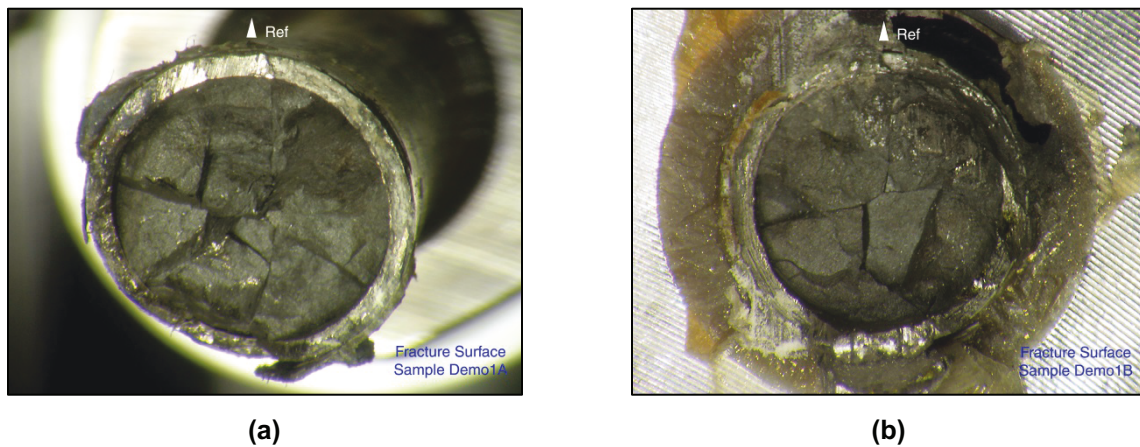


Figure C.3 Mating fracture surfaces of Demo1 (606B2); the reference marker indicates the frontal maximum stress line (facing the operator); $N_f = 3.96 \times 10^3$ cycles under ± 30.48 N·m 5 Hz.

The specimen had been subjected to repeated static loading cycles before the dynamic cycle test.

C.2 STATIC TEST ON SCAL1/ DEMO2/ 606B3B

The test on Scal1/ Demo2 (606B3B, 66.5 GWd/MTU burnup, 100–110 μm oxide layer, 750 ppm H content) was conducted at 0.1 mm/s at each loading point of the U-frame. The rod fractured when the relative displacement reached 22.920 mm, corresponding to a fracture moment of 78.2 N·m. Again, two turning points can be defined clearly near 20 and 50 N·m prior to the failure, as shown in Figure C.4. Rod failure occurred at the middle of the gauge section. The fracture surface of the cladding (Figure C.5) appeared to be very serrated. A large tooth-shaped fragment was attached on the compressive side of the rod, but it broke off during specimen handling. The final fracture of the rod was seemingly related to the fracture of a fuel pellet near a pellet to pellet interface.

Observations:

- The moment at fracture for Scal1 is lower than the maximum moment experienced by Demo1, as discussed above. Therefore, a substantial mechanical property difference is seen between the two rods, although they have the same thickness of oxide layer and the same level of H content.
- Lateral surfaces of the rod were covered with a large number of equally spaced circumferential cracks throughout the gauge section on both the front (facing operator) and the back sides of the rod. Whether the cracks were linked around the whole periphery of the rod is uncertain.
- Extensive subsurface spalling can be seen over the back or tensile side of the rod. Circumferential cracks and spalling also occurred on Demo1 and several other rods, as discussed below.

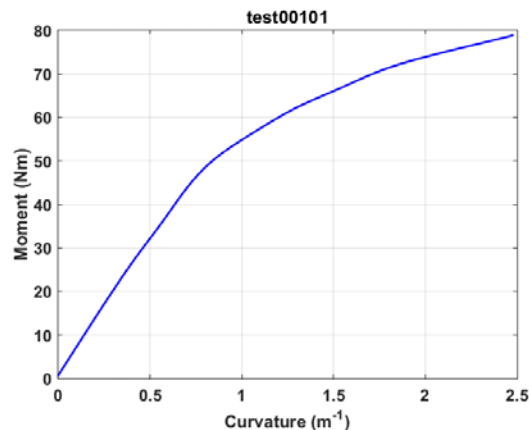


Figure C.4 Moment-curvature curve for Scal1/ Demo2 (606B3B) with a rate of 0.1 mm/sec at the U-frame loading points/ the rod broke at peak moment = 83 N·m

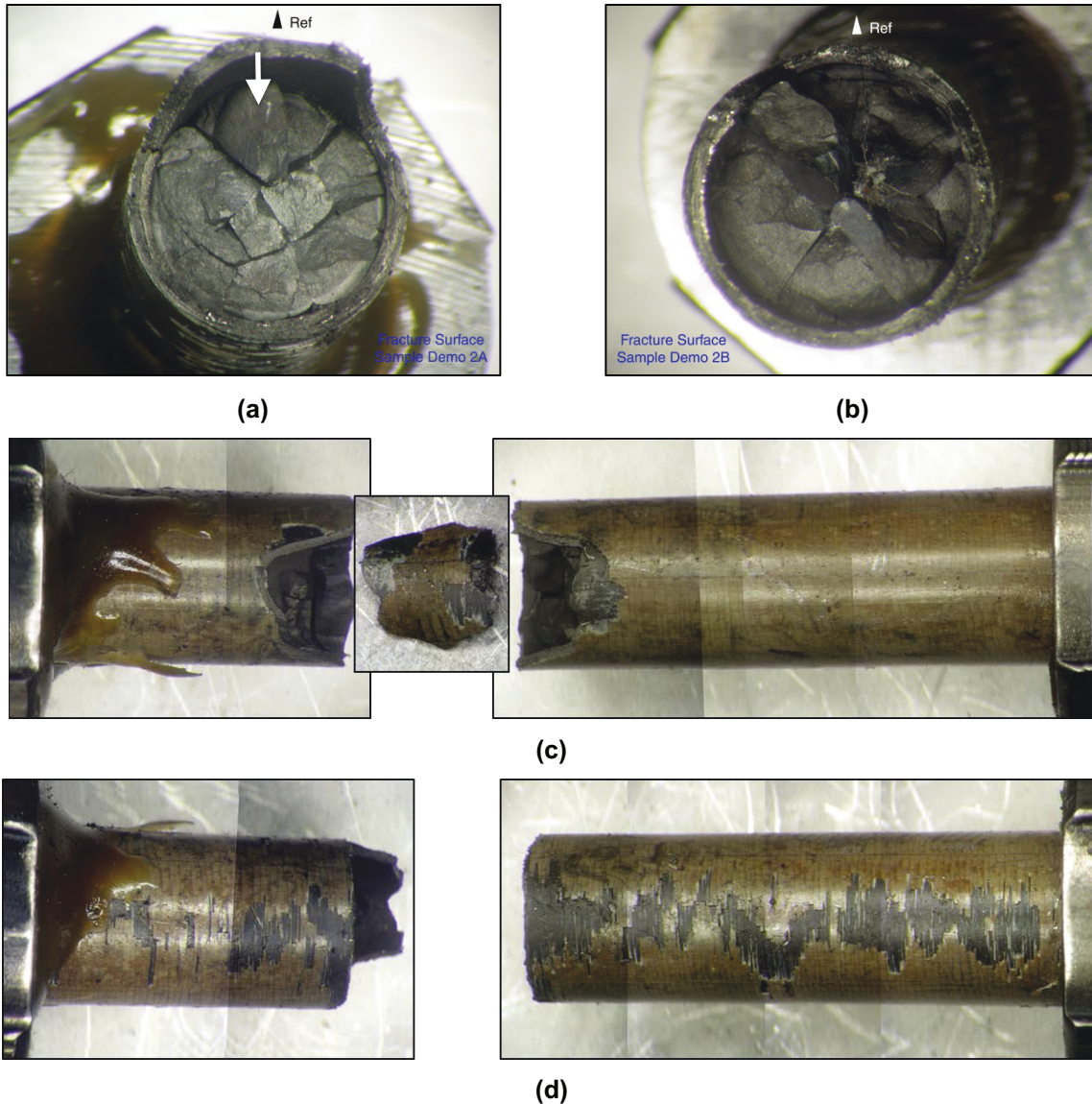


Figure C.5 (a, b) Mating fracture surfaces, (c) front side (compressive), and (d) back side (tensile) of Scal1/ Demo2 (606B3B). The rate was 0.1 mm/sec at the U-frame loading points. The rod broke at peak moment = 78.2 N·m.

C.3 DYNAMIC TEST ON DCAL/ S3/ 605D1F (± 25.4 N·m 5 Hz)

Dynamic cycle testing was conducted on rod Dcal/ S3 (605D1F, 66.5 GWd/MTU burnup, 40–70 μm oxide layer, 360 ppm H content) as a part of system benchmarking. The cycle test was conducted under ± 250 N or 25.40 N·m 5 Hz. The system has been demonstrated to meet the testing requirements for loading and monitoring. A lifetime of 2.5×10^4 cycles was observed. Flexural rigidity was shown to be fairly stable as the cycles accumulated prior to final fracture, as shown in Figure C.6. The associated measurements are shown in Figures C.7 and C.8. Failure was observed in the gauge section near motor 2. A clear cut can be seen from the exposed end faces of neighboring pellets in Figure C.9.

Rod failure was dominated by the pellet-to-pellet interface.

The lateral surface of the rod was shown to be free of the cracks or spalling observed in Demo1, Scal1, and Scal2 (discussed below). It is not clear if the absence of circular cracks was related to the small loading amplitude or to the lesser degree of preexisting oxidation and hydrides in Dcal.

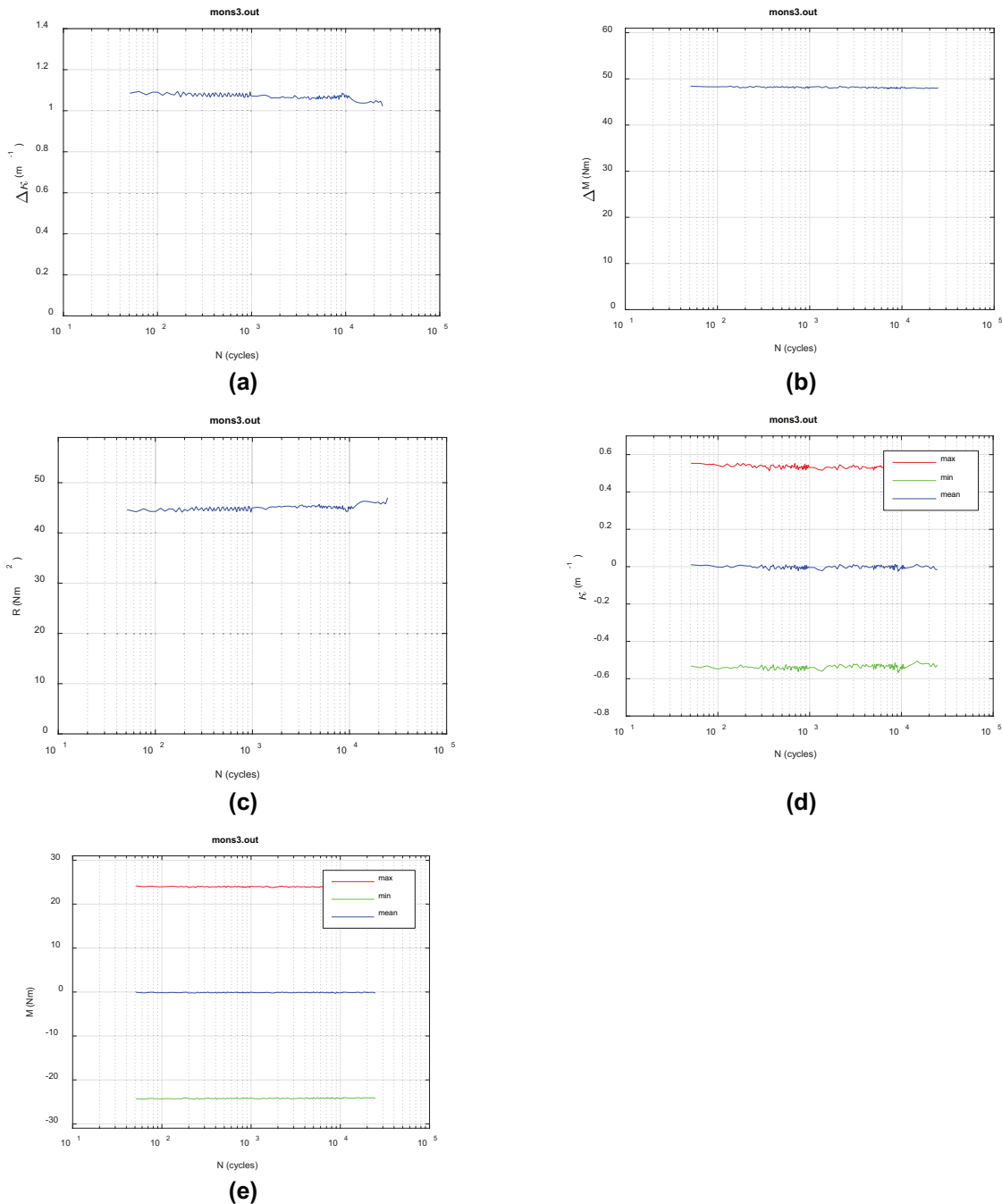
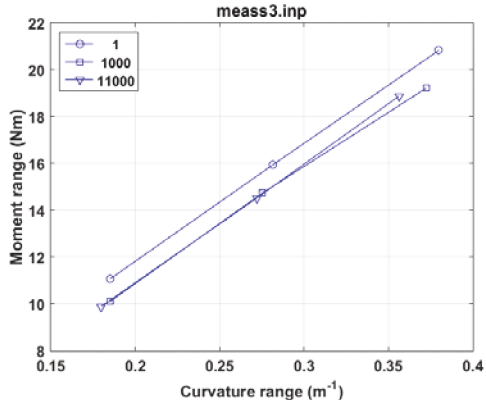
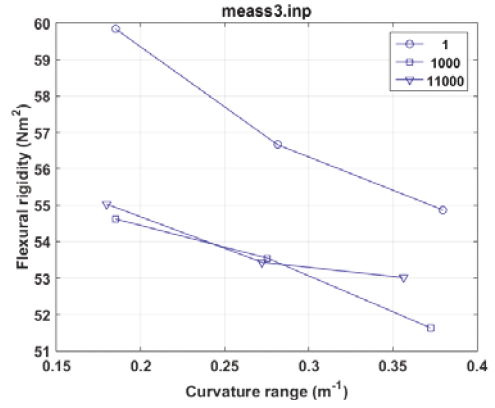


Figure C.6 Variations in (a) curvature range, (b) applied moment range, (c) flexural rigidity, (d) maximum and minimum values of curvature, and (e) maximum and minimum values of moment as a function of number of cycles for Dcal/ S3 (605D1F); $N_f = 2.5 \times 10^4$ cycles under ± 25.4 N·m 5 Hz

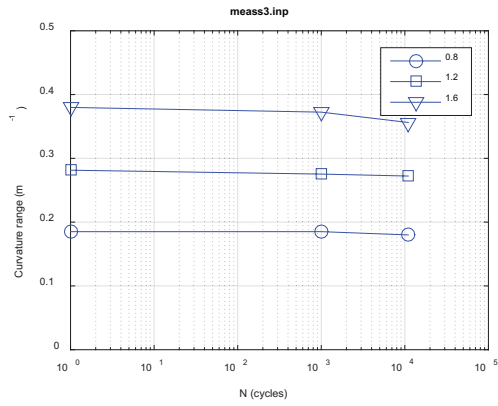


(a)

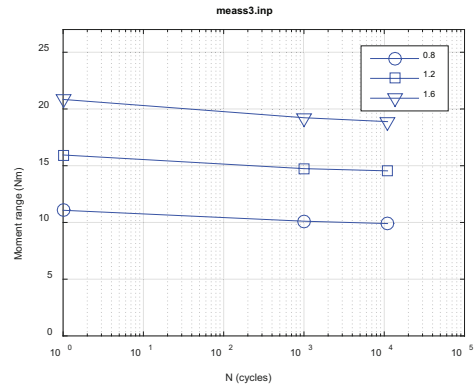


(b)

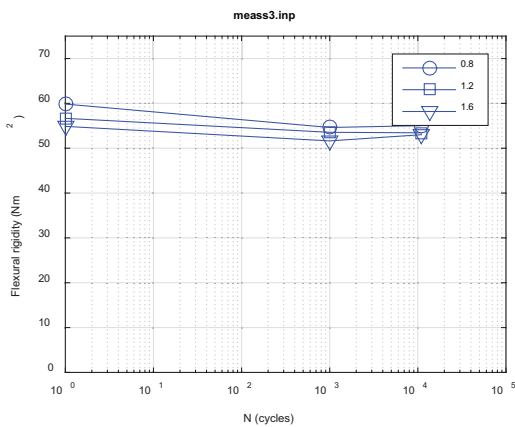
Figure C.7 (a) Moment-curvature relation, and (b) moment-flexural rigidity relation at various numbers of cycles for Dcal/ S3 (605D1F); $N_f = 2.5 \times 10^4$ cycles under ± 25.4 N·m 5 Hz



(a)



(b)



(c)

Figure C.8 Variations in (a) curvature range, (b) applied moment range, and (c) flexural rigidity as a function of number of cycles for Dcal/ S3 (605D1F); $N_f = 2.5 \times 10^4$ cycles under ± 25.4 N·m 5 Hz

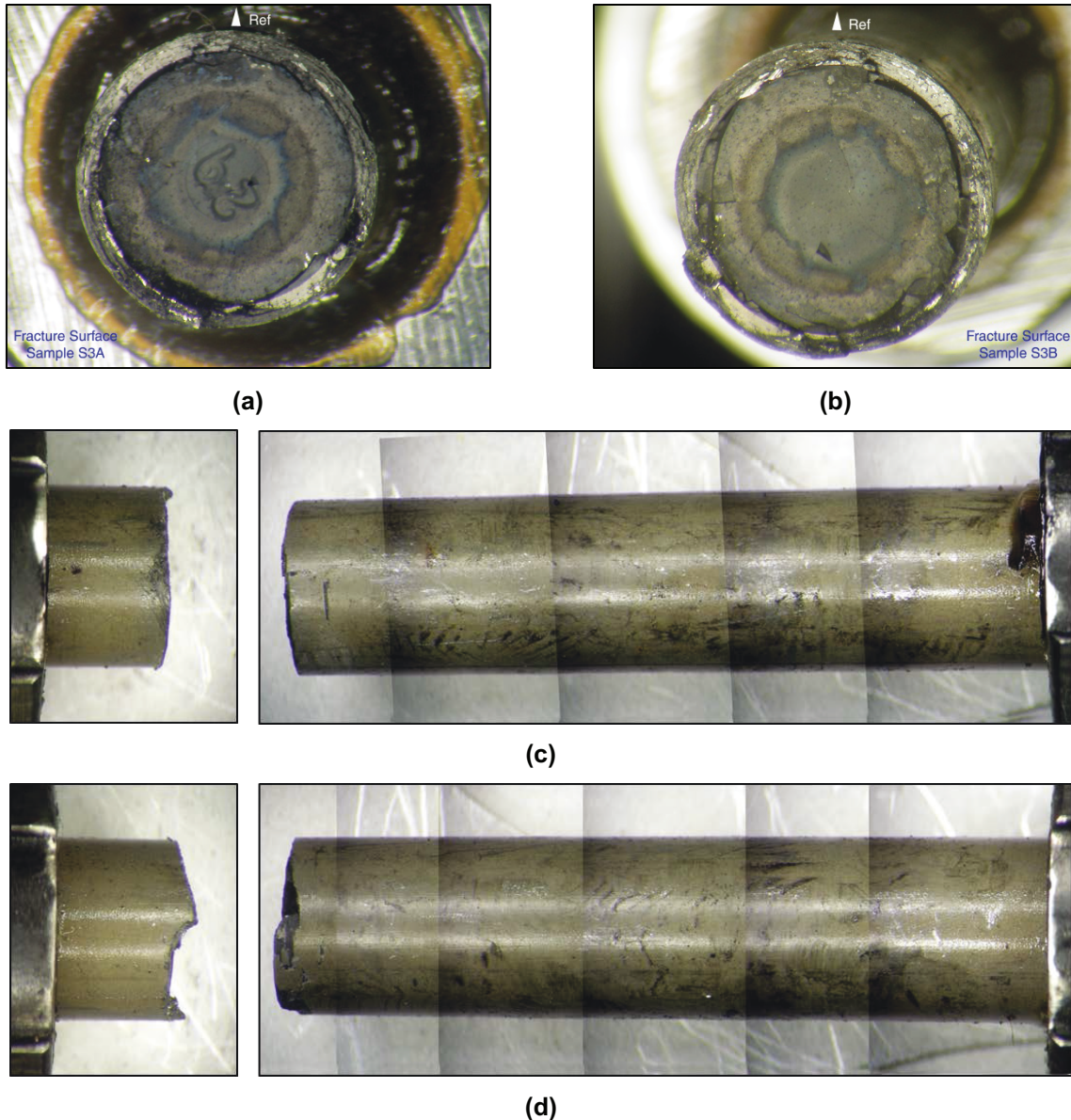


Figure C.9 (a, b) Mating fracture surfaces, (c) front side, and (d) back side of Dcal/ S3 (605D1F); $N_f = 2.5 \times 10^4$ cycles under ± 25.40 N·m 5 Hz

C.4 STATIC TEST ON SCAL2/ S4/ 606C3B

Scal2/ S4 (606C3B, 66.8 GWd/MTU burnup, 70–100 μm oxide layer, 700 ppm H content) fractured at the peak moment near 80.7 N·m at a loading of 0.1 mm/s. A large variety of fragment sizes was revealed in the postmortem analysis (Figure C.10).

The end face of a pellet can be seen clearly from the brownish haze zone. Therefore, the failure took place near a pellet-to-pellet interface, with the fracture involving a neighboring pellet.

Besides the circumferential cracks, a sharp attachment of cladding was outstanding on the frontal or compressive side. On the other side, spalling was not as extensive as in Demo1 and Scal1.

Compared to Scal1 from the same fuel rod but a different segment (606B), the slightly higher failure moment and less spalling in Scal2 are coincident with the lower levels of oxide-layer thickness and H content of the rod segment.

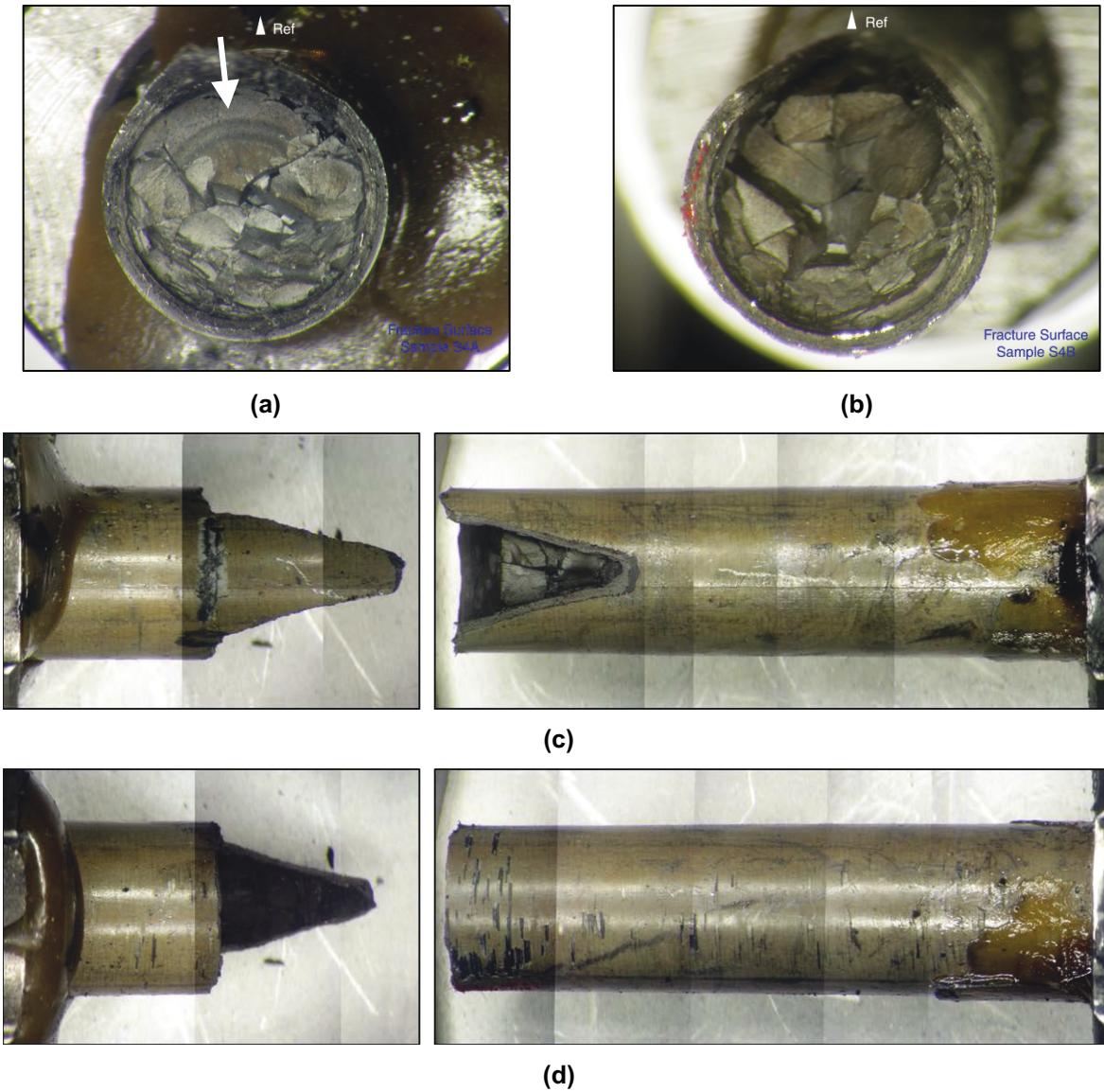


Figure C.10 (a, b) Mating fracture surfaces, (c) front (compressive) side, and (d) back (tensile) side of Scal2/ S4 (606C3B).

The rate at the U-frame loading points was 0.1 mm/sec. The rod broke at peak moment = 80.7 N·m.

APPENDIX D STATIC TEST RESULTS

APPENDIX D STATIC TEST RESULTS

D.1 S1/ 606C3C (+ DYNAMIC)

S1 (606C3C, 66.8 GWd/MTU burnup, 70–100 μm oxide layer, 650 ppm H content) was tested under four repeated static loading cycles before being taken into a dynamic cyclic test. The moment-curvature curve and equivalent stress-strain curve for the initial cycle are presented in Figure D.1 (the curves of subsequent cycles overlaid to a great extent and are not plotted for clarity). Again, the turning points were revealed near 12 and 59 N·m. The rod fractured in a follow-up cyclic test under ± 25.40 to 30.48 N·m 5 Hz near 1.4×10^4 cycles.

Fracture occurred near motor 1 (right side) with a fuel release of 0.9 grams. Fractography using an optical microscope as shown in Figure D.2 revealed that the rod failure was related to fractures of a pellet adjacent to a pellet-to-pellet interface. The exit of the pellet end-face can be identified from the haze zone characterized by the brownish blue color. At the same time, a serrated fracture surface of cladding was observed with a slender attachment (about one rod-diameter length).

The lateral surfaces shown in Figures D.2(c) and (d) near the rod's neutral axis of bending were mostly free of circumferential cracks. On the other hand, one of the stressed lateral surfaces was covered with a large number of circumferential cracks and related subsurface spalling, as seen in Figure D.2(d). It is uncertain whether the spalling was related to tensile stress in static loading, as the specimen ID was 90° off to the stressed sides.

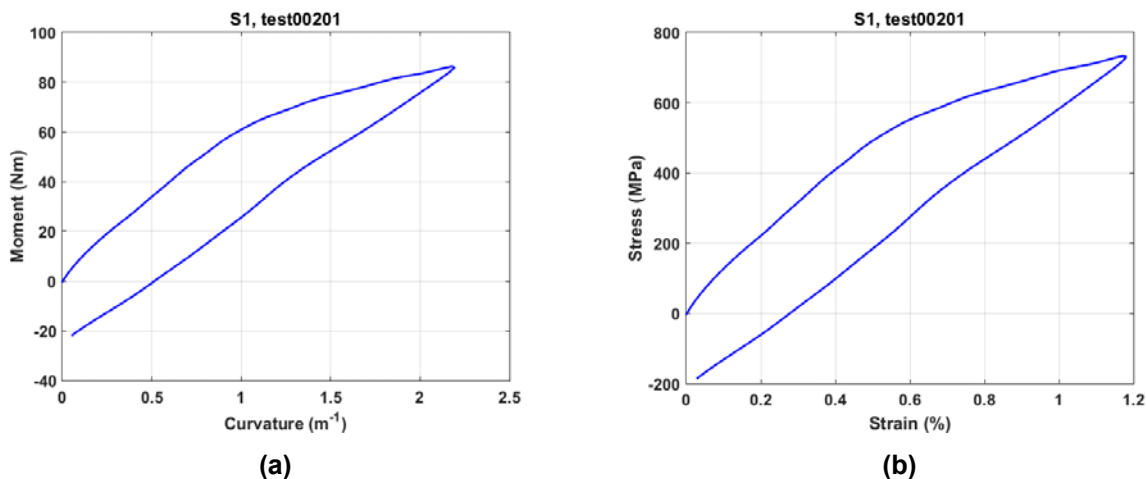


Figure D.1 (a) Curve of moment versus curvature, and (b) equivalent strain–stress curve for S1 (606C3C), based on static loading cycle in which the maximum relative displacement was 24 mm and the rate at the U-frame loading points was set at 0.1 and 0.2 mm/s in loading and unloading, respectively

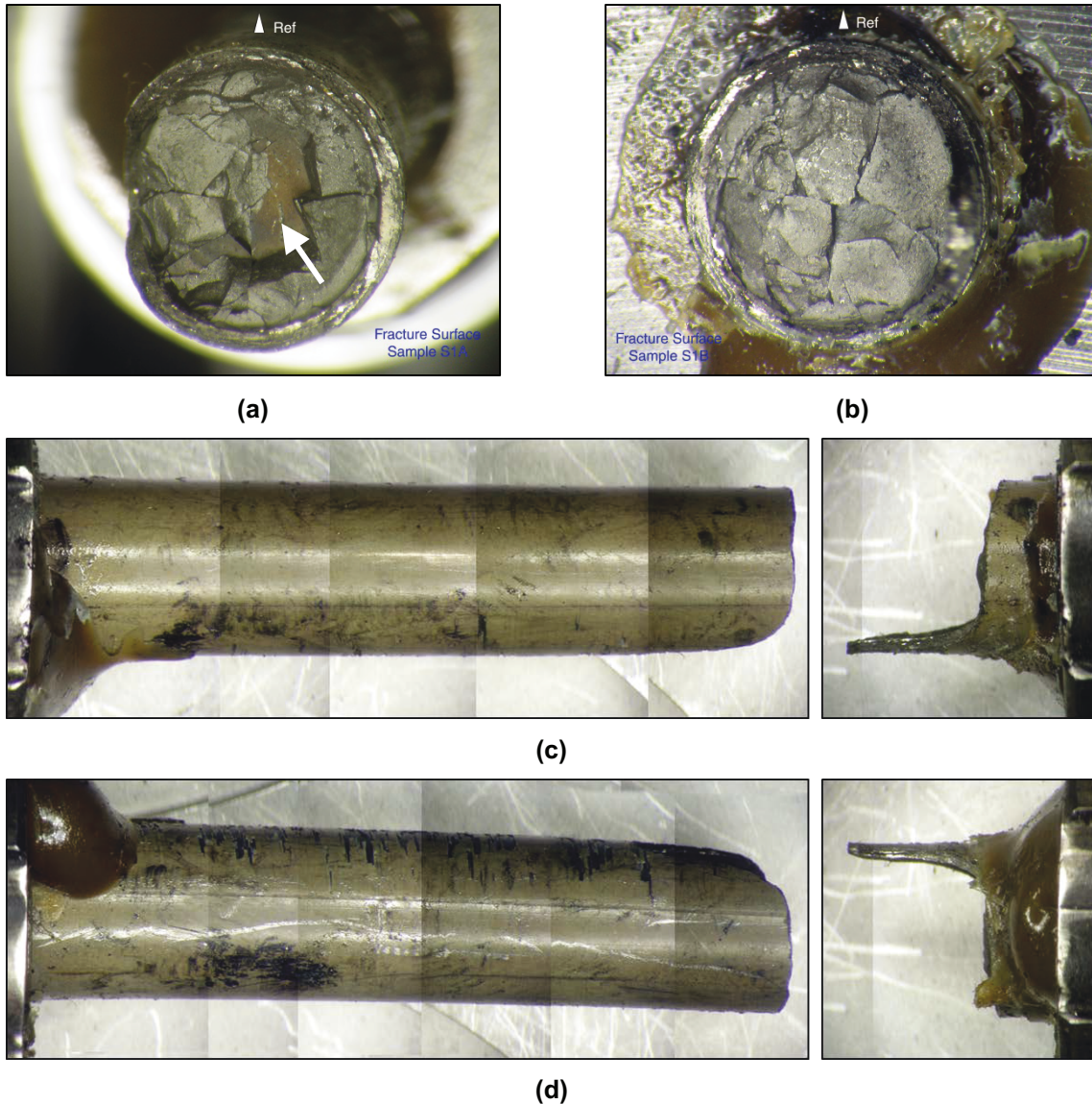


Figure D.2 (a, b) Mating fracture surfaces and (c, d) lateral sides near the rod's neutral axis of bending for S1 (606C3C), which was subjected to four repeated static cycles to 24 mm maximum relative displacement followed by dynamic cyclic loading ± 25.40 to 30.48 N·m 5 Hz; 1.4×10^4 failure cycles, 0.9 gram of fuel particles collected

D.2 S2/ 605D1E (+ DYNAMIC)

S2 (605D1E, 66.5 GWd/MTU burnup, 40–70 μ m oxide layer, 400 ppm H content) was tested by following a routine similar to that used for S1. The specimen survived three cycles of large displacement loading and 7.2×10^3 cycles under ± 30.48 N·m 5 Hz before failure at the middle of the gauge section.

The moment-curvature curve and equivalent stress-strain curve for the initial cycle are presented in Figure D.3. Again, the turning points were revealed near 20 and 62 N·m.

Fracture occurred on a pellet-to-pellet interface, Figure D.4 clearly shows the smooth brownish end face of the adjacent pellet. The attachment shown in Figure D.4(a) is convex-shaped and covers almost $\frac{1}{3}$ of the end face. Several small attachments appear around the peripheral area.

The cladding fracture appeared very serrated with a sizable tooth-shaped attachment on the compressive side of the rod. The lateral stressed surface of the rod was covered by sparsely distributed circumferential spalling. The rod's minor damaged lateral surface of bending agreed with the results of Dcal/ S3, as they were prepared from same segment (605D) and with the same level of preexisting oxides and hydrides.

The fuel release was about 0.6 grams.

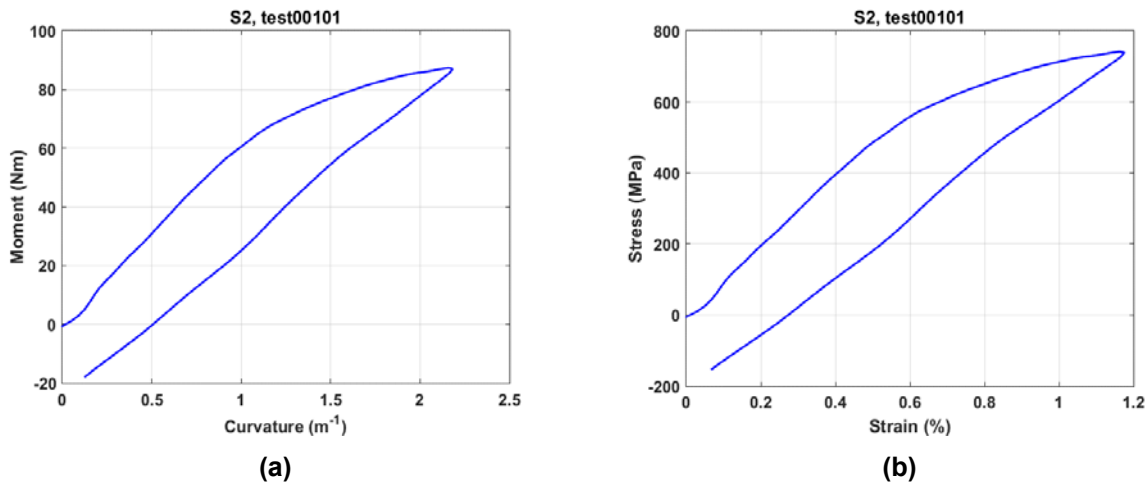


Figure D.3 (a) Curve of moment versus curvature and (b) equivalent strain-stress curve for S2 (605D1E), based on static loading cycle in which maximum relative displacement was 24 mm and the rate at the U-frame loading points was set at 0.1 and 0.2 mm/s in loading and unloading, respectively

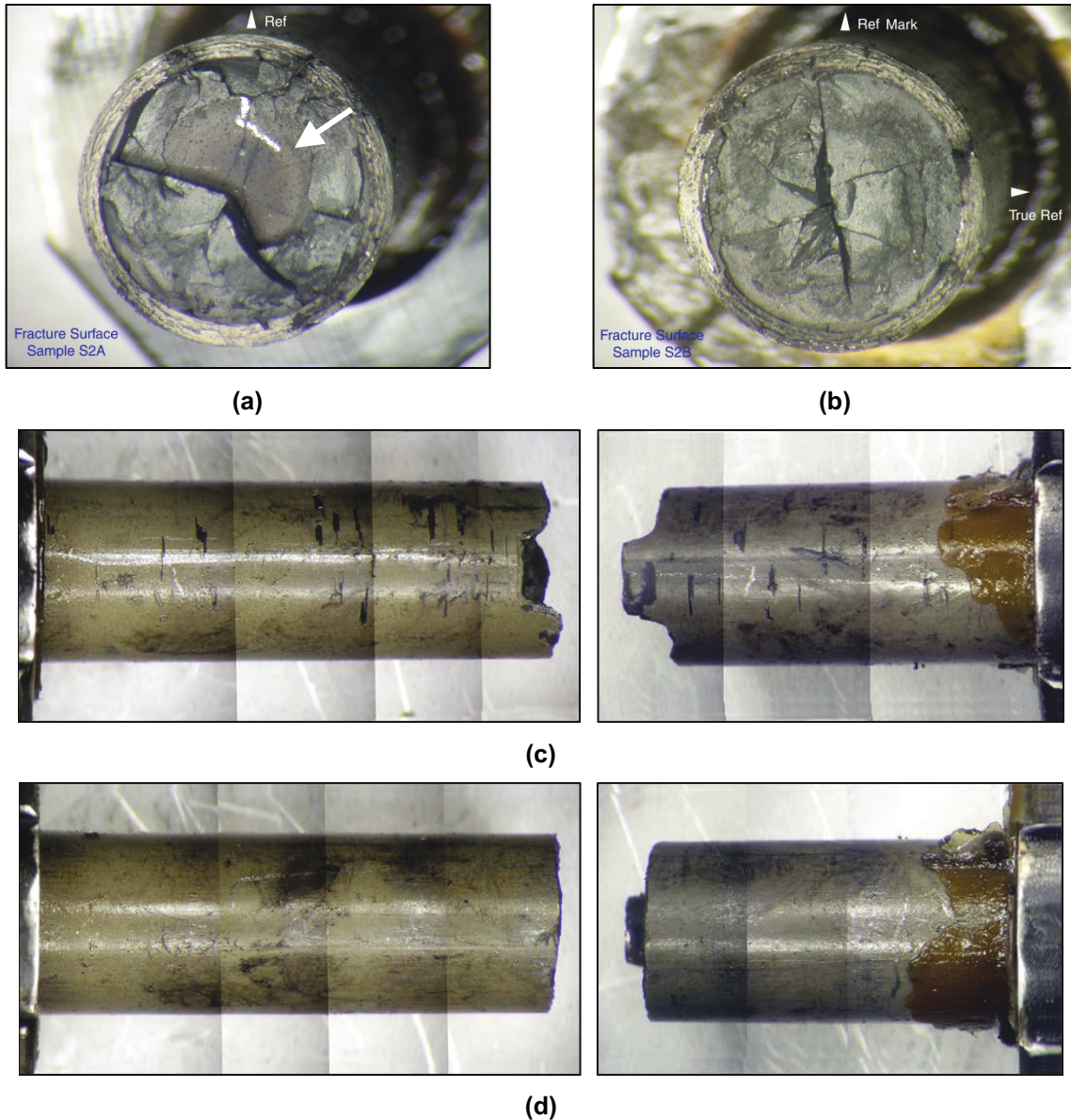


Figure D.4 (a, b) Mating fracture surfaces, (c) front side, and (d) back side of S2 (605D1E), which was subjected to three repeated static cycles to 24 mm maximum relative displacement followed by dynamic cyclic loading ± 30.48 N·m 5 Hz; 7.2×10^3 failure cycles, 0.6 gram of fuel particles collected

D.3 S3/ DCAL/ 609C5 (+ DYNAMIC)

S3/Dcal (609C5, 66.5 GWd/MTU burnup, 70–100 μ m oxide layer, 550 ppm H content) was subjected to three repeated static cycles of 24 mm displacement loading followed by cyclic loading of ± 30.48 N·m 5 Hz. The S3 failed at around 9.6×10^3 cycles at the middle of the gauge section with about 0.2 gram of fuel released.

A three-stage moment-curvature curve was obtained. Figure D.5 shows the two turning points near 18 and 60 N·m.

Rod failure was seemingly related to the fracture of a pellet (Figure D.6). No involvement of the pellet-to-pellet interface can be seen. The fracture surface of the pellet was characterized by attached fragments that were about a quarter the diameter of a typical pellet in size.

A serrated fracture surface was seen again over the cladding. Furthermore, the fracture surface was tilted to a certain degree to the longitudinal axis of the rod. This is in contrast to rods in which the failure actively involves the pellet-to-pellet interface and the fracture surfaces are more or less normal to the longitudinal axis of the rod. Circumferential cracks and spalling can be observed on lateral stressed sides, especially on the tensile side in static loading. The spalls had an extended dimension in the circumferential direction, some of which were overlaid in the longitudinal axis of the rod. However, the extent of overlaying is not as large as seen in Demo1 and Scal1/ Demo2. This can be attributed to less development of oxides and hydrides.

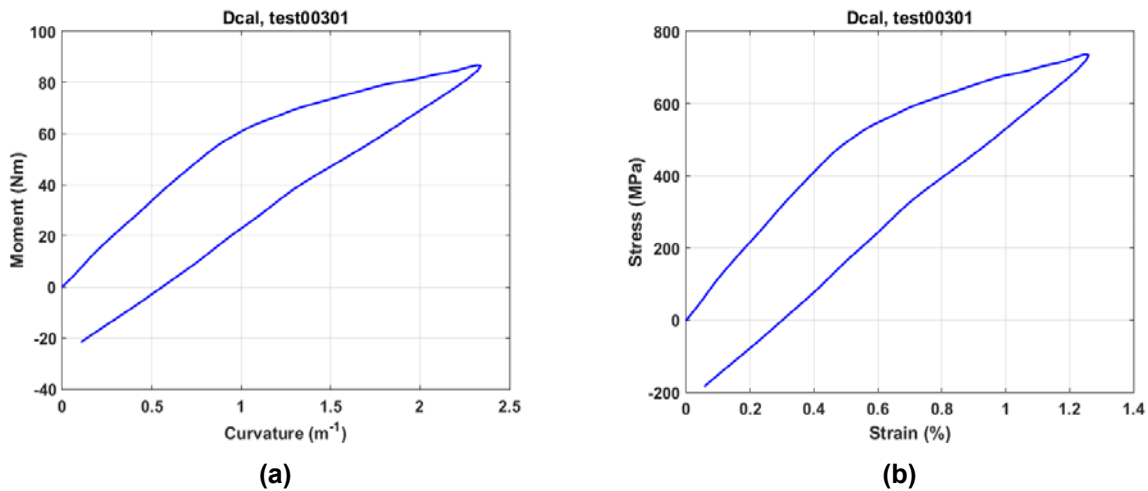
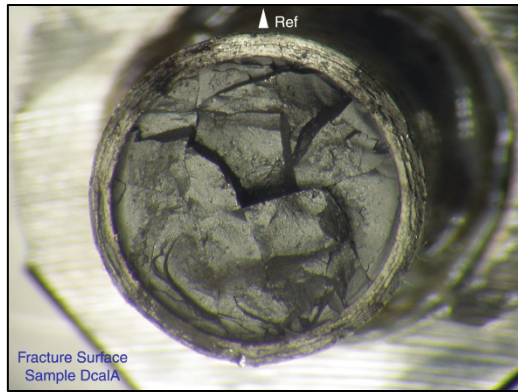
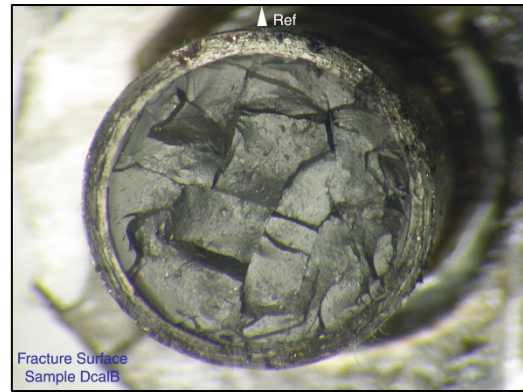


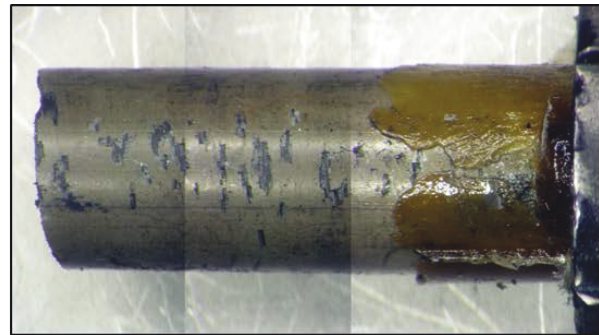
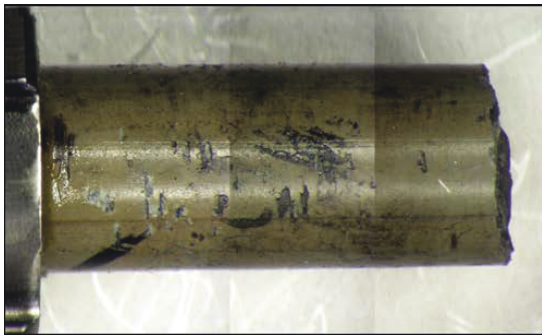
Figure D.5 (a) Curve of moment versus curvature and (b) equivalent strain-stress curve for S3/ Dcal (609C5), based on a static loading cycle in which maximum relative displacement was 24 mm and the rate at the U-frame loading points was set at 0.1 and 0.2 mm/s in loading and unloading, respectively



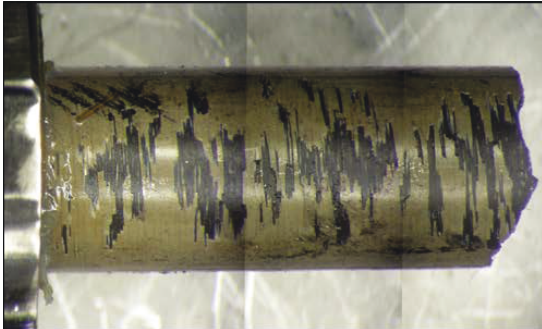
(a)



(b)



(c)



(d)

Figure D.6 (a, b) Mating fracture surfaces, (c) front side, and (d) back side of S3/ Dca1 (609C5), which was subjected to three repeated static loadings to 24 mm maximum relative displacement followed by dynamic loading: ± 30.48 N·m 5 Hz; 9.6×10^3 failure cycles, 0.2 gram of fuel particles collected

D.4 S4/ SCAL/ 609C6

S4/ Scal (609C6, 66.5 GWd/MTU burnup, 70–100 μm oxide layer, 550 ppm H content) sustained three cycles of loading with relative displacement of 24 mm on the U-frame and an additional load with 25 mm before failure. Failure occurred around the peak moment 86.1 N·m. The curves for the initial cycle exhibited a smooth transit from linear to nonlinear as shown in Figure D.7. However, the turning point near 20 N·m is still appreciable based on the discontinuous change in the slope of the moment-curvature curve.

Fracture occurred near motor 2 (left side) and was shown to be related to pellet fractures near a pellet-to-pellet interface as illustrated in Figure D.8. The exit of the end face of the involved pellet can be seen clearly from the bluish haze zone. A serrated fracture surface of cladding can also be seen.

The specimen ID was found to be 90° off the stressed surfaces of the rod. A conspicuous sharp attachment on one side suggests where the intensified compression once resided, inducing the shearing fracture. The opposite side is covered by a certain amount of spalling, as discussed above. The less stressed lateral side near the rod's neutral axis of bending appeared to be clear of circumferential cracks.

Failure of the rod involved a significant amount of fragmentation in the fractured pellet. The released fuel weighed 1.3 grams.

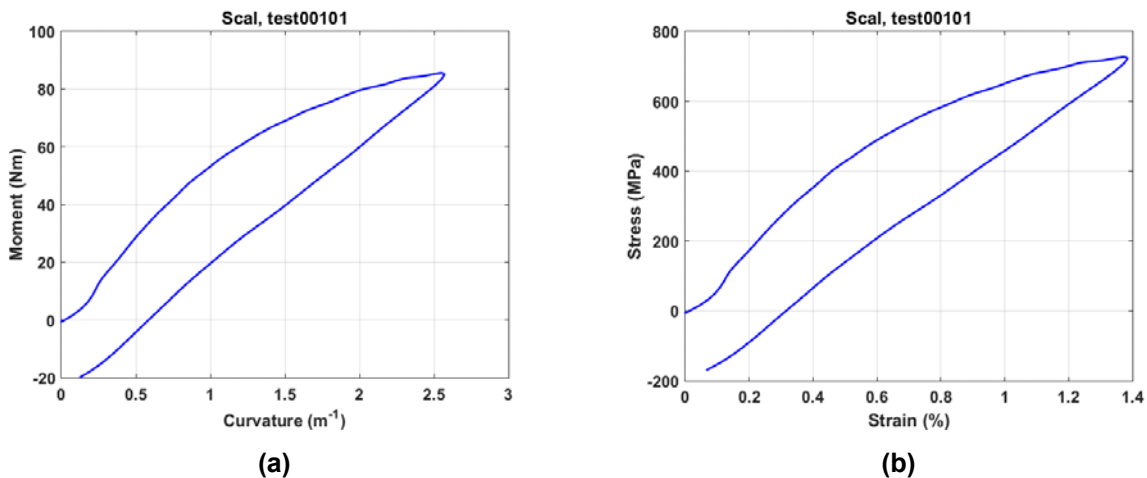


Figure D.7 (a) Curve of moment versus curvature and (b) equivalent strain-stress curve for S4/ Scal (609C6), based on static loading cycle in which maximum relative displacement was 24 mm and the rate at the U-frame loading points was set at 0.1 and 0.2 mm/s in loading and unloading, respectively

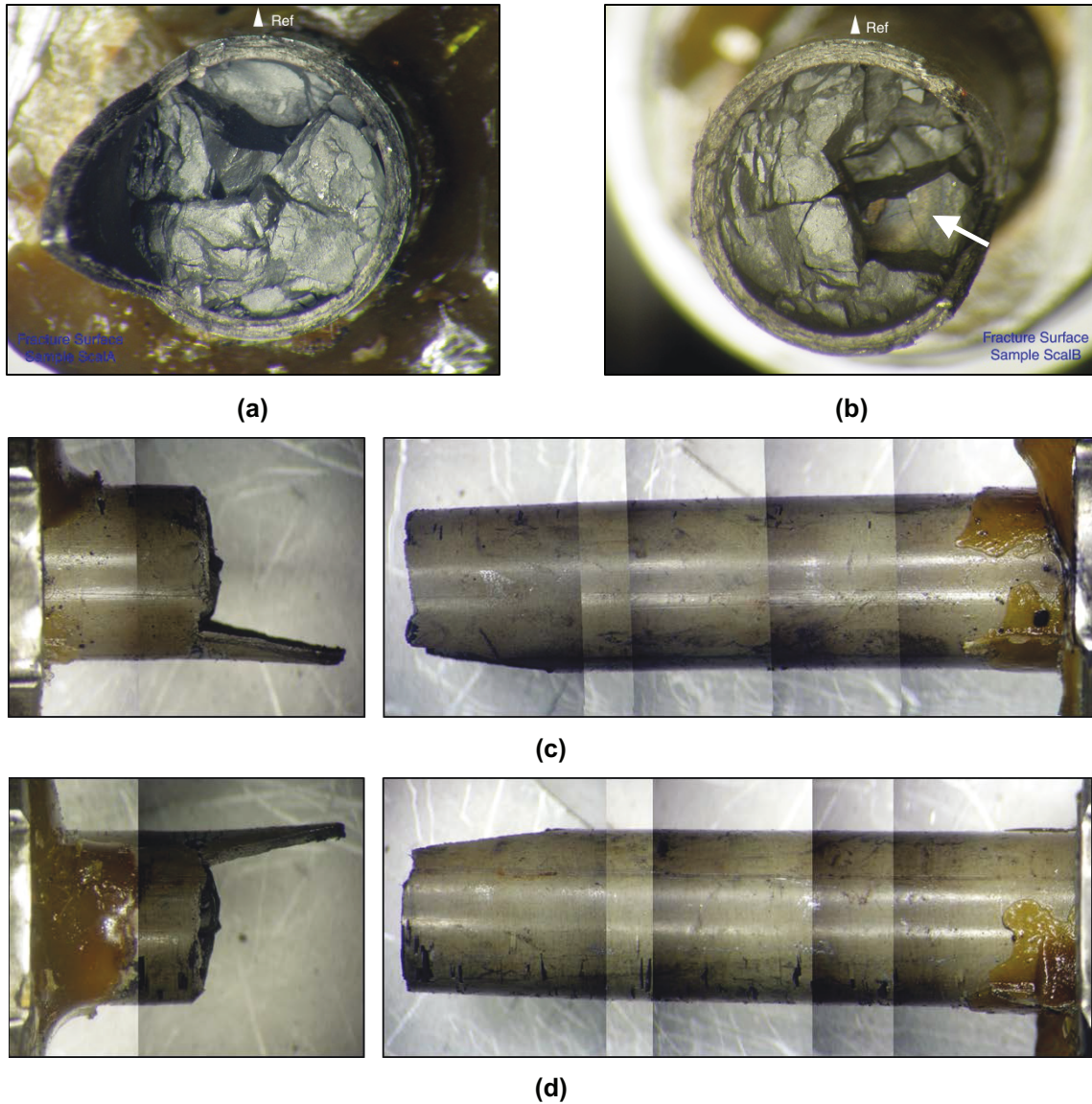


Figure D.8 (a, b) Mating fracture surfaces and (c, d) lateral sides near the rod's neutral axis of bending for S4/ Scal (609C6), which was subjected to repeated static loading to 24 mm maximum relative displacement and failed at 86.1 N-m in the 4th cycle; 1.3 grams of fuel particles collected

D.5 HR2/ 607D4A (+ DYNAMIC)

HR2 (607D4A, 63.8 GWd/MTU burnup, 40–44 μm oxide layer, 400 ppm H content) was tested initially 6 times to the displacement of 12 mm at each U-frame loading point; 0.1 and 0.2 mm/s were used for loading/unloading rates, respectively. Then the rod was tested under reversed load 4 more times to +/-12mm at each loading point at 0.1 mm/s. After that, a dynamic test followed with amplitude 16.26 Nm. The specimen failed at 9.47×10^3 cycles, and the failure occurred within the gauge section.

The responses of the specimen under static loading are represented in Fig. D.9 in terms of moment-curvature and stress-strain curve, and those under dynamic loading are presented in Fig.D.10.

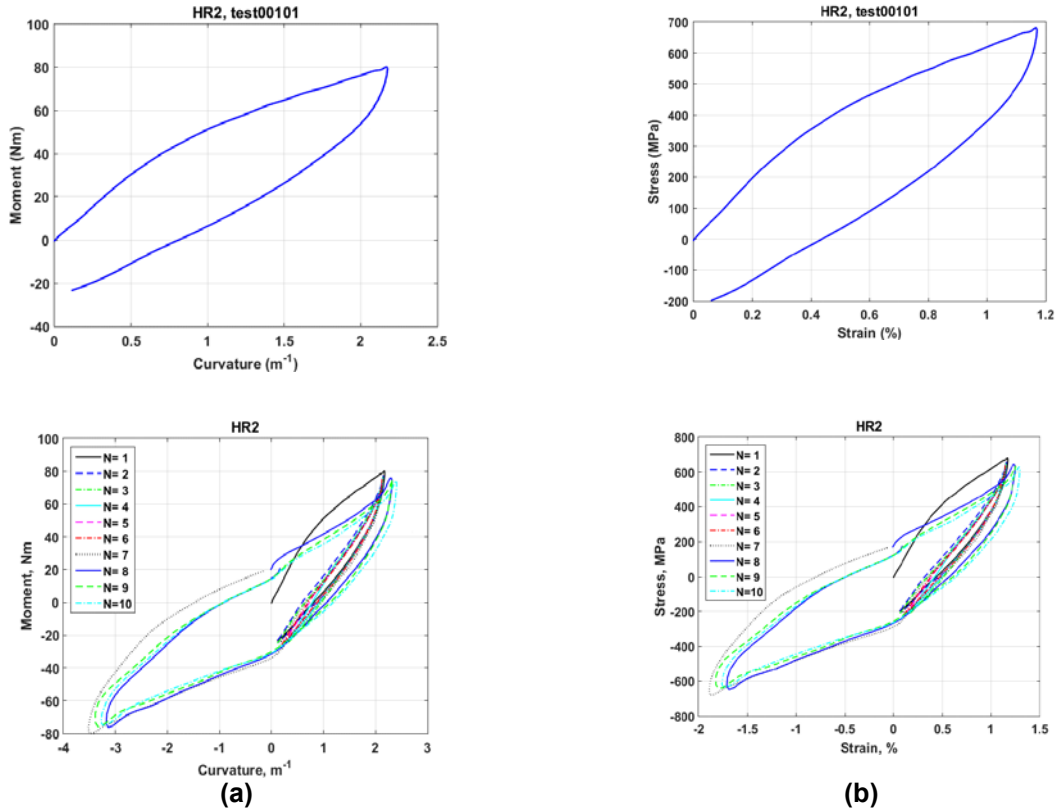
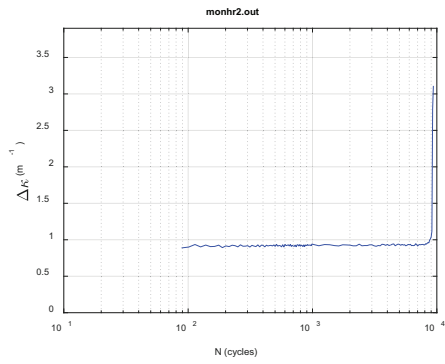
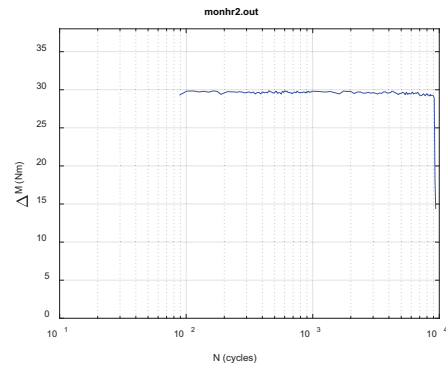


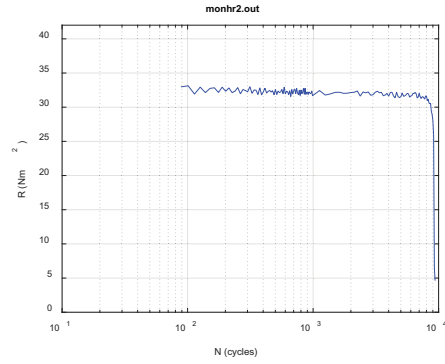
Figure D.9 (a) Curve of moment versus curvature and (b) equivalent strain-stress curve for HR2 (607D4A); tests were conducted with static loading to 12 mm or +/- 12 mm at each U-frame loading point



(a)



(b)



(c)

Figure D.10 Variations in (a) curvature range, (b) applied moment range, and (c) flexural rigidity as a function of number of cycles for HR2 (607D4A); $N_f = 9.47 \times 10^3$ cycles under $\pm 16.26 \text{ N}\cdot\text{m}$ 5 Hz

The specimen was subjected to repeated static loading before the cycle test.

APPENDIX E DYNAMIC TEST RESULTS

APPENDIX E DYNAMIC TEST RESULTS

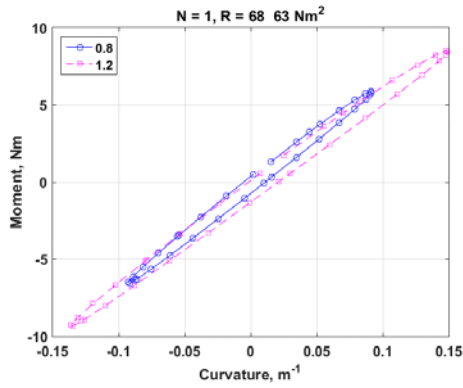
E.1 D1/ DL1/ 607C4B (± 15.24 N·m 5 Hz)

The test on D1/ DL1 (607C4B, 63.8 GWd/MTU burnup, 70–100 μm oxide layer, 700 ppm H content) was conducted under ± 15.24 N·m 5 Hz. A lifetime of 1.1×10^5 cycles was obtained with less than 1 gram of fuel particles collected. The cycle-to-failure of DL1 is apparently longer than that obtained for Dcal. The latter was subjected to a higher amplitude load of 25.40 N·m.

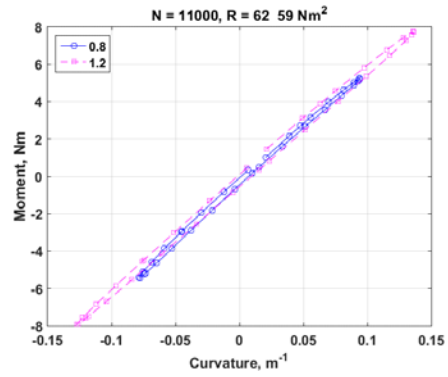
Measurements were conducted under displacement control at two relative displacement levels: 0.8 and 1.2 mm. The curvature-moment loops obtained for $N = 1$ and 111,000 cycles are given in Figure E.1. The loops actually became quite slender with the accumulated cycles, while the amplitude of the loops decreased to a certain degree. The ranges of moment in relation to curvature and flexural rigidity are illustrated in Figure E.2. It can be seen that most of the rigidity degradations occurred in the first 1,000 cycles. Variations of these quantities as a function of the number of cycles are shown in Figure E.3. While the curvature stayed at a consist level as a result of displacement control, the moment decreased. The rigidity of measurements at two displacements appeared to converge before rod failure while exhibiting a slightly declining trend. The curvature, moment, and flexural rigidity based on online monitoring data are presented in Figure E.4. It can be seen that the 0.65 m^{-1} curvature obtained in the cyclic test is higher than those used in measurements as part of the experiment design. Accordingly, the flexural rigidity based on online monitoring was about $50 \text{ N}\cdot\text{m}^2$, which is a little lower than that acquired in measurements. The result agrees with the declining flexural rigidity with increasing curvature as shown in Figure E.3. Overall, the rod exhibited a relatively stable response prior to its final breakage.

Failure was observed in the gauge section near motor 2 (left side). The failure occurred at the pellet-to-pellet interface as illustrated in Figure E.5. The end faces of two neighboring pellets were essentially clean, while the fracture surfaces of the cladding were serrated. Some striations had developed in the circumferential direction, but they were not well differentiated at this magnification.

Both lateral stressed sides of the rod were covered with equally spaced circumferential cracks throughout the gauge section. Spalling only occurred at the local area near the fracture. A similar degree of damage on the lateral stressed sides exhibited by D1/ DL1 is different from that seen from unidirectional bending. The large deformation arising from unidirectional bending can produce a greater extent of damage or spalling on one side and less on the other side, as seen in S3/ Dcal (Figure D.6). The extensive circumferential cracks revealed in D1/ DL1 did not occur in Dcal/ S3, even though the load amplitude in the latter was higher. Therefore, the parallel equally spaced cracks were likely related to a preexisting condition, as D1/ DL1 actually had a thicker layer of oxidation and a higher H content.

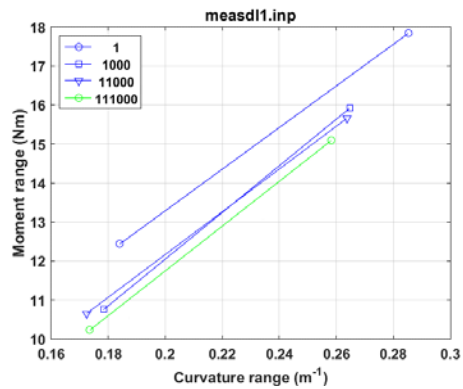


(a)

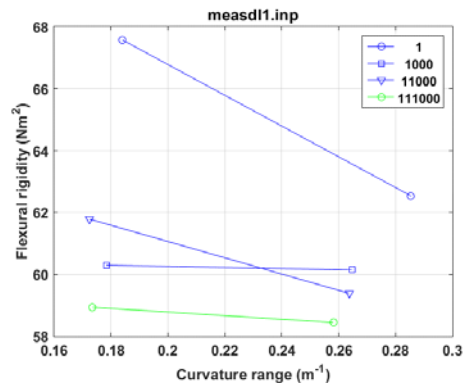


(b)

Figure E.1 Moment-curvature loops based on measurements when (a) $N = 1$ and (b) $N = 111,000$ cycles for D1/ DL1 (607C4B); measurements were made with 0.8 and 1.2 mm relative displacements; $N_f = 1.1 \times 10^5$ cycles under ± 15.24 N·m 5 Hz; fuel particles collected < 1.0 gram

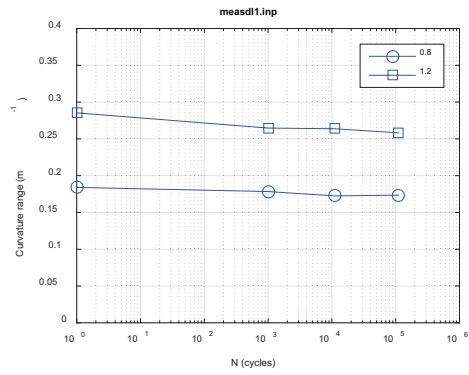


(a)

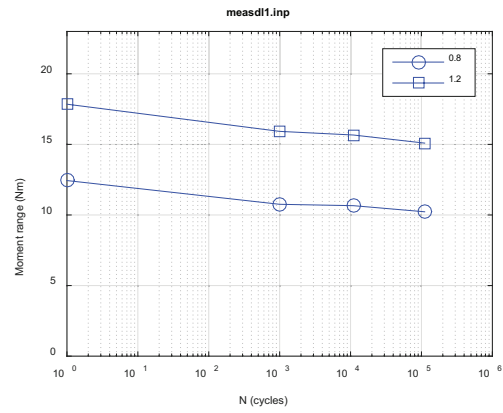


(b)

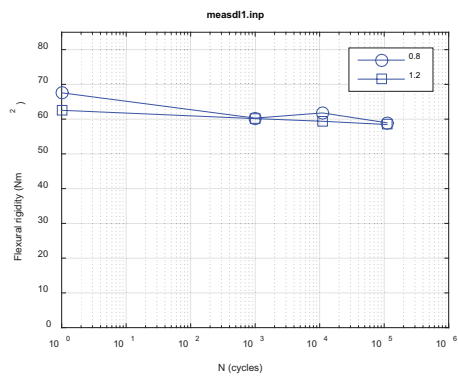
Figure E.2 (a) Moment-curvature relation and (b) moment-flexural rigidity relation at various numbers of cycles for D1/DL1 (607C4B); $N_f = 1.1 \times 10^5$ cycles under ± 15.24 N·m 5 Hz; fuel particles collected < 1.0 gram



(a)

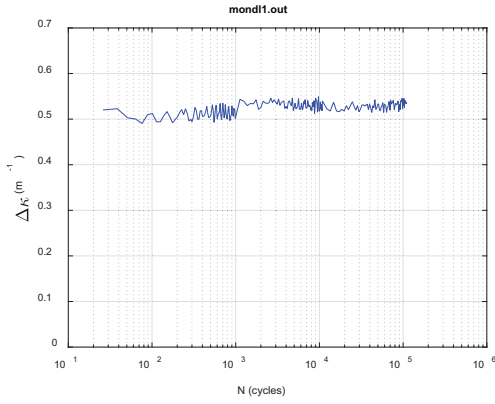


(b)

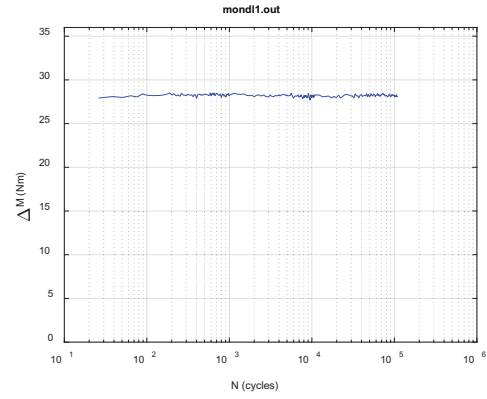


(c)

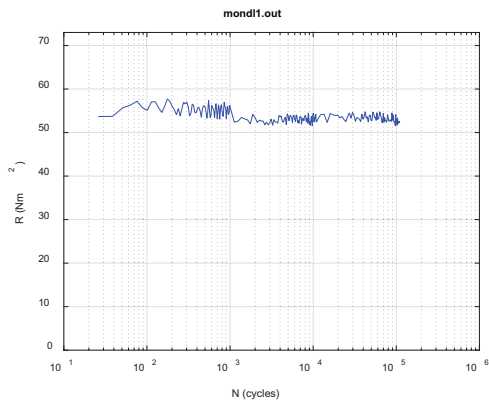
Figure E.3 Variations of (a) curvature range, (b) moment range, and (c) flexural rigidity as a function of the number of cycles for D1/DL1 (607C4B); $N_f = 1.1 \times 10^5$ cycles under ± 15.24 N·m 5 Hz; fuel particles collected < 1.0 gram



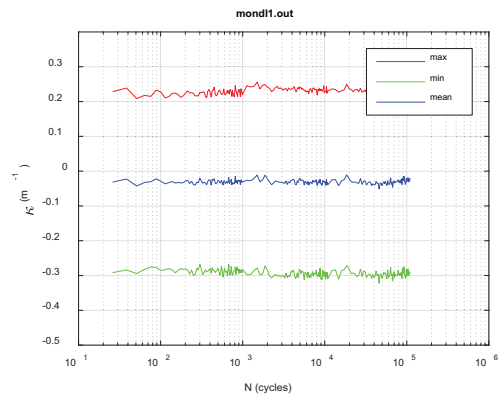
(a)



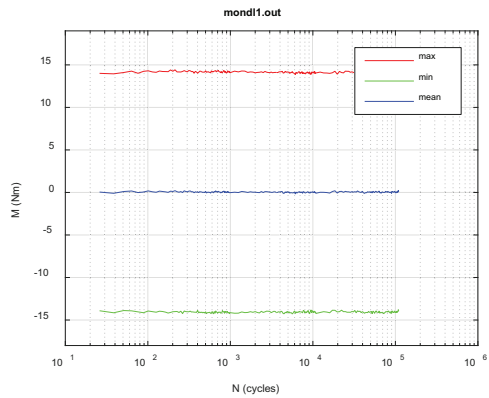
(b)



(c)



(d)



(e)

Figure E.4 Variations of (a) curvature range, (b) applied moment range, (c) flexural rigidity, (d) maximum and minimum values of curvature, and (e) maximum and minimum values of moment as a function of the number of cycles for D1/DL1 (607C4B); $N_f = 1.1 \times 10^5$ cycles under ± 15.24 N·m 5 Hz; fuel particles collected < 1.0 gram

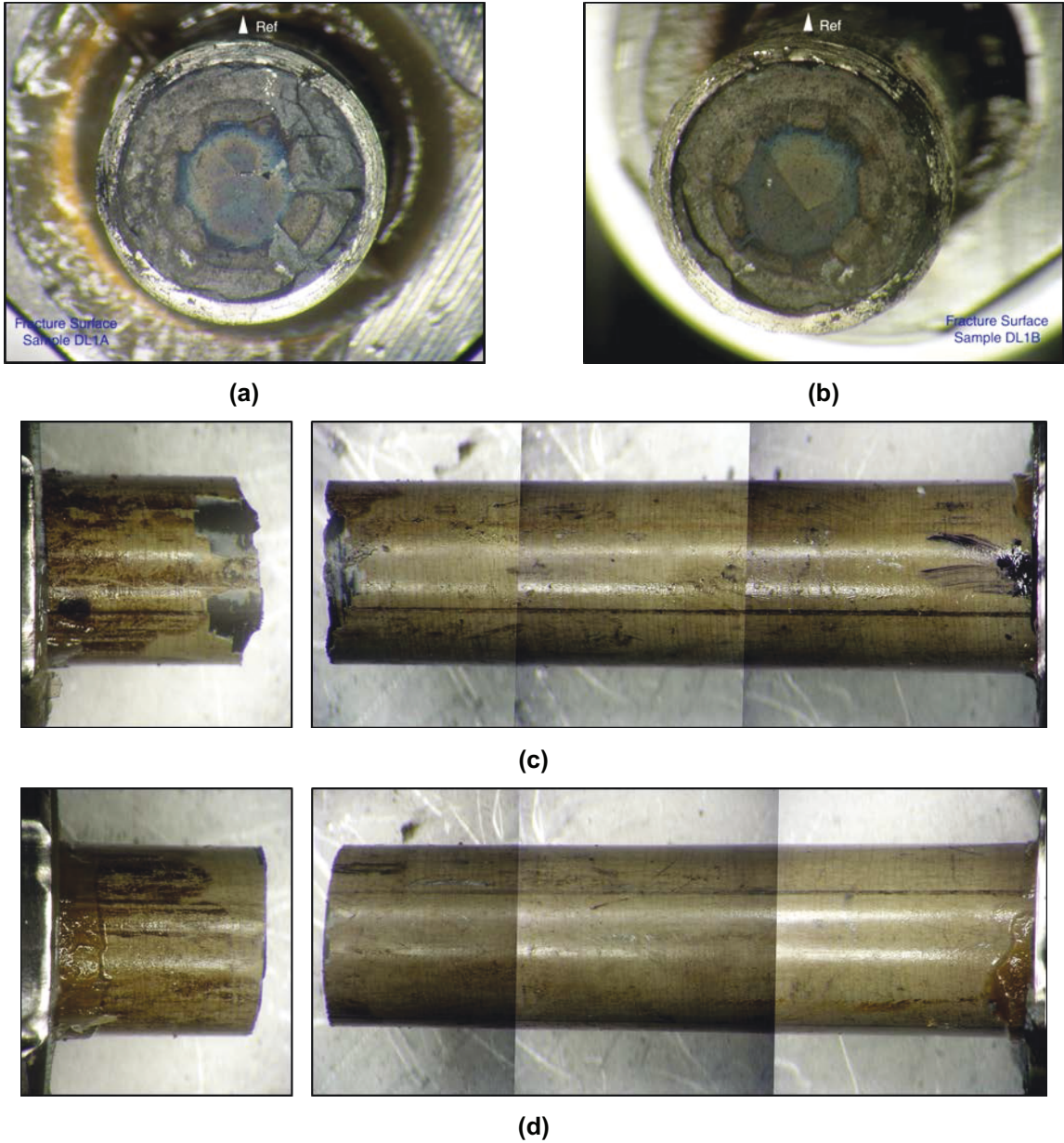
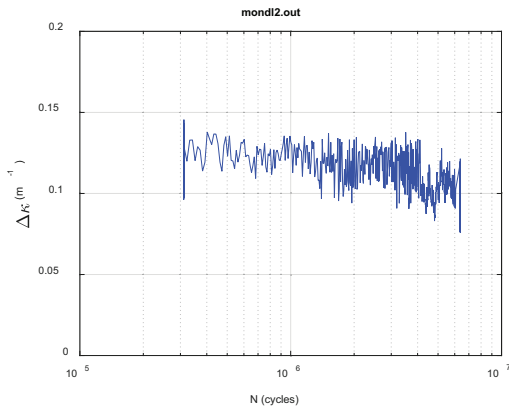


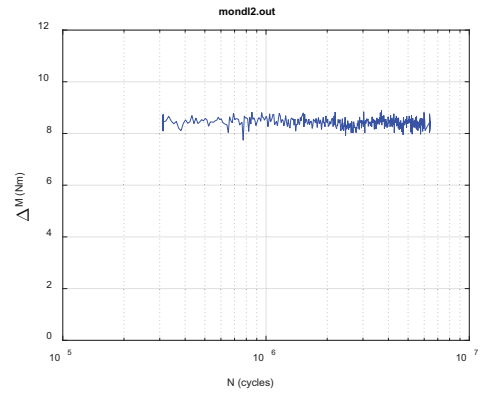
Figure E.5 (a, b) Mating fracture surfaces, (c) front side, and (d) back side of D1/ DL1 (607C4B), $N_f = 1.1 \times 10^5$ cycles under ± 15.24 N·m 5 Hz; fuel particles collected < 1.0 gram

E.2 D2/ DL2/ 608C4B ($\pm 5.08/35.56$ N·m 5 Hz)

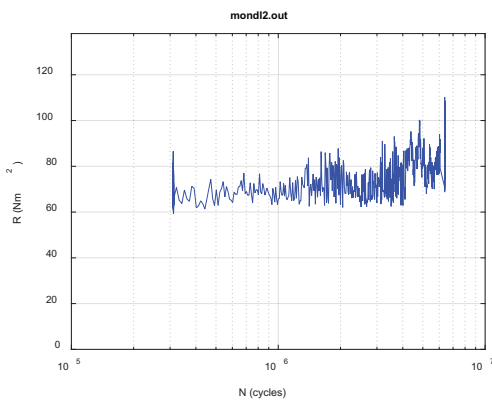
D2/ DL2 (608C4B, 63.8 GWd/MTU burnup, 70–100 μm oxide layer, 700 ppm H content) was tested under ± 5.08 N·m 5 Hz. The measurement was performed using 0.4 mm relative displacement. The rod sustained more than 6.4×10^6 cycles of loading without showing any changes in flexural rigidity in both the on-line monitoring and measurements, as shown in Figures E.6 and E.7. An earlier stage of this test is not shown because the LVDT3 channel did not generate reliable data owing to loose wires.



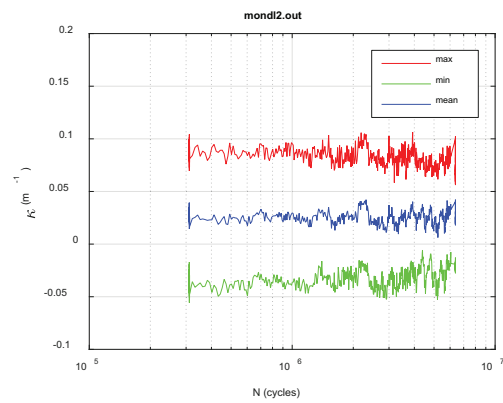
(a)



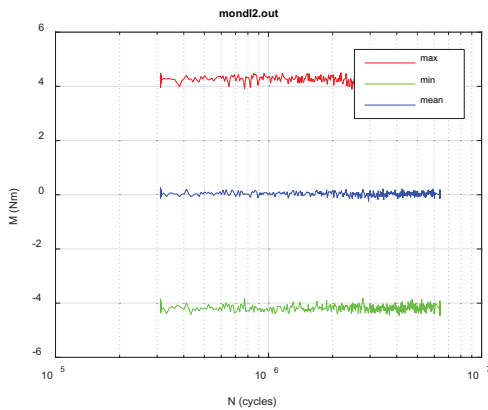
(b)



(c)

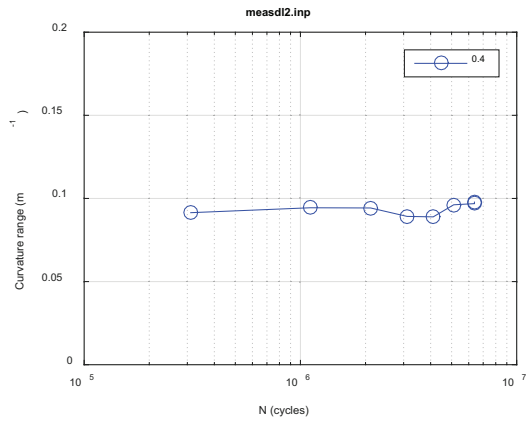


(d)

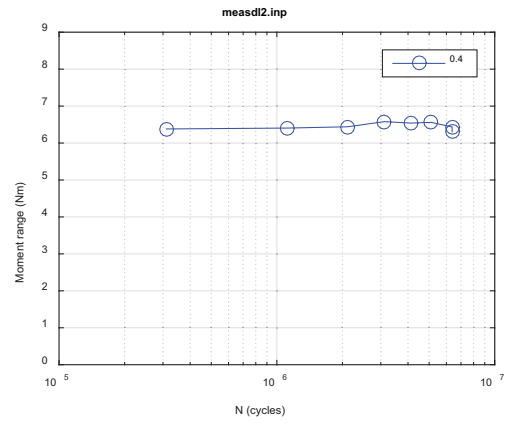


(e)

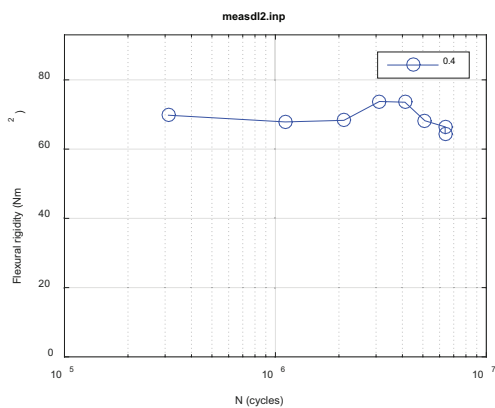
Figure E.6 Variations of (a) curvature range, (b) applied moment range, (c) flexural rigidity, (d) maximum and minimum values of curvature, and (e) maximum and minimum values of moment as a function of the number of cycles for D2/DL2 (608C4B); 6.4×10^4 cycles completed under ± 5.08 N·m 5 Hz without failure



(a)



(b)



(c)

Figure E.7 Variations of (a) curvature range, (b) applied moment range, and (c) flexural rigidity as a function of number of cycles for D2/ DL2 (608C4B) based on measurements with maximum relative displacement 0.4 mm; 6.4×10^6 cycles completed under ± 5.08 N·m 5 Hz without failure

A subsequent cycle test using ± 35.56 N·m 5 Hz was conducted to investigate the failure mode of the tested specimen. The specimen failed near motor 2 (end cap A of the rod specimen) at around 1.8×10^3 cycles. The clean fracture surfaces revealed that failure occurred at the pellet-to-pellet interface (Figure E.8). The lateral view showed that the fracture surface was not a flat cut with a sharp attachment on the front side of the rod with extensive spalling, and circumferential cracks covered the stressed surfaces of the rod.

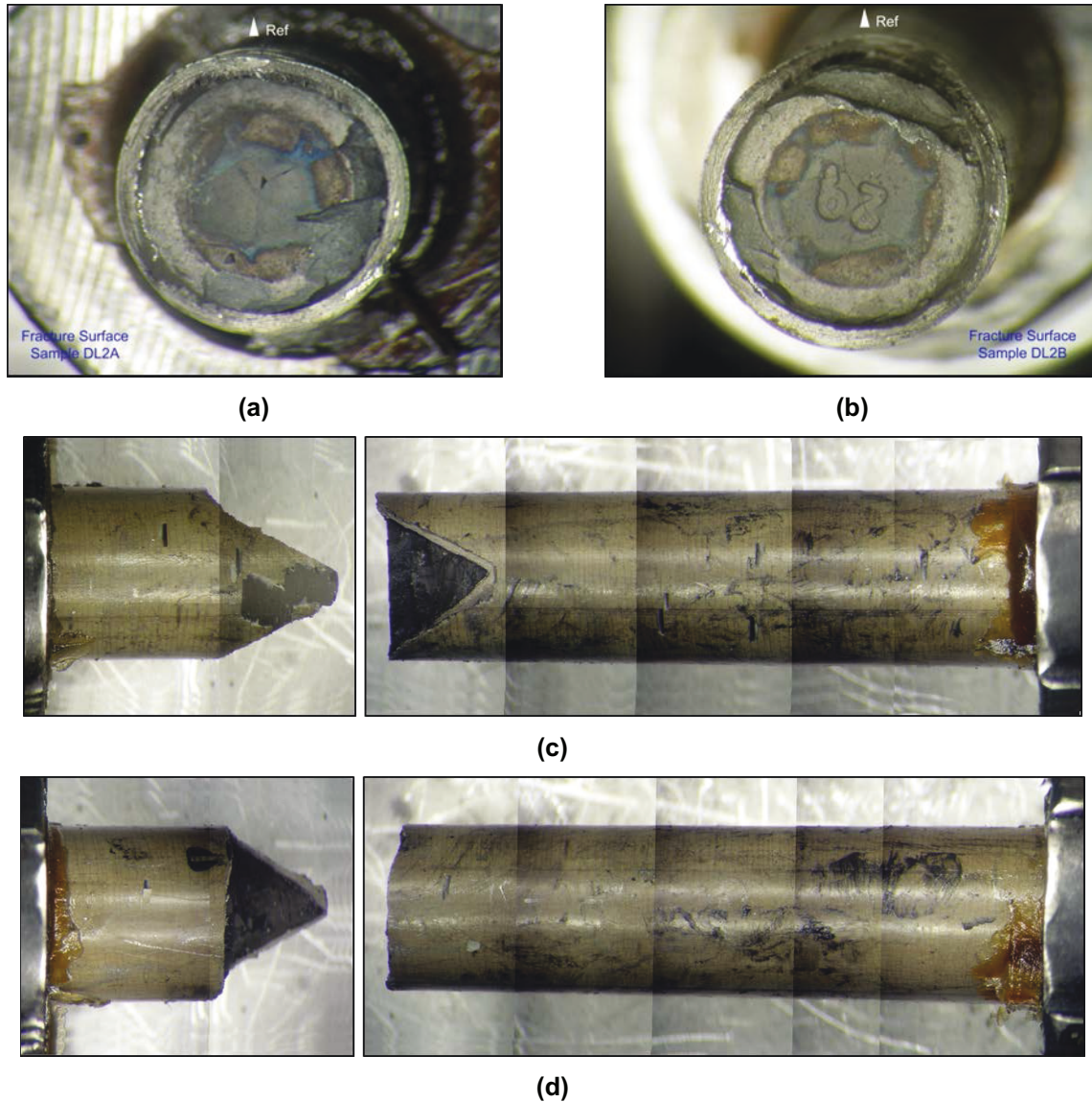
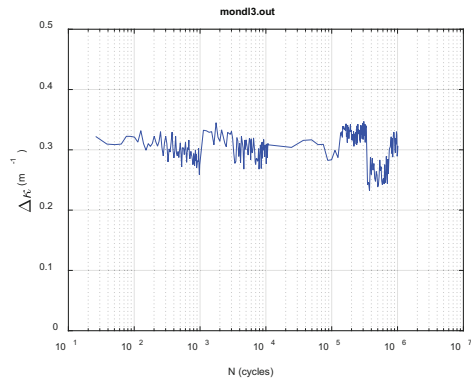


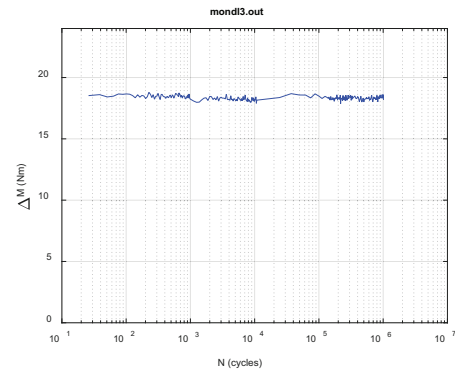
Figure E.8 (a, b) Mating fracture surfaces, (c) front side, and (d) back side of D2/ DL2 (608C4B); follow-up test was conducted with increased amplitude ± 35.56 N·m 5 Hz with $N_f = 1.8 \times 10^3$ cycles

E.3 D3/ DL3/ 605C10A (± 10.16 N·m 5 Hz)

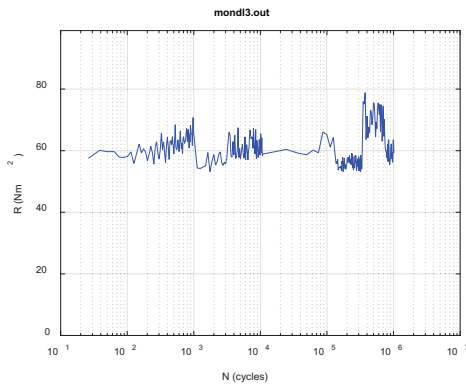
D3/ DL3 (605C10A, 66.5 GWd/MTU burnup, 70–100 μm oxide layer, 550 ppm H content) was tested with ± 10.16 N·m 5 Hz at a lifetime of 1.0×10^6 cycles. The monitoring data revealed a slight increase in flexural rigidity prior to failure, as seen in Figure E.9. The measurements using 0.4 and 0.8 mm demonstrated a trend of fall and rise as shown in Figure E.10. However, the final rigidity values were still lower than the respective pre-fatigue levels. The specimen failed near motor 2 (left side, end cap A of the rod specimen). The fracture surface indicates that failure occurred at the pellet-to-pellet interface, as the end faces of involved pellets can be seen clearly (Figure E.11). No circumferential crack was observed on the stressed surfaces of the rod.



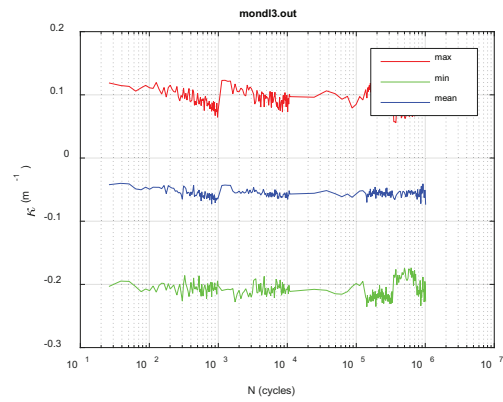
(a)



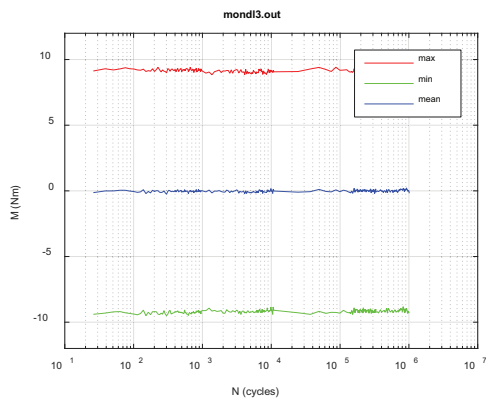
(b)



(c)

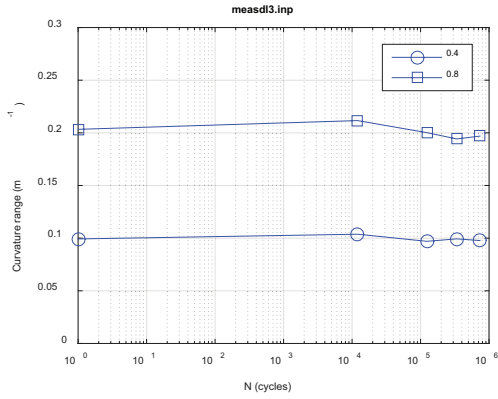


(d)

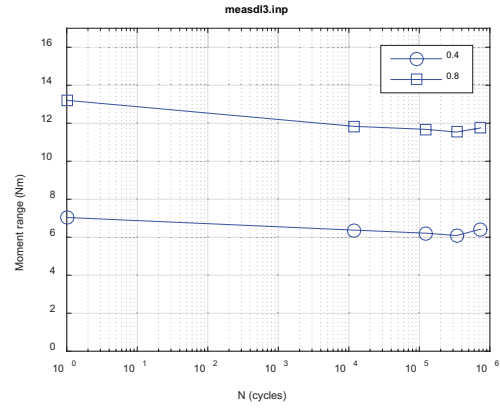


(e)

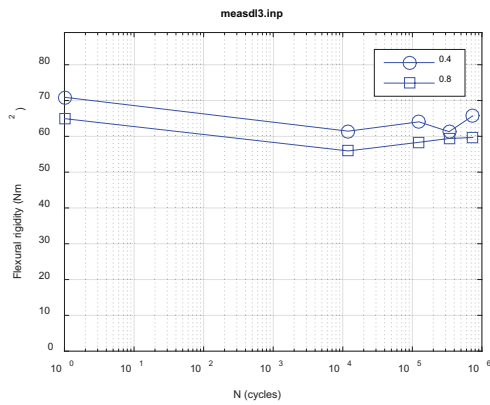
Figure E.9 Variations of (a) curvature range, (b) applied moment range, (c) flexural rigidity, (d) maximum and minimum values of curvature, and (e) maximum and minimum values of moment as a function of the number of cycles for D3/DL3 (60510A); $N_f = 1.0 \times 10^6$ cycles under ± 10.60 N-m 5 Hz



(a)



(b)



(c)

Figure E.10 Variations of (a) curvature range, (b) applied moment range, (c) flexural rigidity as a function of the number of cycles for D3/DL3 (60510A) based on measurements with maximum relative displacement at 0.4 and 0.8 mm; $N_f = 1.0 \times 10^6$ cycles under ± 10.16 N-m 5 Hz

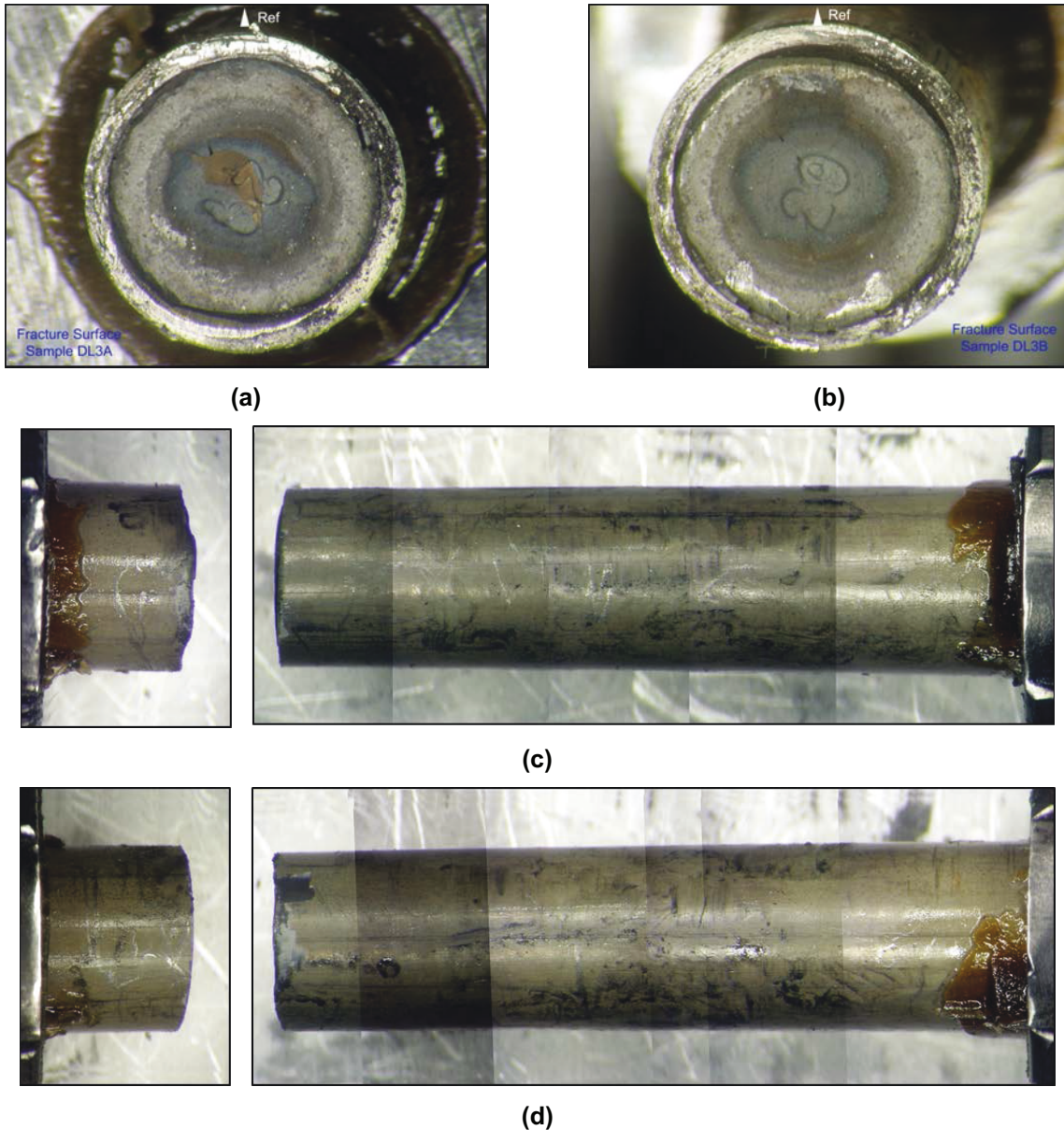
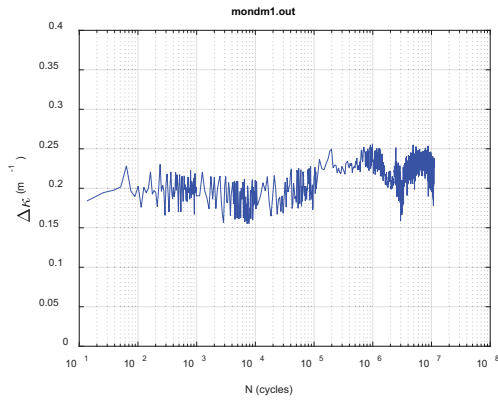


Figure E.11 (a, b) Mating fracture surfaces, (c) front side, and (d) back side of D3/ DL3 (605C10A); $N_f = 1.0 \times 10^6$ cycles under ± 10.16 N·m 5 Hz

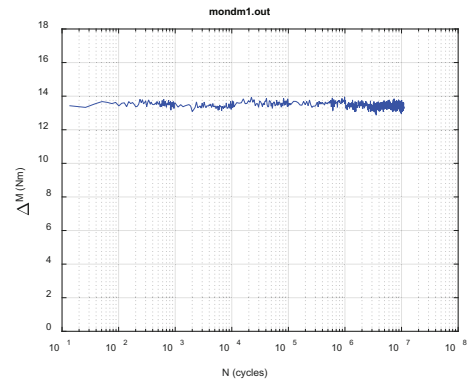
E.4 D4/ DM1/ 605D1C (± 7.62 N·m 5 Hz)

D4/DM1 (605D1C, 66.5 GWd/MTU burnup, 40–70 μm oxide layer, 500 ppm H content) was tested under ± 7.62 N·m 5 Hz as the result of an effort to define a possible fatigue limit for the SNF rod. DM1 finished the target of 1.1×10^7 cycles without any sign of significant fatigue during the cyclic test, and the test was stopped.

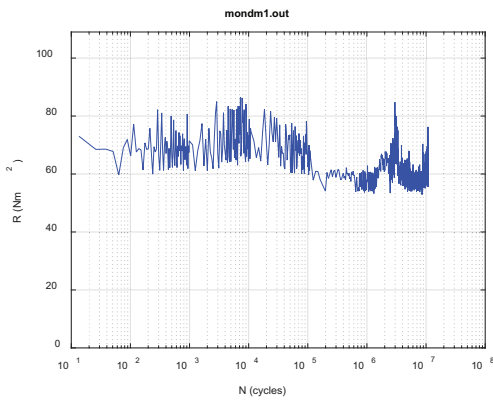
Online monitoring demonstrated that the flexural rigidity fluctuated between 42–49 N·m², with a marginal decrease near the end of the test (Figure E.12). The measurements using 0.4 and 0.6 mm also demonstrated a certain amount of drop in rigidity near the end-of-cycle test, as shown in Figure E.13.



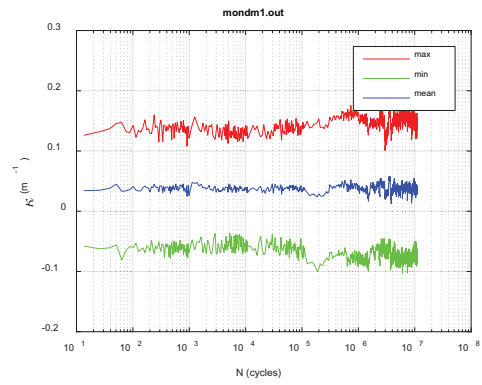
(a)



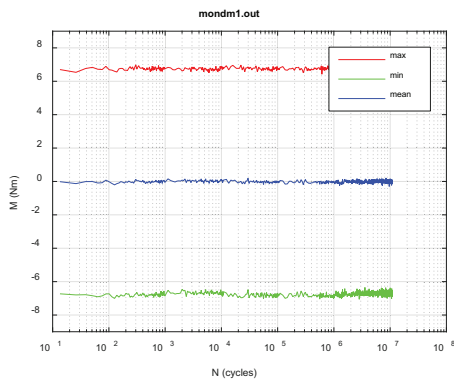
(b)



(c)

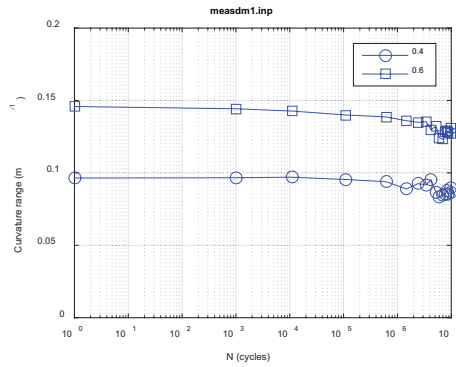


(d)

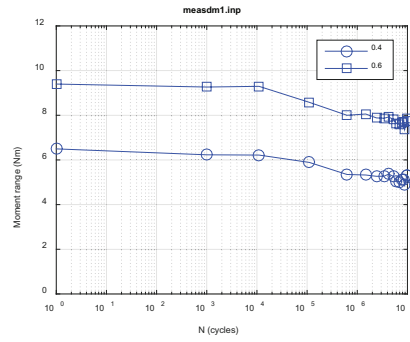


(e)

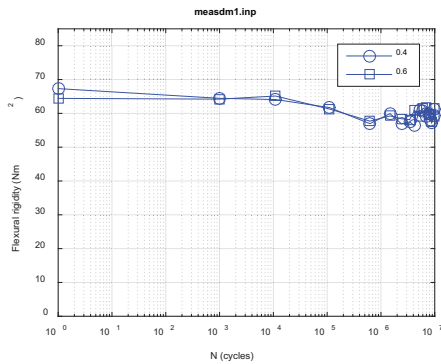
Figure E.12 Variations of (a) curvature range, (b) applied moment range, (c) flexural rigidity, (d) maximum and minimum values of curvature, and (e) maximum and minimum values of moment as a function of the number of cycles for D4/DM1 (605D1C); $N = 1.0 \times 10^7$ cycles under ± 7.62 N·m 5 Hz



(a)



(b)



(c)

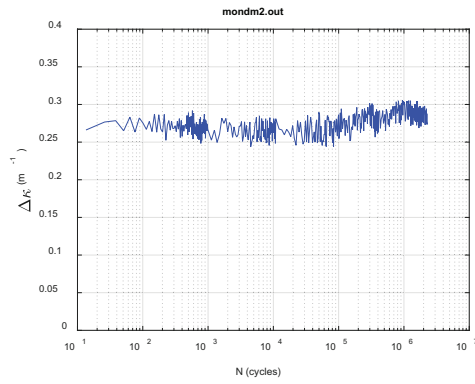
Figure E.13 Variations of (a) curvature range, (b) applied moment range, and (c) flexural rigidity as a function of the number of cycles for D4/ DM1 (605D1C) based on measurements with maximum relative displacement at 0.4 and 0.6 mm; $N = 1.0 \times 10^7$ cycles under ± 7.62 N·m 5 Hz

E.5 D5/ DM2/ 605D1B (± 9.14 N·m 5 Hz)

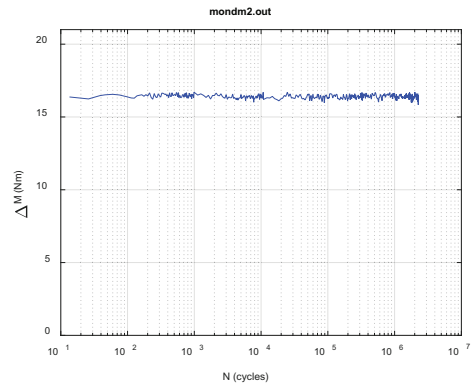
The cycle test on D5/ DM2 (605D1B, 66.5 GWd/MTU burnup, 40–70 μ m oxide layer, 550 ppm H content) was conducted under ± 9.14 N·m 5 Hz. DM2 fractured near 2.3×10^6 cycles.

Online monitoring demonstrated that the flexural rigidity fluctuated between 47 and 51 N·m², with a marginal decrease near the end of test (Figure E.14). The measurements using 0.4 and 0.8 mm also showed a similar degree of drop in rigidity near the end of the test, as shown in Figure E.15.

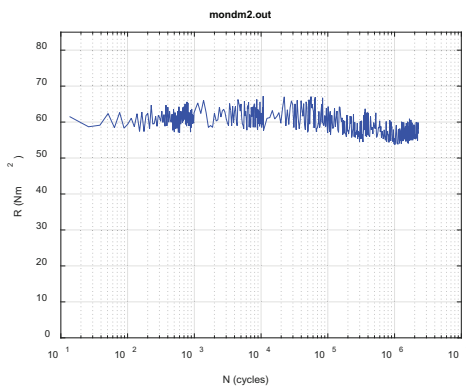
DM2 fractured in the gauge section near motor 2 (left side), as shown in Figure E.16. The involvement of the pellet-to-pellet interface was not quite clear because no end face of a pellet can be identified. No circumferential cracking can be seen on either of the stressed surfaces of the rod, but spalling was observed near the fracture.



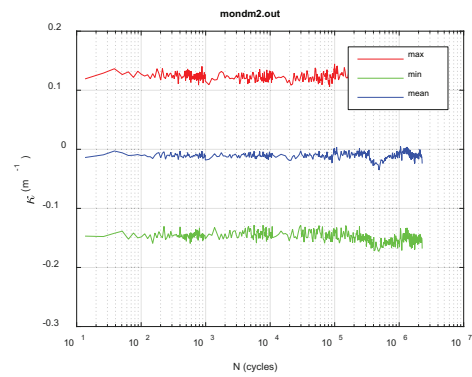
(a)



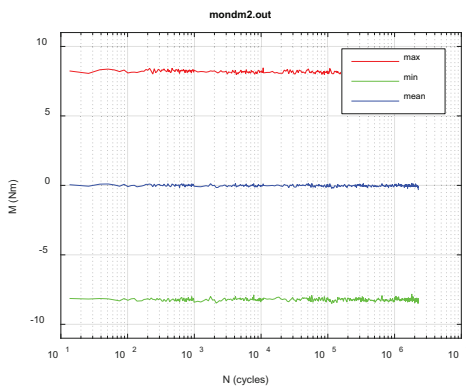
(b)



(c)

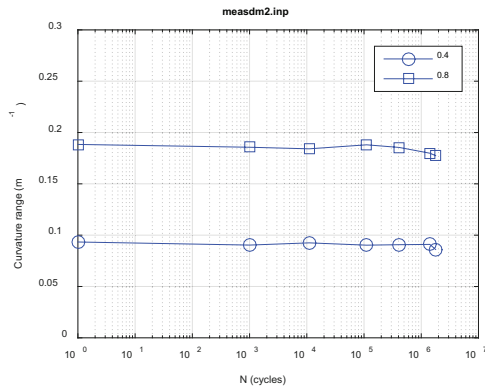


(d)

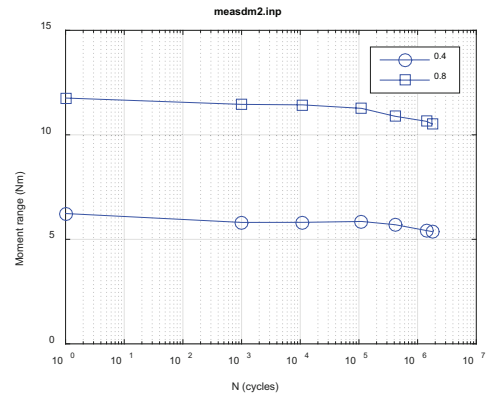


(e)

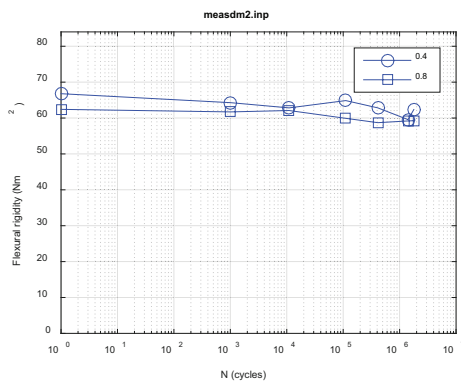
Figure E.14 Variations of (a) curvature range, (b) applied moment range, (c) flexural rigidity, (d) maximum and minimum values of curvature, and (e) maximum and minimum values of moment as a function of the number of cycles for D5/DM2 (605D1B); $N_f = 2.3 \times 10^6$ cycles under ± 9.14 N·m 5 Hz



(a)



(b)



(c)

Figure E.15 Variations of (a) curvature range, (b) applied moment range, and (c) flexural rigidity as a function of the number of cycles for D5/DM2 (605D1B) based on measurements with maximum relative displacement at 0.4 and 0.8 mm; $N_f = 2.3 \times 10^6$ cycles under ± 9.14 N·m 5 Hz.

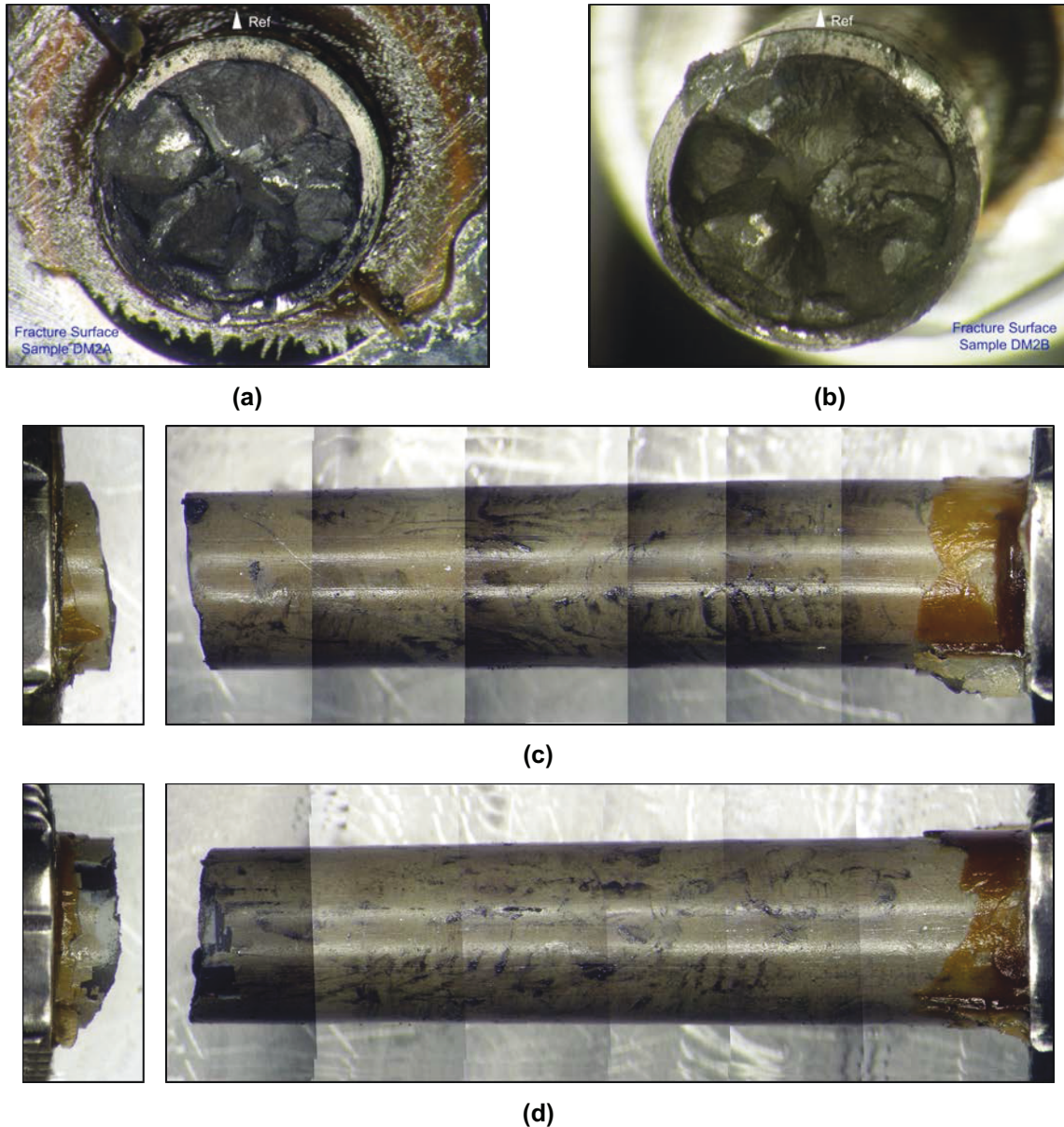


Figure E.16 (a, b) Mating fracture surfaces, (c) front side, and (d) back side of D5/ DM2 (605D1B); $N_f = 2.3 \times 10^6$ cycles under ± 9.14 N·m 5 Hz.

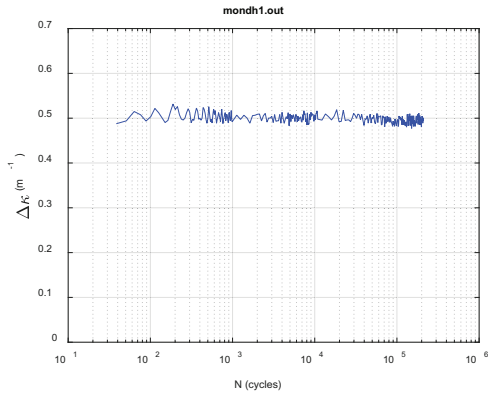
E.6 D6/ DH1/ 609C4 (± 12.7 N·m 5 Hz)

The cycle test on D6/DH1 (609C4, 66.5 GWd/MTU burnup, 70–100 μm oxide layer, 700 ppm H content) was conducted under ± 12.7 N·m 5 Hz. D6/DH1 fractured at around 2.4×10^5 cycles.

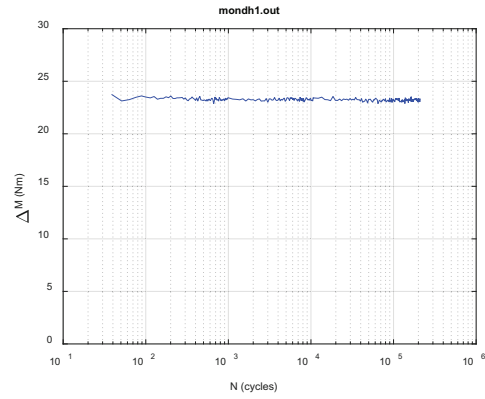
Online monitoring demonstrated that the flexural rigidity remained between 42–45 N·m² over the cycle test with a slight increase (Figure E.17). The measurements using 0.4 and 0.8 mm also showed a similar variation in rigidity, as shown in Figure E.18.

DH1 fractured in the gauge section near motor 2 (left side), as shown in Figure E.19. The involvement of the pellet-to-pellet interface was not quite clear because no end face of a pellet

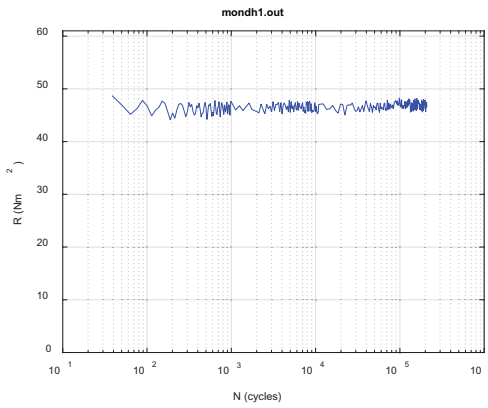
can be seen. However, equally spaced circumferential cracks exist on both stressed surfaces of the rod.



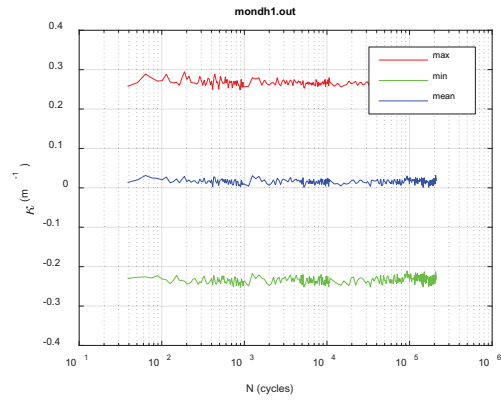
(a)



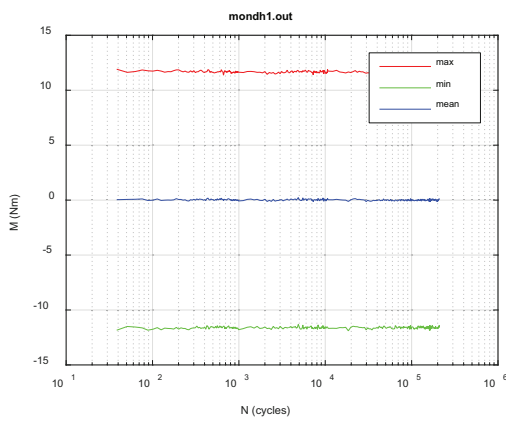
(b)



(c)

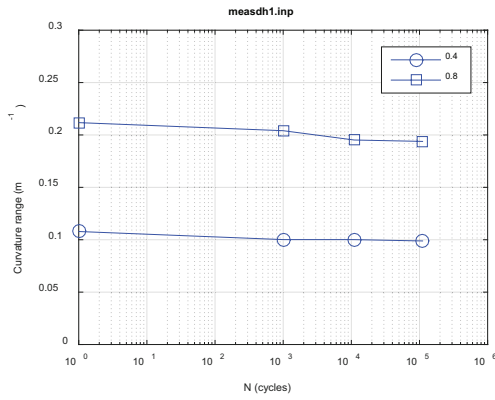


(d)

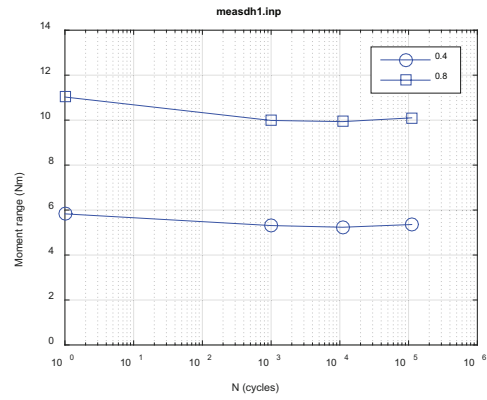


(e)

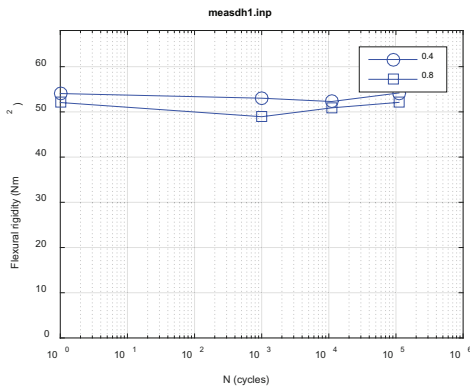
Figure E.17 Variations of (a) curvature range, (b) applied moment range, (c) flexural rigidity, (d) maximum and minimum values of curvature, and (e) maximum and minimum values of moment as a function of the number of cycles for D6/ DH1 (609C4); $N_f = 2.4 \times 10^5$ cycles under ± 12.7 N·m 5 Hz



(a)

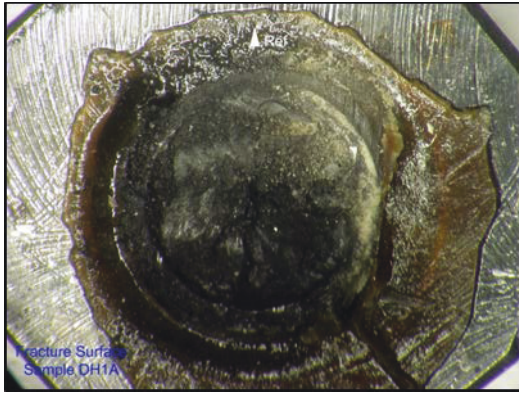


(b)

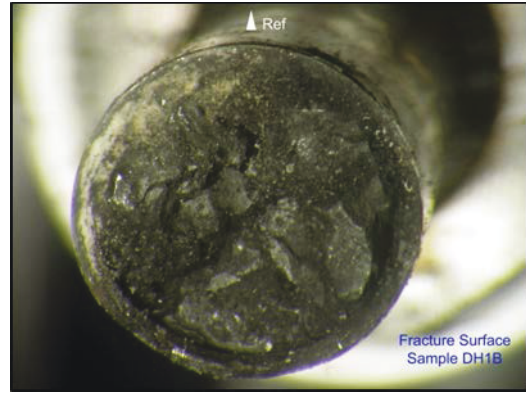


(c)

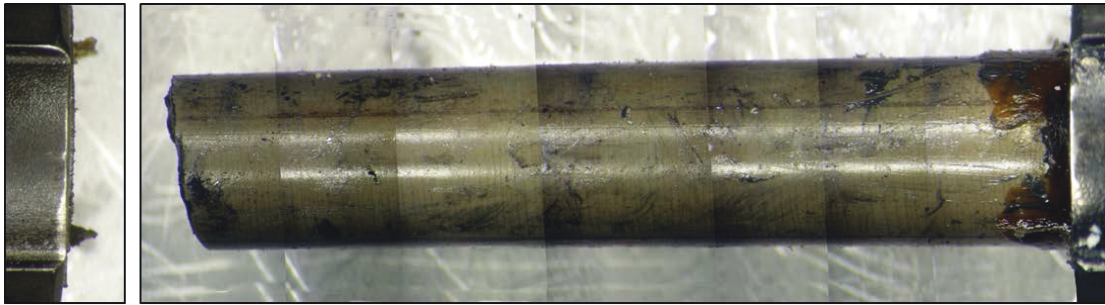
Figure E.18 Variations of (a) curvature range, (b) applied moment range, and (c) flexural rigidity as a function of the number of cycles for D6/DH1 (609C4) based on measurements with maximum relative displacement at 0.4 and 0.8 mm; $N_f = 2.4 \times 10^5$ cycles under ± 12.7 N·m 5 Hz



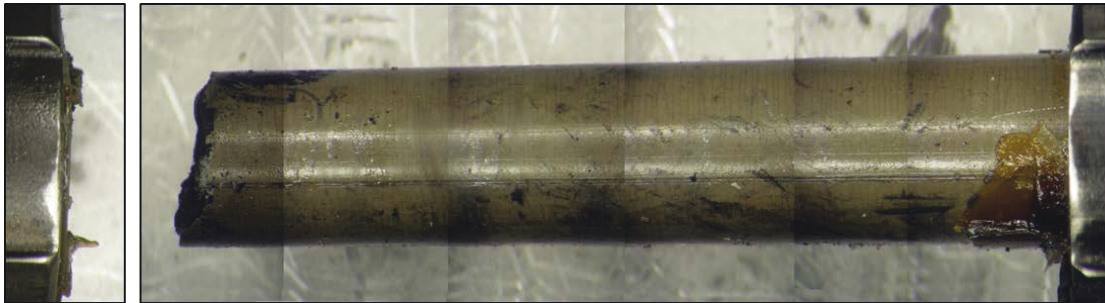
(a)



(b)



(c)



(d)

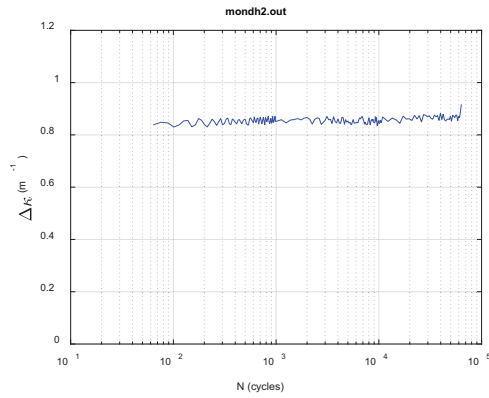
Figure E.19 (a, b) Mating fracture surfaces, (c) front side, and (d) back side of D6/DH1 (609C4); $N_f = 2.4 \times 10^5$ cycles under ± 12.7 N·m 5 Hz

E.7 D7/ DH2/ 609C3 (± 20.32 N·m 5 Hz)

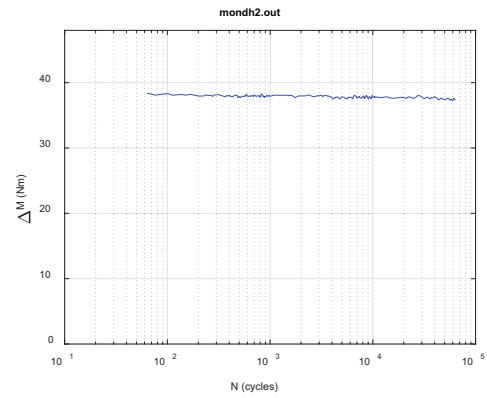
The cycle test on D7/DH2 (609C3, 66.5 GWd/MTU burnup, 70–100 μm oxide layer, 750 ppm H content) was conducted under ± 20.32 N·m 5 Hz. DH2 fractured around 6.5×10^4 cycles.

Online monitoring displayed a steady decrease throughout the cycle test with a sudden drop near the end (Figure E.20). The measurements using 0.8 and 1.2 mm also showed a similar rigidity variation as given in Figure E.21.

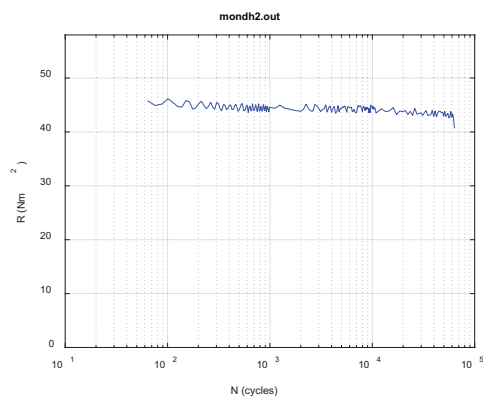
DH2 fractured in the middle of the gauge section on a pellet-to-pellet interface, as evidenced by the clean cut in Figure E.22. Equally spaced circumferential cracks can be observed over both stressed surfaces of the rod, with some spalling near the fracture.



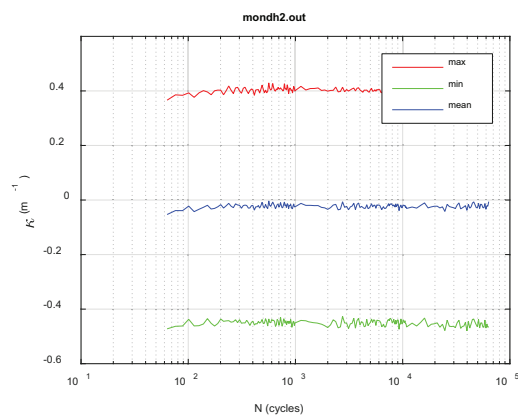
(a)



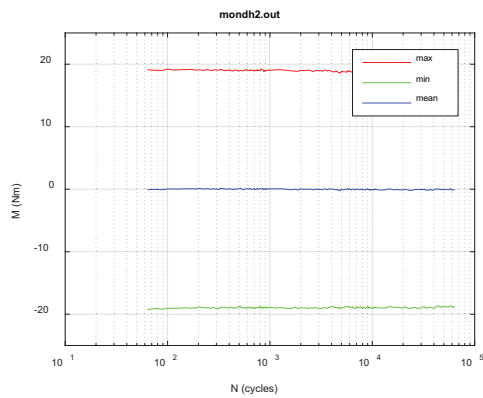
(b)



(c)

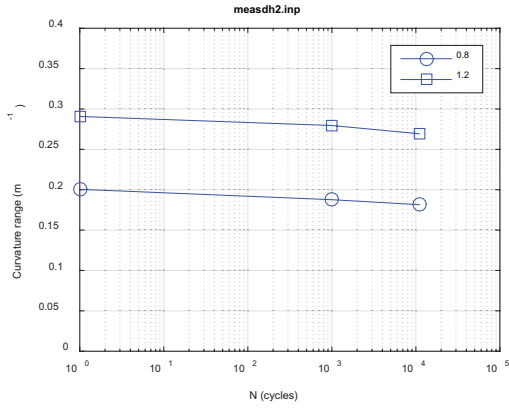


(d)

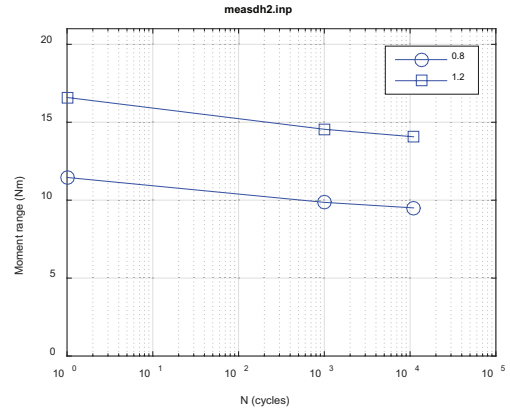


(e)

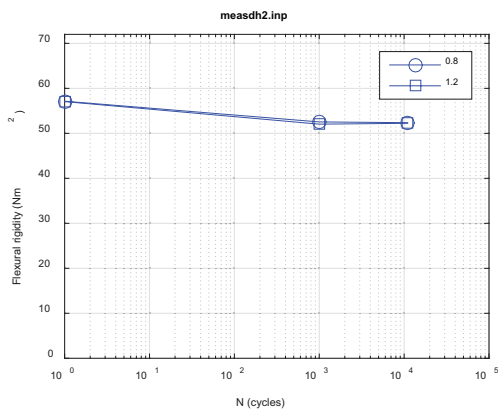
Figure E.20 Variations of (a) curvature range, (b) applied moment range, (c) flexural rigidity, (d) maximum and minimum values of curvature, and (e) maximum and minimum values of moment as a function of the number of cycles for D7/DH2 (609C3); $N_f = 6.5 \times 10^4$ cycles under ± 20.32 N·m 5 Hz



(a)



(b)



(c)

Figure E.21 Variations of (a) curvature range, (b) applied moment range, (c) flexural rigidity as a function of the number of cycles for D7/DH2 (609C3) based on measurements with maximum relative displacement at 0.8 and 1.2 mm; $N_f = 6.5 \times 10^4$ cycles under ± 20.32 N·m 5 Hz

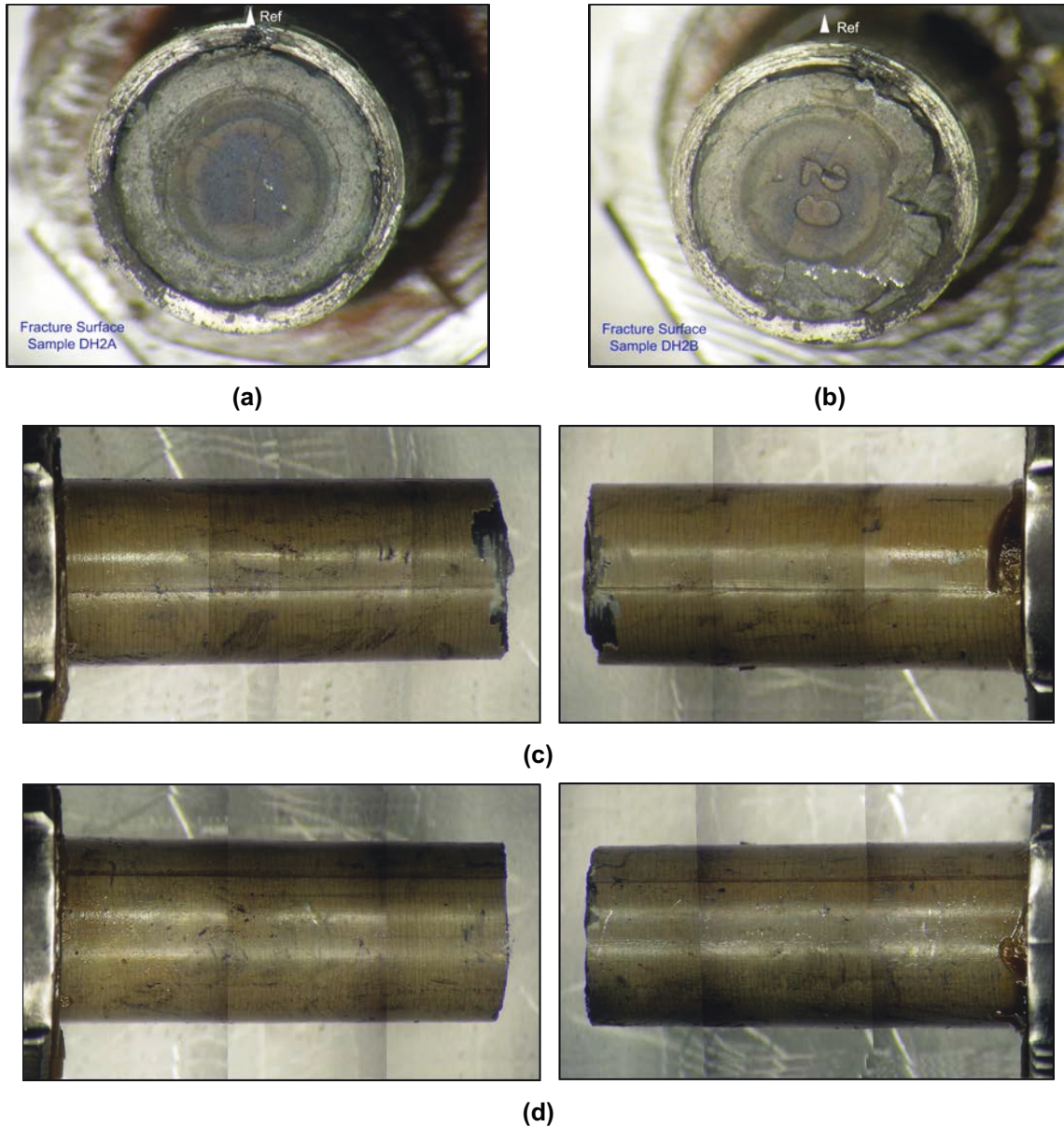
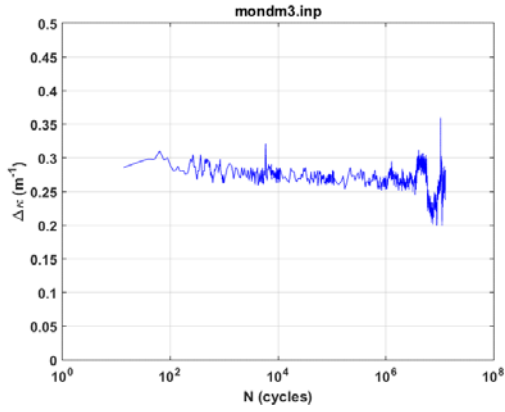


Figure E.22 (a, b) Mating fracture surfaces, (c) front side, and (d) back side of D7/DH2 (609C3); $N_f = 6.5 \times 10^4$ cycles under $\pm 20.32 \text{ N}\cdot\text{m}$ 5 Hz

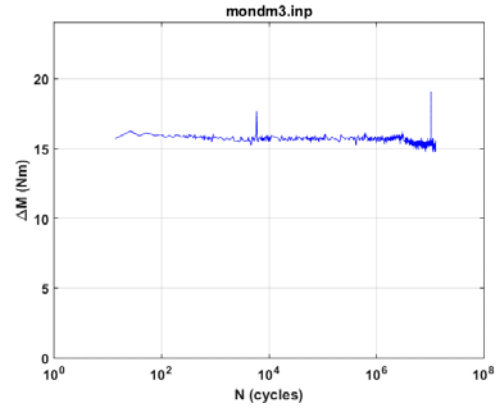
E.8 D8/ DM3/ 606C3E ($\pm 8.89 \text{ N}\cdot\text{m}$ 5 Hz)

D8/DM3 (606C3E, 66.8 GWd/MTU burnup, 70–100 μm oxide layer, 550 ppm H content) sustained a long testing period under $\pm 8.89 \text{ N}\cdot\text{m}$ 5 Hz. Testing was stopped after 1.3×10^7 cycles.

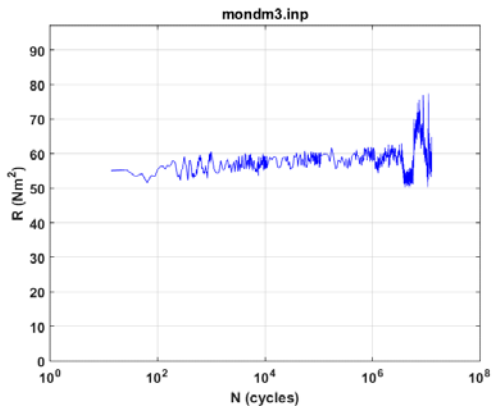
Online monitoring displayed a stable flexural rigidity response, followed by a fluctuation or fall-and-rise near 4×10^6 cycles (Figure E.23). The fluctuation was limited within the range of 45–50 $\text{N}\cdot\text{m}^2$. The measurements using 0.8 and 1.2 mm also revealed a variation of a quite similar pattern in rigidity, as shown in Figure E.24.



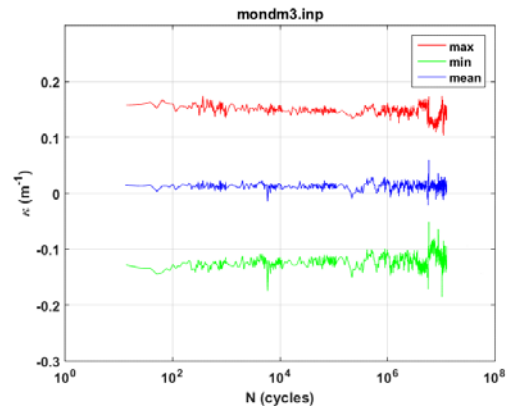
(a)



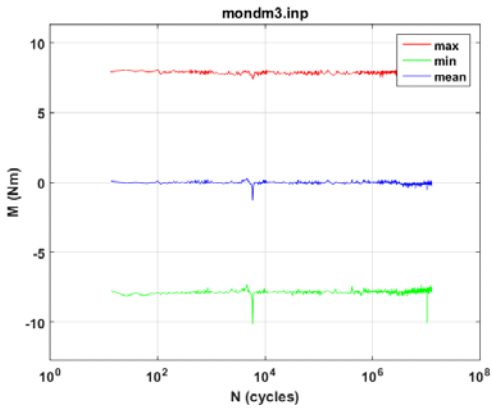
(b)



(c)

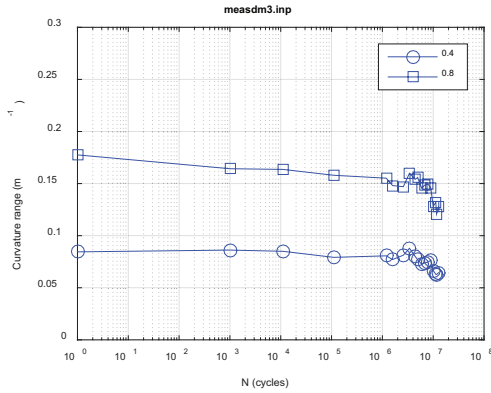


(d)

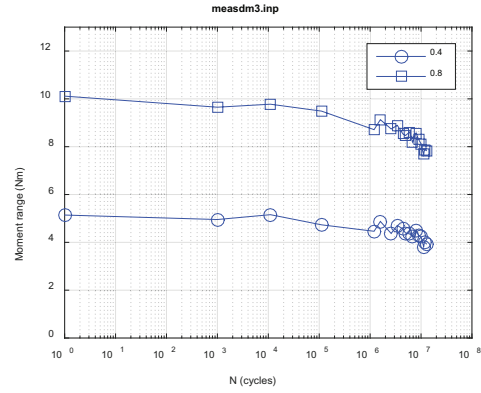


(e)

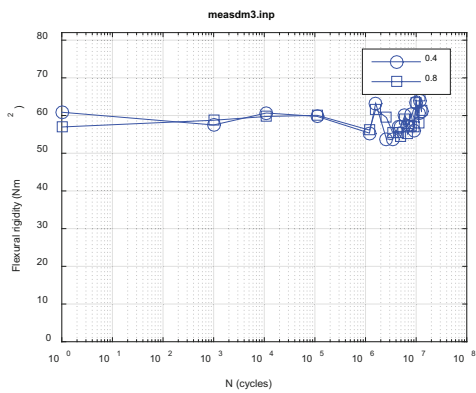
Figure E.23 Variations of (a) curvature range, (b) applied moment range, (c) flexural rigidity, (d) maximum and minimum values of curvature, and (e) maximum and minimum values of moment as a function of the number of cycles for D8/DM3 (606C3E); $N = 1.3 \times 10^7$ cycles under ± 8.89 N·m 5 Hz



(a)



(b)



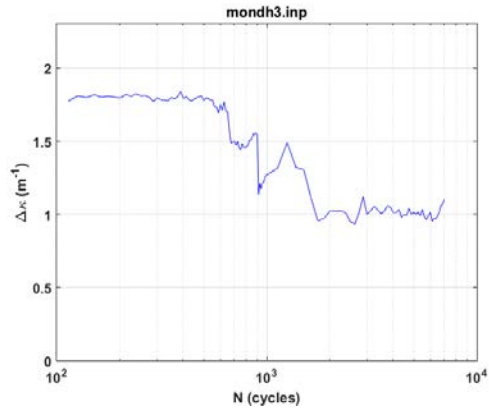
(c)

Figure E.24 Variations of (a) curvature range, (b) applied moment range, and (c) flexural rigidity as a function of the number of cycles for D8/DM3 (606C3E) based on measurements with maximum relative displacement at 0.4 and 0.8 mm; $N = 1.3 \times 10^7$ cycles under ± 8.89 N·m 5 Hz

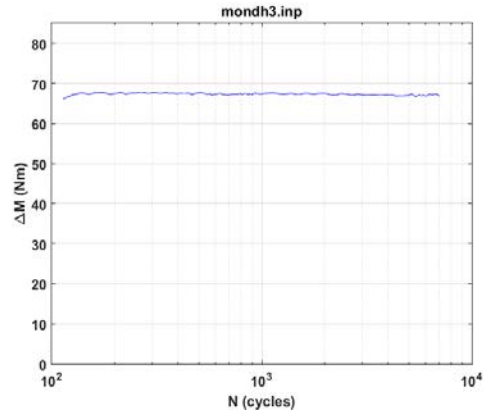
E.9 D9/ DH3/ 609C7 (± 35.56 N·m 5 Hz)

The cycle test on D9/ DH3 (609C7, 66.5 GWd/MTU burnup, 70–100 μ m oxide layer, 550 ppm H content) was conducted under ± 35.56 N·m 5 Hz. The specimen failed near 7.13×10^3 cycles within the gauge section.

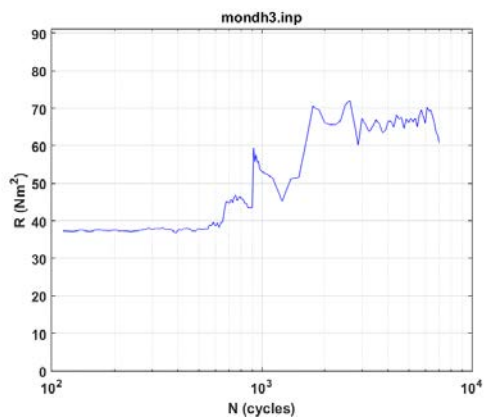
Online monitoring exhibited a relatively flat response in flexural rigidity before 6.5×10^2 cycles, and then it fluctuated or rose substantially, as shown in Figure E.25. Although the cause of the fluctuation was not clear, it can be seen that a sudden drop occurred prior to rod failure. The measurements using 0.8, 1.2, and 1.6 mm relative displacements also revealed a considerable increase in rigidity at 10^3 cycles, as shown in Figure E.26. The increase observed in both online monitoring and measurement remains to be studied.



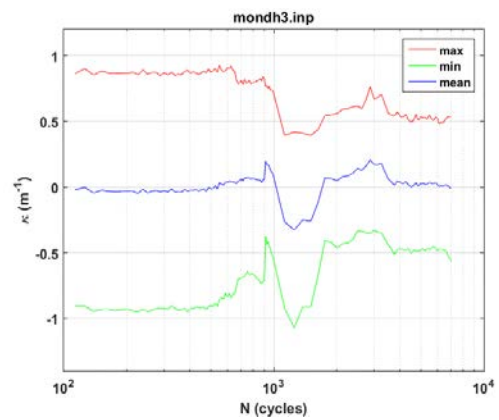
(a)



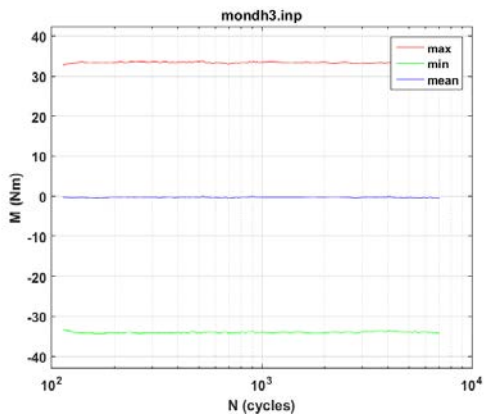
(b)



(c)

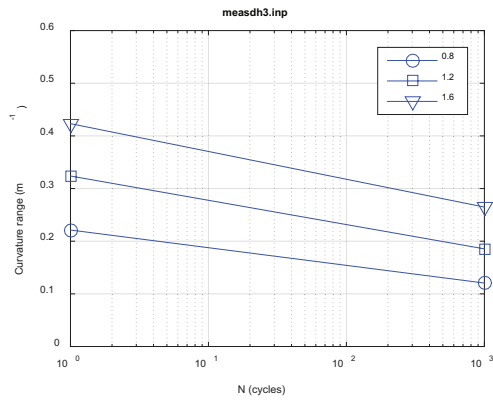


(d)

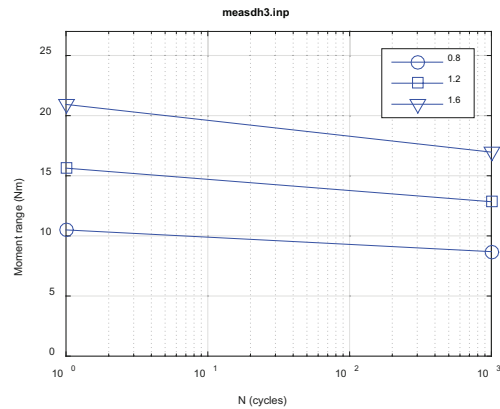


(e)

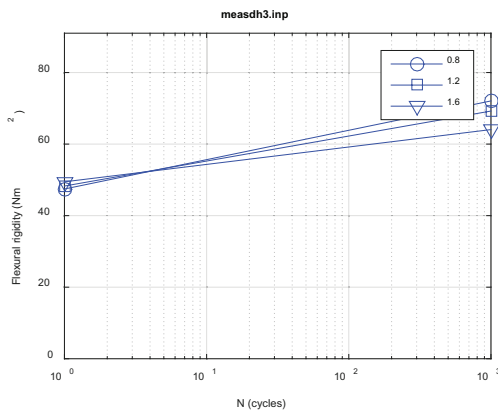
Figure E.25 Variations of (a) curvature range, (b) applied moment range, (c) flexural rigidity, (d) maximum and minimum values of curvature, and (e) maximum and minimum values of as a function of the number of cycles for D9/DH3 (609C7); $N_f = 7.13 \times 10^3$ cycles under ± 35.56 N·m 5 Hz



(a)



(b)



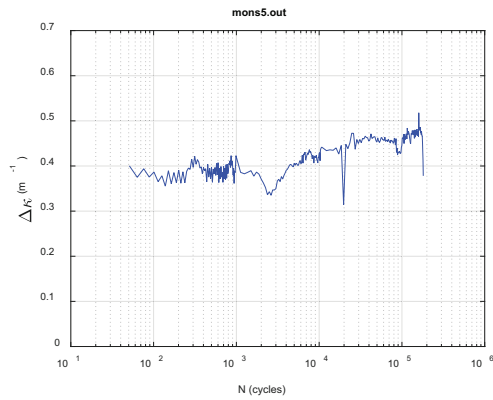
(c)

Figure E.26 Variations of (a) curvature range, (b) applied moment range, and (c) flexural rigidity as a function of number of cycles for D9/DH3 (609C7); $N_f = 7.13 \times 10^3$ cycles under ± 35.56 N·m 5 Hz

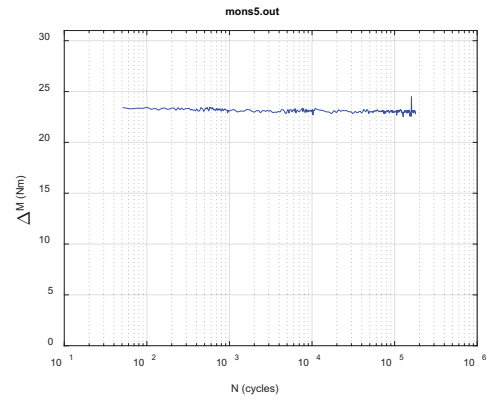
E.10 D10/ S5/ 606C3A (± 12.70 N·m 5 Hz)

The cycle test on D10/S5 (606C3A, 66.8 GWd/MTU burnup, 70–100 μm oxide layer, 750 ppm H content) was conducted under ± 12.70 N·m 5 Hz. The testing condition was the same as that used in DH1, in which failure took place near the edge of the rigid sleeve. The test was repeated to confirm the lifetime and failure position under the same testing condition. In fact, S5 failed at around 1.81×10^5 cycles within the gauge section. The lifetime was therefore shorter than that of DH1. The difference may be related to the preexisting condition, as a higher estimated H content was seen in S5.

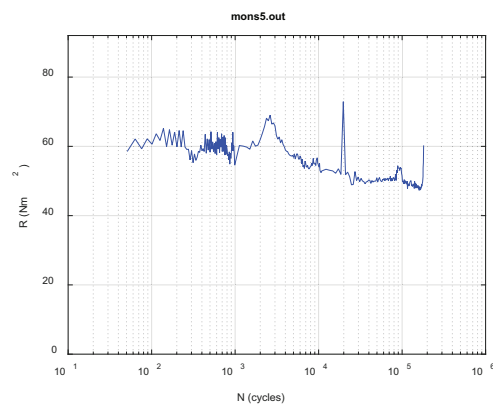
The equivalent decrease in flexural rigidity prior to final failure in both monitoring and measurement can be seen clearly from Figures E.27 and E.28, respectively. Detailed examination showed a certain degree of curvature waveform drift toward the positive direction. The positively biased curvature wave corresponded to an absolute extreme value as great as 0.4 m⁻¹. The level of extreme curvature in D10/S5 was clearly higher than that observed in D6/DH1, which was also partly responsive to the shorter lifetime in the former case.



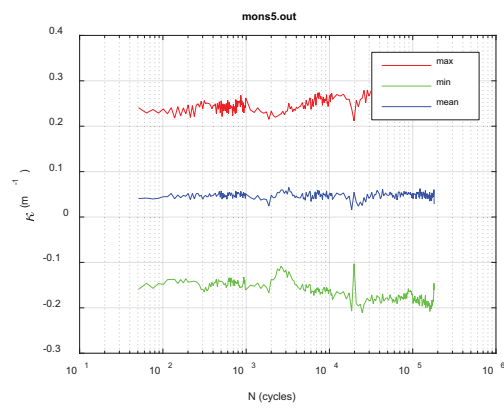
(a)



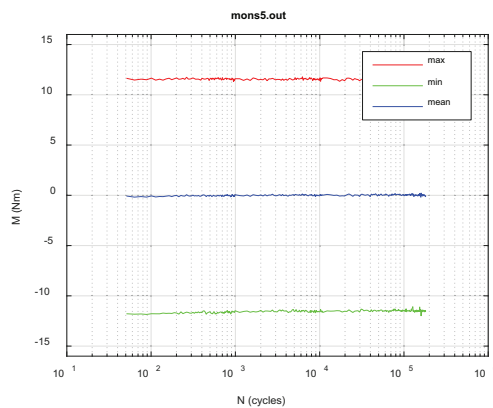
(b)



(c)

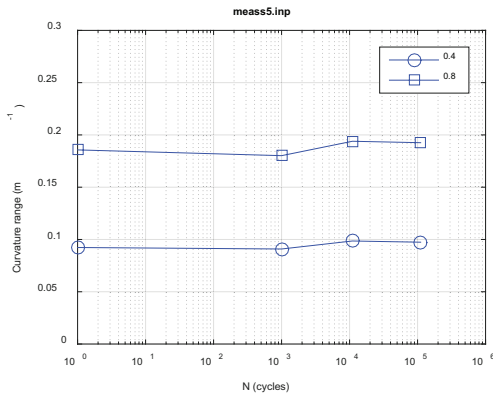


(d)

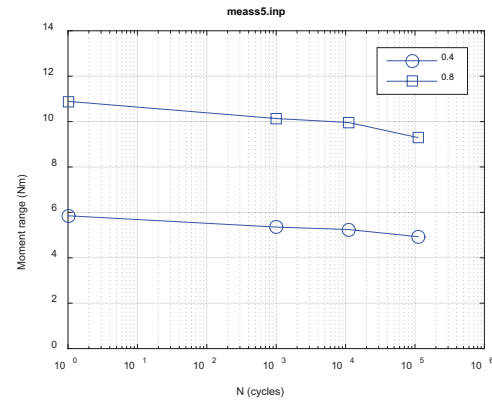


(e)

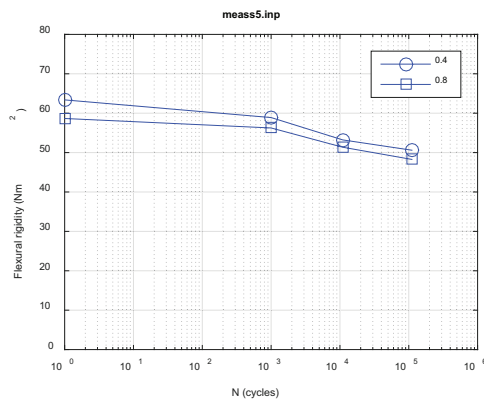
Figure E.27 Variations of (a) curvature range, (b) applied moment range, (c) flexural rigidity, (d) maximum and minimum values of curvature, and (e) maximum and minimum values of moment as a function of the number of cycles for D10/S5 (606C3A); $N_f = 1.81 \times 10^5$ cycles under ± 12.70 N·m 5 Hz



(a)



(b)

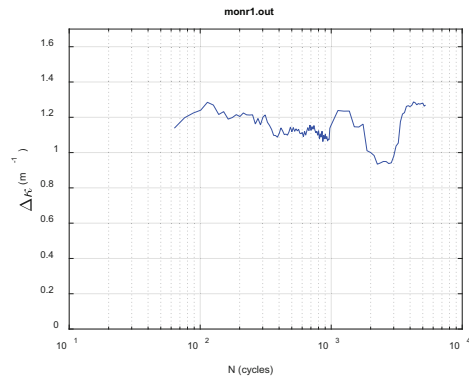


(c)

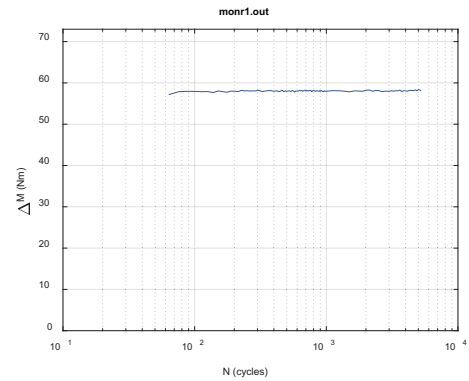
Figure E.28 Variations of (a) curvature range, (b) applied moment range, and (c) flexural rigidity as a function of the number of cycles for D10/S5 (606C3A); $N_f = 1.81 \times 10^5$ cycles under ± 12.70 N·m 5 Hz

E.11 D11/ R1/ 607C4A (± 30.48 N·m 5 Hz)

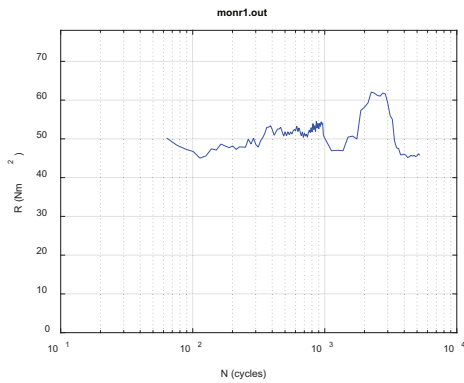
The cycle test on D11/R1 (606C3A, 63.8 GWd/MTU burnup, 70–100 μm oxide layer, 700 ppm H content) was conducted under ± 30.48 N·m 5 Hz. R1 failed at around 5.5×10^3 cycles within the gauge section. Significant fall and rise were observed in online monitoring between 1×10^3 and 4×10^3 cycles, as shown in Figure E.29. On the other hand, the measurements using 0.8, 1.2, and 1.6 mm relative displacement at loading points demonstrated a defined decrease in flexural rigidity, as seen in Figure E.30. Such lifetime was obviously shorter than that expected from the result of D9/DH3, where a longer lifetime was obtained with an even higher moment level. Considering that the H content of D9/DH3, 550 ppm, was much lower than that of D11/R1, it is believed that the preexisting condition of specimens played a certain role in controlling failure in high burnup irradiated rods, as can be seen from the estimated H contents in both rod segments.



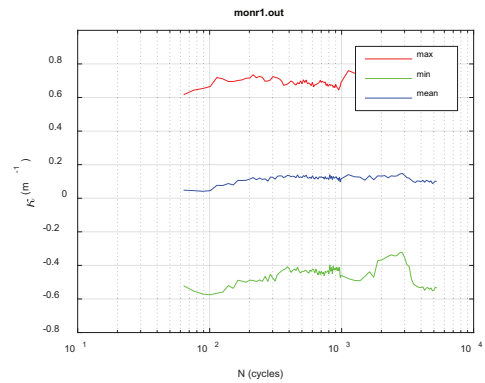
(a)



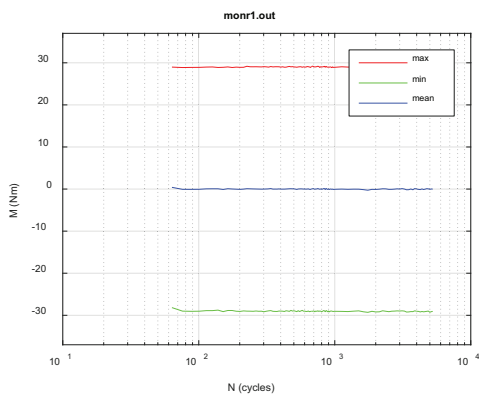
(b)



(c)

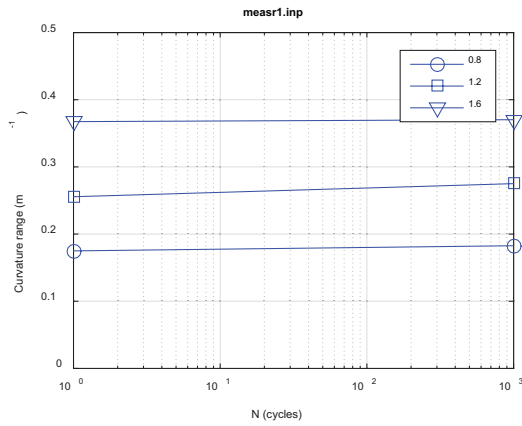


(d)

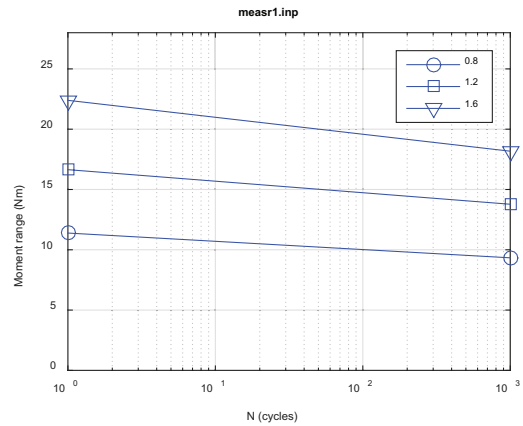


(e)

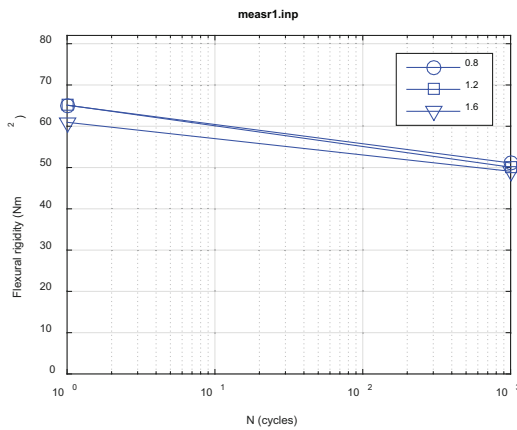
Figure E.29 Variations of (a) curvature range, (b) applied moment range, (c) flexural rigidity, (d) maximum and minimum values of curvature, and (e) maximum and minimum values of moment as a function of the number of cycles for D11/R1 (607C4A); $N_f = 5.5 \times 10^3$ cycles under ± 30.48 N·m 5 Hz



(a)



(b)



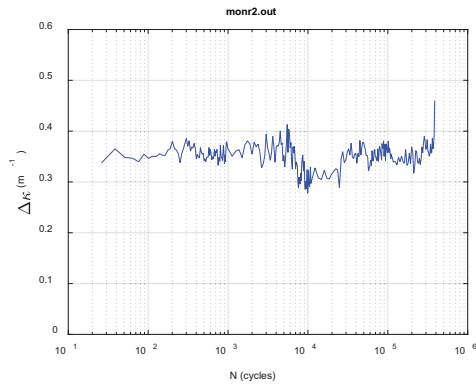
(c)

Figure E.30 Variations of (a) curvature range, (b) applied moment range, and (c) flexural rigidity as a function of the number of cycles for D11/R1 (607C4A); $N_f = 5.5 \times 10^3$ cycles under ± 30.48 N·m 5 Hz

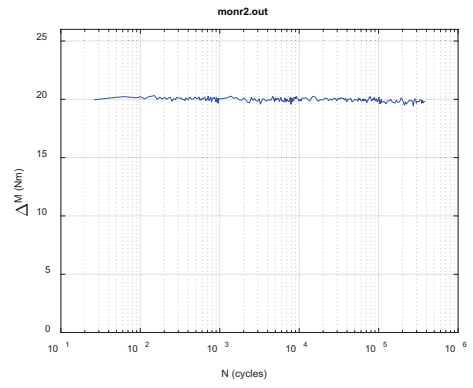
E.12 D12/ R2/ 608C4A (± 11.18 N·m 5 Hz)

The cycle test on D12/R2 (608C4A, 63.8 GWd/MTU burnup, 70–100 μm oxide layer, 700 ppm H content) was conducted under ± 11.18 N·m 5 Hz. R2 failed at around 3.86×10^5 cycles within the gauge section.

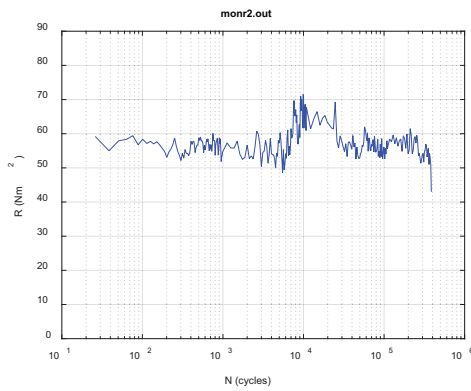
A certain amount of fluctuation was observed in online monitoring and measurement data sets, as illustrated in Figures E.31 and E.32, respectively. This can be seen at around 104 cycles. The peak/valley monitoring indicated that the curvature waveform downshifted throughout the cycle test process. An abrupt drop in flexural rigidity was captured prior to the final failure in both monitoring and measurement.



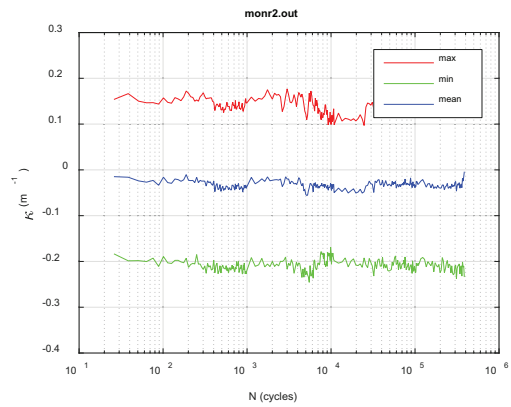
(a)



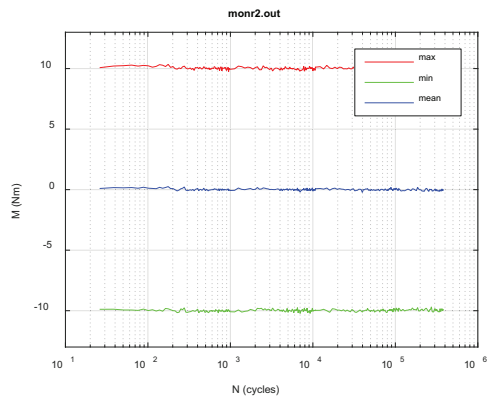
(b)



(c)

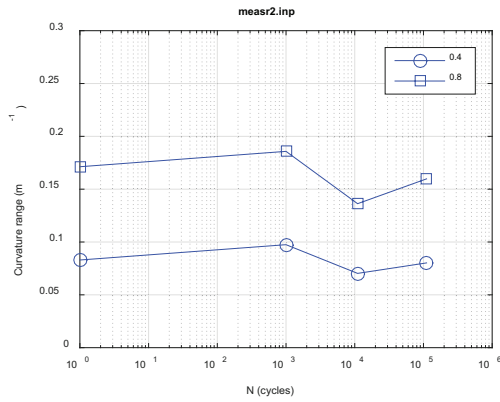


(d)

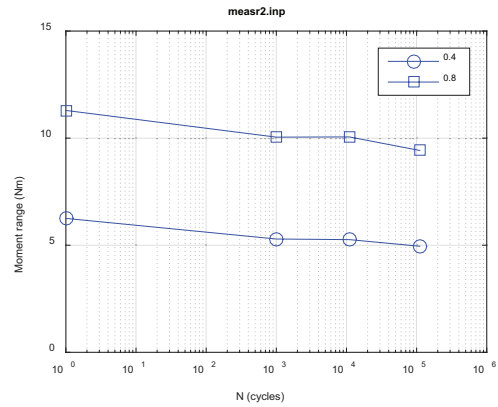


(e)

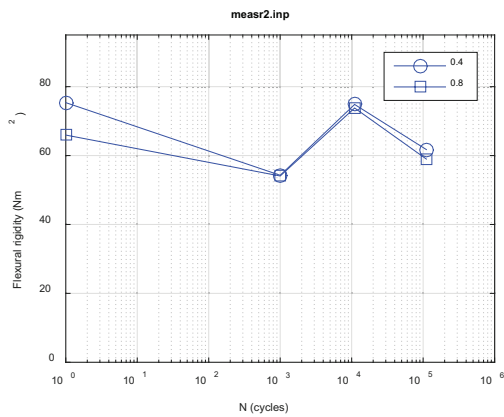
Figure E.31 Variations of (a) curvature range, (b) applied moment range, (c) flexural rigidity, (d) maximum and minimum values of curvature, and (e) maximum and minimum values of moment as a function of the number of cycles for D12/R2 (608C4A); $N_f = 3.86 \times 10^5$ cycles under ± 11.18 N·m 5 Hz



(a)



(b)



(c)

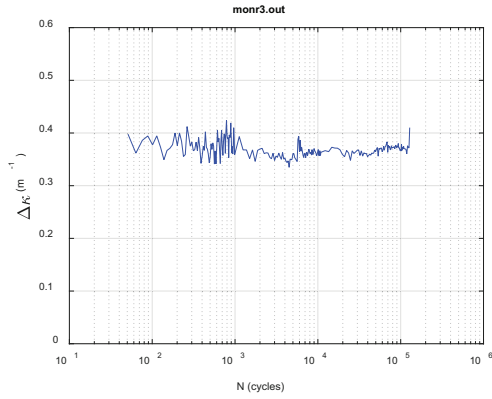
Figure E.32 Variations of (a) curvature range, (b) applied moment range, and (c) flexural rigidity as a function of the number of cycles for D12/ R2 (608C4A); $N_f = 3.86 \times 10^5$ cycles under ± 11.18 N·m 5 Hz

E.13 D13/ R3/ 606B3E (± 13.72 N·m 5 Hz)

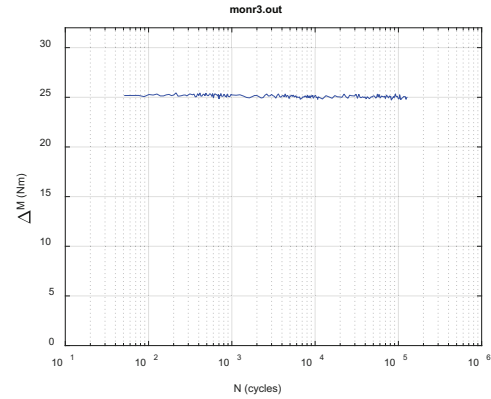
The cycle test on D13/ R3 (606B3E, 66.5 GWd/MTU burnup, 100–110 μm oxide layer, 750 ppm H content) was conducted under ± 13.72 N·m 5 Hz. R3 failed at around 1.29×10^5 cycles within the gauge section.

Testing revealed that the online monitoring rigidity sustained a certain increase prior to the final drop at failure because of the continuous decrease in curvature range, as shown in Figure E.33. The monitoring of the peak and valley of curvature indicated that the decreased curvature range is mainly due to the drop in peak value.

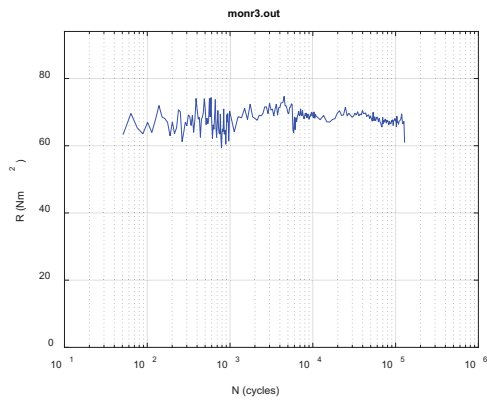
The cause of such single-sided change in curvature waveform during the cyclic test is unknown, but decreased rigidity was seen in the measurement shown in Figure E.34.



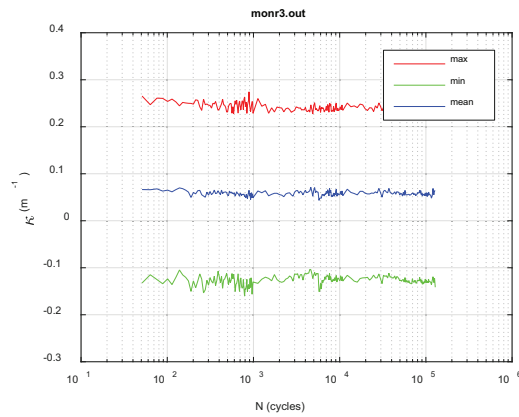
(a)



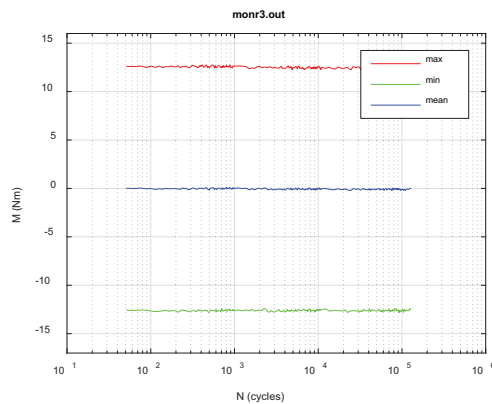
(b)



(c)

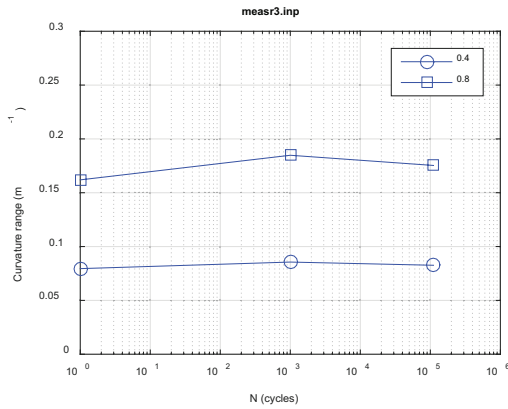


(d)

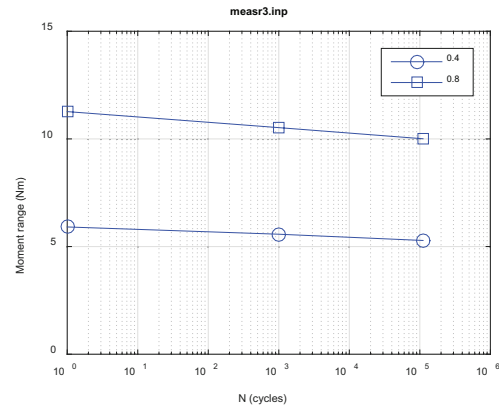


(e)

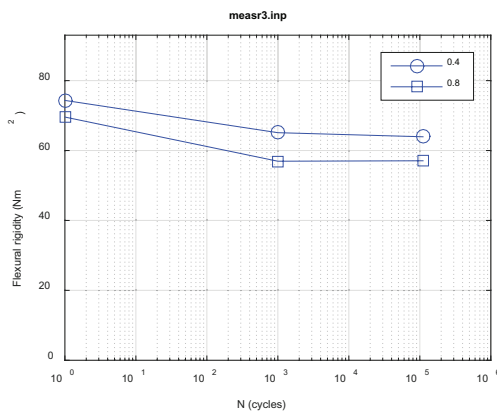
Figure E.33 Variations of (a) curvature range, (b) applied moment range, (c) flexural rigidity, (d) maximum and minimum values of curvature, and (e) maximum and minimum values of moment as a function of the number of cycles for D13/R3 (606B3E); $N_f = 1.29 \times 10^5$ cycles under ± 13.72 N·m 5 Hz



(a)



(b)



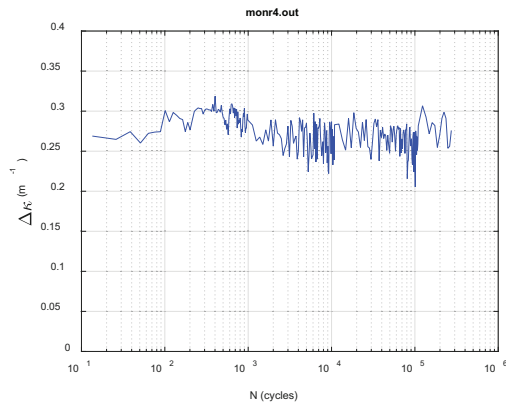
(c)

Figure E.34 Variations of (a) curvature range, (b) applied moment range, and (c) flexural rigidity as a function of the number of cycles for D13/ R3 (606B3E); $N_f = 1.29 \times 10^5$ cycles under ± 13.72 N·m 5 Hz

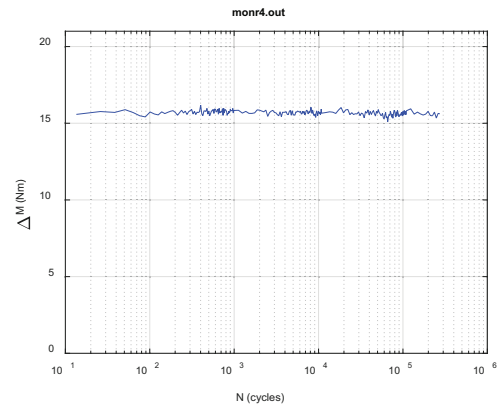
E.14 D14/ R4/ 606B3D (± 8.89 N·m 5 Hz)

The cycle test on D14/R4 (606B3D, 66.5 GWd/MTU burnup, 100–110 μm oxide layer, 750 ppm H content) was conducted under ± 8.89 N·m 5 Hz. This testing condition was the same as that of DM3. The test on R4 was used to generate an additional observation on the same testing condition as DM3. R4 exhibited a relatively short lifetime, with 2.7×10^5 cycles to failure. The short lifetime may have been due to a different preexisting specimen condition, as can be seen from the estimated H content. The H content of R4 was around 750 ppm, while that of DM3 was as low as 550 ppm.

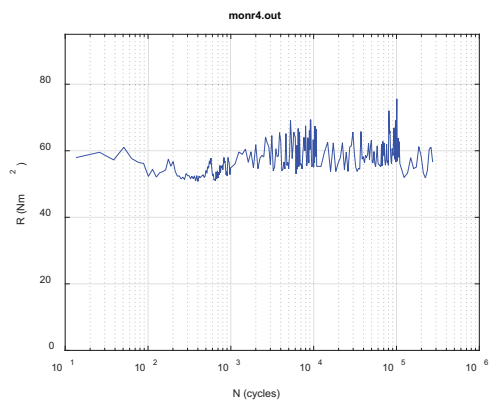
Online monitoring demonstrated a flat response of rigidity with a slight drop prior to final failure, as shown in Figure E.35. The measurement showed that rigidity increased slightly, also as seen in Figure E.36.



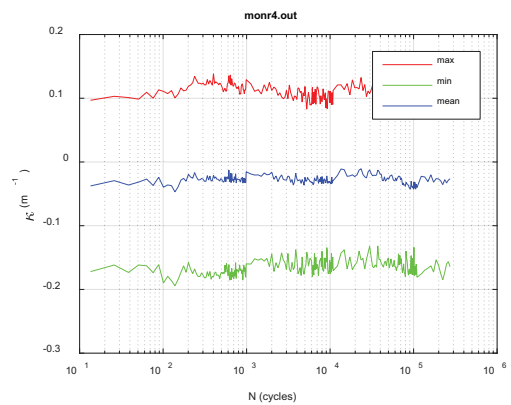
(a)



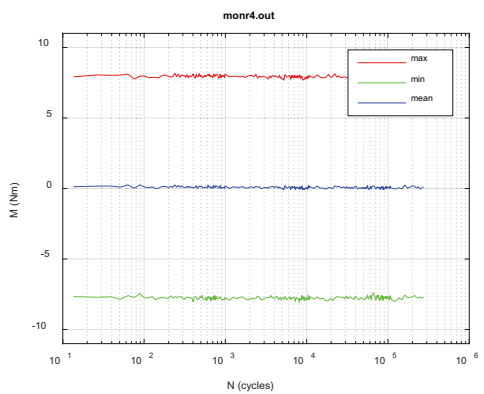
(b)



(c)

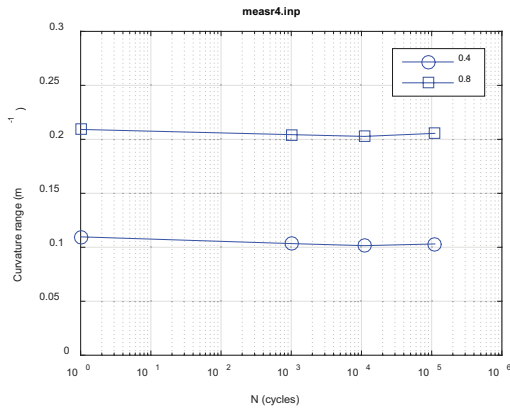


(d)

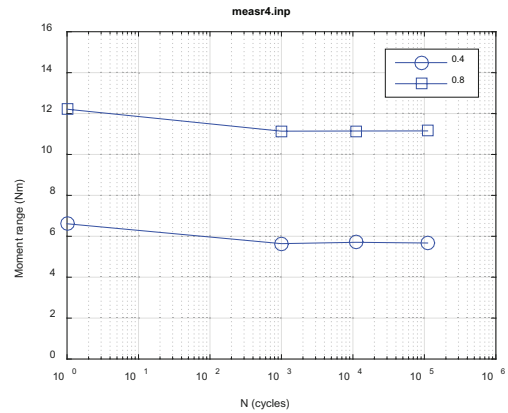


(e)

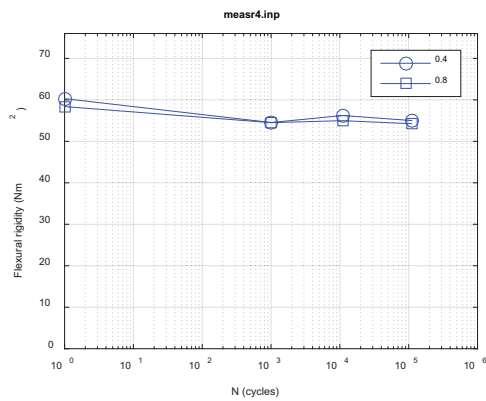
Figure E.35 Variations of (a) curvature range, (b) applied moment range, (c) flexural rigidity, (d) maximum and minimum values of curvature, and (e) maximum and minimum values of moment as a function of the number of cycles for R4 (606B3D); $N_f = 2.7 \times 10^5$ cycles under ± 8.89 N·m 5 Hz



(a)



(b)



(c)

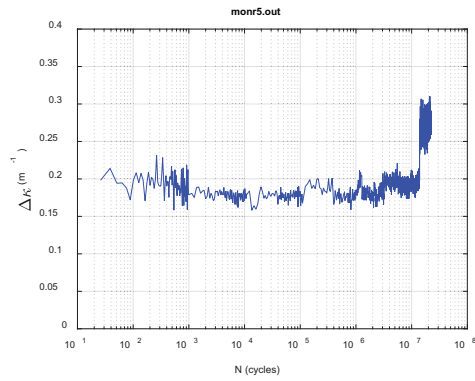
Figure E.36 Variations of (a) curvature range, (b) applied moment range, and (c) flexural rigidity as a function of the number of cycles for R4 (606B3D); $N_f = 2.7 \times 10^5$ cycles under ± 8.89 N·m 5 Hz

E.15 D15/ R5/ 606B3C (± 7.62 N·m 5 Hz)

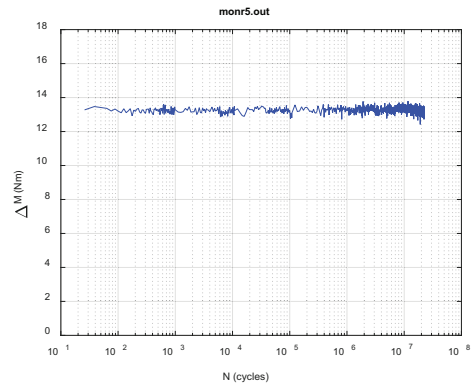
The cycle test on R5 (606B3C, 66.5 GWd/MTU burnup, 100–110 μm oxide layer, 750 ppm H content) was conducted under ± 7.62 N·m 5 Hz. The moment range used for R5 is same as that used in DM1. The test on R5 thus provides the opportunity to examine the variation of fatigue response between different rods. The test on R5 was stopped after 2.23×10^7 cycles had been accumulated because no sign of failure could be seen.

The analysis based on the monitoring data indicated that the flexural rigidity was fairly stable and limited within a range of 40–50 N·m². A drop was observed after the rod was taken off and re-mounted to the testing machine. The reason was not clear at this point, but the rod appeared to be stable in subsequent cycling processes.

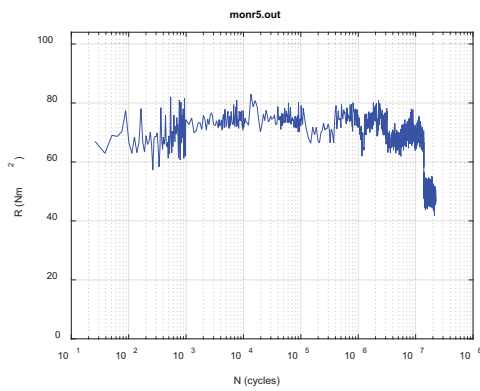
The online monitoring and measurement data are given in Figures E.37 and E.38, respectively.



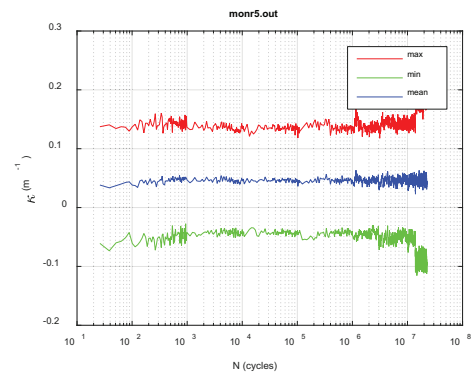
(a)



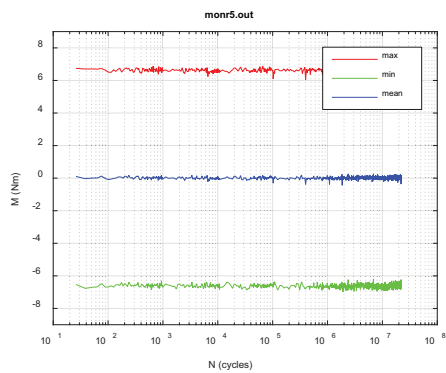
(b)



(c)

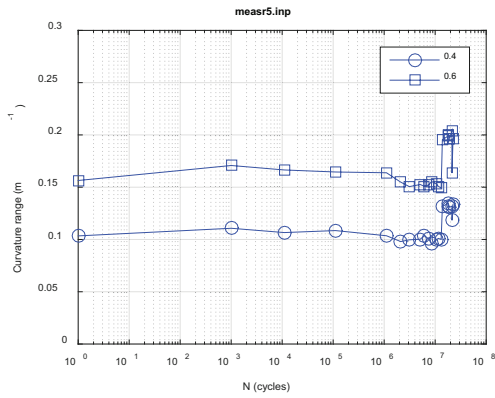


(d)

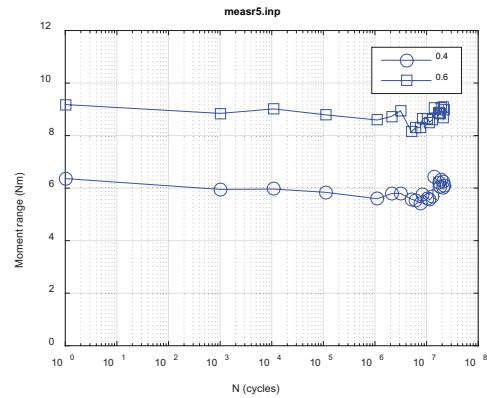


(e)

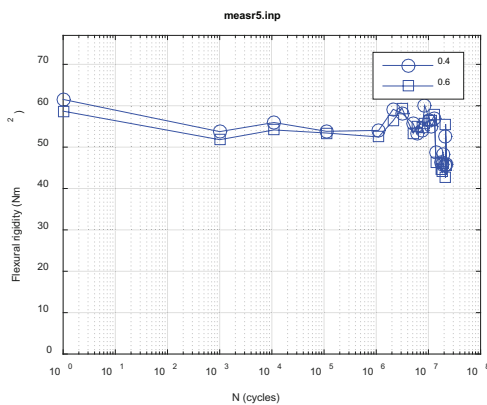
Figure E.37 Variations of (a) curvature range, (b) applied moment range, (c) flexural rigidity, (d) maximum and minimum values of curvature, and (e) maximum and minimum values of moment as a function of the number of cycles for R5 (606B3C); $N = 2.23 \times 10^7$ cycles under ± 7.62 N·m 5 Hz



(a)



(b)



(c)

Figure E.38 Variations of (a) curvature range, (b) applied moment range, and (c) flexural rigidity as a function of the number of cycles for R5 (606B3C); $N = 2.23 \times 10^7$ cycles under ± 7.62 N·m 5 Hz

E.16 HR1 / 607D4C (± 15.24 N·m 5 Hz)

The cycle test on HR1 (607D4C, 63.8 GWd/MTU burnup, 40–44 μm oxide layer, 400 ppm H content) was conducted under ± 15.24 N·m 5 Hz. The moment range used for HR1 is the same as that used in DL1. The test on HR1 thus provides the opportunity to examine the variation of fatigue response between the two rods. The test on HR1 was completed with a lifetime of 4.19×10^4 cycles.

The online monitoring and measurement data are given in Figures E.39 and E.40, respectively.

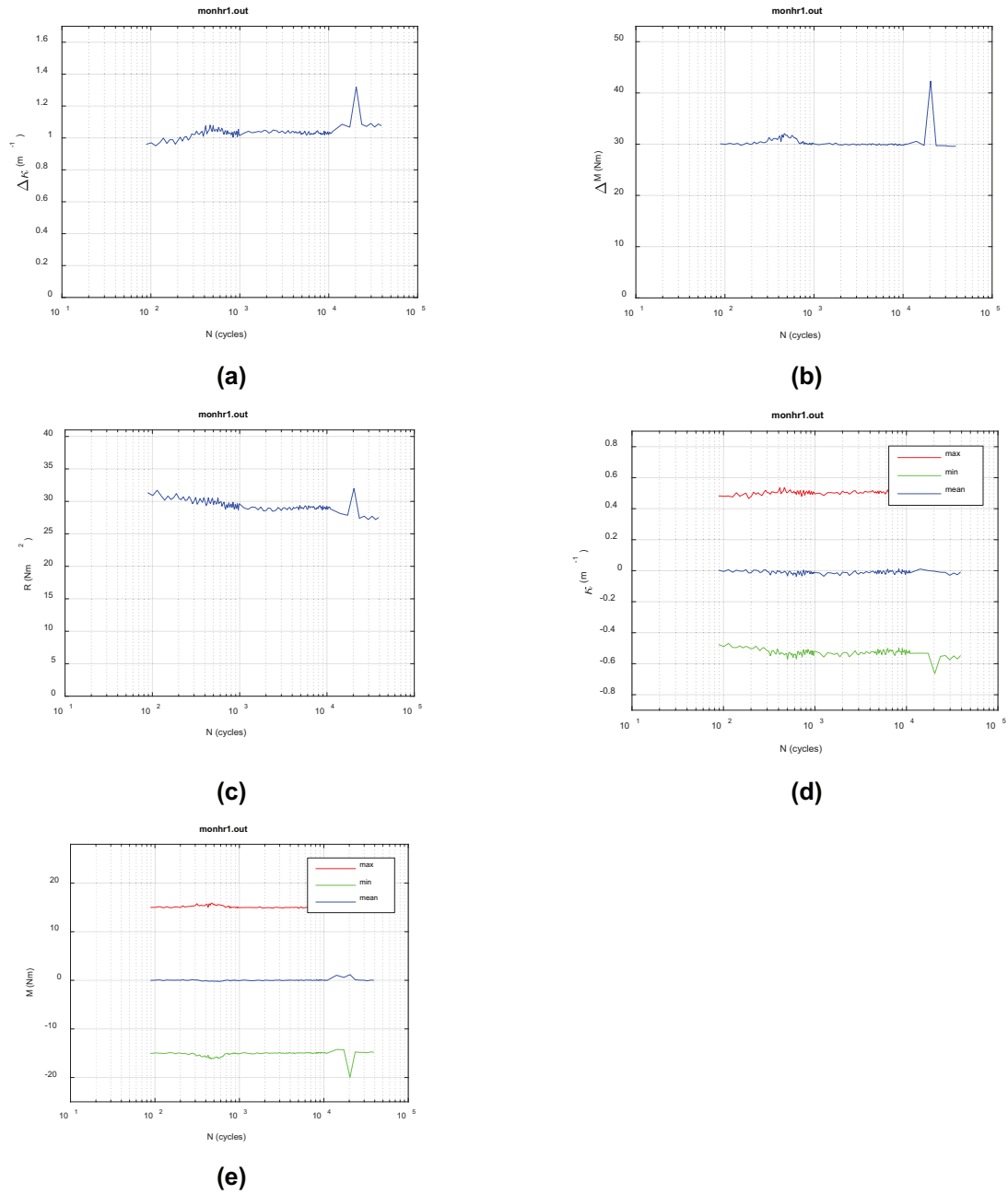
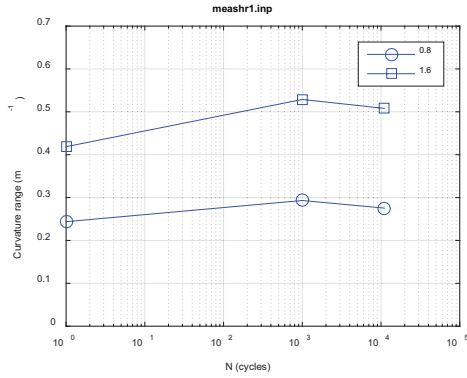
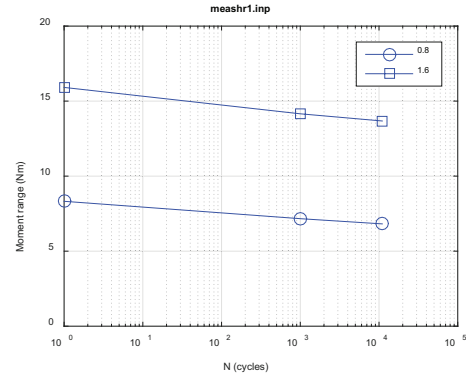


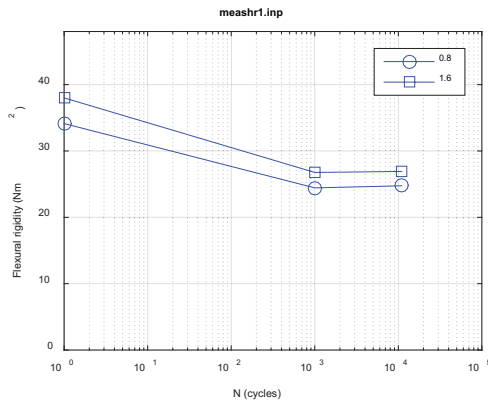
Figure E.39 Variations of (a) curvature range, (b) applied moment range, (c) flexural rigidity, (d) maximum and minimum values of curvature, and (e) maximum and minimum values of moment as a function of the number of cycles for HR1 (607D4C); $N = 4.19 \times 10^4$ cycles under ± 15.24 N·m 5 Hz



(a)



(b)



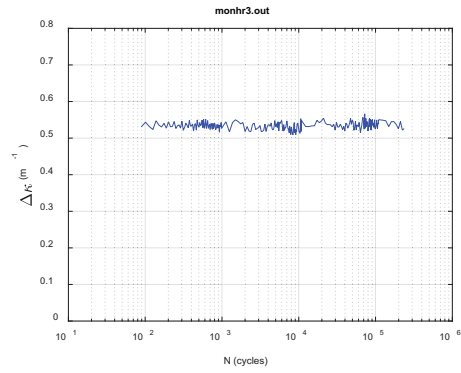
(c)

Figure E.40 Variations of (a) curvature range, (b) applied moment range, and (c) flexural rigidity as a function of the number of cycles for HR1 (607D4C); $N = 4.19 \times 10^4$ cycles under ± 15.24 N·m 5 Hz

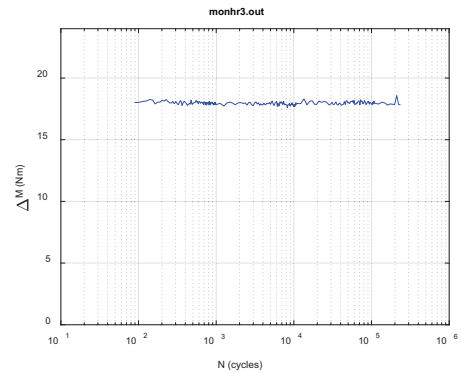
E.17 HR3 / 608D4A (± 10.16 N·M 5 Hz)

The cycle test on HR3 (608D4A, 63.8 GWd/MTU burnup, 40–44 μm oxide layer, 400 ppm H content) was conducted under ± 10.16 N·m 5 Hz. The moment range used for HR3 is same as that used in DL3. The test on HR3 thus provides the opportunity to examine the variation of fatigue response between the two rods. The test on HR3 was completed with a lifetime of 2.44×10^5 cycles.

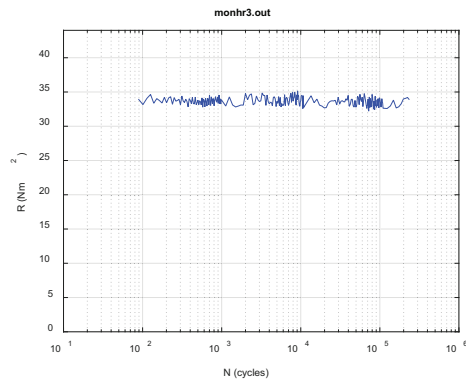
The online monitoring and measurement data are given In Figures E.41 and E.42, respectively.



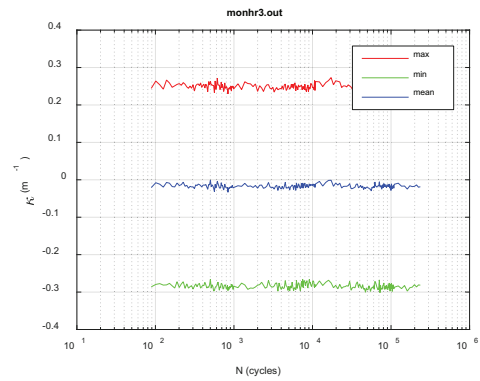
(a)



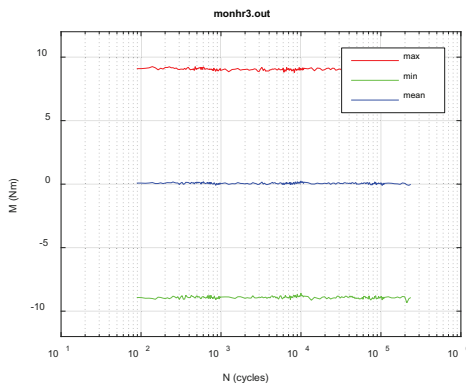
(b)



(c)

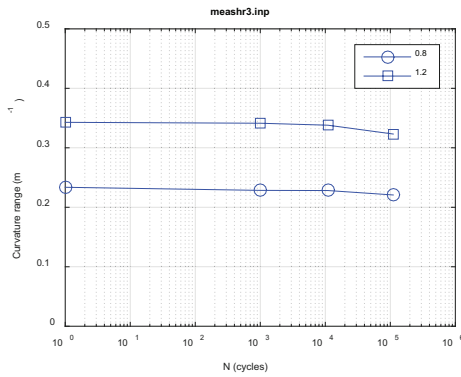


(d)

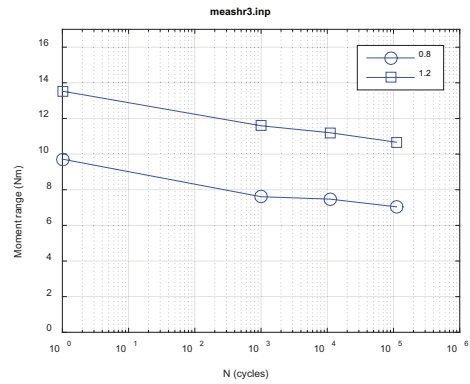


(e)

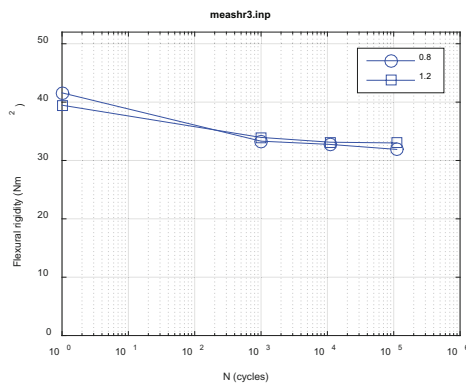
Figure E.41 Variations of (a) curvature range, (b) applied moment range, (c) flexural rigidity, (d) maximum and minimum values of curvature, and (e) maximum and minimum values of moment as a function of the number of cycles for HR3 (608D4A); $N = 2.44 \times 10^5$ cycles under ± 10.16 N·m 5 Hz



(a)



(b)



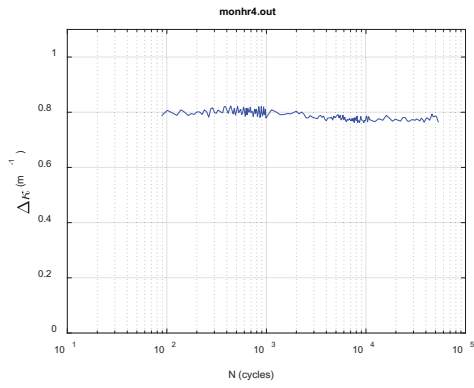
(c)

Figure E.42 Variations of (a) curvature range, (b) applied moment range, and (c) flexural rigidity as a function of the number of cycles for HR3 (608D4A); $N = 2.44 \times 10^5$ cycles under ± 10.16 N·m 5 Hz

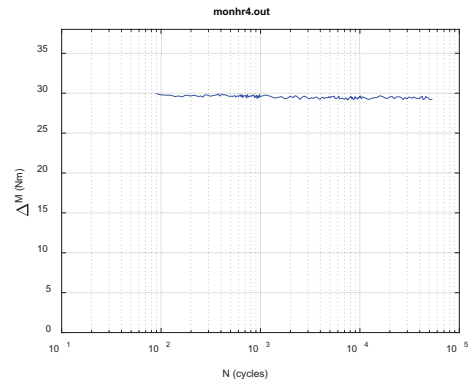
E.18 HR4 / 608D4C (± 16.26 N·M 5 Hz)

The cycle test on HR4 (608D4C, 63.8 GWd/MTU burnup, 40–44 μm oxide layer, 400 ppm H content) was conducted under ± 16.26 N·m 5 Hz. The moment range used for HR4 is same as that used in the follow-up test on HR2. The test on HR4 thus provides the opportunity to examine the variation of fatigue response between the two rods. The test on HR4 was completed with a lifetime of 5.47×10^4 cycles.

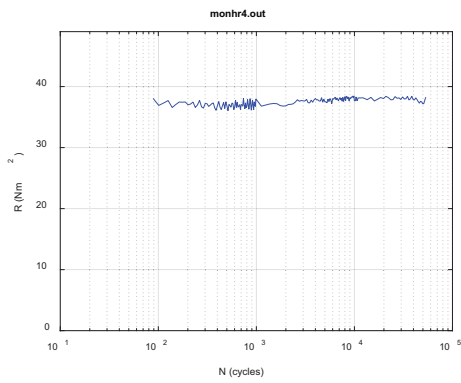
The online monitoring and measurement data are given in Figures E.43 and E.44, respectively.



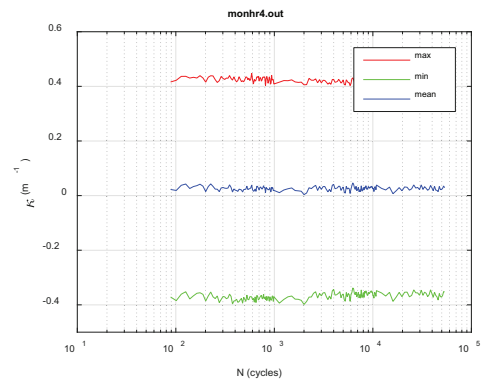
(a)



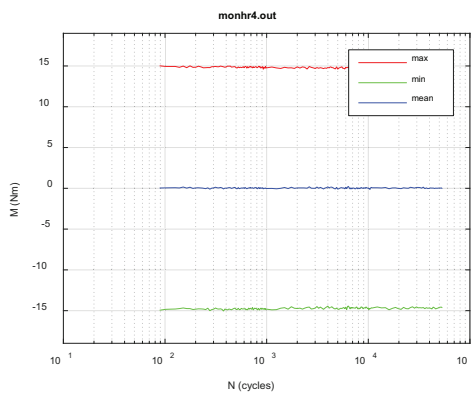
(b)



(c)

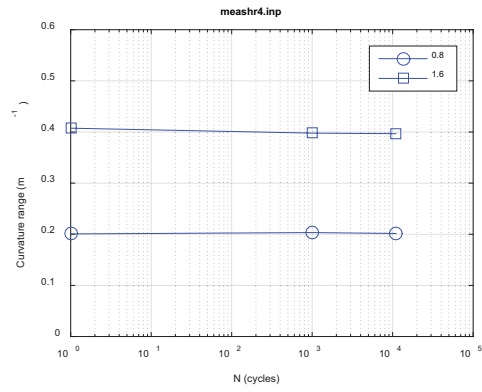


(d)

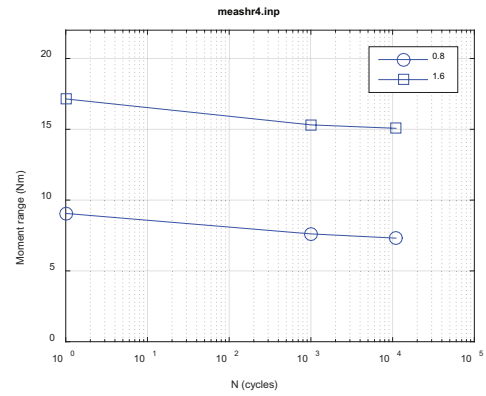


(e)

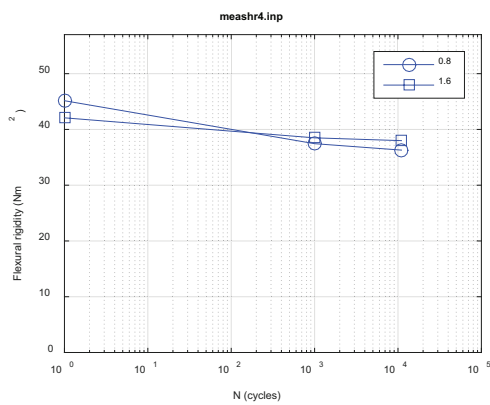
Figure E.43 Variations of (a) curvature range, (b) applied moment range, (c) flexural rigidity, (d) maximum and minimum values of curvature, and (e) maximum and minimum values of moment as a function of the number of cycles for HR4 (608D4C); $N = 5.47 \times 10^4$ cycles under ± 16.26 N·m 5 Hz



(a)



(b)



(c)

Figure E.44 Variations of (a) curvature range, (b) applied moment range, and (c) flexural rigidity as a function of number of cycles for HR4 (608D4C); $N = 5.47 \times 10^4$ cycles under ± 16.26 N·m 5 Hz

APPENDIX F POST-IRRADIATION EXAMINATION (PIE)

APPENDIX F POST-IRRADIATION EXAMINATION (PIE)

F.1 Preparation of specimens

Axial section

PIE on the axial section was conducted for one untested rod segment, on a fractured specimen from static test S2, and on three tested specimens from dynamic tests (one unfailed—DM1, and two fractured—DL3 and DM2).

For the tested and fractured specimen, the preparation of axial cross sections mainly involved the following steps: (1) cut a one-inch segment on the fracture end, (2) mount the segment with the bending plane in horizontal direction and cut the top half away, (3) back-pot the remaining half to keep all the fuel in place, and (4) grind and polish the section to the required finishing of metallography. Examinations were then carried out by using an optical microscope.¹⁸

The section preparation for other segments/specimens was similar to the above procedure. The untested rod segment was taken from a section of the same father fuel rod with same estimated amount of hydrogen content as those in other PIE specimens. The section for a tested and unfailed specimen was taken from the gauge section of the specimen.

Transverse section

PIE on transverse section was conducted only on D3.

The section was prepared by using an approximately 0.25-inch length of cladding cut away from the remaining half of specimen D3 (specimen holder A). The segment was defueled by using hot nitric acid. The defueled cladding was removed from the hot cell and cleaned with water and alcohol in an ultrasonic cleaner. The inside and outside surfaces of the clad were then coated with a thin layer of epoxy. The section was then ground and polished to the required finish for examination using scanning electron microscopy (SEM).

F.2 Untested segment 605D1D

The untested section was prepared one-inch fuel segment from segment 605D1D. Adjacent segments indicated that the estimated hydrogen content is around 400–500 ppm. An optical image of the section is given in Figure F.1a.

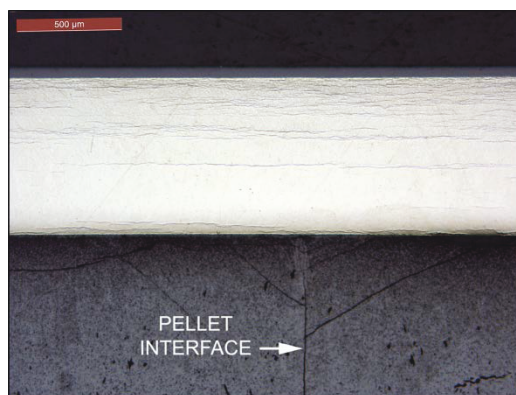
The three dished fuel pellets can be easily identified. Two primary fractures were developed roughly along and normal to the axial direction. A detail study (Figure F.1b) showed that the pellet-to-pellet interface near the edge of dish and the pellet-to-clad interface were fairly close, without any visible gap. Secondary fractures were developed within pellets near the peripheral area close to the pellet-to-clad interfaces. The cavity is also observed around some triple boundaries of pellets and clad.

The parallel axial hydride layers can also be seen clearly over the whole thickness. The axial hydrides are widely spaced in the large middle part of wall. The density of hydrides becomes much higher toward the outside of clad and in the clad-pellet interface area. The axial hydride layers are sizable, and in the middle of clad wall, the layers can be over 1000 μm .

The outside surface of clad is covered with a continuous thin oxide layer that is measured at about 75 μm .



(a)



(b)

Figure F.1 Optical images for (a) overall axial cross section and (b) enlarged area A

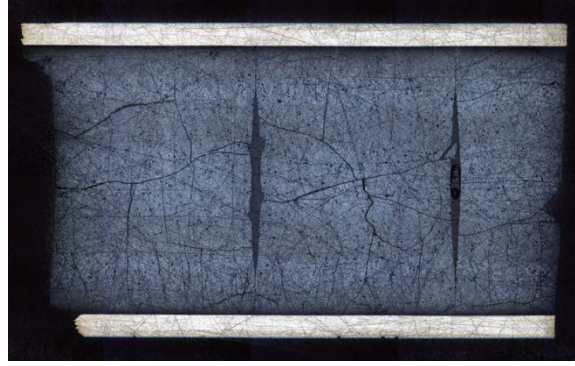
F.3 Fractured in static test S2/605D1E

S2 was based on segment 605D1E, with an estimated hydrogen and oxide layer thicknesses of 400 ppm and 40–70 μm , respectively. S2 failed in a dynamic test ($\pm 30.48 \text{ N}\cdot\text{m}$, 5Hz) after three cycles of unidirectional loading.

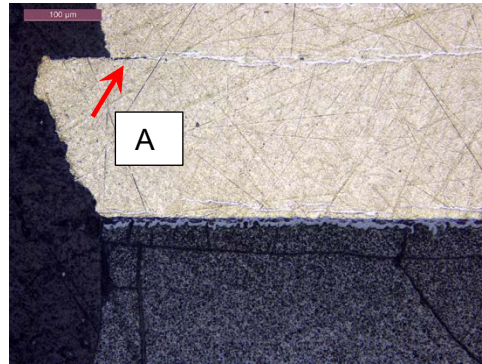
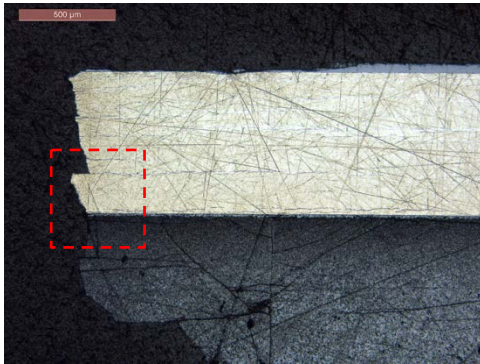
The failure occurred at the pellet-to-pellet interface, as seen in Figure F.2. The primary fractures in the same range of pellet size can be seen clearly. Unlike to the fractures in the untested fuel segment, the axial fractures did not align, but tilted toward the axial direction.

The pellet-to-clad interface appeared tight. The fracture surface in clad exhibited a zigzag pattern on the back and front sides of specimen. The unique pattern resulted from the combination of brittle fracture of hydrides and ductile failure of metal matrix under tension. Delamination can be seen over hydride layers near the fracture surface.

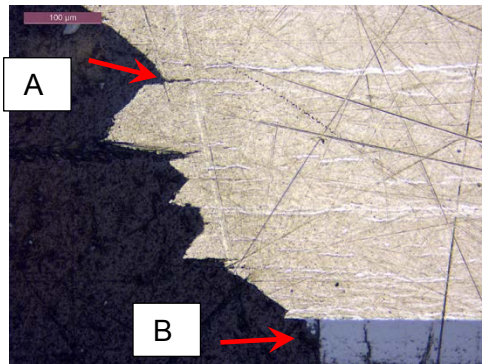
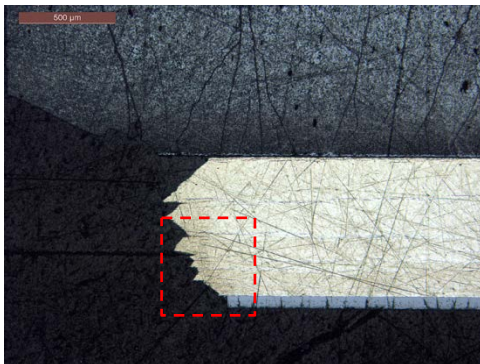
In addition, spalling and cracking of surface oxide layer can be seen on the back and front sides.



(a)



(b)



(c)

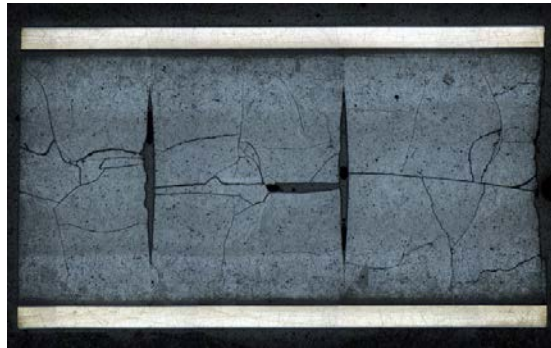
Figure F.2 (a) Axial cross section of S2/605D1E, (b) fracture surface near back side of rod and an enlarged area, and (c) fracture surface near front side of rod and an enlarged area; label A shows delamination, and label B illustrates cracking of the oxide layer

F.4 Tested and un-failed in dynamic test D4/DM1/605D1C

D4/DM1 was based on segment 605D1C, with estimated hydrogen and oxide layer thicknesses of 500 ppm and 40–70 μm . D4 survived 1.1×10^7 cycles of dynamic test under $\pm 7.62 \text{ N}\cdot\text{m}$, 5Hz) without failure.

The axial section of a one-inch segment is shown in Figure F.3. The primary fractures in the same range of pellet size can be seen clearly. The fracture size and fracture pattern were similar to those observed for untested fuel segments. The figure also illustrates closely spaced fractures that interacted and resulted in slender fragments aligned in the axial direction. One fragment was pulled out in the grinding process.

The pellet-to-clad interface appeared tight. The axial hydrides are similar to those observed in the untested fuel segment, as they were neighboring segments in the same father fuel rod. In addition, the surface oxide layer was intact, even though the specimen experienced a high-cycle reversible bending fatigue test.



(a)



(b)



(c)

Figure F.3 (a) Axial cross section of DM1/605D1C, (b) back side of rod, and (c) front side of rod

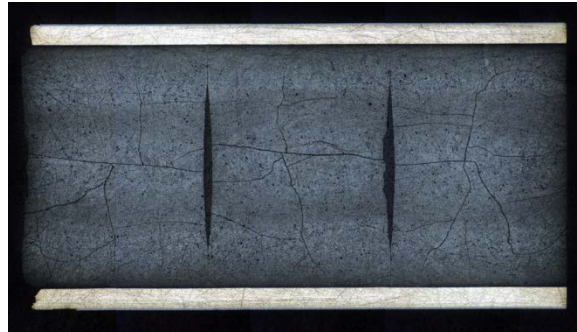
F.5 Fractured in dynamic test D3/ DL3/ 605C10A

Axial section

D3/DL3 was based on segment 605C10A with an estimate hydrogen content of 550 ppm and an oxide layer of 70–100 μ m. As mentioned earlier, D3 was tested under ± 10.16 N·m 5Hz with a lifetime 10^6 cycles.

The optical image of axial cross section is presented in Figure F.4 . The fracture surface was located at the left side at a pellet-to-pellet interface. It can be seen that the development of irradiation-induced primary fractures was similar to that of the specimens examined above.

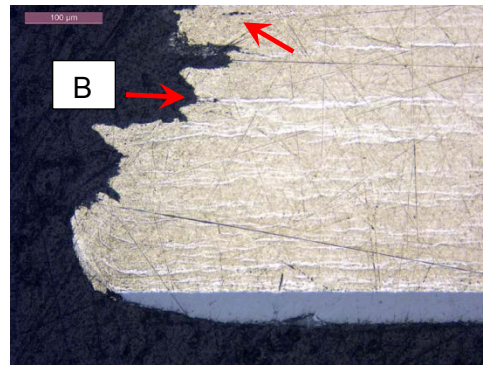
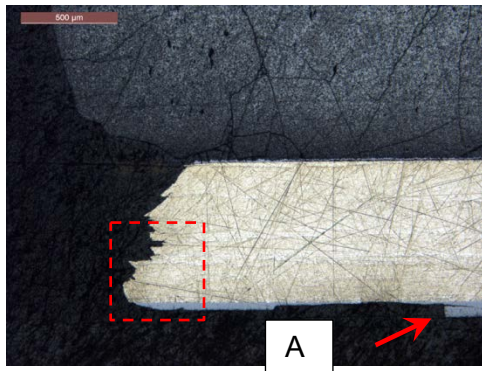
The part of clad fracture surface near the front side was not preserved. The fractured surface near back side of specimen is highly serrated. The cavity can be seen near the fracture that may have resulted from the hydride cracking since they are coincident with the axial hydride layers. Spalling of outside oxide layer was again seen near the fracture surface.



(a)



(b)



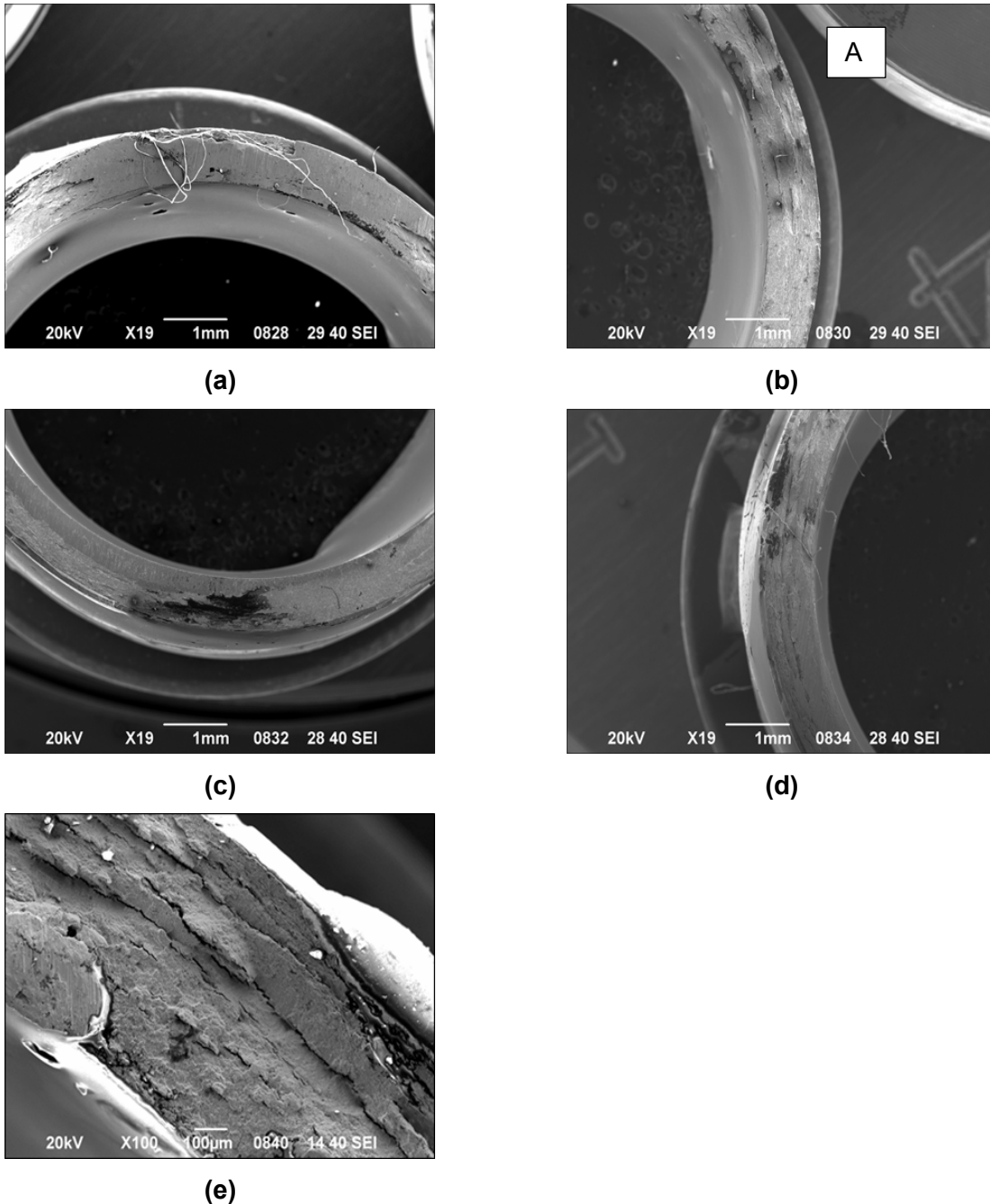
(c)

Figure F.4 (a) Axial cross section of D3/605C10A, (b) fracture surface near front side of rod, and (c) fracture surface near back side of rod and an enlarged area; label A indicates spalling of the oxide layer, and label B shows the cavity aligning with the axial hydride layer

Transverse section

A set of SEM images is presented in Figures F.5 (a–d), which show the different areas of the transverse cross section. The images corresponding to the 12 and 6 o'clock positions represent

the maximum alternating stress areas of the rods subjected to potential crack initiation. The cladding was apparently flattened at the maximum stress areas after the fracture, and the failure origin was not preserved. However, the areas near the 3 and 9 o'clock positions of the fractured surface revealed a clear laminate structure, as seen in Figure F.5(e). This may be related to the preexisting circumferential hydride structure in the HBU Zry-4 cladding.



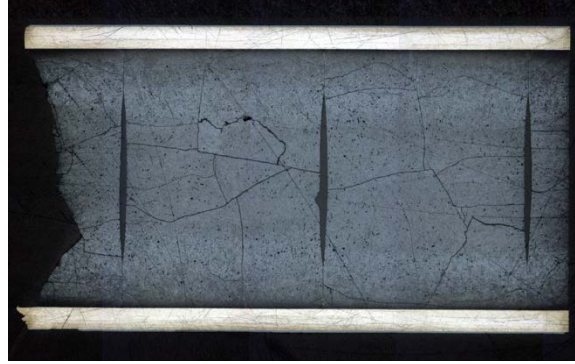
**Figure F.5 SEM images of clad cross section based on the defueled D3:
(a) 12 o'clock (reference mark), (b) 3 o'clock, (c) 6 o'clock, (d) 9 o'clock, and
(e) enlarged area (labeled A)**

F.6 Fractured in dynamic test D5/ DM2/ 605D1B

D5/DM2 was based on segment 605D1B, with an estimated hydrogen content of 550 ppm and an oxide layer of 40–70 μ m. As mentioned above, D5 was tested under ± 9.14 N·m 5Hz with a lifetime of 2.3×10^6 cycles.

The optical image of the axial cross section is shown in Figure F.6 . The fracture surface was located at the left side within a pellet. The primary fractures, which were the same size scale as a pellet, were similar to those revealed in the specimens examined above. The primary fractures were preexisting and may result from the radiation effect because they were similar in size and pattern to those observed in untested fuel segments. One primary fracture system normal to the axial direction of fuel corresponded to the fracture surface of fuel and thus served as a main contributor to the failure.

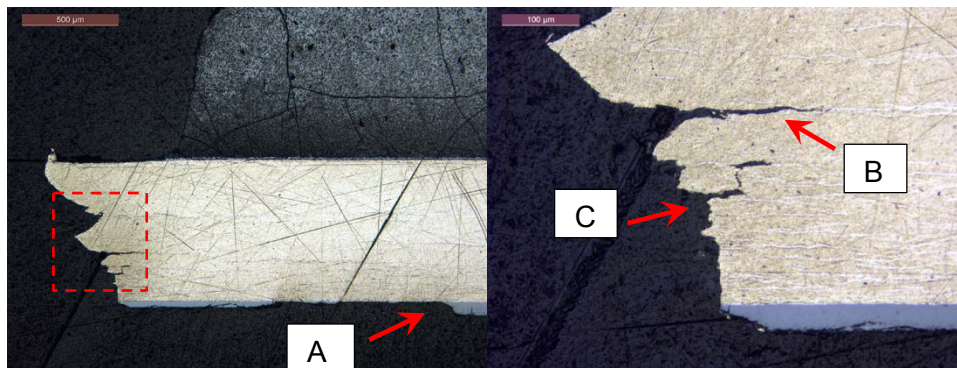
The part of the clad fractured surface near the front side was flattened due to the impacts of fracture surfaces before the machine reached the predetermined termination condition. The part of fractured surface near the back side of specimen was preserved and exhibited a highly serrated fractured surface. The delamination and connected cavities can be seen near the fracture, which may be attributed to the hydride cracking since they are coincident with the axial hydride layers. Spalling of outside the oxide layer was seen near the fractured surface.



(a)



(b)



(c)

Figure F.6 (a) Axial cross section of D5/605D1B, (b) fractured surface near the front side of the rod, and (c) fractured surface near the back side of the rod and an enlarged area; label A indicates the spalling of the oxide layer; label B indicates the delamination, and label C shows the connected cavities aligning with the axial hydride layers

APPENDIX G VERIFICATION OF CURVATURE MEASUREMENT

APPENDIX G VERIFICATION OF CURVATURE MEASUREMENT

G.1 TECHNICAL APPROACH

Several methods were used to verify and justify the three-LVDT curvature measurement. The work was conducted in an out-of-cell study by using surrogate fuel rods; the observations and suggestions are presented in this appendix. While the curvature measurement based on disk-head LVDTs is used as a baseline, the following methods are examined:

- 1) **Use of the chisel head in the curvature measurement.** It is believed that the main contribution of curvature measurement deviating from the ideal measurement condition is caused by the disk head. The contact point may be shifted during the measurement, which may change the probe or sensor spacing (h) used in the equation of curvature. Use of the chisel head is expected to reduce such effect.
- 2) **Use of sensor spacing adjustment (Δh) in the curvature measurement with disk-head.** The adjustment or correction was based on the assumption of the equal gauge length in both the peak and the valley of one data block (two cycles of input). The half gauge length $Lg/2$ was calculated according to the equation as follows:

$$Lg/2 = \sqrt{2d_2 / \kappa}$$

where d_2 is the middle LVDT reading in m, and κ is the calculated curvature in m^{-1} .

- 3) **Use of strain based on curvature measurement.** The outer fiber strain of the bending rod can be obtained according to the measured curvature (either disk head or chisel head):

$$\varepsilon = \kappa y_{\max},$$

where y_{\max} is the maximum distance to the neutral axis of the test rod and is measured by the radius of the rod.

- 4) **Use of strain gauge.** The gauge-based strain is obtained according the following equation,

$$\varepsilon = 10^6 / (0.25V_{BR}AS_g),$$

where ε is micro strain or $\mu\varepsilon$, V_{BR} is the bridge voltage, A is the amplification, and S_g is the gauge factor.

- 5) **Calculation of strain based on given flexural rigidity.** The curvature can be estimated by

$$\varepsilon = (M / EI)y_{\max}$$

where M is the moment amplitude input and EI is given rigidity of the rod.
EI= 42.8 Nm², y_{max} = 4.78 mm for a SS304 rod.

G.2 EXPERIMENTAL TECHNIQUE

Two surrogate fuel rods were used.

- 1) The first rod was made of SS304 tube-only and tested under small amplitude input. The tests were conducted using sine waveforms under displacement control at 0.05Hz and load control at 5Hz. Tested items include disk-head LVDT, chisel-head LVDT, and strain gauge.
- 2) The second was made of polycarbonate rod and was tested in a large amplitude input under displacement. A ramping waveform and a 0.05 Hz sine wave were tested. Disk head, chisel -head, and strain gauge were investigated.

The tests using ramping wave followed the procedure established in the static test, and those using 0.05 and 5Hz sine waves followed the dynamic test procedure.

A P3 strain indicator and recorder and a strain signal conditioning amplifier 2310B were used. Two types of strain gauges (Micro-Measurements, Raleigh, NC) were identified for this study, and the gauge factors are given in Table G.1. The setups of surrogate rods with the strain gauge mounted are shown in Figures G.1 and G.2.

Table G.1 Strain gauges used in out-cell verification tests

Surrogate rod	Strain gauge designation	Gauge factor
SS304 surrogate rod	EA-06-250BF-350	2.055 +/- 0.5%
Polycarbonate rod	CEA-06-125UW-350	2.095+/-0.5%

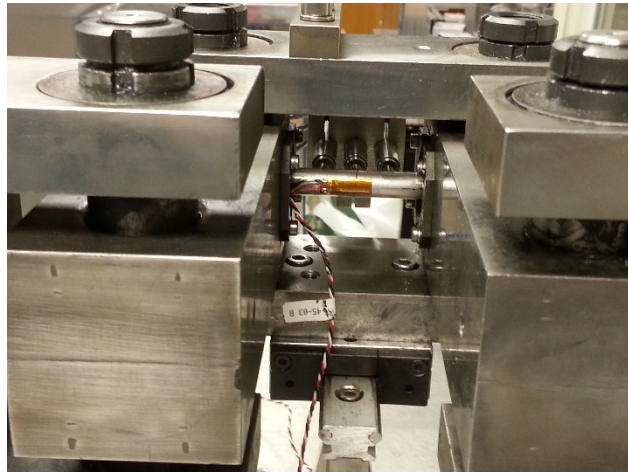


Figure G.1 Setup of SS304 surrogate rod with strain gauge mounted in CIRFT testing

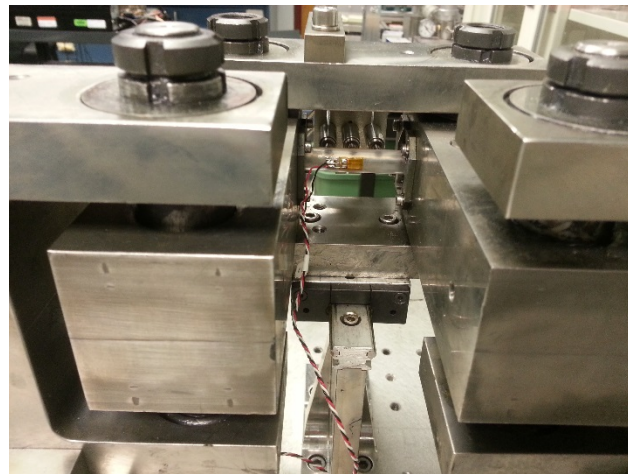


Figure G.2 Setup of polycarbonate surrogate rod with strain gauge mounted in CIRFT testing

G.3 RESULTS ON SS304 SURROGATE ROD

The proposed curvature correction was tested against several established methods, including curvature measurement, using a chisel type probe and a strain gauge.

G.3.1 Chisel type probe as calibration method

Testing on surrogate rod SS30402 was conducted at 0.05 Hz and 5 Hz to simulate the static and dynamic loading (Table G.2).

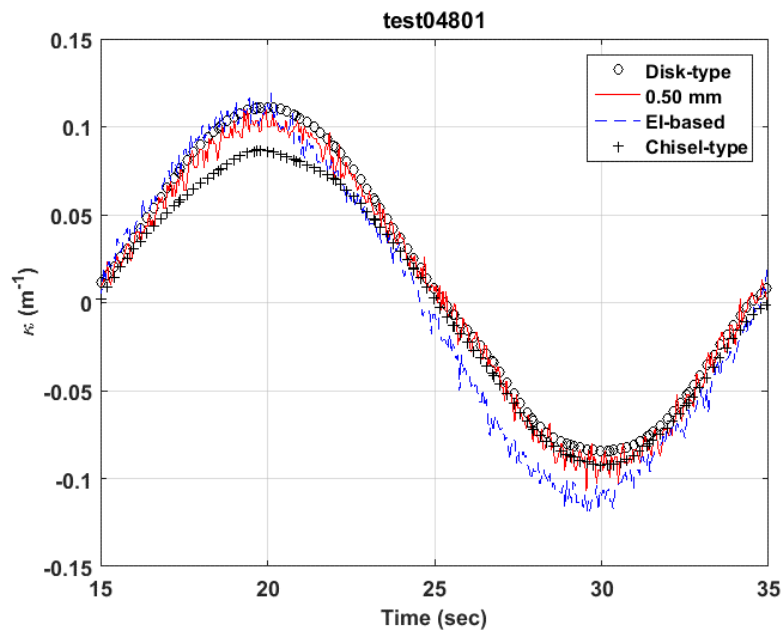
Table G.2 Testing condition of surrogate rod SS30402 with disk and chisel types

No.	pk1 (mm, N)	pk2 (mm, N)	Frequency	Cycles	Sum	LVDT type
44	-0.4	0.4	0.05	3		Flat disk, D6
45	-0.6	0.6	0.05	3		Flat disk, D6
46	-0.8	0.8	0.05	3		Flat disk, D6
47	-75	75	5	500	500	Flat disk, D6
48	-0.4	0.4	0.05	3		Flat disk, D6
49	-0.6	0.6	0.05	3		Flat disk, D6
50	-0.8	0.8	0.05	3		Flat disk, D6
51	-100	100	5	500	1000	Flat disk, D6
52	-0.4	0.4	0.05	3		Flat disk, D6
53	-0.6	0.6	0.05	3		Flat disk, D6
54	-0.8	0.8	0.05	3		Flat disk, D6
55	-125	125	5	500	1500	Flat disk, D6
56	-0.4	0.4	0.05	3		Chisel, D6
57	-0.6	0.6	0.05	3		Chisel, D6
58	-0.8	0.8	0.05	3	0	Chisel, D6
59	-75	75	5	500	500	Chisel, D6
60	-0.4	0.4	0.05	3		Chisel, D6
61	-0.6	0.6	0.05	3		Chisel, D6
62	-0.8	0.8	0.05	3		Chisel, D6
63	-100	100	5	500	1000	Chisel, D6
64	-0.4	0.4	0.05	3		Chisel, D6
65	-0.6	0.6	0.05	3		Chisel, D6
66	-0.8	0.8	0.05	3		Chisel, D6
67	-125	125	5	500	1500	Chisel, D6

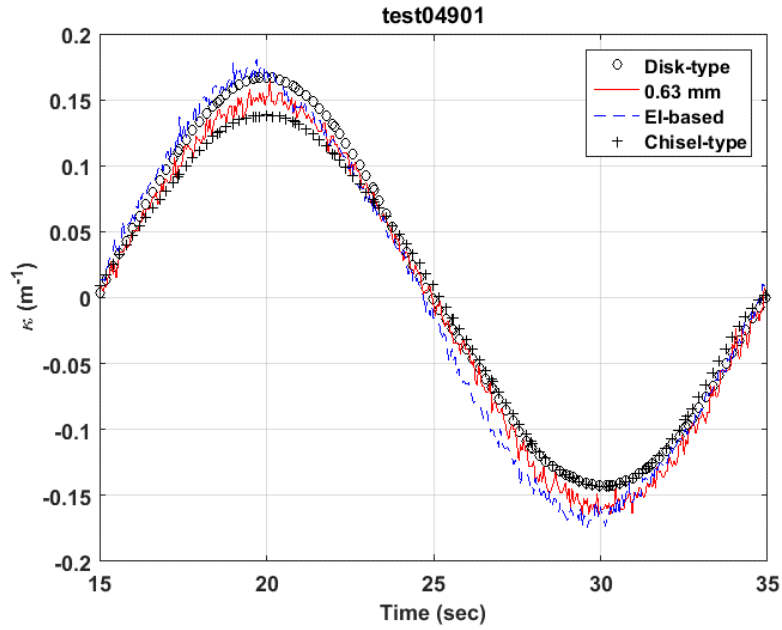
The curvature values based on the disk-type probe and the corrected values are presented in the Figures G.3–G.6, along with those based on flexural rigidity (EI) and the chisel type probe. The major observations can be summarized as follows,

- 1) Measurement with the chisel type probe showed uncertainty in curvature; no defined trend can be seen in the measured curvatures as compared to those using the disk-type probe.

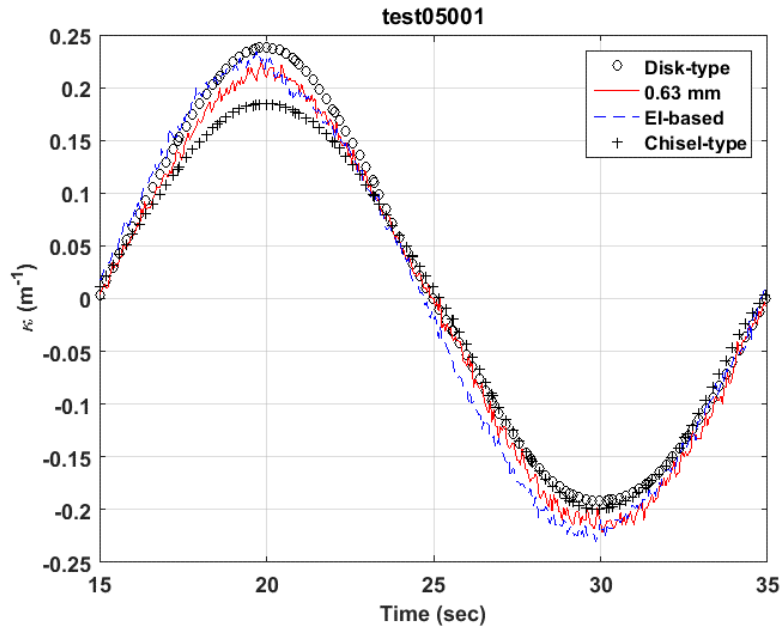
- 2) The tests with the chisel- and disk-type probes were not conducted concurrently. The probe contact condition was changed in the session when the probe was changed, and the three LVDTs were remounted. The sensor spacing was sensitive to the change of contact condition.
- 3) The corrected curvature was shown to be close to the EI-based curvature.
- 4) Spacing correction (Δh) seemed to exhibit a trend to increase with the level of displacement input (disp1 on the side of motor 1). However, a large variance of correction was seen near the small displacement.
- 5) The level of correction was also far less than those based on the calibration of the chisel-type probe (2.40 or 2.90 mm).



(a) 0.4 mm

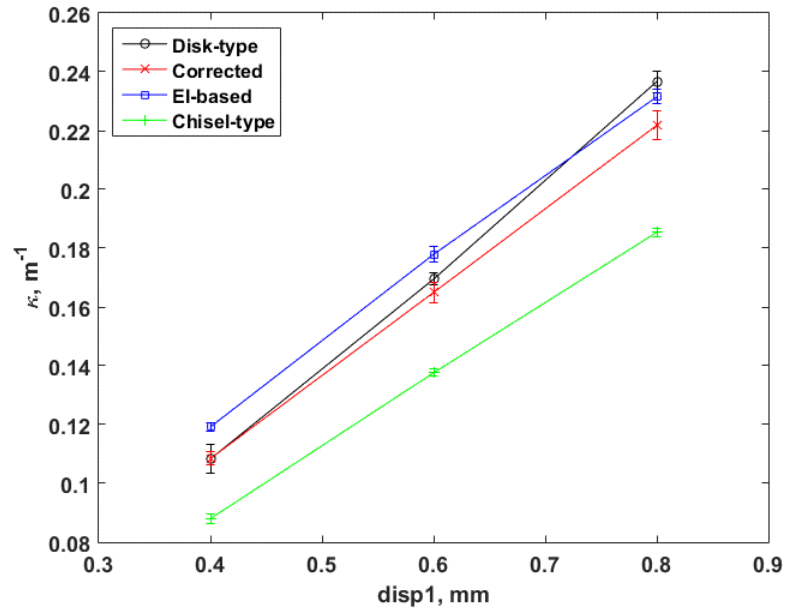


(b) 0.6 mm

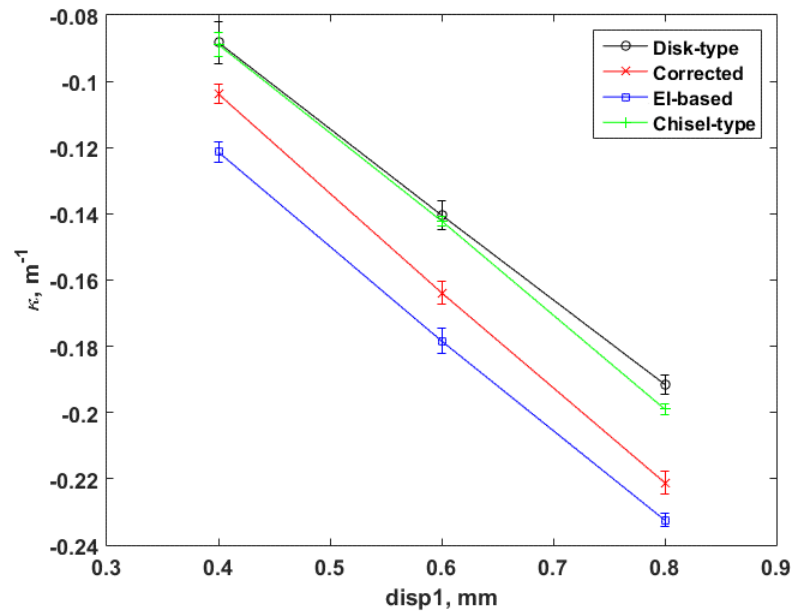


(c) 0.8 mm

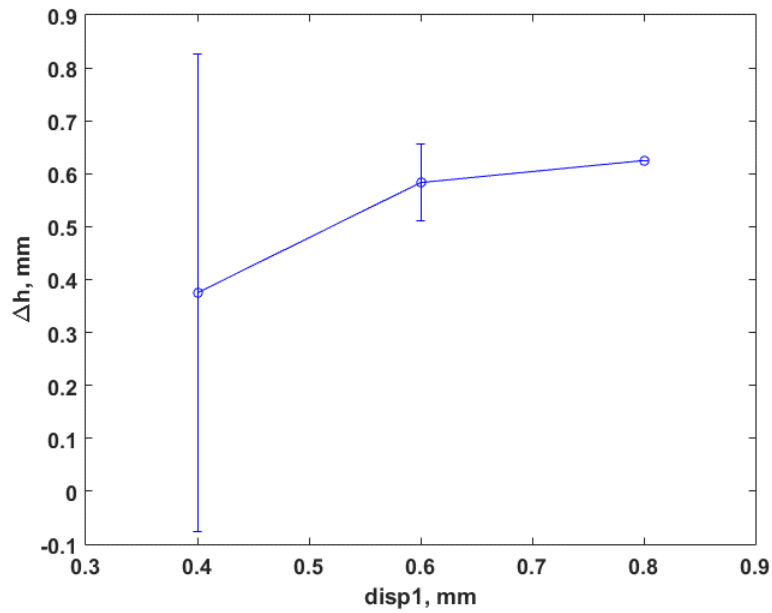
Figure G.3 Curvature curves based on disk-type probe, corrected, EI-based, and chisel-type probe, for 0.05 Hz displacement at loading point of U-frame arm: (a) 0.4 mm, (b) 0.6 mm, and (c) 0.8 mm. $EI=42.8 \text{ Nm}^2$



(a) Peak

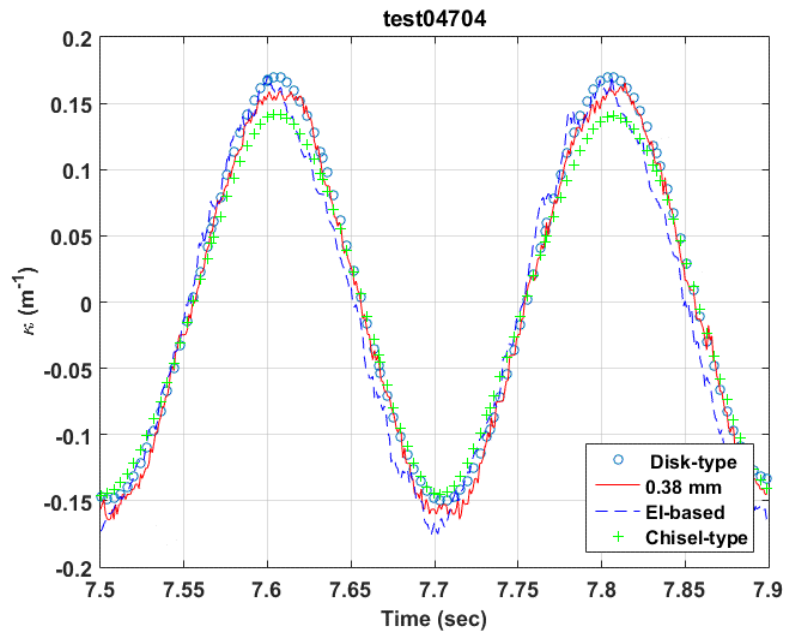


(b) Valley

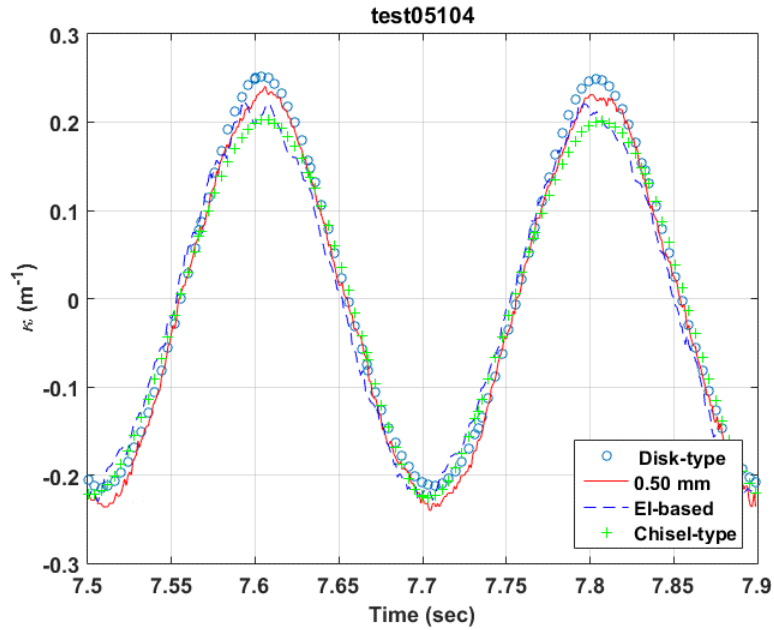


(c) Spacing correction

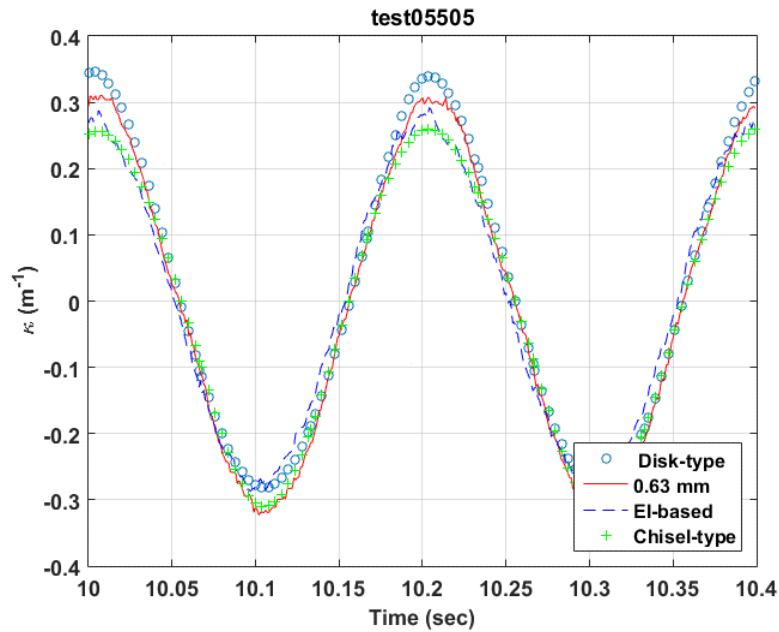
Figure G.4 (a) Peak and (b) valley responses of curvature waveform, and (c) spacing corrections under various disp1 amplitudes at 0.05Hz



(a) 75N

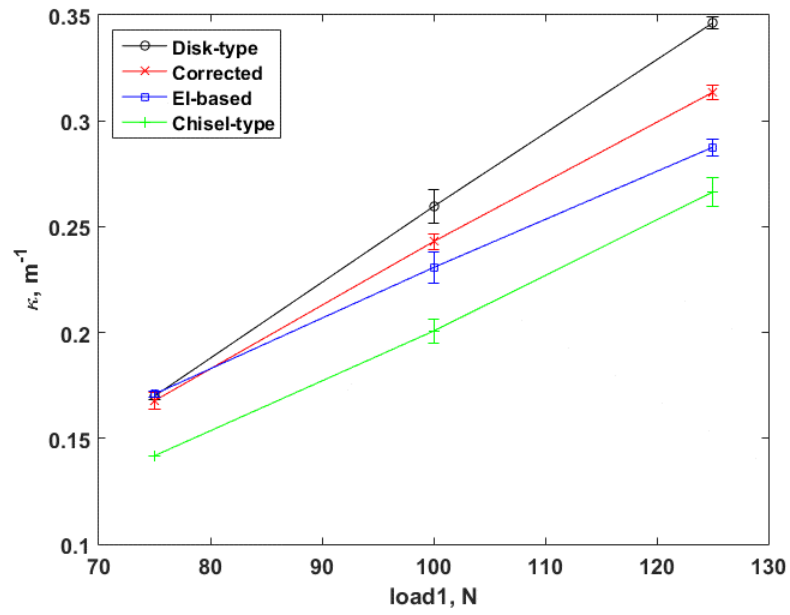


(b) 100N

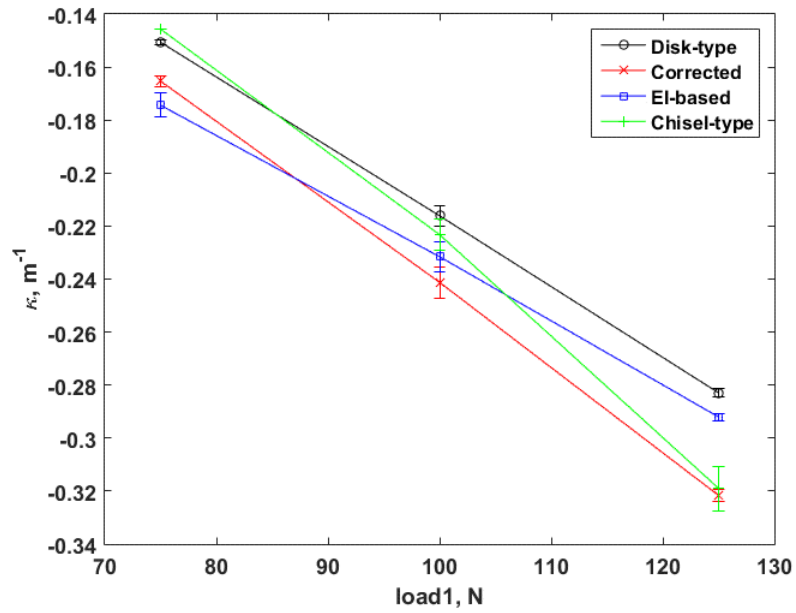


(c) 125N

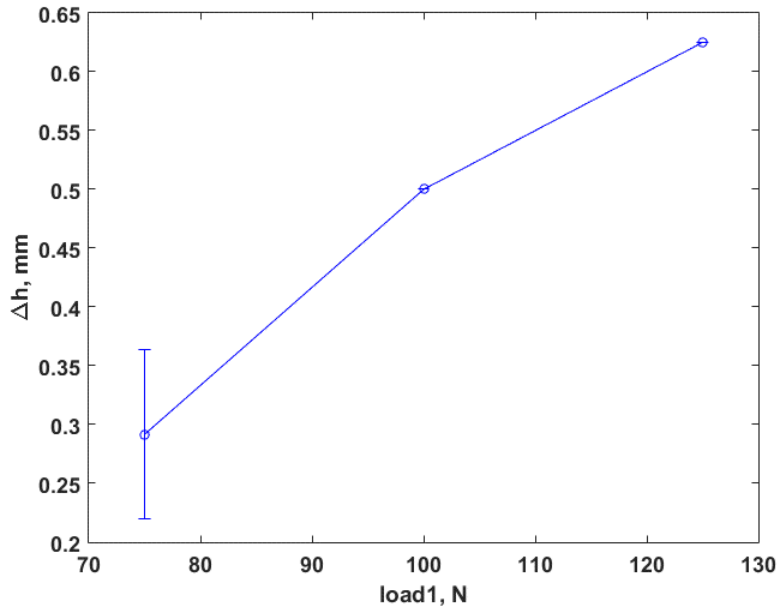
Figure G.5 Curvature curves based on disk-type probe, corrected, EI-based, and chisel-type probe for 5 Hz load at loading point of U-frame arm: (a) 75 N, (b) 100 N, and (c) 125 N. $EI=42.8 \text{ Nm}^2$



(a) Peak



(b) Valley



(c) Spacing correction

Figure G.6 (a) Peak and (b) valley responses of curvature waveform, and (c) spacing corrections under various load1 amplitudes at 5Hz

G.3.2 Strain gauge as calibration method

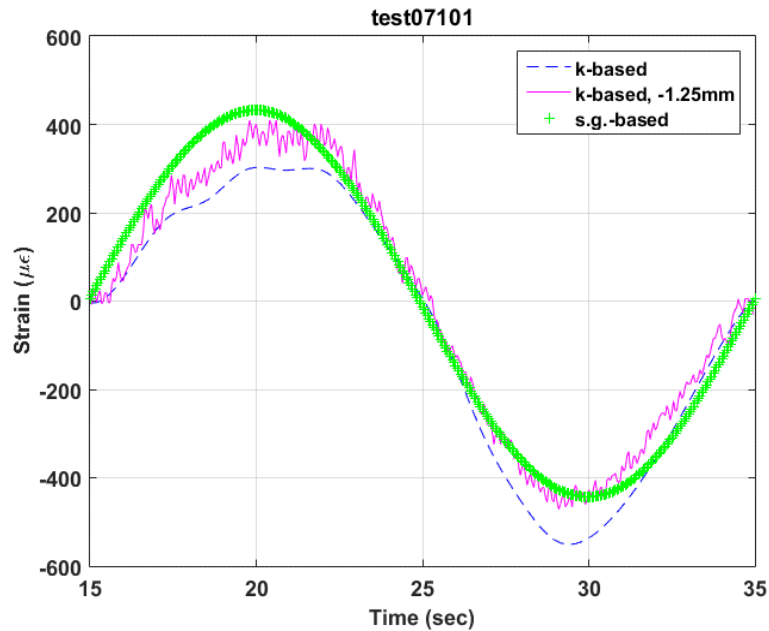
The strain gauge was installed on the surface of the bending rod opposite to the three LVDTs, as shown in Figure 1. The test conditions using the 0.05 Hz sine wave with varying amplitudes are presented in Table 3. The strains were acquired in items 71–73 using a P3 strain indicator and recorder (Vishay Micro-Measurement, Raleigh, NC) and in items 81–84 using a strain signal conditioning amplifier 2310B (Vishay Micro-Measurement, Raleigh, NC).

Table G.3 Test condition with strain gauge installed

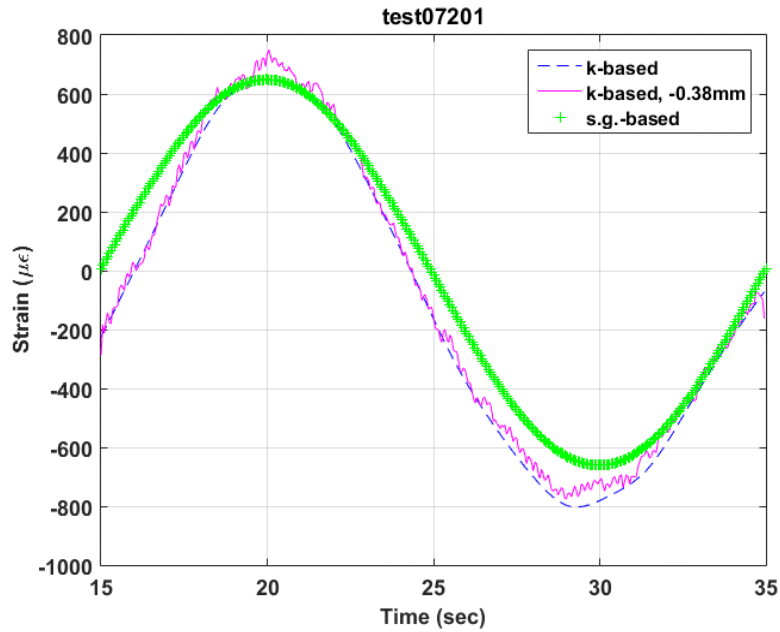
No.	pk1 (mm, N)	pk2 (mm, N)	Frequency	Cycles	LVDT type
71	-0.4	0.4	0.05	3	Flat disk, D5
72	-0.6	0.6	0.05	3	Flat disk, D5
73	-0.8	0.8	0.05	3	Flat disk, D5
81	-0.4	0.4	0.05	3	Flat disk, D5
82	-0.6	0.6	0.05	3	Flat disk, D5
83	-0.8	0.8	0.05	3	Flat disk, D5
84	-100	100	5	500	Flat disk, D5

The curvatures measured using three LVDTs were converted into the maximum strain at the outer fiber of the bending rod. The results of test items 71–73 are illustrated in Figures G.7 and G.8.

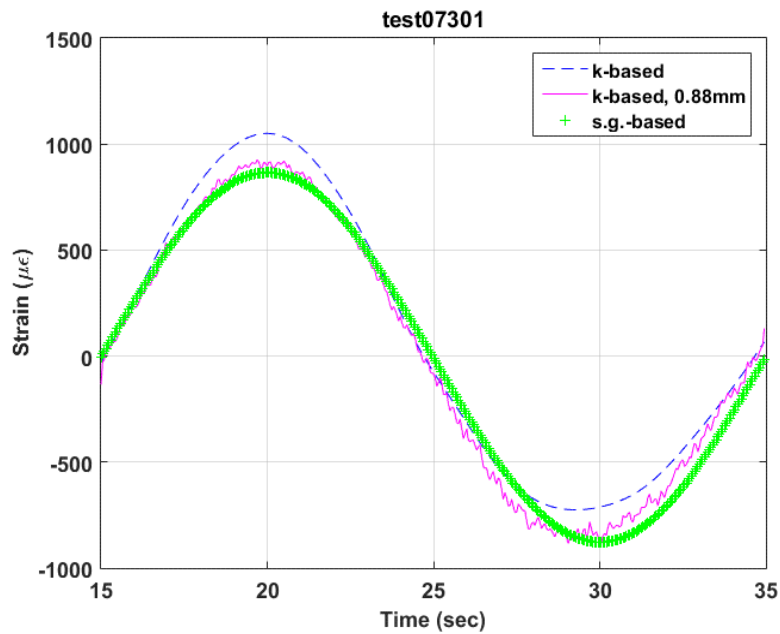
- 1) Overall, the strain gauge has a synchronized response with curvature-based strain, although the curvature-based strain at 0.6 mm lagged in the first half of period.
- 2) Peak/ valley response of curvature-based strain with the correction applied matched the strain gauge measurement well.
- 3) Again, spacing correction (Δh) demonstrated an increasing trend with the displacements, but the correction at small displacement input showed a lower level than in the previous test session (Figure G.4).



0.4 mm

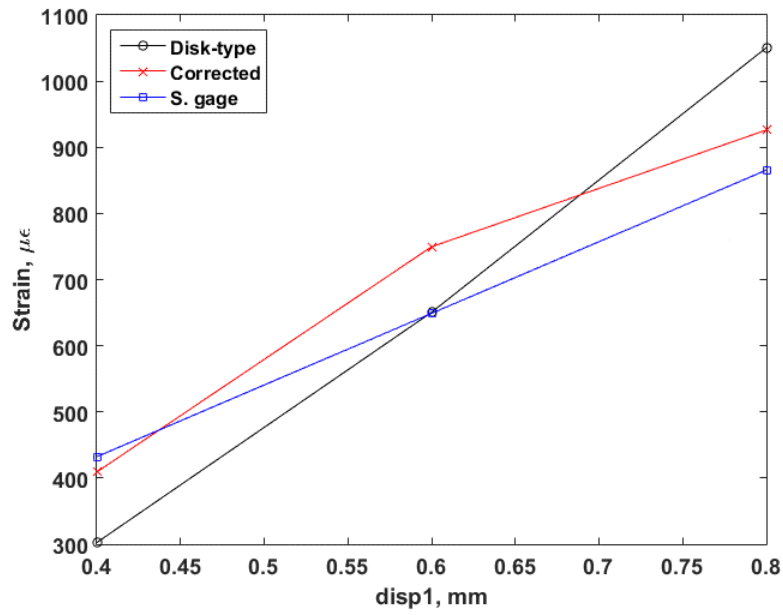


0.6 mm

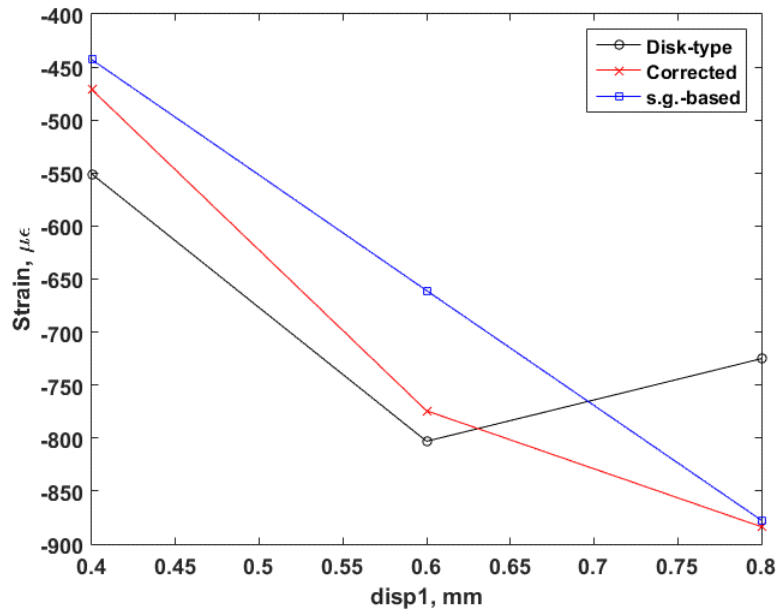


0.8 mm

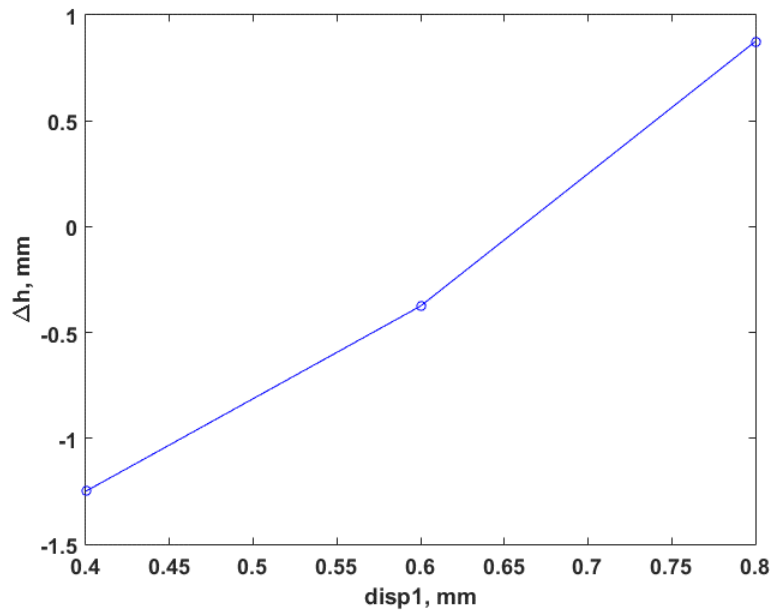
Figure G.7 Strain curves based on original disk-type curvature, corrected curvature, and strain gauge for 0.05 Hz displacement at the loading point of the U-frame arm: (a) 0.4 mm, (b) 0.6 mm, and (c) 0.8 mm



(a) Peak



(b) Valley

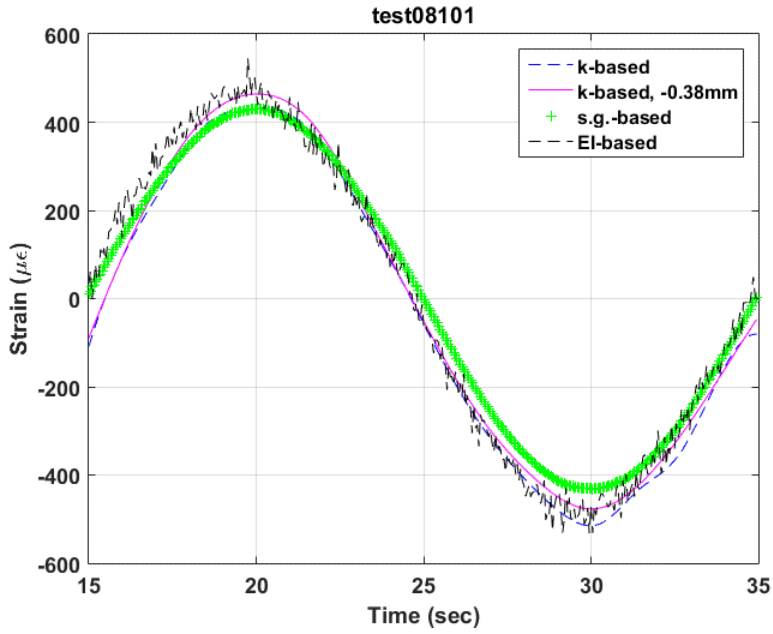


(c) Spacing correction

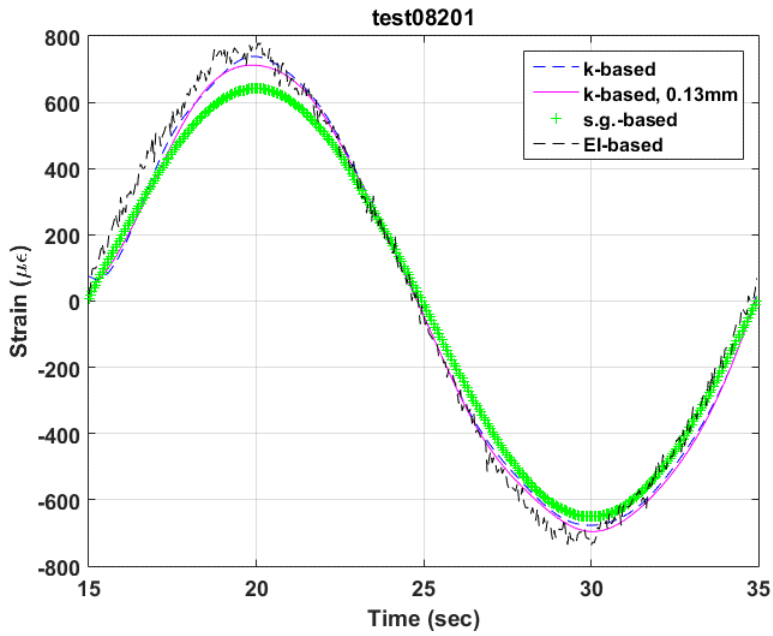
Figure G.8 (a) Peak and (b) valley responses of strain waveform, and (c) spacing corrections under various disp1 amplitudes at 0.05 Hz

The results of test items 81– 84 are given in Figure G.9 for 0.05 Hz and G.10 for 5 Hz. The following observations can be made:

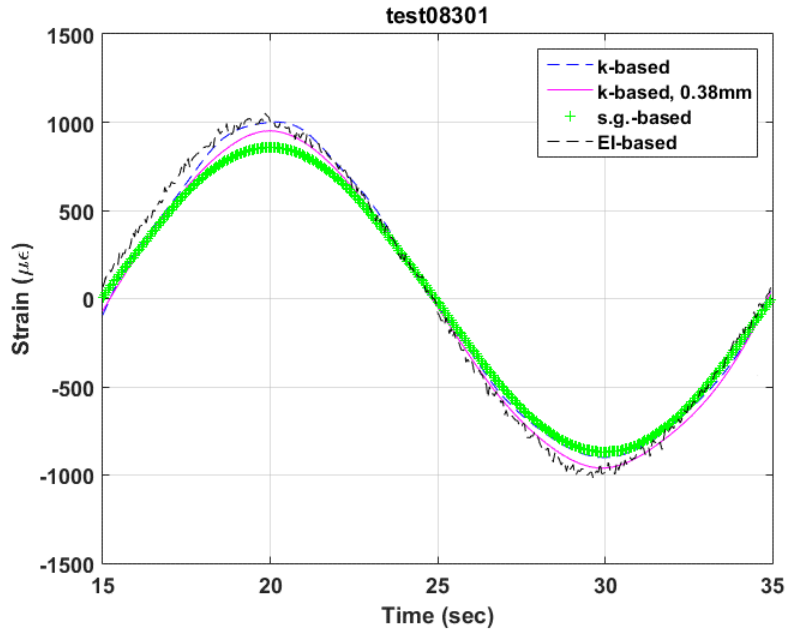
- 1) Strain gauge showed a lower level of strain than those of curvature-based strain.
- 2) The spacing correction Δh and its variation with displacements were smaller compared with previous tests (Figures G.4 and G.8). The degree of correction on κ -based strain was smaller as well.
- 3) The corrected curvature-based strains were seen close to the EI-based strains.



(a) Displacement amplitude 0.4 mm

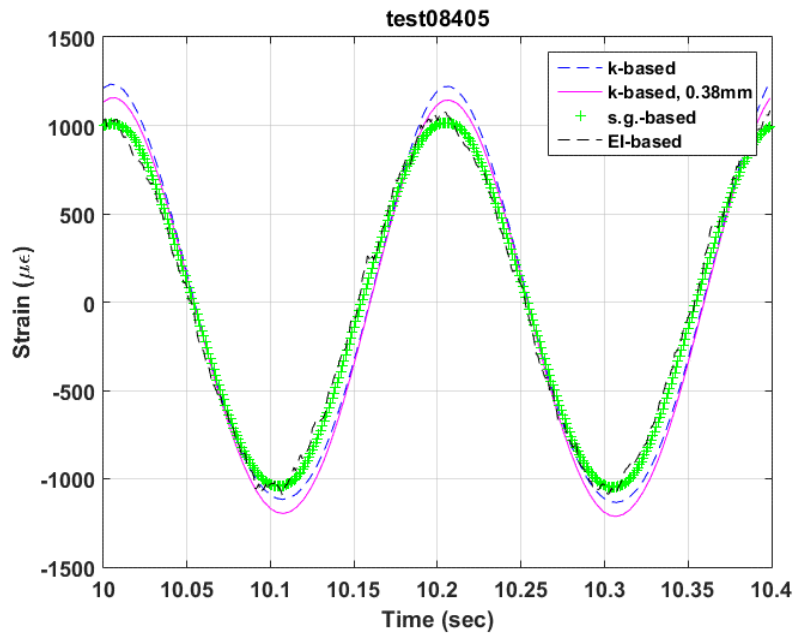


(b) Displacement amplitude 0.6 mm

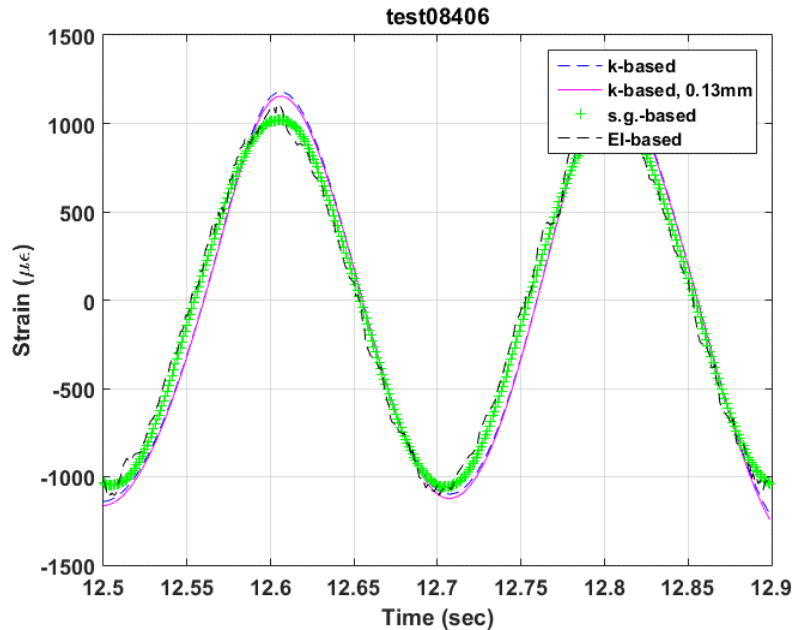


(c) Displacement amplitude 0.8 mm

Figure G.9 Strain results based on original curvature, corrected curvature, stain gauge, and flexural rigidity EI for 0.05 Hz tests under three displacement amplitudes



(a) Data block 5



(b) Data block 6

Figure G.10 Strain results based on original curvature, corrected curvature, stain gauge, and flexural rigidity EI for 5 Hz tests under amplitude 100N

G.3.3 Summary

The use of SS304 surrogate rod in out-cell study provided the opportunity to examine the small curvature measurement currently used in CIRFT tests. The following summarizes the major observations:

- 1) The corrected curvature was shown to be close to the EI-based curvature; the corrected-curvature-based strain was also demonstrated to agree with the strain gauge measurement.
- 2) The spacing correction (Δh) was smaller than those based on a large curvature measurement. The degree of correction on curvature-based strain was smaller, as well.
- 3) The spacing correction exhibited a defined trend to increase with the level of displacement input, but it also showed a large variance at the small displacements.
- 4) The level of spacing correction in specified displacement input varied among tests sessions. The change of contact condition between the probe and the surface of rod is believed to contribute to the variation.

G.4 RESULTS ON POLYCARBONATE SURROGATE ROD

The test condition on a polycarbonate rod PC01 consists of two load waveforms: ramp and sine.

G.4.1 Ramp waveform test

The displacement at each loading point of the U-frame ramped up to a designated level and then down to zero; one loading cycle was used. The bending in the ramp was unidirectional, with a single pulse pointed in either a positive or negative direction.

Two types of LVDT probes were tested: flat disk type and chisel type. Test condition can be seen in Table G.4.

Table G.4 Test condition using ramp process

No.	pk1 (mm)	pk2 (mm)	rate(mm/s)	Cycles	LVDT
1	0	6	0.2	1	flat disk, D5
2	0	-6	0.2	1	flat disk, D5
7	0	6	0.2	1	chisel, D5
8	0	-6	0.2	1	chisel, D5

The data sets for a specified probe were assembled to obtain a whole waveform of reversed bending. The three LVDT-based curvatures obtained with both disk type and chisel type probes are presented, along with the corrected curvature in Figure G.11, in which $EI = 1.8 \text{ Nm}^2$ was used for the EI-based estimate.

- 1) The correction procedure suggested that a sensor spacing correction of 2.50 mm is needed. With the suggested procedure, only one correction is needed instead of two corrections in the positive (2.90 mm) and negative (2.40 mm) directions as used before.
- 2) The corrected curvature showed a good correspondence with the both-chisel type measurement and the EI-based estimate.

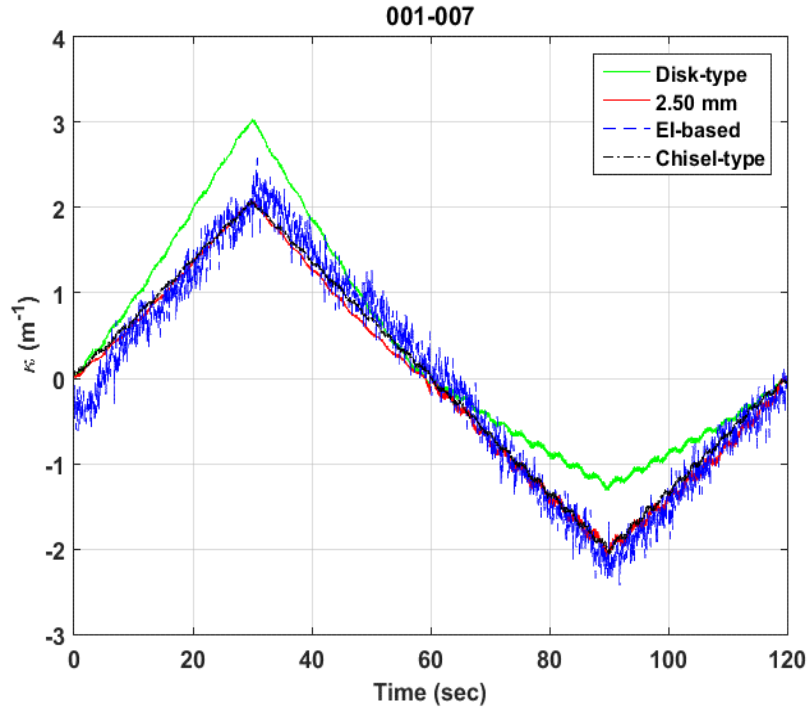


Figure G.11 Curvature measurements of polycarbonate surrogate rod based on disk- and chisel-type probe, 2.50 mm sensor spacing correction, and EI-based estimate

G.4.2 Sine waveform test

Reversed bending was conducted directly by using a 0.05 Hz sine wave, and 12 amplitudes were tested with one LVDT probe, the flat disk type. Strain gauge measurement was enabled, and strains were acquired using a P3 strain indicator and recorder. The test conditions are detailed in Table G.5.

Table G.5 Test condition using sine wave

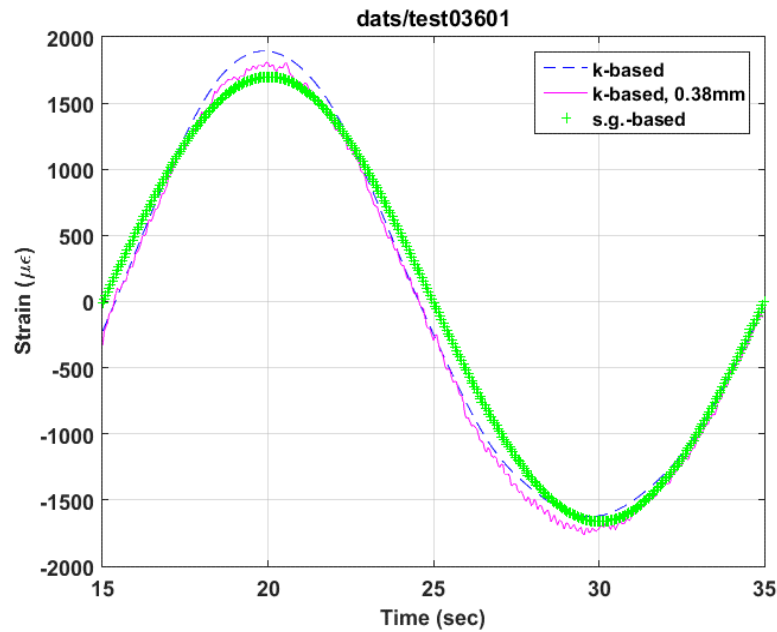
No.	pk1 (mm)	pk2 (mm)	F(Hz)	Cycles	LVDT
35	0.5	-0.5	0.05	3	flat disk, D5
36	1	-1	0.05	3	flat disk, D5
37	1.5	-1.5	0.05	3	flat disk, D5
38	2	-2	0.05	3	flat disk, D5
39	2.5	-2.5	0.05	3	flat disk, D5
40	0.3	-0.3	0.05	3	flat disk, D5
41	0.3	-0.3	0.05	3	flat disk, D5
42	0.3	-0.3	0.05	3	flat disk, D5
43	0.5	-0.5	0.05	3	flat disk, D5
44	0.5	-0.5	0.05	3	flat disk, D5
45	0.5	-0.5	0.05	3	flat disk, D5
46	1	-1	0.05	3	flat disk, D5

47	1	-1	0.05	3	flat disk, D5
48	1.5	-1.5	0.05	3	flat disk, D5
49	1.5	-1.5	0.05	3	flat disk, D5
50	2	-2	0.05	3	flat disk, D5
51	2	-2	0.05	3	flat disk, D5
52	2.5	-2.5	0.05	3	flat disk, D5
53	2.5	-2.5	0.05	3	flat disk, D5
54	3	-3	0.05	3	flat disk, D5
55	3	-3	0.05	3	flat disk, D5
56	3	-3	0.05	3	flat disk, D5
57	3.5	-3.5	0.05	3	flat disk, D5
58	3.5	-3.5	0.05	3	flat disk, D5
59	3.5	-3.5	0.05	3	flat disk, D5
60	4	-4	0.05	3	flat disk, D5
61	4	-4	0.05	3	flat disk, D5
62	4	-4	0.05	3	flat disk, D5
63	4.5	-4.5	0.05	3	flat disk, D5
64	4.5	-4.5	0.05	3	flat disk, D5
65	4.5	-4.5	0.05	3	flat disk, D5
66	5	-5	0.05	3	flat disk, D5
67	5	-5	0.05	3	flat disk, D5
68	5	-5	0.05	3	flat disk, D5
69	5.5	-5.5	0.05	3	flat disk, D5
70	5.5	-5.5	0.05	3	flat disk, D5
71	5.5	-5.5	0.05	3	flat disk, D5
72	6	-6	0.05	3	flat disk, D5
73	6	-6	0.05	3	flat disk, D5
74	6	-6	0.05	3	flat disk, D5
75	6	-6	0.05	3	flat disk, D5

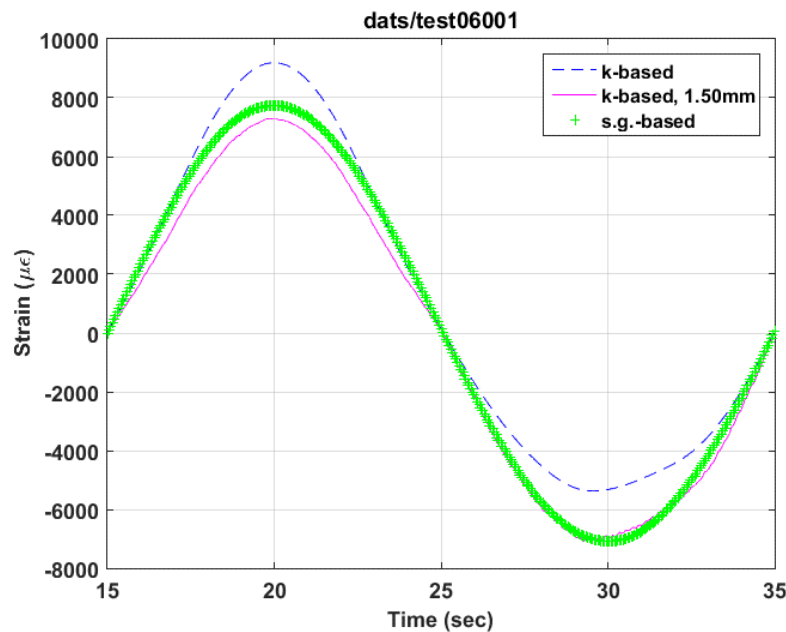
The typical results from tests with 0.05 Hz sine wave are given in Figure G.12. The peak and valley values of the strain waveforms obtained for various cases are shown in Figure G.13, including strains based on original curvature (disk-type probe), corrected curvature, and strain gauge. The variation of spacing correction as a function of displacement input is also presented.

- 1) The strains from the strain gauge usually agreed well with those based on the corrected curvatures, but they deviated from the corrected curvature-based strain at high levels.
- 2) The spacing correction (Δh) again exhibited a defined trend to increase with the displacement input, and also a larger variance at the small displacements.
- 3) The spacing corrections were again lower than those obtained in ramping.

- 4) The corrected ultimate curvatures obtained in ramp and sine waveforms were the same (around 2 m^{-1} at 6.00 mm disp1). There may have been a significant change of the contact condition between probe and surface of rod, as the tests were carried out in different periods of the project.

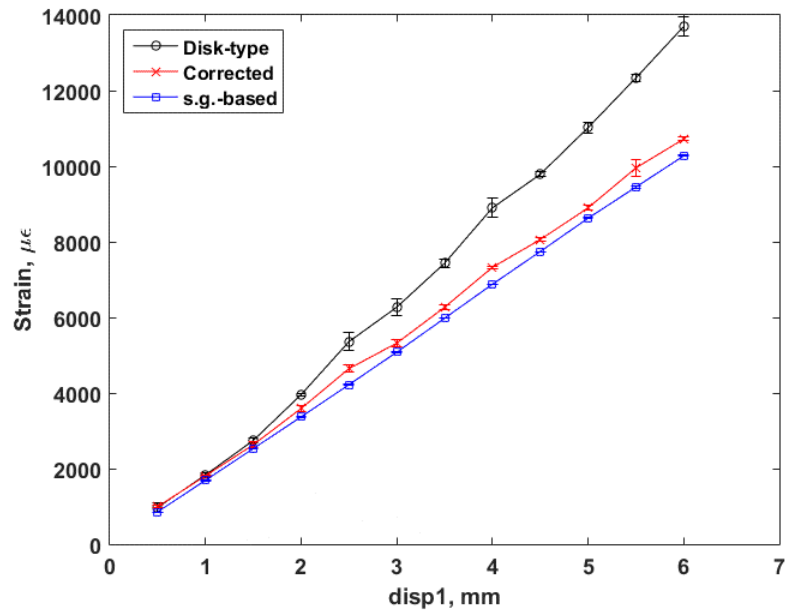


(a)

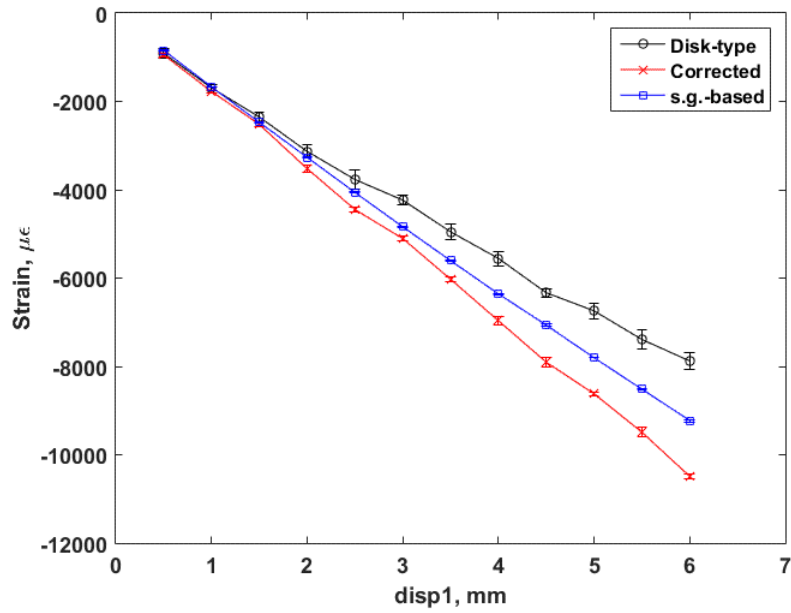


(b)

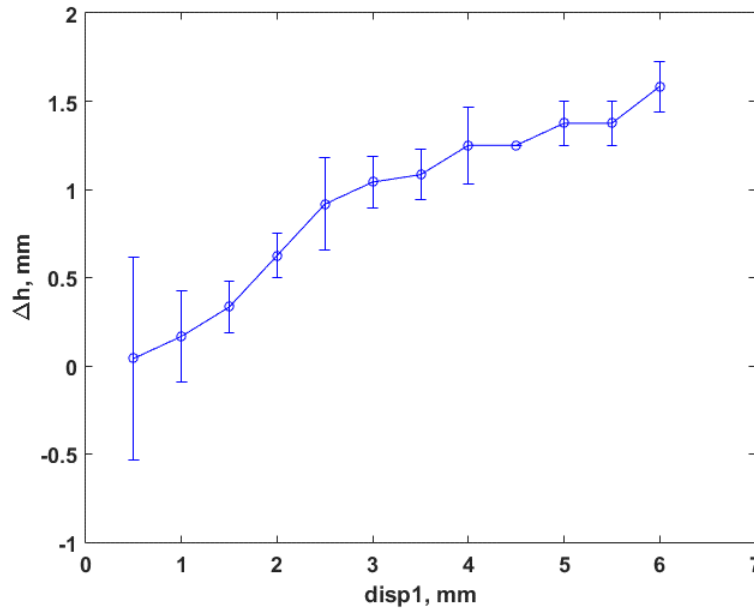
Figure G.12 Strain wave forms obtained from original curvature, corrected curvature, and strain gauge: (a) displacement amplitude 1.00 mm, and (b) 4.00 mm



(a) Peak



(b) Valley



(c) Spacing correction

Figure G.13 (a) Peak and (b) valley responses of strain waveform, and (c) spacing corrections under various disp1 amplitudes at 0.05 Hz

G.4.3 Summary

Based on the tests of polycarbonate rod, main observations with respect to disk-type curvature measurement and correction can be summarized as follows:

- 1) The corrected curvature showed a good correspondence with chisel-type measurement and EI-based estimate. The agreement of corrected-curvature-based strain was also found with strain gauge measurement, particularly near small-to-immediate levels of displacement input.
- 2) The spacing correction (Δh) again exhibited a defined trend to increase with the displacement input, and also a larger variance at the small displacements.
- 3) The correction procedure suggested a spacing correction of 2.50 mm (at 6.00 mm disp1) other than dual corrections reported in ramping (2.40 mm in negative curvature and 2.90 mm in positive curvature). However, the corrected ultimate curvatures obtained in ramp and sine waveforms were the same (around 2 m^{-1} at 6.00 mm disp1).
- 4) The change of the contact condition between the probe and the surface of the rod in different test sessions was believed to be responsible for the variation of spacing correction observed.

G.5 RECOMMENDATION

The corrected curvature based on disk-type probes agrees to a varying extent with the EI-based estimate in both small and large curvature measurements and with chisel-type probe measurements in large curvature cases. The corrected-curvature-based strain was also illustrated to correspond to the strain gauge measurement, particularly at the small-to-immediate level of displacement input.

It is suggested that the proposed correction procedure be applied to data analysis. In the monotonic test, $\Delta h = 2.50$ mm obtained from the calibration can be used for spacing correction in data analysis. In the reversed cyclic bending, the Δh can be obtained directly using the data block because the peak and valley pair is available.

APPENDIX H HYDRIDE REORIENTATION SAMPLE PREPARATION

APPENDIX H HYDRIDE REORIENTATION SAMPLE PREPARATION

H.1 INTRODUCTION

The objective of Phase II testing was to collect experimental data on HBR Zircaloy-4 HBU fuels following simulated drying-transfer operation conditions. This appendix describes a procedure used to reorient hydrides from the circumferential orientation to the radial orientation. Normal operation of nuclear fuel in a reactor results in the formation of a waterside corrosion layer (oxide) and the introduction of hydrogen into the zirconium cladding via the reaction $2\text{H}_2\text{O} + \text{Zr} \rightarrow \text{ZrO}_2 + 4\text{H}$. With increasing corrosion, the hydrogen concentration in the cladding will exceed its terminal solid solubility, and brittle zirconium hydrides ($\text{Zr} + 2\text{H} \rightarrow \text{ZrH}_2$) may precipitate as the cladding cools.

Under pool storage conditions after fuel is discharged from reactors, the precipitated hydride platelets are oriented in a circumferential direction. Circumferential hydrides—in combination with hardening caused by irradiation effects—will decrease cladding ductility in response to axial and hoop loads; however, even with circumferential hydrides, the cladding still retains some ductility. At elevated temperatures during drying-transfer operations, some of the hydrogen may go into solution (up to 200 wppm at 400 °C). The pressure-induced cladding tensile hoop stress during drying-transfer operations is high relative to in-reactor and pool storage conditions. During cooling under tensile hoop stress, some of the dissolved hydrogen will precipitate in the radial direction across the cladding wall when the hoop stress is sufficient. Further cooling during storage may result in radial-hydride-induced embrittlement. This was confirmed by recent research [1–5] that featured hydrided Zircaloy-4 cladding and high burnup zirconium alloy samples that were exposed to a tensile hoop stress from the internally pressurized cladding at ≈ 400 °C—conditions similar to drying operations of the SNF.

H.2 MATERIALS, EQUIPMENT, AND TEST METHODS

H.2.1 Description of Cladding Material and High-Burnup Fuel Segments

The out-of-cell experiments were conducted with unirradiated, 15 × 15 pressurized water reactor (PWR) Zircaloy-4 cladding material provided by AREVA; the material has dimensions, oxygen content, and mechanical properties similar to those of the HBR cladding. After the cladding was received by Oak Ridge National Laboratory (ORNL), measurements were performed to determine the outer diameter (OD) and wall thickness. Table H.1 summarizes the dimensions and chemical compositions of the unirradiated AREVA-provided clad compared with the nominal commercial Zircaloy-4 cladding alloys.

Table H.1 Dimensions and chemistry of H. B. Robinson (HBR) type Zircaloy-4 used in the Oak Ridge National Laboratory test program (--- = below the detection limit)

Parameter	15 × 15 Zircaloy-4 HBR-type cladding ^a	Nominal composition of commercial Zircaloy-4 ^{b,c} cladding alloys
Outer diameter, mm	10.76	10.72
Wall thickness, mm	0.76	0.617
Tin, wt %	---	1.29 ± 0.1
Niobium, wt %	---	---
Oxygen, wt %	≈0.13	0.120
Iron, wt %	---	---
Chromium, wt %	---	---
Nickel, wppm	---	---
Sulfur, wppm	---	---
Carbon, wppm	---	---
Hafnium, wppm	---	---
Silicon, wppm	---	---
Nitrogen, wppm	---	---
Hydrogen, wppm	≈20	5

^aORNL data based on AREVA lots received in 2014.

^bASTM B811. Source: M. C. Billone, T. Burtseva, and Y. Yan. "Overview of Spent Nuclear Fuel Program: Test Plan and High Burnup Cladding at ANL," *NRC Program Review Meeting*, Argonne National Laboratory, Argonne, IL, July 7, 2010.

^cORNL/TM-9591/V1&R1, "Physical and Decay Characteristics of Commercial LWR Spent Fuel," January 1986.

Irradiated materials used in the ORNL test program are HBU HBR PWR fuel rods received by ORNL in 2008. They were from a 15 × 15 assembly of the HBR plant Unit 2 [6] that was operated for seven cycles and reached a rod-average burnup of 67 GWd/MTU (73 GWd/MTU peak pellet). The fuel enrichment is 2.90%. The nominal fuel pellet dimensions are 9.06 mm diameter × 9.93 mm height, and the active fuel height is 3.66 m. The cladding is cold-worked/stress-relieved Zircaloy-4 measuring 10.77 mm OD and 9.25 mm inner diameter (ID), with a nominal tin content of 1.42%. The rods were pressurized with helium to 2.0 MPa during initial fabrication. A detailed description of the as-fabricated cladding, the irradiation history, and the nondestructive testing results (eddy current, profilometry, fission-gas release, etc.) is provided in a 2001 Electric Power Research Institute report [6].

Irradiated HBR fuel used in the ORNL test program is summarized in Table H.2. Detailed characterization was performed to determine the fuel morphology, fuel-cladding bond, corrosion layer, and hydride morphology. Figure H.1 shows a low magnification image of the fuel morphology, which reveals the typical reactor start-up and shut-down cracks.

Table H.2 Characteristics of HBU HR fuel rods for tORNL hydride reorientation (HR) test^a

Parameter	H. B. Robinson
Reactor	Pressurized water reactor
Enrichment, wt %	2.90
Rod average burnup, GWd/MTU	63–67
Discharge date	1995
Fast fluence, 10 ²⁵ n/m ²	14
Cladding	15 × 15 Zircaloy-4
Initial wall thickness, mm	0.76
OD oxide, μm	≤ 100
Hydrogen pickup, wppm	≤ 800
Fueled	Yes



Figure H.1 HBU HBR fuel morphology for Sample 607D4A.

H.2.2 Equipment for Sample Preparation

Hydride reorientation (HR) tests were conducted with Zircaloy-4 cladding samples 152 mm in length (see Table H.1 for cladding geometry) which were hydrogen charged for a target hydrogen concentration of 300 wppm. After hydrogen charging, the hydrided samples were subjected to HR to simulate drying-transfer operation conditions. This which consists of a high pressure piping system and test chamber within a programmable crucible furnace. The hydrided sample was sealed (end-cap welded) at one end and connected to the high pressure piping system within the test chamber at the other end. The piping system was used to internally pressurize the sample to cause a hoop stress ranging up to 150 MPa.

The hydriding apparatus consists of a closed stainless steel tube that contains zirconium alloy specimens and hydrogen gas, as shown in Figure H.2. The tube is heated to facilitate hydrogen absorption by the metal. By controlling the initial hydrogen gas pressure in the vessel and the temperature profile, hydrogen concentration can be processed selectively. A typical pressure and temperature profile is shown in Figure H.3.



Figure H.2 Hydrogen charging apparatus

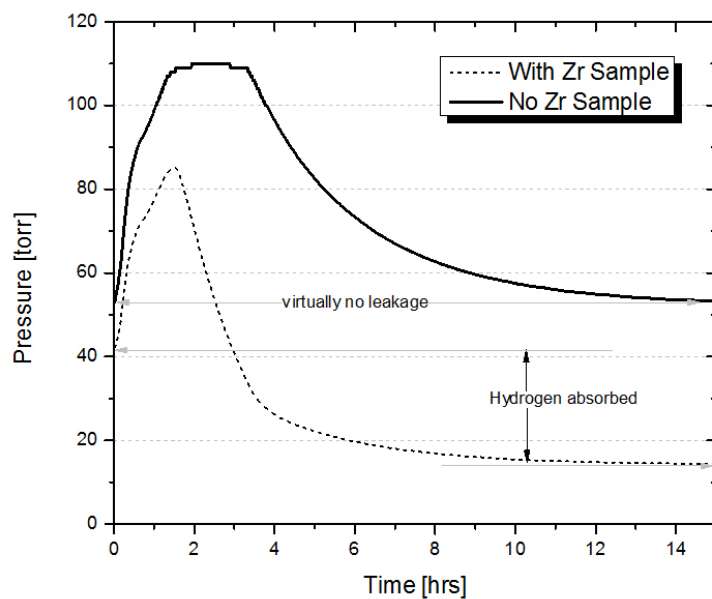


Figure H.3 Typical pressure and temperature profile of the hydrogen charging process

An Astro Arc Polysoude welder (see Figure H.4) was used for automatic orbital welding of the cladding. A circular movement of the welding torch/electrode around fuel cladding, controlled by the welder power source, creates an orbital weld. This welder can be operated remotely with manipulators in a hot cell.



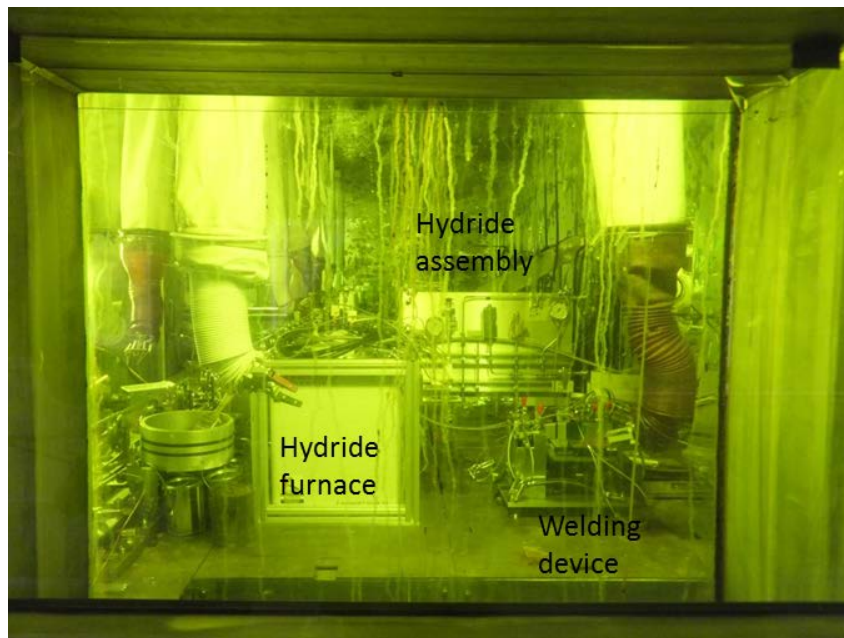
Figure H.4 An Astro Arc Polysoude tubing welder

H.2.3 Hydride Reorientation System

The reorientation system consists of a high pressure piping system and test chamber within a programmable crucible furnace (see Figure H.5). The system was installed into the hot cell in FY16. Calibrations and benchmark tests were performed with unirradiated materials. For each experiment, a specimen 6 inches in length was welded with two end plugs, with one end sealed and the other end connected to the high-pressure piping system within the test chamber. The test chamber was purged with pure argon gas to remove air and moisture contents, and then the sample was internally pressurized to cause a hoop stress ranging from 0–150 MPa [5]. Pressurized samples were subjected to a preprogrammed temperature profile for up to five cycles, with each cycle being heated to 400 °C, held for 2 hours, and slow-cooled/heated (1 °C/min) to 170 °C; the final cycle cooled from 170 °C to room temperature (RT). Hoop stress was calculated using values $r = 4.62$ mm for inner radius and $t = 0.76$ mm for the wall thickness of the HBR Zircaloy-4 cladding.



(a)



(b)

Figure H.5 The HR system (a) before and (b) after being installed in the hot cell

H.3 MATERIALS HYDRIDING AND CHARACTERIZATION

The Zircaloy-4 cladding samples were hydrogen charged by the gaseous method as described in Section H.2. Gas charging was conducted under stress-free conditions. For this work, the

Zircaloy-4 was hydrided to a target concentration of 300–400 wppm, which is similar to the hydrogen content of HBR HBU cladding to be tested in a hot cell.

Metallographic examinations were performed on hydrided Zircaloy-4 samples. As shown in Figure H.6, the hydride density increases as the hydrogen concentration in the sample increases. Hydrogen measurements indicated that the hydrogen content of the specimens shown in Figure H.6 range from 70–320 wppm.

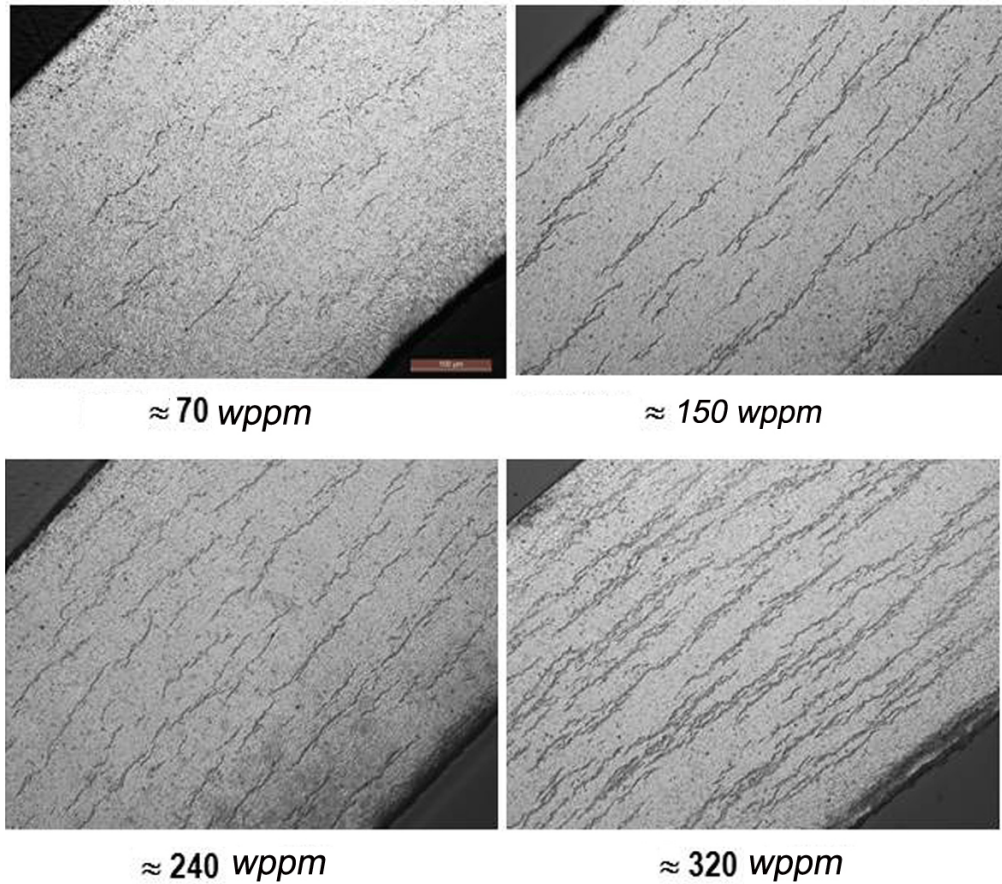


Figure H.6 Micrographs showing typical, uniform circumferential hydride distributions in hydrogen charged ry-4

H.4 OUT-OF-CELL HYDRIDE REORIENTATION TESTING

To optimize the in-cell test condition, four out-of-cell HR tests with hydrided HBR cladding were performed. The out-of-cell test results provided a guideline to in-cell HR procedures with HBU HBR fuel segments.

H.4.1 HR-HBR#1, 145 MPa at 400 °C, one cycle

An HR test HR-HBR#1 on a hydrided 15×15 Zircaloy-4 specimen was conducted at the maximum hoop stress of 145 MPa and the hold temperature $T = 400$ °C. The specimen was heated to 400 °C, held at 400 °C for 2 hours, cooled at 5 °C/h to 170°C, then cooled at a faster rate from 170 °C to RT. The total test time was over 72 hours. The internal pressure was dynamically monitored with a digital pressure transducer.

Figure H.7 shows the temperature and pressure history for a drying-storage simulation experiment conducted with a 2-hour hold time and one-cycle cooling. The plotted temperature is a thermocouple reading near the specimen's surface.

Figure H.8 shows the hydride morphology of Sample HR-HBR#1 with hydrogen content $H \approx 274$ wppm. The specimen was sectioned at the midplane of a sample 6 inches long. The radial hydrides can be observed clearly. The maximum length of radial hydrides is about 50–60 μm , as they often are terminated when intersecting with circumferential hydrides. Figure H.9 includes micrographs taken in eight areas in different circumferential directions of Sample HR-HBR#1, which shows that hydrides are uniformly distributed in circumferential directions.

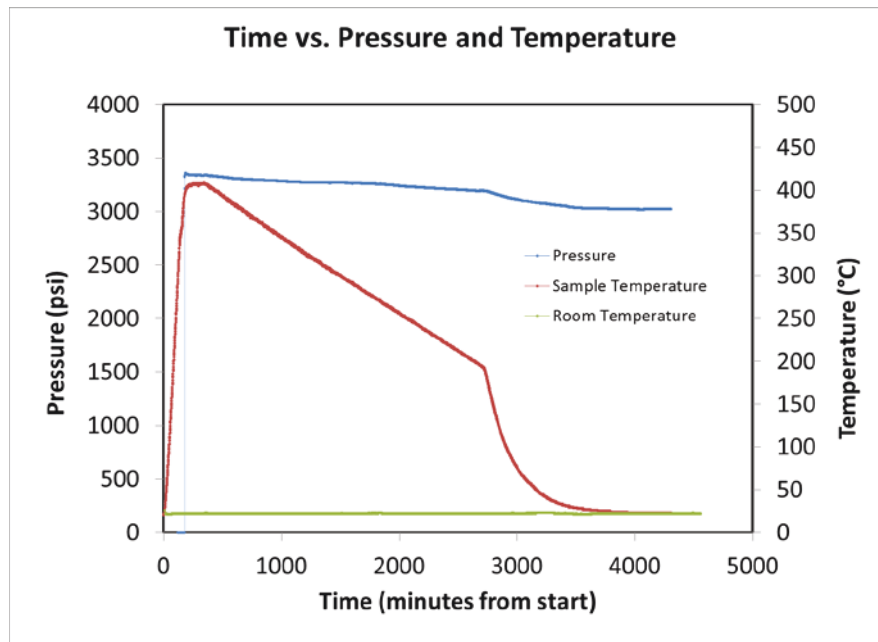


Figure H.7 Pressure and sample temperature as a function of time for Test HR-HBR#1

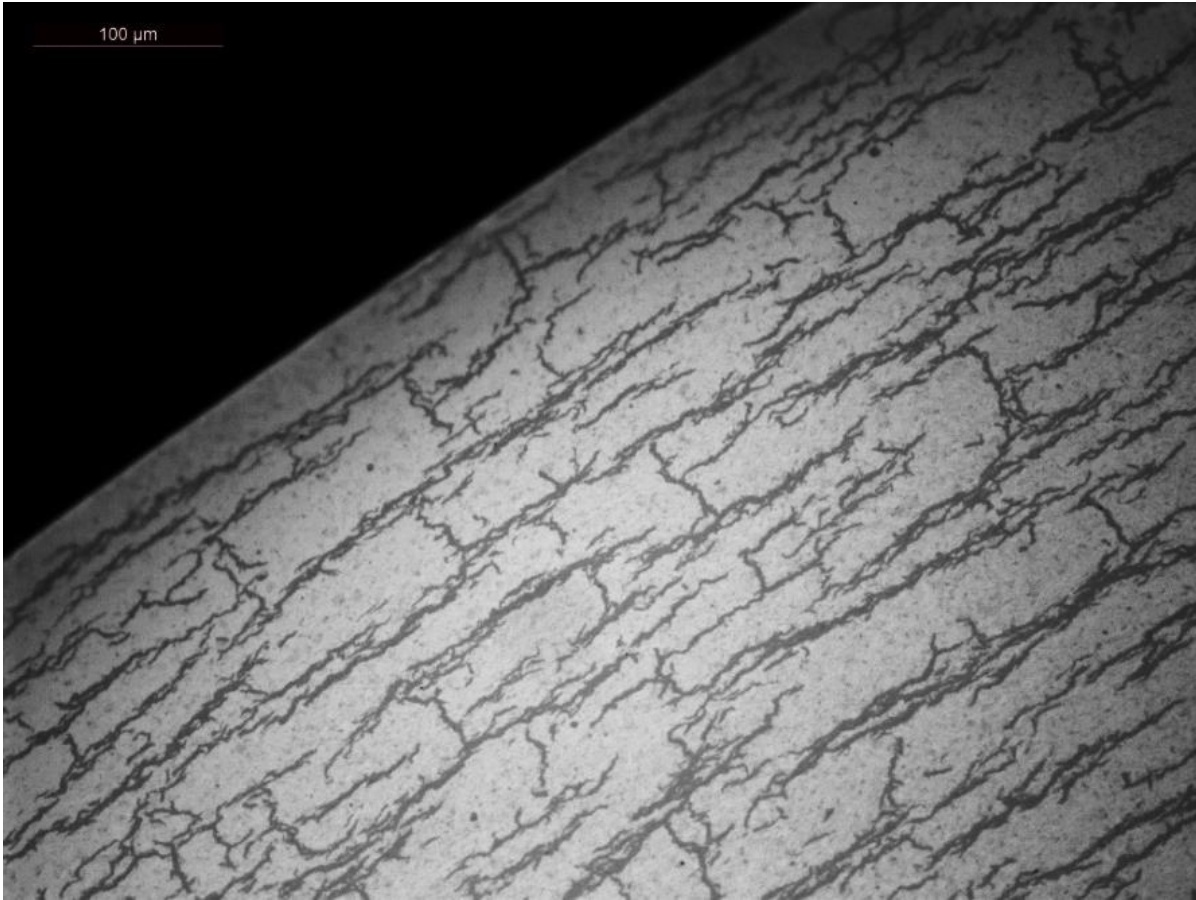


Figure H.8 High magnification micrograph showing radial hydrides of Sample HR-HBR#1 with hydrogen content $H \approx 274$ wppm; the specimen was sectioned at the midplane of a sample 6 inches in length

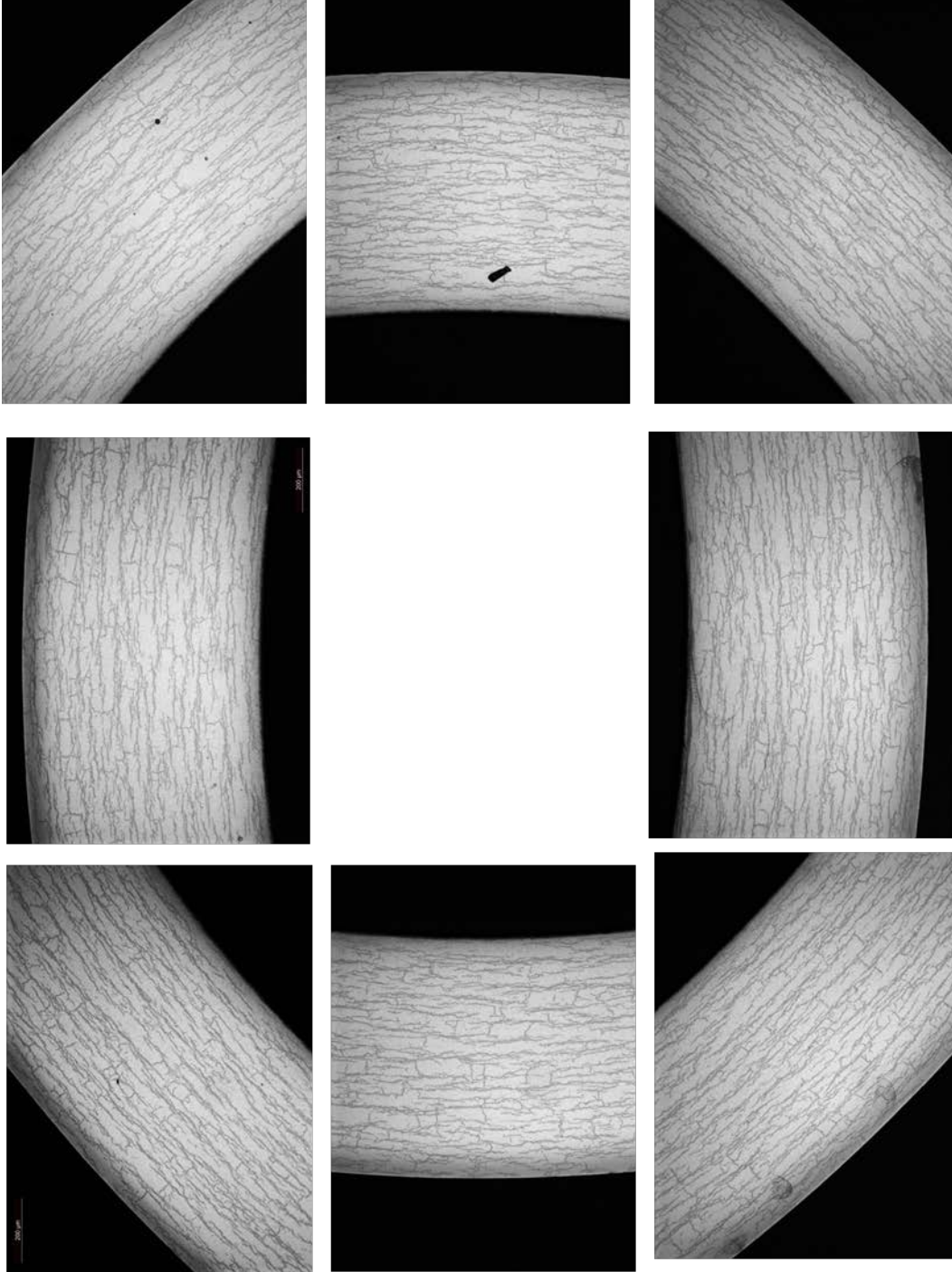


Figure H.9 Radial hydride distribution shown in eight areas in different circumferential directions of Sample HR-HBR#1 the specimen was sectioned at the midplane of a sample 6 inches in length

H.4.2 HR-HBR#2, 145–150 MPa at 400°C, five cycles

Test HR-HBR#2 was conducted on a hydrided 15×15 Zircaloy-4 specimen at the maximum hoop stress of 145 MPa and the target hold temperature $T = 400^\circ\text{C}$. Thermal cycling was performed to increase the radial hydrides. The specimen was assembled into a holder within the furnace for heating to target temperature 400°C , held for 2 hours, cooled at $1^\circ\text{C}/\text{min}$ to 170°C , and then heated at $1^\circ\text{C}/\text{min}$ to target hold temperature 400°C again for five cycles. The sample was furnace cooled from 170°C to RT for the last cycle. Figure H.10 shows the temperature and pressure history for HR-HBR#2. The plotted temperature is a thermocouple reading near the specimen's surface.

Figure H.11 shows the hydride morphology of Sample HR-HBR#2 with hydrogen content $H \approx 286$ wppm. The specimen was sectioned at the midplane of a sample 6 inches in length. Radial hydrides can be observed clearly. The maximum length of the radial hydrides is about $50\text{--}60\ \mu\text{m}$, similar to HR-HBR#1. However, the density of radial hydrides in HR-HBR#2 is much higher than the density in HR-HBR#1, which is mainly attributed to the use of multiple thermal cycles. Figure H.12 shows radial hydride distribution in eight areas in different circumferential directions of Sample HR-HBR#2.

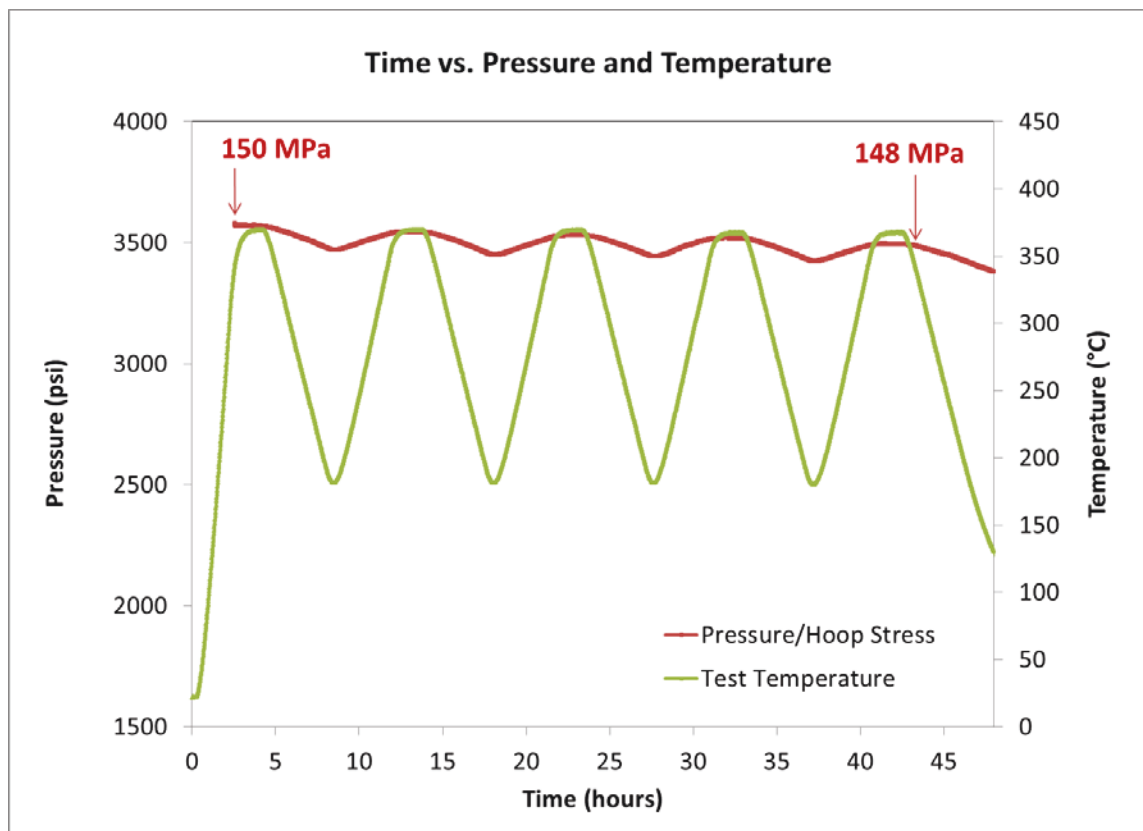


Figure H.10 Pressure and sample temperature as a function of time for Test HR-HBR#2

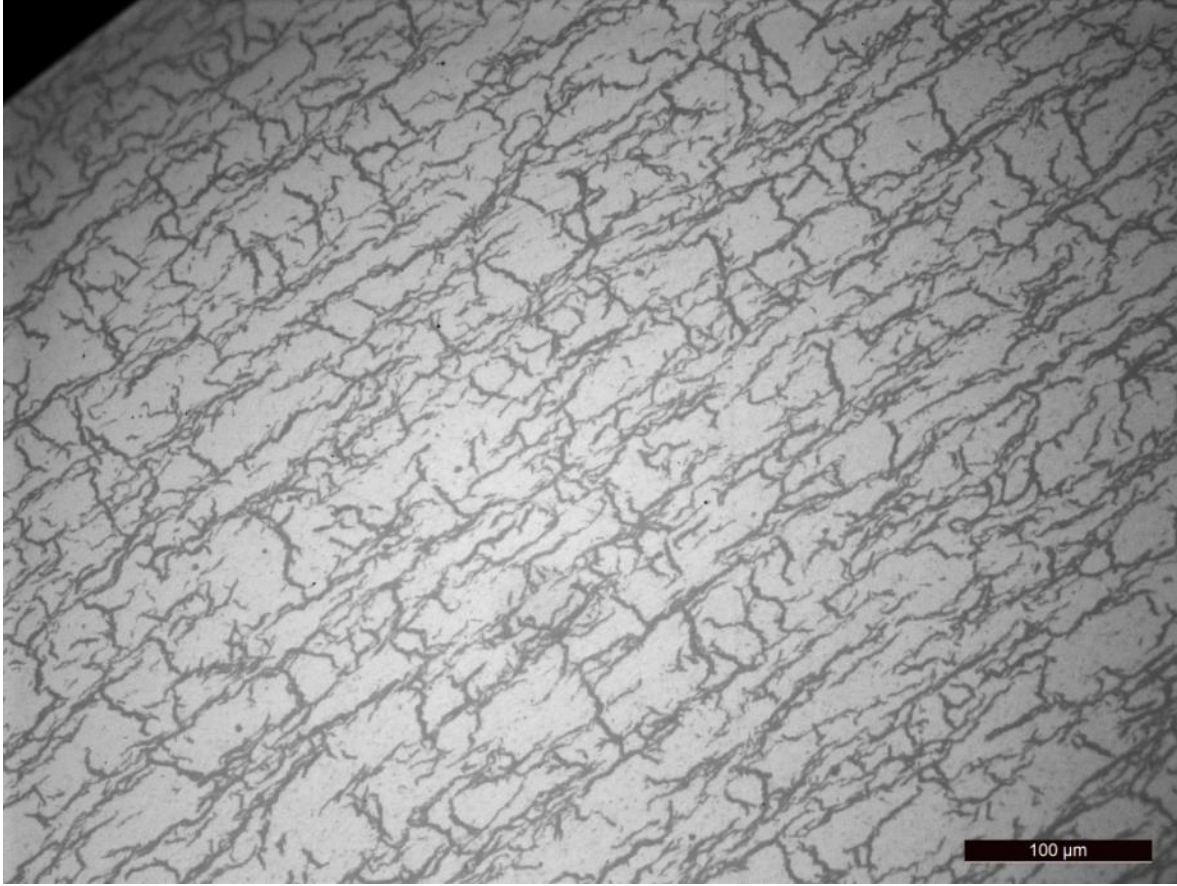


Figure H.11 High magnification micrograph showing radial hydrides of Sample HR-HBR#2 with hydrogen content $H \approx 286$ ppm. The specimen was sectioned at the midplane of a sample 6 inches in length

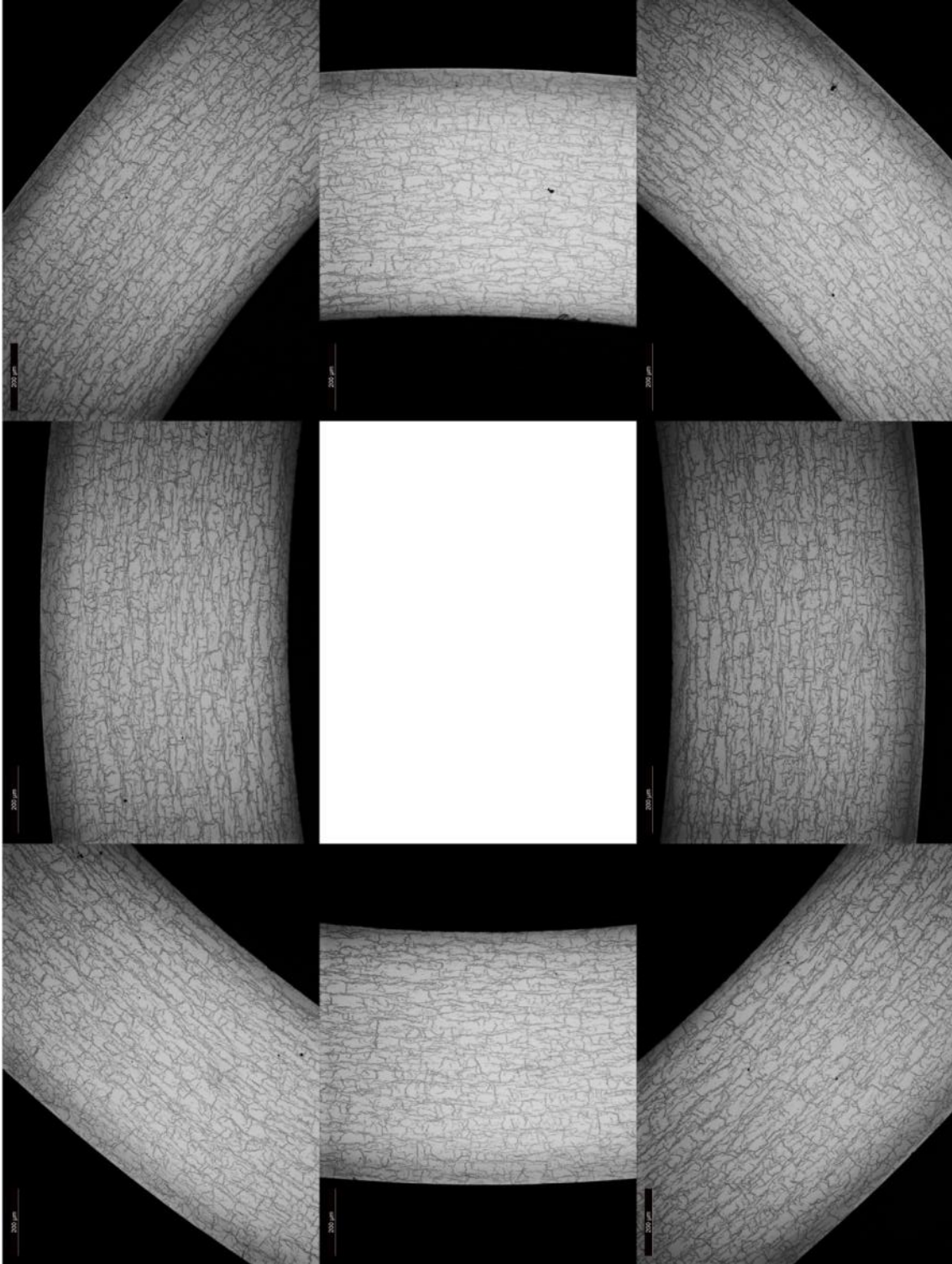


Figure H.12 Radial hydride distribution shown in eight areas in different circumferential directions of Sample HR-HBR#2; the specimen was sectioned at the midplane of a sample 6 inches in length

H.4.3 HR-HBR#3, 100 MPa at 400°C, five cycles

Test HR-HBR#3 was conducted on a hydrided 15 × 15 Zircaloy-4 specimen at the maximum hoop stress of 100 MPa and the hold temperature $T = 400\text{ }^{\circ}\text{C}$. The specimen was assembled into a holder within the furnace for heating to $400\text{ }^{\circ}\text{C}$, held at $400\text{ }^{\circ}\text{C}$ for 2 hours, cooled at $1^{\circ}\text{C}/\text{min}$ to $170\text{ }^{\circ}\text{C}$, and then heated at $1^{\circ}\text{C}/\text{min}$ to $400\text{ }^{\circ}\text{C}$ again for five cycles. The sample was furnace cooled from $170\text{ }^{\circ}\text{C}$ to RT for the last cycle. Figure H.13 shows the temperature and pressure history for HR-HBR#3. The plotted temperature is a thermocouple reading near the specimen surface.

Figure H.14 shows the hydride morphology of Sample HR-HBR#3 with hydrogen content $H \approx 310\text{ wppm}$. The specimen was sectioned at the midplane of a sample 6 inches in length. The radial hydrides can be observed clearly in Figure H.14. The maximum length of the radial hydride is $< 30\text{ }\mu\text{m}$. The radial hydride ratio of HR-HBR#3 also is lower than HR-HBR#2. Figure H.15 shows radial hydride distribution in eight areas in different circumferential directions of Sample HR-HBR#3.

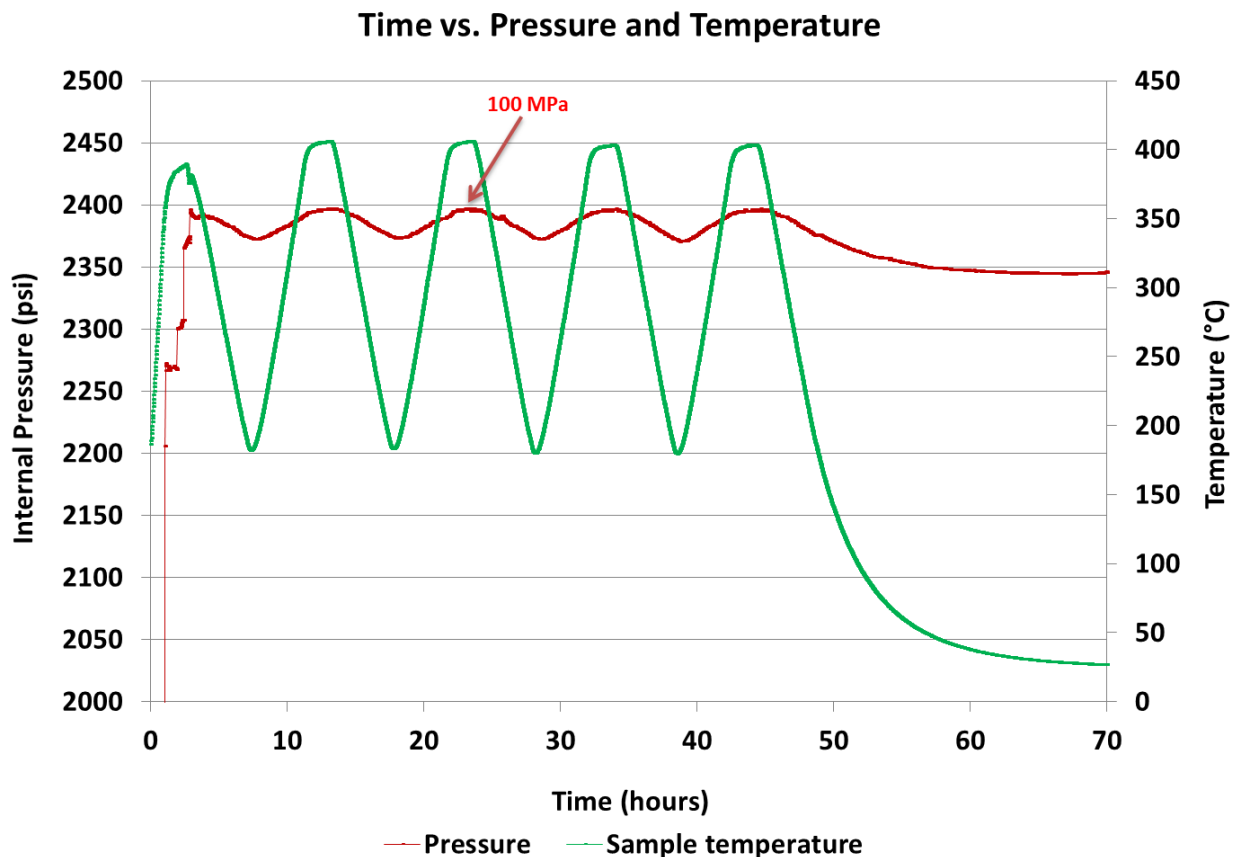


Figure H.13 Pressure and sample temperature as a function of time for Test HR-HBR#3

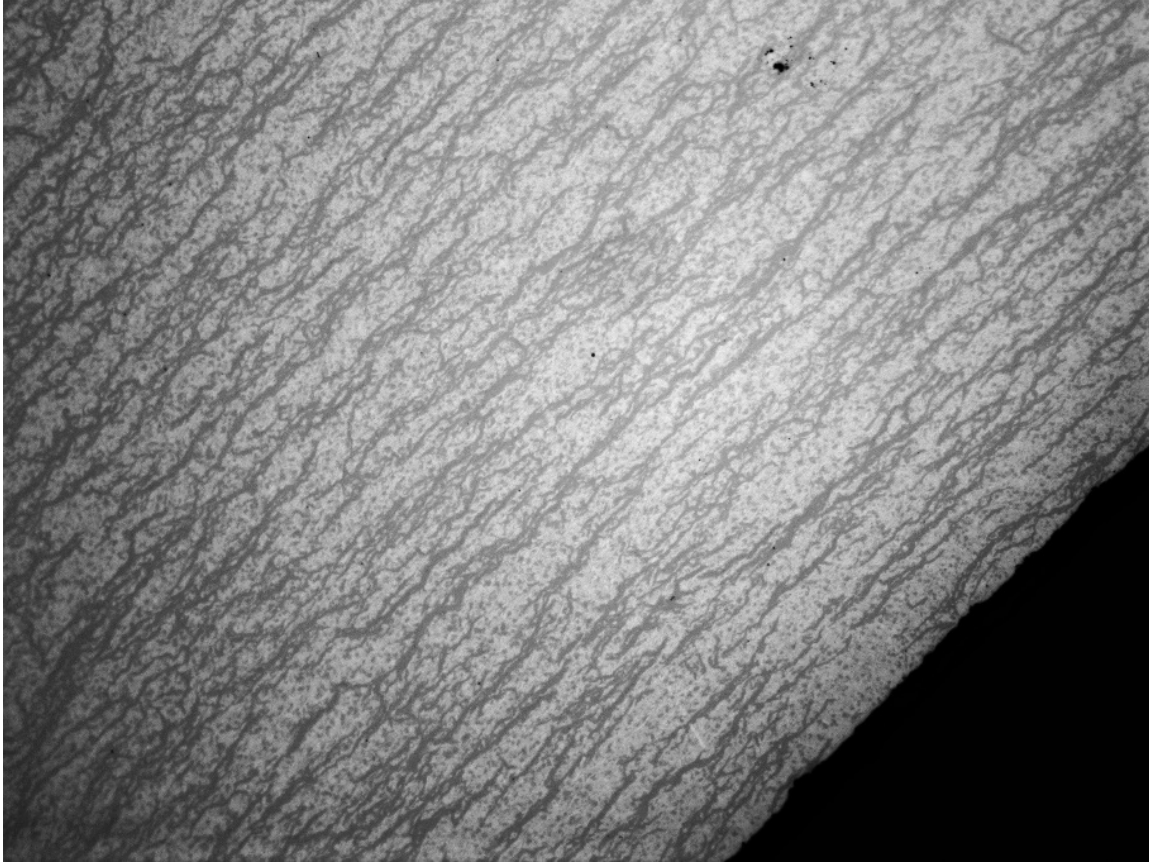


Figure H.14 High magnification micrograph showing radial hydrides of Sample HR-HBR#3 with hydrogen content $H \approx 310$ ppm; the specimen was sectioned at the midplane of a sample 6 inches in length

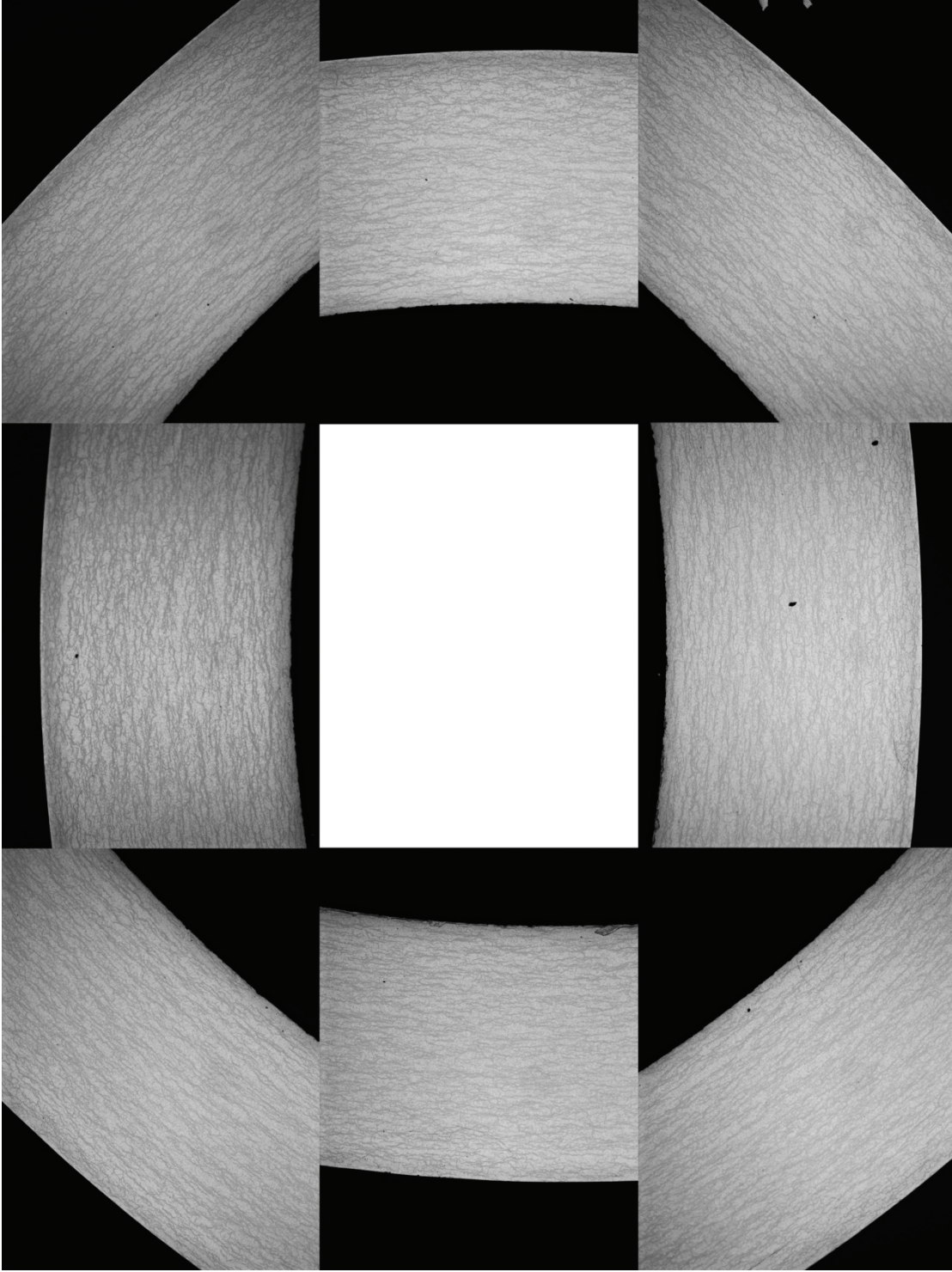


Figure H.15 Radial hydride distribution shown in eight areas in different circumferential directions of Sample HR-HBR#3; the specimen was sectioned at the midplane of a sample 6 inches in length

H.4.4 HR-HBR#4, 120 MPa at 400°C, five cycles

Test HR-HBR#4 was conducted on a hydrided 15 × 15 Zircaloy-4 specimen at the maximum hoop stress of 120 MPa and the hold temperature $T = 400\text{ }^{\circ}\text{C}$. The specimen was assembled into a holder within the furnace for heating to $400\text{ }^{\circ}\text{C}$, held at $400\text{ }^{\circ}\text{C}$ for 2 hours, cooled at $1\text{ }^{\circ}\text{C}/\text{min}$ to $170\text{ }^{\circ}\text{C}$, and then heated at $1\text{ }^{\circ}\text{C}/\text{min}$ to $400\text{ }^{\circ}\text{C}$ again for five cycles. The sample was furnace cooled from $170\text{ }^{\circ}\text{C}$ to RT for the last cycle. Figure H.16 shows the temperature and pressure history for HR-HBR#4. The plotted temperature is a thermocouple reading near the specimen surface.

Figure H.17 shows the hydride morphology of Sample HR-HBR#4 with hydrogen content $H \approx 312\text{ wppm}$. The specimen was sectioned at the midplane of a sample six inches in length. Radial hydrides can be observed. The maximum length of the radial hydrides is $< 30\text{ }\mu\text{m}$. The radial hydride ratio of HR-HBR#4 also is lower than the ratio of HR-HBR#2. However, the radial hydride ratio of HR-HBR#4 is higher than that of HR-HBR#3 because of the higher pressure. Figure H.18 shows radial hydride distribution in eight areas in different circumferential directions of Sample HR-HBR#4.

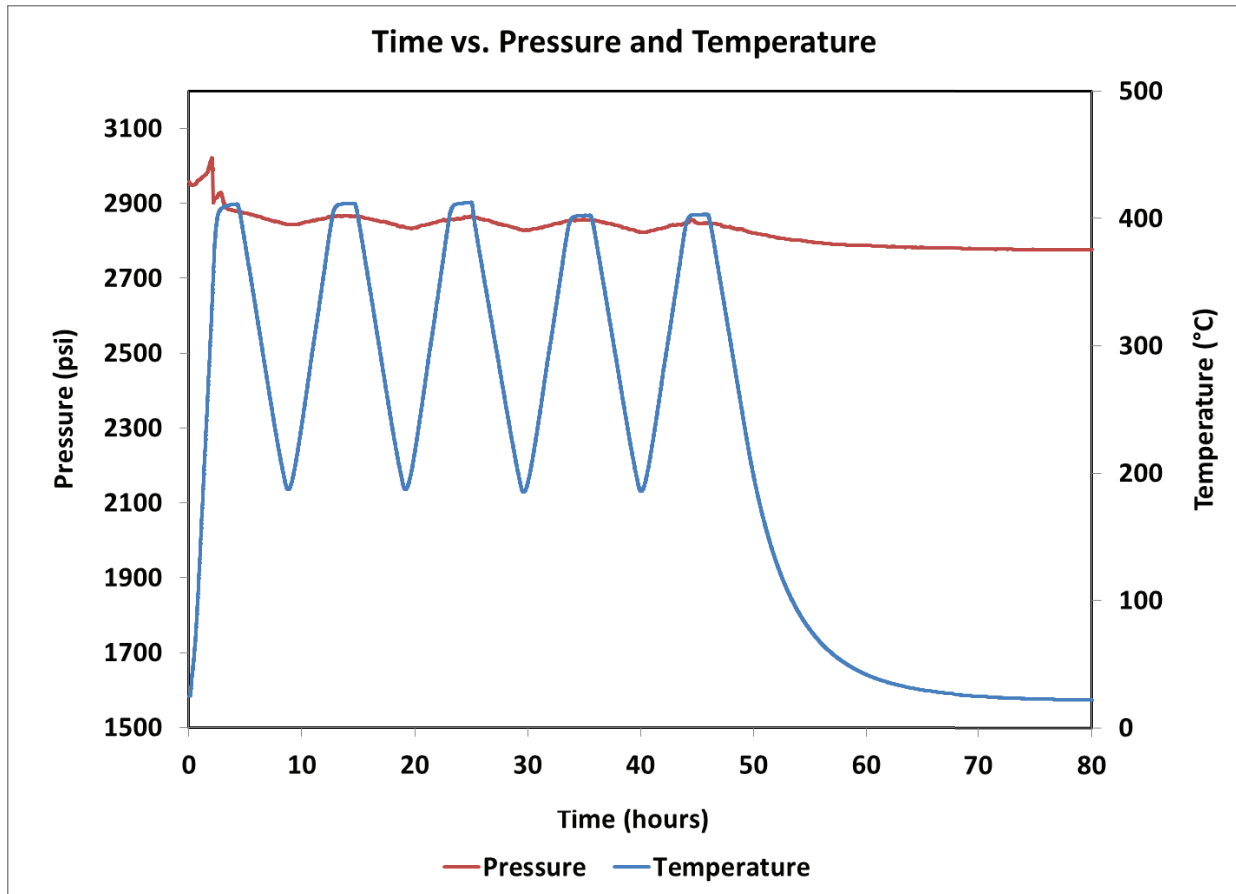


Figure H.16 Pressure and sample temperature as a function of time for Test HR-HBR#4

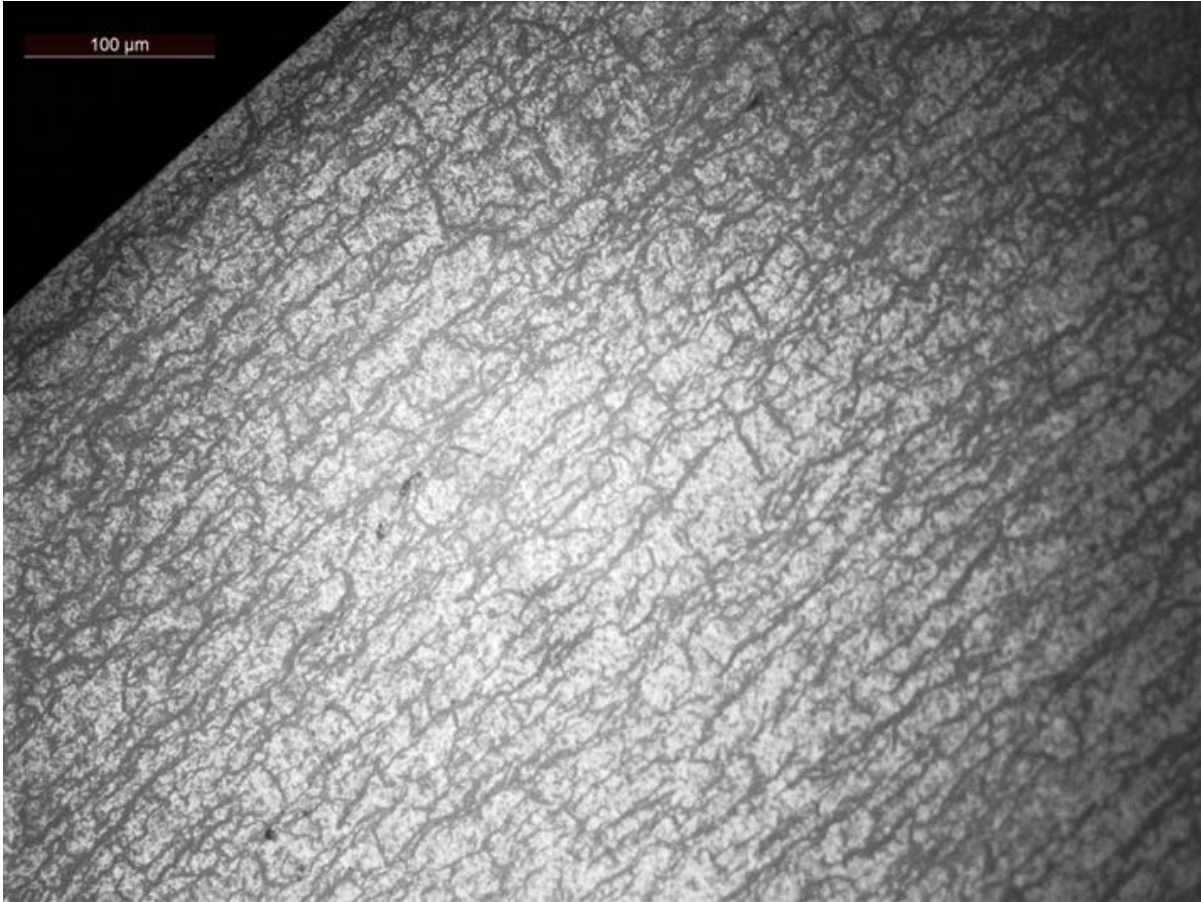


Figure H.17 High magnification micrograph showing radial hydrides of Sample HR-HBR#4 with hydrogen content $H \approx 312$ ppm; the specimen was sectioned at the midplane of a sample 6 inches in length

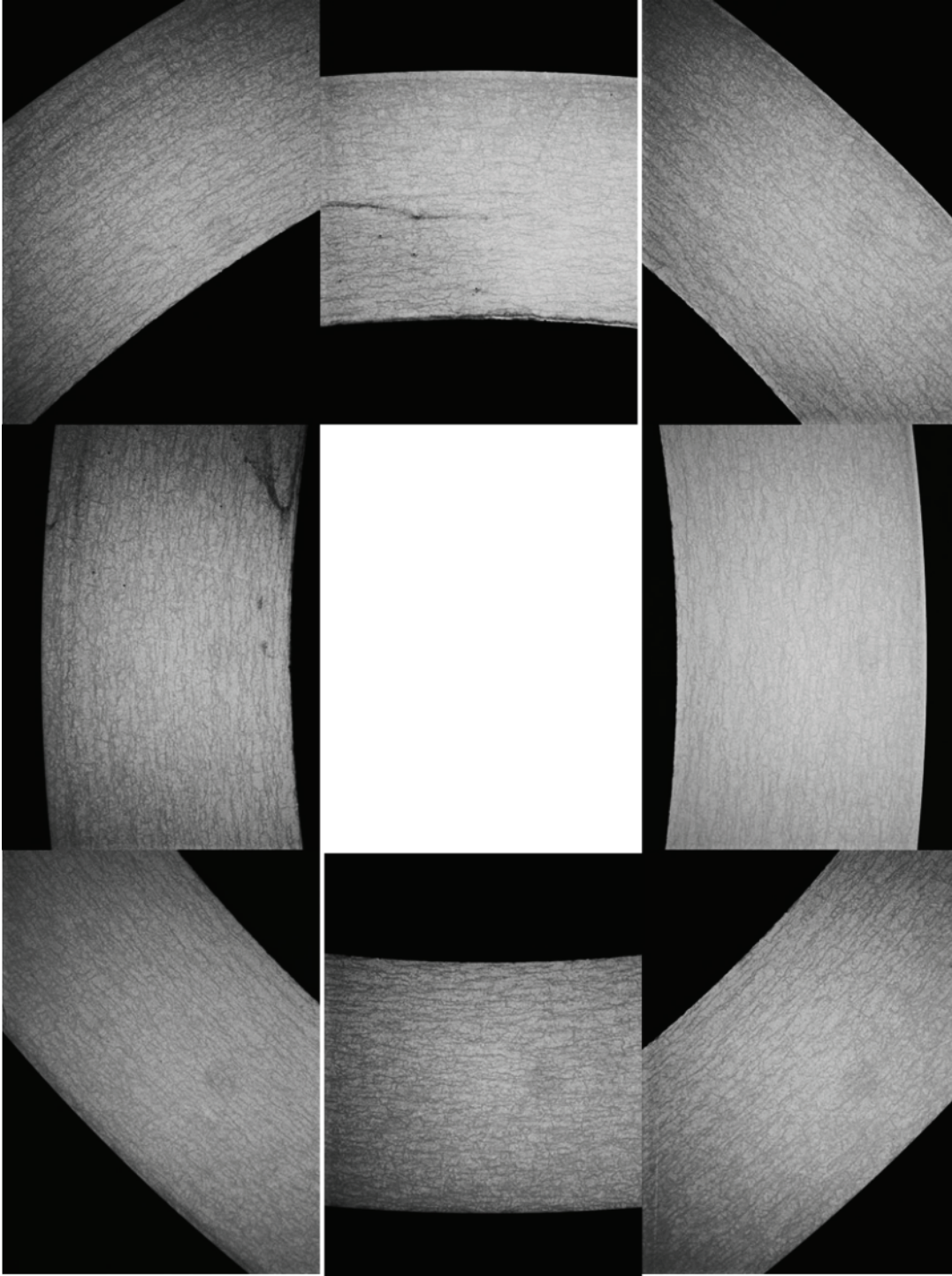


Figure H.18 Radial hydride distribution shown in eight areas in different circumferential directions of Sample HR-HBR#4; the specimen was sectioned at the midplane of a sample 6 inches in length

H.5 DISCUSSION

In this work, the hydrided tubing samples have been pressurized internally to produce a hoop stress up to 150 MPa to form radial hydrides using the HR system (see Section H.4). Tests HR-HBR#1 and HR-HBR#2 indicate that multithermal cycling will increase the ratio of radial hydrides under the same maximum temperature and maximum internal pressure. In addition, the results of Tests HR-HBR#2 through HR-HBR#4 reveal that the ratio of radial hydrides decreases as the internal pressure decreases when the temperature and pressure profiles remain the same.

The goal of Phase II testing was to investigate the impact of radial hydrides on HBU fuel cladding ductility. To gain insight into bounding effects of radial hydrides, it was desirable to produce a reasonably high percentage of radial hydrides within the cladding by the HR tests. The out-of-cell tests were important to support planning of the in-cell HR tests, as they established a test procedure and provided a guideline for in-cell test conditions. Based on the four out-of-cell tests, it was decided to perform in-cell HR treatment (HRT) test under the same test conditions of HR-HBR#2 to maximize the radial hydride condition.

H.5.1 Hydride Reorientation Treatment for Phase II HBU Tests

Four CIRFT evaluations were completed on the HBR specimens following HRT. Five cycles at 140 MPa hoop stress and 400 °C were conducted for segments HR1–HR3. Due to a welded endcap leak, only thermal heat treatment was applied to the HR4 sample.

The HBU fuel samples for Phase II tests were prepared in the irradiation fuel examination laboratory. After the samples were sectioned into pieces 6 inches in length, the surface oxide layer and fuel material were removed from both ends to a depth of approximately 0.5 inches. Endcaps were welded at both ends, and the fuel specimens were then pressurized with argon gas at a maximum hoop stress level of 140 MPa and a target hold temperature ($T = 400\text{ °C}$). Thermal cycling was performed to increase the radial hydrides. All in-cell tests had the same temperature profiles. Figure H.19 shows the temperature history of the first in-cell HR test, HR1, with an HBU HBR sample. The same procedure was used for HR2 and HR3. Due to a welded endcap leak, only thermal heat treatment was applied to the HR4 sample.

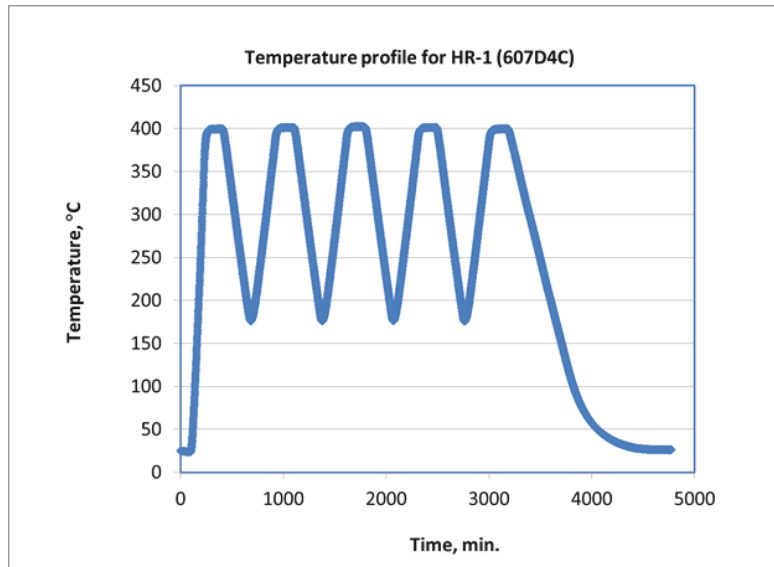
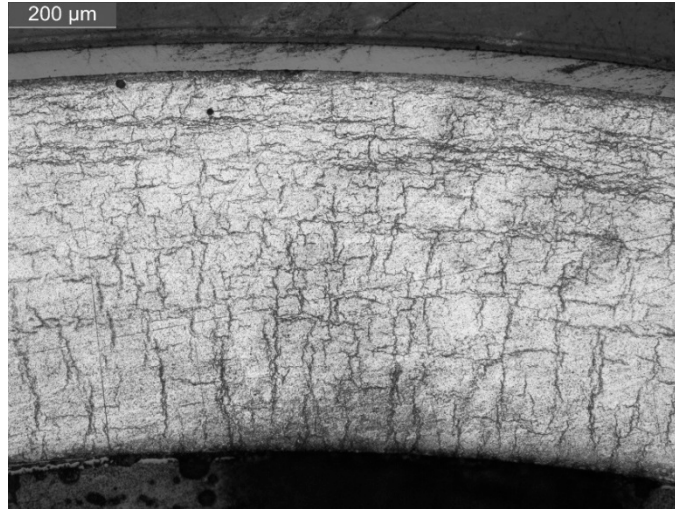
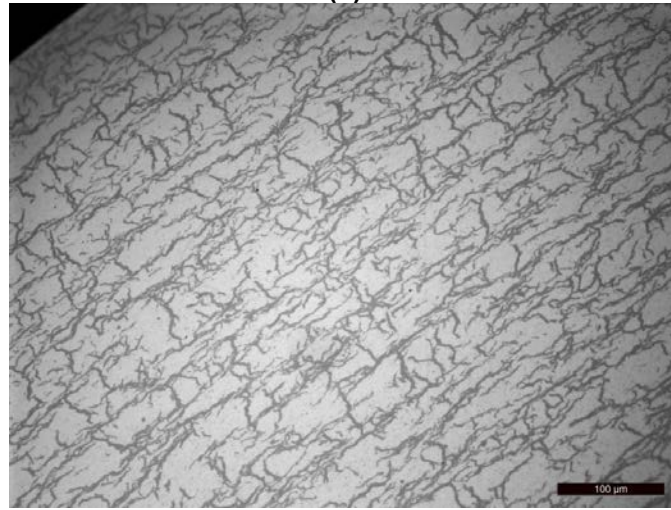


Figure H.19 Sample temperature as a function of time for in-cell HR test HR-1.

The samples were subjected to CIRFT testing at RT to evaluate the materials' performance after HRT. After the tests were completed in the CIRFT, the specimens were examined to verify that the radial hydrides had been generated. Figure H.20 shows the hydride morphology of HR sample HR1. The hydrogen concentration of this sample was about 360–400 wppm. The metallographic examination (MET) mount specimen was sectioned at the midplane of a sample 6 inches long. Although the in-cell HR test conditions were the same as the out-of-cell test HR-HBR#2 and the hydrogen concentration of these two samples were compatible, the morphology of HBU sample HR1 was different from hydrided sample HR-HBR#2. For the unirradiated sample, the circumferential hydrides were uniformly distributed across the wall, and the maximum length of its radial hydrides was about 50–60 μm . For HBU samples, the radial hydrides were mainly distributed near the inner surface, and the circumferential hydrides were mostly seen near the outer surface. The length of the radial hydride of the HBU sample, Figure H.20(a), was also much longer than the unirradiated sample, Figure H.20(b).



(a)



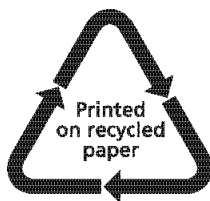
(b)

Figure H.20 (a) High magnification micrograph showing radial hydrides of HBU HBR Sample HR-1 ($H \approx 360\text{--}400$ ppm) following HRT; the HBU HBR specimen was pressurized to 140 MPa at 400 °C with five thermal cycles; (b) high magnification micrograph showing radial hydrides of the unirradiated Sample HR-HBR#2 ($H \approx 286$ ppm) following the same HRT procedure

H.6 REFERENCES

1. M. C. Billone, T. Burtseva, and Y. Yan. "Overview of Spent Nuclear Fuel Program: Test Plan and High Burnup Cladding at ANL," *NRC Program Review Meeting*, Argonne National Laboratory, Argonne, IL, July 7, 2010.
2. R. Daum, H. Tsai, Y. Liu, and M. Billone, "High-Burnup Cladding Mechanical Performance during Cask Storage and Post-Storage Handling and Transportation," *Nuclear Safety Research Conference*, Washington, DC, October 25–27, 2004.
3. Y. Yan et al., "Observation and Mechanism of Hydride in Zircaloy-4 and Local Radial Hydride Induced by High Pressure at High Temperatures," *2013 International High-Level Radioactive Waste Management*, Albuquerque, NM, April 28–May 2, 2013.
4. Y. Yan, L. K. Plummer, H. Ray, T. Cool, and H. Z. Bilheux, "Ductility Evaluation of As-Hydrated and Hydride Reoriented Zircaloy-4 Cladding under Simulated Dry-Storage Condition," *2013 MRS Fall Meeting Proceeding*, Boston, MA, December 1–6, 2013.
5. M. C. Billone, T. A. Burtseva, and Y. Yan, *Ductile-to-Brittle Transition Temperature for High-Burnup Zircaloy-4 and ZIRLO™ Cladding Alloys Exposed to Simulated Drying-Storage Conditions*, Argonne National Laboratory letter report to the Nuclear Regulatory Commission, ANL-13/13, September 28, 2013. Available online as ML12181A238 at <http://www.nrc.gov/reading-rm/adams.html>.
6. E. J. Ruzauska and K. N. Fardell, "Design, Operation, and Performance Data for High Burnup PWR Fuel from the H. B. Robinson Plant for Use in the NRC Experimental Program at Argonne National Laboratory," Electric Power Research Institute report 1001558, May 2001.

NRC FORM 335 (12-2010) NRCMD 3.7	U.S. NUCLEAR REGULATORY COMMISSION 1. REPORT NUMBER (Assigned by NRC, Add Vol., Supp., Rev., and Addendum Numbers, if any.) NUREG/CR-7198, Rev. 1				
BIBLIOGRAPHIC DATA SHEET (See instructions on the reverse)					
2. TITLE AND SUBTITLE Mechanical Fatigue Testing of High-Burnup Fuel for Transportation Applications	3. DATE REPORT PUBLISHED <table border="1" style="width: 100%;"> <tr> <td style="width: 50%; text-align: center;">MONTH</td> <td style="width: 50%; text-align: center;">YEAR</td> </tr> <tr> <td style="text-align: center;">October</td> <td style="text-align: center;">2017</td> </tr> </table>	MONTH	YEAR	October	2017
	MONTH	YEAR			
October	2017				
	4. FIN OR GRANT NUMBER				
5. AUTHOR(S) Jy-An Wang and Hong Wang	6. TYPE OF REPORT Technical				
	7. PERIOD COVERED (Inclusive Dates)				
8. PERFORMING ORGANIZATION - NAME AND ADDRESS (If NRC, provide Division, Office or Region, U. S. Nuclear Regulatory Commission, and mailing address; if contractor, provide name and mailing address.) Oak Ridge National Laboratory Managed by UT-Battelle, LLC Oak Ridge, TN 37831-6069					
9. SPONSORING ORGANIZATION - NAME AND ADDRESS (If NRC, type "Same as above", if contractor, provide NRC Division, Office or Region, U. S. Nuclear Regulatory Commission, and mailing address.) Division of Systems Analysis Office of Nuclear Regulatory Research U.S. Nuclear Regulatory Commission Washington, DC 20555-0001					
10. SUPPLEMENTARY NOTES					
11. ABSTRACT (200 words or less) This report describes testing designed to determine the ability of high burnup (HBU) (>45 GWd/MTU) spent fuel to maintain its integrity under normal conditions of transportation. Since the initial publication of this NUREG in May 2015, several new factors were identified that influence the recorded curvature measurement data. Because these factors were not accounted for in the first publication, the initial quantitative results are not considered valid. This revision provides updated results of the 2015 CIRFT tests. After the 2015 publication, a new phase of testing was implemented that used samples treated to induce radial hydrides. This revision includes the results of CIRFT tests on segments subjected to hydride reorientation treatment (HRT), thus broadening the applicability of the research results. This first revision entirely replaces the initial May 2015 publication.					
12. KEY WORDS/DESCRIPTORS (List words or phrases that will assist researchers in locating the report.) Spent nuclear fuel, mechanical properties, spent fuel transportation, fatigue testing of spent nuclear fuel, bending stiffness of nuclear fuel	13. AVAILABILITY STATEMENT unlimited				
	14 SECURITY CLASSIFICATION (This Page) unclassified				
	(This Report) unclassified				
	15. NUMBER OF PAGES				
	16. PRICE				



Federal Recycling Program



UNITED STATES
NUCLEAR REGULATORY COMMISSION
WASHINGTON, DC 20555-0001

OFFICIAL BUSINESS



@NRCgov



NUREG/CR-7198, Rev. 1

Mechanical Fatigue Testing of High-Burnup Fuel for Transportation Application

October 2017